Optimisation and validation of three-dimensional polymer gel dosimetry and radiochromic gel dosimetry for clinical applications

Jan Vandecasteele

2013

Optimisation and validation of three-dimensional polymer gel dosimetry and radiochromic gel dosimetry for clinical applications

JAN VANDECASTEELE

2013

Promotor:
Prof. Dr. Yves De Deene

Faculty of Medicine and Health Sciences
Department of Radiation Oncology and Experimental Cancer Research

Thesis submitted in fulfillment of the requirements for the degree of Doctor in Medical Sciences

Universiteit Gent
Faculteit Geneeskunde en Gezondheidswetenschappen
Vakgroep Radiotherapie en Experimenteel
Kankeronderzoek

Optimalisatie en validatie van driedimensionale polymeer gel dosimetrie en radiochrome gel dosimetrie voor klinische applicaties

Optimisation and validation of three-dimensional polymer gel dosimetry and radiochromic gel dosimetry for clinical applications

---

Jan Vandecasteele

Promotor: prof. dr. Yves De Deene
Proefschrift tot het bekomen van de graad van
Doctor in de Medische Wetenschappen

Vakgroep Radiotherapie en Experimenteel Kankeronderzoek
Faculteit Geneeskunde en Gezondheidswetenschappen
Oktober 2013

Vandecasteele, Jan
Optimisation and validation of three-dimensional polymer gel dosimetry and radiochromic gel dosimetry for clinical applications
PhD Thesis Ghent University, Department of Radiotherapy and Experimental Cancer Research

Financial support for this PhD work:
Jan Vandecasteele was financially supported as PhD fellow by the Agency for Innovation by Science and Technology in Flanders (IWT-Vlaanderen)

ISBN: 978-94-6197-146-3

"Flying is learning how to throw yourself at the ground and miss. "
Douglas Adams, *The Hitchhiker's Guide to the Galaxy*

“Don’t just trust, but also verify ”
President Barack Obama, September 9th 2013

Promotor:
prof. Yves De Deene

Members of the doctoral guidance committee

prof.	Hubert Thierens	Ghent University
prof.	Luc Van Hoorebeke	Ghent University

Members of the examination board:

prof.	Ronald Verbeeck	(a)	Ghent University	BEL
prof.	Klaus Bacher	(b)	Ghent University	BEL
prof.	Werner De Gersem	(c)	Ghent University	BEL
dr.	Frederic Duprez	(c)	Ghent University	BEL
prof.	Dirk Verellen	(c)	Free University Brussels	BEL
dr.	Simon Doran	(c)	Institute of Cancer Research	GBR
prof.	David Thwaites		University of Sydney	AUS

(a) chairman
(b) secretary
(c) member of the reading committee

Research funded by a Ph.D. Fellowship of the Agency for Innovation by Science and Technology in Flanders (IWT-Vlaanderen).

Ghent University
Faculty of Medicine and Health Sciences

Department of Radiation Oncology
and Experimental Cancer Research
De Pintelaan 185, P7
B-9000 Gent, Belgium

Acknowledgment

I acknowledge all people that have contributed to the realisation of this work, especially my mentor and dear friend Yves. Our philosophical debates covered science and society, religion and beer. And sometimes all at once.

Ghent, October 2013
Jan Vandecasteele

Table of Contents

List of Acronyms

A

Aam	Acrylamide
AdapRT	Adaptive Radiotherapy

B

BGRT	Biological Guided RadioTherapy
Bis	N,N'-methylene-Bis-acrylamide

C

CCl_4	Carbon tetrachloride
CCl_3COOH	Trichloroacetic acid
$CHCl_3$	Chloroform
CMC	Critical Micelle Concentration
CBCT	Cone-Beam Computed Tomography
CT	Computed Tomography
CTAB	Cetyl TrimethylAmmonium Bromide
CTV	Clinical Target Volume

D

0D	Pseudo Zero-Dimensional
2D	Two-Dimensional
3D	Three-Dimensional
2D-RT	Two-dimensional RadioTherapy

3D-CRT	Three-dimensional conformal RadioTherapy
D	Radiation Dose
DNA	DeoxyriboNucleic Acid

E

E	Energy
EPID	Electronic Portal Imaging Device

F

FEP	Fluorinated Ethylene Propylene
FXG	Ferrous sulphate Xylenol orange Gel

G

GTV	Gross Target Volume

I

I	Initiator
ICRU	International Commission on Radiation Units
IGRT	Image Guided RadioTherapy
IMAT	Intensity Modulated Arc Therapy
IMRT	Intensity Modulated RadioTherapy

L

LCV	LeucoCrystal Violet
LET	Linear Energy Transfer
LMG	LeucoMalachite Green

M

M	Monomer
MAGAT	Methacrylic Acid in Gelatin with THPS
MAGIC	Methacrylic acid and Ascorbic acid in Gelatin Initiated by Copper
M_n	Polymer with n monomer units
MRI	Magnetic Resonance Imaging
MLC	Multi-Leaf Collimator
MVCT	Mega Voltage Computer Tomography

N

NCI	National Cancer Institute
NMR	Nuclear Magnetic resonance
NTCP	Normal Tissue Complications Probability

O

OD	Optical Density

P

PABIG	Poly(ethylene glycol) diacrylate And Bis in Gelatine gel
PAGAT	PolyAcrylamide Gelatine gel fabricated at ATmospheric conditions
PAGE	PolyAcrylamide Gel Electrophoresis
PET	Positron Emission Tomography
pHi	Isoelectric point
PMMA	Polymethylmethacrylate
PTV	Planned Target Volume

Q

QA	Quality Assurance

qMRI	Laboratory for Quantitative Nuclear Magnetic Resonance in Medicine and Biology

R

R	Reactive particle
R_1	NMR spin-lattice relaxation rate
R_2	NMR spin-spin relaxation rate
rBW	receiver Band Width
RPC	Radiological Physics Centre
RTAP	Resolution-Time-Accuracy-Precision

S

SD	Standard Deviation
SDS	Sodium DodecylSulphate

T

T	Tesla
T_1	NMR spin-lattice relaxation time
T_2	NMR spin-spin relaxation time
TCP	Tumour Control Probability
THPS	Tetrakis (Hydroxymethyl) Phosphonium Sulphate
TLD	Thermoluminescense Detector
TPS	Treatment Planning System

V

VIPAR	N-Vinylpyrrolidone and Bis in gelatine gel

W

WHO	World Health Organisation

X

XO	Xylenol Orange

Samenvatting
Summary

Samenvatting

Radiotherapie is erop gericht om een cytotoxische stralingsdosis te geven aan biologisch abnormale cellen terwijl het omringende gezonde weefsel gespaard blijft. Om dit te bereiken, wordt de patiënt doorheen een complexe behandelingsketen geleid bestaande uit medische beeldopnames, behandelingsplanning en behandelingssimulatie resulterend in de uiteindelijke stralingsbehandeling. Recente bestralingstechnieken maken gebruik van een modulering van het aantal bestralingsvelden, de hoek van waaruit zij op de patiënt invallen en de stralingsfluentie in ieder veld om de driedimensionale (3D) stralingsdosisverdeling te boetseren naar de vorm van de tumor. Uitgebreide kwaliteitswaarborging (QA) is nodig om te verzekeren dat de beoogde stralingsdosisverdeling werkelijk aan de patiënt wordt afgeleverd. Hiervoor worden ééndimensionale en tweedimensionale stralingsdosimeters routinematig toegepast. De meting van de volledige geïntegreerde 3D stralingsdosisverdeling in hoge resolutie ontbreekt echter nog in de huidige praktijk. Het doel van dit werk is om een betrouwbare gel dosimeter te ontwikkelen die gebruikt kan worden voor de kwaliteitswaarborging van de behandelingsketen bestaande uit onder andere de behandelingsplanning, simulatie en de uiteindelijke radiotherapiebehandeling. Deze techniek stelt ons in staat om de stralingsdosisverdeling in alle punten van de driedimensionale ruimte op te meten in een fantoom met humanoïde vorm.

Als onderdeel van deze doctoraatsscriptie, werd een radiochromatische gel dosimeter, die wordt uitgelezen met een optische laser Computergestuurde Tomografie (CT) scanner geoptimaliseerd en vergeleken met een polymeergel dosimeter die wordt uitgelezen met Magnetische Resonantie Beeldvorming (MRI).

De polymeergel dosimeter bestaat uit vinylmonomeren en een antioxidant, die zijn opgelost in een gelatine matrix. Bij bestraling, worden polymeerstructuren gevormd via een stralingsgeïnduceerde polymerisatiereactie. De gecreëerde polymeermoleculen worden geïmmobiliseerd door de gelatine matrix en de ruimtelijke verdeling van deze polymeren kan worden opgemeten met behulp van MRI. In eerdere studies werd aangetoond dat deze dosimeter superieure radiofysische eigenschappen bezat voor radiotherapie dosimetrie. De polymeergel dosimeter was echter onbetrouwbaar en behaalde geen klinisch aanvaardbaar niveau in termen van dosimetrische nauwkeurigheid wat ervoor zorgde dat slechts enkele radiotherapieklinieken wereldwijd in staat waren om gel dosimetrie te integreren in hun QA pro-

gramma's. De eerste doelstelling van dit werk was om de dosimetrische en geometrische onzekerheden van polymeergel stralingsdosimeters te kwantificeren. Wij hebben gefocust op de validatie van polymeergel dosimeters als "gouden standaard"3D stralingsdosimeters waartegen alle alternatieve 3D dosimetriesystemen kunnen worden getoetst. Door het uitvoeren van een reproduceerbaarheidsstudie werd een zwakke dosimetrische nauwkeurigheid vastgesteld die kan worden toegeschreven aan de kalibratie via kleine kalibratieproefbuisjes. In een tweede onderzoeksluik werd een analyse van de chemische en radiofysische eigenschappen van de polymeergel uitgevoerd om de invloed van een temperatuursverloop (vóór, tijdens en na bestraling), blootstelling aan zuurstof (na bestraling) en wandeffecten te kwantificeren. Al deze effecten bleken slechts een geringe invloed te hebben op de totale nauwkeurigheid van de gel dosimeter. In een derde studie werden verschillende MRI-gerelateerde bronnen van onzekerheden gekwantificeerd, zoals B_0 - veld en B_1 - veld inhomogeniteiten, diëlektrische effecten (verliezen en staande golven) en een temperatuursdrift tijdens de beeldvorming. Deze studie toonde aan dat temperatuursstabilisatie van de dosimeters essentieel is bij het uitvoeren van nauwkeurige dosismetingen. De resultaten van deze doctoraatscriptie bieden een handleiding voor het opmeten van stralingsdosisverdelingen van radiotherapiebehandelingen met polymeergel dosimeters op een nauwkeurige en betrouwbare manier. Wanneer strikte experimentele protocols worden gehandhaafd, kan de totale dosimetrische onzekerheid beperkt blijven tot ongeveer 5 %. Om deze mate van nauwkeurigheid te bereiken moet de gebruiker echter veel tijd investeren in de optimalisatie van de aanmaak, bestraling en uitlezen van de gel.

In radiochromatische gel dosimeters, worden micellen gebruikt om een leucokleurstof homogeen op te lossen in een gelatine matrix. De leucokleurstof wordt bij bestraling geoxideerd tot zijn chromatische vorm en kan dan worden opgemeten via optische transmissiemetingen met een eigen ontwikkelde optische laser CT scanner, de *Optoscan* genaamd. Om willekeurige en systematische onzekerheden in radiochromatische gel dosimetrie te kwantificeren, werd een onderzoek uitgevoerd naar de radiofysische eigenschappen van de gel. In deze studie werd aangetoond dat de gel dosis-tempo-afhankelijk is, wat de maximale dosimetrische nauwkeurigheid uiteindelijk beperkt. Chemische experimenten suggereren dat er ruimte is voor verbetering. Onderzoek naar de chemie van radiochromatische gel dosimeters en optimalisering van de formulering zijn nodig om een verdere vermindering van de dosis-tempo-afhankelijkheid te bekomen. Daarnaast werden ook onzekerheden, veroorzaakt door temperatuurschommelingen (tijdens de bestraling en uitlezing), ruimtelijke instabiliteit en atomaire samenstelling gekwantificeerd. Ten slotte werden radiochromatische gel dosimeters, uitgelezen met behulp van de *Optoscan* vergeleken met polymeergel dosimeters, uitgelezen met behulp van MRI voor een dosisverificatie van een klinische intensiteitsgemoduleerde radiotherapiebehandeling (IMRT) van een hersentumor. Deze studie toonde aan dat de radiochromatische gel te kampen

heeft met radiofysische onnauwkeurigheden veroorzaakt door *Schlieren* artefacten gecombineerd met beeldvormingsgerelateerde onnauwkeurigheden veroorzaakt door een mismatch van de brekingsindex en fantoom positioneringsonnauwkeurigheden. Deze onnauwkeurigheden kunnen gereduceerd worden door het optimaliseren van de chemische samenstelling, het aanmaakprotocol en het includeren van een reproduceerbare positionering van de gel dosimeter in de *Optoscan* scanner. De verwachting bestaat dat radiochromatische geldosimetrie een vergelijkbaar niveau van nauwkeurigheid kan bereiken als polymeergel dosimetrie, met het potentiëel van een lage kostprijs, eenvoudige aanmaak, snelle uitlezing en lineaire dosis-respons over een groot dynamisch bereik.

Het hier voorgestelde onderzoek werd uitgevoerd aan het Laboratorium voor Kwantitatieve Nucleair Magnetische Resonantie in Geneeskunde en Biologie (qMRI, onderdeel van de afdeling Radiotherapie en Experimenteel Kankeronderzoek) van de Universiteit Gent. De stralingsdosimetrie experimenten werden uitgevoerd in de faciliteiten van de afdeling Radiotherapie van het Universitair Ziekenhuis Gent. De MRI-metingen werden uitgevoerd op de afdeling Radiologie van het Universitair Ziekenhuis Gent. Dit werk resulteerde in vijf publicaties als eerste auteur in internationale tijdschriften en verschillende abstracts op internationale (9) en nationale (4) conferenties.

Summary

Radiotherapy aims at delivering a cytotoxic dose of radiation to biologically abnormal cells while the surrounding, healthy tissues are spared. To achieve this, the patient is treated following a complex chain of image acquisition, treatment planning and treatment simulation. Recent, advanced treatment delivery techniques modulate the number of fields, the angle from which they incident the patient and the radiation fluence within each field to tailor the three-dimensional (3D) dose distribution to the shape of the tumour. Comprehensive quality assurance (QA) techniques are needed to verify that the planned radiation dose distribution is actually delivered to the patient. For this, one-dimensional and two-dimensional dosimeters are routinely applied. However, the measurement of the full, integrated 3D dose distribution in high resolution is lacking in routine QA applications. The goal of this work is to provide a reliable 3D gel dosimeter which allows for the quantitative measurement of the radiation dose distribution in all points of 3D space in a phantom of humanoid shape as an important tool for end-to-end verifications of radiotherapy treatments.

As part of this Ph.D. dissertation, a polymer gel dosimeter, read out with Magnetic Resonance Imaging (MRI) and a radiochromic gel dosimeter, read out with an optical laser Computer Tomography (CT) scanner were optimised and benchmarked.

The polymer gel dosimeter consists of vinyl monomers and an antioxidant which are dissolved in a gelatin matrix. Upon irradiation, polymer structures are formed due to a radiation induced polymerisation reaction. The created polymer molecules are immobilised by the gelatin matrix and the spatial distribution of these polymers can be imaged using MRI. In previous studies, this dosimeter was shown to have superior radio-physical properties for radiotherapy dosimetry. The normoxic polymer gel dosimeter, however, had a low accuracy and precision resulting in only a few clinics worldwide able to incorporate it in their QA programs. The first objective of this work was to quantify the dosimetric and geometric uncertainties of normoxic polymer gel dosimeters with MRI readout. We focussed here on validating polymer gel dosimeters as a "gold standard" 3D gel dosimeter against which all alternative 3D dosimetry systems could be benchmarked. By performing a reproducibility study, a poor dosimetric accuracy was found which was attributed to the calibration using small calibration vials. In a concurrent study, an analysis of the chemical and radio-physical charac-

teristics of the polymer gel was performed to quantify the influence of the temperature history (pre-, during and post-irradiation), oxygen exposure (post-irradiation) and recipient wall effects. These effects were shown to have only a minor influence on the overall uncertainty of the gel dosimeter. In a third study, several MRI related sources of uncertainties were quantified, such as B_0-field and B_1-field non-uniformities, dielectric effects (losses and standing waves) and temperature drifts during scanning. This study demonstrated that temperature stabilisation techniques are vital in performing accurate dose measurements. The results from this Ph.D. dissertation provide a recipe to measure radiotherapy delivered dose distributions with polymer gel dosimeters with reduced uncertainties within clinical acceptable levels. When strict experimental procedures are followed, the overall uncertainty is limited to approximately 5 %. To achieve this degree of certainty however, the user has to invest a lot of time in optimising fabrication, irradiation and scanning protocols.

In radiochromic gel dosimeters, micelles are used to homogeneously dissolve a leucodye in a gelatine matrix. The leucodye is oxidised to its chromatic form upon irradiation and can be imaged with optical transmission measurements using an in-house built optical laser CT scanner, the Optoscan. To quantify random and systematic uncertainties associated with radiochromic gel dosimetry, a study was performed to investigate the radiophysical characteristics of the gel. In this study, the gel was shown to be dose rate dependent, ultimately limiting the minimal dosimetric uncertainty. However, chemical modifications suggest that there is room for improvement. Research into the chemistry of radiochromic gels and optimisation of the formulation is needed to further reduce the dose rate dependency. Furthermore, uncertainties related to temperature variations (during irradiation and scanning), spatial instability and atomic composition were quantified. Finally, the radiochromic gel which is read out using the Optoscan was benchmarked against the polymer gel which is read out using MRI for a dose verification of a clinical Intensity Modulated Radiotherapy Treatment (IMRT) of a brain tumour. This study revealed that the radiochromic gel suffered from radio-physical uncertainties originating from *Schlieren* artefacts combined with scanning related uncertainties from a refractive index solution mismatch and phantom positioning irreproducibility. These uncertainties can be reduced by optimising the chemical composition and fabrication protocol of the gel and further adaptation of the optical laser CT scanner by incorporating a highly reproducible technique in positioning the phantom. It is expected that radiochromic gel dosimetry can reach a comparable level of uncertainty as polymer gel dosimetry, with the expectation of reduced cost, easier fabrication, fast readout and linear dose response over a large dynamic range.

The research presented here was conducted at the Laboratory for Quantitative Nuclear Magnetic Resonance in Medicine and Biology (qMRI, part of the Department for Radiation Oncology and Experimental Cancer Re-

search) of the Ghent University. The radiation dosimetry experiments were performed at the facilities of the Radiotherapy Department of the Ghent University Hospital. The MRI measurements were performed at the Department of Radiology of the Ghent University Hospital. This work resulted in five publications as first author in international journals and several abstracts and proceedings at international (9) and national (4) conferences.

Optimisation and validation of three-dimensional polymer gel dosimetry and radiochromic gel dosimetry for clinical applications

1 Introduction

1.1 Preface

Radiotherapy, surgery and systemic therapies are the principal therapeutic treatment modalities in the fight against cancer. Radiotherapy uses ionizing radiation or particles to sterilise or kill malignant cells. Ionizing radiation creates ionisations and free radicals which damage the genetic material of irradiated tissue. The cell damage is caused by either direct or indirect ionisation of the atoms which make up the genetic material (deoxyribonucleic acid or DNA chain). Indirect ionisations originate from the ionisation of water abundantly available in each cell, creating free radicals, which then damage the DNA. Tumour cells are less effective in repairing the inflicted DNA damage compared to healthy cells which is the basis of the curative nature of radiotherapy (Levitt *et al* 2006).

To produce high energy radiation beams, typically photons or electrons, linear accelerators are used which have undergone considerable development since their introduction in the late 1950s. Until the mid 1980s conventional two dimensional radiotherapy (2D-RT) was performed by aiming a single, geometrically quite simple, radiation beam from one to four directions to intersect at the tumour. A conventional radiotherapy treatment is simulated by using a special diagnostic x-ray machine known as a simulator which recreates the linear accelerator geometric actions. The aim of simulation is to accurately target or localize the volume which is to be treated. 2D-RT is limited by the amount of radiation that can be delivered to normal healthy

tissues without resulting in complications and toxicity (Khan 1993).

The invention of computed tomography (CT), the multileaf collimator (MLC) and the increasing computational power created a shift from 2D to 3D radiotherapy planning and delivery. In three-dimensional conformal radiotherapy (3D-CRT), treatment planning typically uses a beam's eye view approach. In other words, a variable number of radiation beams are designed to follow the shape of the tumour more closely, so the radiation beam avoids healthy tissue as much as possible (Bortfeld *et al* 2005).

Intensity-modulated radiation therapy (IMRT) is a recent advance and is now widely available in high income countries. It allows modulation of the intensity (or more correctly, the fluence) of each radiation beam by moving the MLC across the field, so each field has multiple areas of high fluence radiation and any number of lower fluence within the same field, thus allowing for greater control of the dose distribution. By modulating both the number of fields, the angle from which they approach the patient and the fluence of radiation within each field, the radiation dose can be sculpted into limitless shapes. This highly customized radiation dose distribution is intended to maximize tumour doses while simultaneously protecting the surrounding normal tissue. Several variations of this principle have been adopted in the clinic, including the multiple-static field MLC technique, the dynamic MLC technique, Intensity Modulated Arc Therapy (IMAT), static and helical tomotherapy and Cyberknife (Bortfeld *et al* 2005).

Overconfidence in the accuracy of patient positioning and associated organ localisation may increase the chance of missing lesions that are invisible on the planning image data set or that move between or during treatments. New techniques are therefore being developed to better control this uncertainty, for example, real-time imaging during treatment. This new technology is called image-guided radiotherapy (IGRT) and will probably become the new standard (Korreman *et al* 2012).

The ultimate treatment delivery technique incorporates all real-time patient data acquired from functional and anatomical imaging techniques and is called adaptive radiotherapy (AdapRT). AdaptRT is however a broad concept. Originally it was proposed to deal with positioning uncertainties based on the knowledge of patient set-up and organ motion obtained from imaging during treatment (Yan *et al.* 1997). Another approach of AdapRT focusses on changes in the tumour's (or normal tissues) morphology and biology to alter the radiotherapy treatment. This definition will be used in the dissertation. Such AdapRT may use cone-beam CT images for treatment monitoring and treatment planning on a daily or weekly basis to compensate for any changes in the patients anatomy during the treatment course. Additional information on important biological factors such as hypoxia and

glucose metabolism acquired from MRI or PET imaging are also included in the treatment process. Furthermore, by delivering a heterogeneous radiation dose based on the biological profile of the tumour, these regions in the tumour that show a higher biological abnormality will receive a higher dose, i.e. dose painting or biological IGRT (BGRT, Steward and Li 2007).

From the previous paragraphs, it can be concluded that modern radiotherapy is a multidisciplinary speciality based on a complex treatment chain of image acquisition, treatment planning and treatment delivery over the course of several weeks. Treatment effectiveness depends strongly on the accuracy of the radiotherapy dose delivery. This warrants the need for adequate quality assurance (QA) measures which validate and monitor all individual steps as well as the whole sequence of interventions which result in the treatment of the patient.

1.2 Uncertainties

A well-designed quality assurance program should address all uncertainties that are involved in the treatment delivery procedures. Firstly, this includes the possibility of human error which is of course an important element to counteract using a dedicated QA program. Furthermore, all individual steps contributing to the treatment of a patient are associated with inherent uncertainties. To consider uncertainty in more detail, the definitions of "accuracy" and "error" are first clearly defined. The accuracy of a (dose) measurement is defined as the closeness of agreement of a measured or calculated physical quantity (measurand) to its actual or true value. The associated error is the difference between the measured value and the true value. This total error value is composed of two parts, a random component and a systematic component. As proposed by the Joint Committee for Guides in Metrology (JCGM 2008), a "random error 'presumably' arises from unpredictable or stochastic temporal and spatial variations of influence quantities" and a systematic error is defined as "the mean that would result from an infinite number of measurements of the same measurand carried out under repeatability conditions minus a true value of the measurand" (JCGM 2008). Random errors are caused by random effects (unpredictable or stochastic variations) and systematic errors are caused by systematic effects (recognized effect of an influence quantity on a measurement result). The problem with the concepts "accuracy" and "error" lies in the fact that they are related to a "true" value. However this true value is ultimately unknown and thus "error" and "accuracy" are idealized concepts of which the actual values also cannot be exactly known. This problem can be dealt with by introducing the term "uncertainty". Uncertainties are divided into

two categories based on their method of evaluation: type A and type B (Giacomo 1981). Type A is obtained from a series of independent observations from which the standard deviation can be extracted. In other words, type A uncertainties are obtained from statistical analyses. Type B uncertainties are obtained from an analysis of the measurement procedure during which uncertainty values are allocated to all steps involved based on a degree of belief (in other word type B uncertainties are evaluated by other means than statistical, *e.g.* manufacturer given calibration factors or textbooks data). Thus the difference between type A and type B uncertainties is distinguished based on their origins and not on the concepts "random" and "systematic". Finally the definition of precision of a measurement is the closeness of agreement between multiple repeated but independent measurements of a physical quantity under identical conditions (reproducibility).

To illustrate the concepts of accuracy and precision in radiotherapy the following hypothetical example is given. In the specific situation of radiotherapy treatments within one department and one treatment modality, the precision of the administered radiation doses is the most critical parameter. In other words, the reproducibility which is affected by random effects is much more important than actual dose. However, when different modalities, fractionation schemes, or institutions are compared, the knowledge of any systematic effects on the absolute dose should also be evaluated. The total uncertainty can be calculated by squaring both type A and type B uncertainties, followed by a summation and taking the square root of the sum (Mijnheer 2007).

1.3 Estimation of uncertainties in radiotherapy

The clinical outcome of a radiotherapy treatment depends predominately on the ability to have a successful tumour control while minimising the dose to surrounding critical structures. The success is thus determined by both the geometrical and dosimetric uncertainties. The geometrical uncertainty is mainly affected by the clinical localisation of the target volume during the treatment planning and the ability to cover the tumour volume during treatment delivery. From a medical physics point of view, an accurate tumour coverage poses the biggest challenges. Although recent developments have resulted in highly conformal radiotherapy techniques which add to the possibility of treating the tumour volume in a geometrical highly conformal manner, the complexity of the techniques and the many uncertainties in patient localisation, machine tolerances, set-up variations and others can lead to a partial incorrect spatial dose deposition or even a total miss of the tar-

get. For these uncertainties, margins around the gross target volume (GTV, defined as the volume that can be seen, palpated or imaged) or clinical target volume (CTV = GTV + microscopic infiltration in the surrounding tissues presenting itself as sub-clinical disease) are incorporated during the planning process expanding the CTV to a planned target volume (PTV). The expansion size of this margin is a compromise between unavoidable geometrical uncertainties and irradiating a large amount of healthy tissue resulting in toxicity. Despite the use of tolerant safety margins, geometric uncertainties will always affect the dose distribution, evermore so in highly conformal treatment modalities were dose painting is used to vary the dose inside the tumour based on biological data. It is however difficult to quantify the required geometrical accuracy for radiotherapy. Several groups of authors have concluded that an uncertainty within 2 to 4 mm at the field edges in relation to the PTV are required (Mijnheer *et al* 1987). However set-up uncertainties and organ motion both strongly influence the geometrical uncertainties. Set-up uncertainties can result in variations of up to 4 mm (abdomen and pelvis) and organ motion can be as large as 20 mm in bladder and lung cases (Hartmann 2009). There is no general consensus on an exact baseline but the increasing availability and use of on-line imaging systems such as portal imaging (MVCT) and cone-beam CT (CBCT) will help decreasing the geometrical uncertainties (Bujold *et al* 2012).

Besides the geometrical accuracy, the success rate of treatments depends on the accuracy of the absolute delivered dose level of which the importance can be demonstrated by dose-response curves. In figure 1.1, curves for both tumour control probability (TCP) and normal tissue complications probability (NTCP) are shown which have a characteristic sigmoid shape.

These curves illustrate that a small variation in dose level (ΔD) can have a considerable influence on the probability of tumour control (ΔP_T) and also on the occurrence of local normal tissue complications (ΔP_{NT}). Clinical data have shown that a difference in absorbed dose of 7 % to the target can lead to normal tissue reactions (Dutreix *et al* 1984). Moreover, a thorough knowledge of the absorbed dose is vital from the point of view of tumour control. A dose difference of 10 % clearly affects the tumour control probability as shown by multiple studies (Hanks *et al* 1990, Morrison *et al* 1975, Shukovsky *et al* 1970, Perez *et al* 1980).

The risk of mild to moderate toxicity to patients from dosimetric and geometric errors was found to be approximately 1500 per million treatment courses ($\sim$ 0.15 % per treatment course) (Shafiq *et al* 2009, WHO 2008). The risk of serious injuries is between 50 and 100 per million treatment courses (Munro 2007). These risks do not take into account the errors that are likely to go undetected such as under-dosage. A good example for this

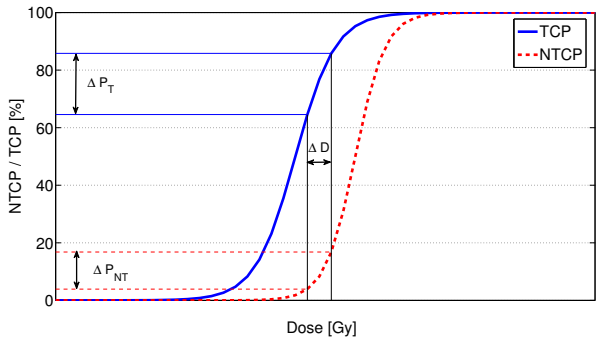

Figure 1.1: *A typical tumour control probability (TCP) curve and normal tissue complications probability (NTCP) curve are shown to demonstrate the effect of a small dose error (ΔD) on the control probability of the tumour (ΔP_T) as well as the occurrence of local complications (ΔP_{NT}).*

was found in the UK were approximately 1000 patients over a period of 10 years suffered an under-dosage between 5 % to 35 %. About 50 % (N=492) of these patients developed local recurrences that could be attributed to the irradiation error (Ash and Bates 1994).

The complexity of an accurate radiotherapy treatment delivery is furthermore demonstrated by a study performed between 2001 and 2009 by the Radiological Physics Centre (RPC) that functions under the auspicious of the National Cancer Institute (NCI) while credentialing radiotherapy centres in the United States for using IMRT (Ibott 2010). The RPC provided institutions participating in IMRT clinical trials with anthropomorphic phantoms (of head and pelvis) containing various dosimeters. The centres were given an IMRT objective and asked to irradiate the phantom using their usual IMRT planning and delivery technique. The results were staggering: about one third of the centres failed the RPC credentialing phantom test on the first attempt despite generous criteria (7 % dose difference and 4 mm distance to agreement) in the high dose regions near the organ at risk. The RPC experience, the results by various individuals in their clinics, and the deliberations of working groups are leading some to conclude that radiation therapy quality assurance programs need to be reconsidered for IMRT (Bisonette *et al* 2008, Basran *et al* 2008, Both *et al* 2007, Broggi *et al* 2008, Howell *et al* 2008, Jin *et al* 2008, Marks *et al* 2007).

The ICRU Report No. 24 (1976) suggested that the radiation dose should be delivered within 5 % of the prescribed dose. However, several

other studies have concluded that the accuracy should be even better, up to 3.5 % (Mijnheer *et al* 1987) or 3 % (Brahme *et al* 1988). In a recent study, it is recommended that this figure of 3 % is too strict and should be defined at 5 % (1 standard deviation (SD)) which has a realistic chance of being fulfilled in practice (Hartmann 2009).

It should be noted that the 5 % - 4 mm dosimetric and geometric uncertainties only act as a general guideline. In some cases such as palliative treatments, a larger deviation seems acceptable while in other cases more stringent parameters should be applied.

1.4 Quality assurance in radiotherapy

To achieve a high level of geometrical and dosimetric accuracy, strong demands on the quality assurance of the treatment must be made. According to World Health Organisation (WHO 1988) guidelines: "Quality assurance (QA) in radiotherapy is all procedures that ensure consistency of the medical prescription, and safe fulfilment of that prescription, as regards to the dose to the target volume, together with minimal dose to normal tissue, minimal exposure of personnel and adequate patient monitoring aimed at determining the end result of the treatment". Thus, the aim of quality assurance is to produce and maintain consistent and continuing quality in treatment. An adequate quality assurance programme should minimize errors and accidents.

Modern radiotherapy clinics use a variety of QA methods to investigate the quality of the treatment delivery on a (routine) basis. Pseudo zero dimensional (0D, commonly known as one dimensional) dosimeters have long been regarded as the workhorses of radiotherapy QA. Ionisation chambers excel in obtaining point-dose measurements to commission a treatment unit, calibrate output or verify dose delivery. They have excellent stability, linear response, energy independence, directional independence and can be used in real time. However, in conformal treatments in which high dose gradients, inhomogeneous dose distributions and small field size are used, the size of an ionisation chamber can pose a serious challenge. The use of small volume ionisation chambers such as the microLion chamber with measuring volume of 1.7 mm^3, (PTW type 31018, Freiburg, Germany) can solve some of these limitations. Nevertheless, ionisation chambers inherently only measure in one point resulting in limited information on the dose distribution inside a volume. In rotational therapy settings such as tomotherapy, great care should be taken when using ionisation chambers because some of the reference conditions such as field size and measuring depth can not be achieved. Solid state detectors such as silicon diode de-

tectors, diamond detectors and thermoluminescence detectors (TLD's) have attractive properties for megavoltage dosimetry. Silicon diodes and diamond detectors have good characteristics for measuring small radiation fields but conformal treatment verification can pose challenges because of dose rate dependence (diamond detector) or sensitivity to low energy photons and directional dependence (diodes). TLD's are reliable dosimeters but are very labour intensive to obtain a dosimetric precision of only 3 % (Low *et al* 2011, Schreiner 2006, 2011).

Two dimensional (2D) dosimetry has the advantage of probing a plane in a dose distribution which enables the medical physicist to assess additional spatial information. The common options are radiographic films, radiochromic films, arrays of diodes or ionisation chambers and electronic portal imaging devices (EPID's). Radiographic films can be used as a relative dosimeter for treatment verifications although many important considerations apply such as development conditions, inter batch differences and densitometry artefacts, making this technique complex and labour intensive. Radiochromic films have largely replaced radiographic film dosimeters in radiotherapy clinics. Although radiochromic film dosimeters have suffered from vendor switches which resulted in some low quality batches. Recent studies are showing excellent results when a dedicated protocol is used to correct for film history and processing and readout system inhomogeneities (Micke *et al* 2011, Mayer *et al* 2012). 2D arrays of diodes or ionisation chambers are a popular dosimetric verification device because of their ability to perform multiple dose readings per beam which can be immediately interpreted. As a compromise, they have a limited spatial resolution (as compared to films) which results in the need for interpolation of the measured data using dedicated software. Furthermore, 2D arrays do not integrate the dose of a treatment which limits the knowledge of the clinical relevance of any accumulated errors from multiple individual beams. EPID based dosimetry is a very attractive tool which hovers in between 2D and 3D dose verification. As a 2D dosimeter they measure the fluence exiting a patient or phantom using an imaging panel and compare this fluence map with the anticipated exit fluence predicted by the treatment planning system. The complexity associated with the correction for scatter and detector response however limit the widespread availability of this technique (Low *et al* 2011, Schreiner 2006, 2011).

Pseudo three dimensional (3D) dosimeters have become more and more adopted in routine dose verifications of conformal treatments (IMRT and IMAT). These pseudo 3D systems use detector arrays of diodes of ionisation chambers distributed inside a phantom. The commercially available systems provide topologies in a plane, (MatriXX and MultiCube phantom IBA, Bel-

gium and Map Check, Sun Nuclear, USA), a ring (Arc Check, Sun Nuclear), a rotating plane (Octavius, PTW, Germany) or two cross-sectioning planes (Delta4, Scandidos, Sweden). These systems provide a fast and convenient technique to validate complex treatments. Although the same limitations as for 2D arrays still apply. These detectors require a careful calibration in reference conditions which may not always be the same conditions used during measurement of a specific radiation treatment. Full 3D dosimetry is possible with EPID's and chemical dosimeters. EPID's can calculate the 3D dose distribution inside a patient or phantom based on the measured exit fluence using dedicated algorithms to project back the measured data. As such they can be used as the ultimate *in vivo* dosimeter. This technique is in its early stage of clinical implementation. Commercial transit dosimetry software has been developed to verify actual daily radiation doses using the EPID devices already available in the hospital (EPIgray, Dosisoft, Cachan, France and Dosimetry Check, Oncology Systems Limited, Shrewsbury, UK). This system marks a new era in *in vivo* dosimetry although some limitations still need to be considered including the limited size of radiation fields that can be measured. 3D chemical dosimeters most commonly known as gel dosimeters will be further discussed in section 1.6.

1.5 Where does 3D dosimetry fit in the clinic?

The verification of 3D dose distributions is essential to the effective delivery of radiation therapy as both geometrical and dosimetric accuracy hold a pivotal role in the clinical outcome as described above. In the specific case of highly conformal techniques such as IMRT and IMAT, the doses are furthermore delivered dynamically during which multiple beam defining parameters such as the dose rate, radiation fluence and shape of the beam vary continuously. This warrants the need for an integrating dosimetry technique. In an integrating dosimeter, accumulated errors can be immediately linked to their clinical relevance. After an error is detected, one should assess in which stage of the radiotherapy process the error manifested and perform an in-depth analysis including further dosimetric measurements using more suitable dosimeters. This allows to detect any breaches in the QA system and safeguards the whole treatment chain (3D imaging of the patient, transfer of scans to treatment planning computer, treatment planning, positioning the patient, transfer of treatment protocol to the treatment machine and treatment delivery, figure 1.2).

A chain is as strong as its weakest link, so QA and dosimetric (and geometric) measurements should be performed as a holistic protocol. As Leer *et al* 1998 suggested, radiotherapy quality assurance should not be

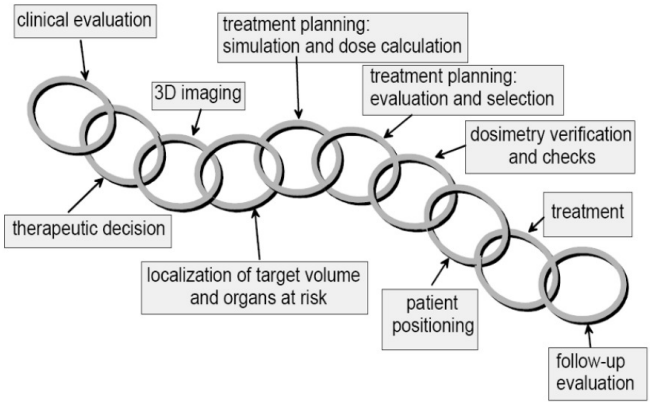

Figure 1.2: *The treatment chain of radiotherapy from clinical evaluation of the patient to follow up after treatment (taken from Hartmann et al 2009).*

limited to the technical aspects of the treatment delivery but should include all activities in a radiation oncology centre from the moment the patient enters until the moment the patient leaves.

In section 1.3 it was shown that the dose distribution resulting from conformal treatments are designed to be highly conformed around the target volumes, increasing the risk of (partially) missing the target. Therefore the focus of dosimetry and QA has shifted from absolute dose determination in a single point to verifying the whole 3D dose distribution. With 0D and 2D dosimeters only a partial sampling of the whole dose distribution is achieved. Therefore, 3D dosimetry techniques are highly desirable in the preparatory steps towards implementation of a new and more complex method of dose delivery (such as IGRT and AdapRT).

3D Chemical dosimeters such as gels and radiochromic plastics are inherently 3D dosimeters and have an advantage over the traditional dosimeters such as ionisation chambers and films in applications of radiotherapy dosimetry. Since the dose distribution is recorded in 3D, gel dosimeters play a role in validating the commissioning of a treatment planning system. Especially, in smaller radiation therapy clinics, 3D gel dosimetry can facilitate and help in the introduction of advanced treatment techniques. Gel dosimetry can furthermore support multi-centre clinical trials on the implementation of new advanced radiotherapy treatment techniques and play a vital role in developing and implementing nationwide credentialing programmes.

As 3D gel dosimeters can be moulded in humanoid shapes, they mimic a patient during the whole treatment starting with the acquisition of a set of medical images (CT and/or MRI). The image data set of the gel dosimeter phantom is transferred to the treatment planning computer. Subsequently, a treatment plan is designed and optimised for the gel dosimeter phantom (corresponding to a realistic treatment plan of a patient). A reference coordinate system is then transferred onto the gel dosimeter phantom which corresponds to the virtual phantom in the treatment plan. The gel dosimeter is then positioned on the treatment table with a similar degree of accuracy as is possible with a real patient and the actual radiation therapy treatment is performed. The dose distribution recorded within the gel dosimeter is read out by a dedicated readout system. The measured dose distribution is then compared with the planned dose distribution. When X-ray imaging techniques are used to verify the actual positioning of the target during the course of the treatment, the additional radiation doses are also recorded by the gel dosimeter as they are also added to the patients dose.

Adaptive radiotherapy where treatment planning is optimised on a daily or weekly basis based on anatomical or functional images is on the verge of clinical application. 3D dosimeters can prove to be of great importance to simulate the effect of dose accumulation in deforming anatomy and to validate software algorithms that calculated the dose-warping in a patient. Gel dosimeters are easily deformed (Yeo *et al* 2012) and their compositions are easily changed depending on the mechanical properties that are needed. Patient set-up and tumour and organ motions studies especially in rotational and dynamic techniques can further benefit from 3D dose measurements to validate robust treatment planning algorithms and tumour tracking efficacy. These examples show some of the areas where gel dosimeters will assist radiation oncologists and medical physicists in optimising treatment protocols what is suspected to ultimately result in an increased treatment effectiveness.

Gel dosimeters can play an important role in the dose verification strategies in radiotherapy as demonstrated in De Wagter 2004 and in figure 1.3. This figure, which is an adaptation of the figure presented in De Wagter 2004, illustrates a top-down model of radiotherapy QA in which the top layers count on the strengths of the layers below them. For the quality assurance of new delivery techniques or the application of existing techniques in a new clinical situation, the QA starts at the top of the pyramid by performing a 3D dosimetry measurement of an entire treatment. If dosimetric or geometric uncertainties are revealed exceeding predefined tolerance levels, QA measures in the lower levels of the pyramid can be applied to explore the origins of the uncertainties.

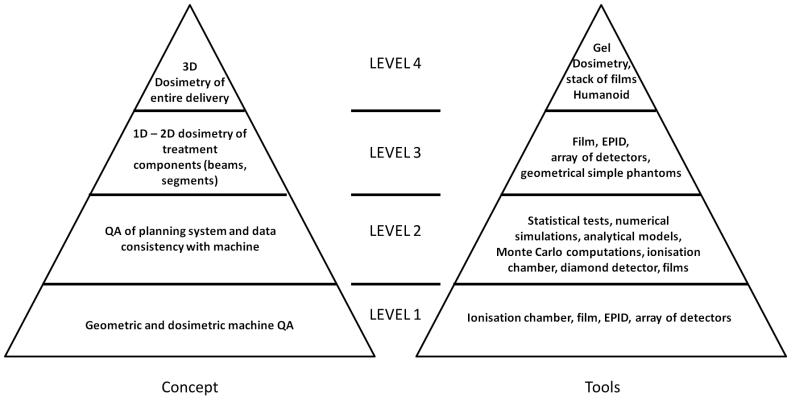

Figure 1.3: *Top-Down model of the various levels of QA in radiotherapy (Adapted from De Wagter 2004).*

In the next section, a brief historical overview of gel dosimetry is given followed by a discussion of the composition and chemical reactions which result in the recording of the 3D dose information of gel dosimeters.

1.6 Gel dosimetry

1.6.1 Fricke gel dosimeters

The first gel dosimeters proposed for radiation therapy were developed by Gore *et al* in 1984 who added a ferrous sulphate solution into a chemical gel matrix to contain the 3D dose information which then could be measured using nuclear magnetic relaxometry (NMR) (Gore *et al* 1984). These gel dosimeters were based on the Fricke solution in which ferrous (Fe^{2+}) ions are converted to ferric (Fe^{3+}) ions upon irradiation (Fricke and Morse 1927). Both ions have a different NMR spin-lattice relaxation rate ($R_1 = 1/T_1$) which allows the use of quantitative MRI sequences to image the amount of radiation induced conversion of ferrous to ferric ions. These Fricke gel dosimeters were fairly quickly shown to suffer from spatial instabilities originating from the diffusion of ferric and ferrous ions within the gel matrix following the irradiation (Olsson *et al* 1992). The diffusion rate of the reporter molecules inside the dosimeter was found to be affected by the type of gelling agent (*e.g.* gelatin (Olsson *et al* 1990), agarose (Appleby *et al* 1987), sephadex (Hiraoka *et al* 1992), polyvinylalcohol (Chu *et al* 2000)), the concentration of the gelling agent and other properties of the dosimeter (Baldock *et al* 2001a). Additionally, metal chelators such as xylenol orange

(XO) succeeded in improving the spatial stability of the recorded dose distribution while also allowing for a visible inspection due to a colour change of the gel upon irradiation (Gupta and Gomathy 1974, Gupta *et al* 1982, Gupta *et al* 1985 and Appleby *et al* 1991). The chemical fine-tuning did not entirely eliminate the diffusion of ferric ions which still resulted in a limited timespan during which the quantitative dose distribution could be imaged with MRI. In the gel dosimetry community, the search for more spatially stable dosimeters was therefore proceeded.

1.6.2 Polymer gel dosimeters

In 1992, a novel gel dosimeter formulation was proposed which was based on the radiation induced polymerisation of the acrylamide (Aam) with a crosslinker N,N'-methylene-Bis-acrylamide (Bis) incorporated in a gel matrix (Maryanski *et al* 1992, Maryanski *et al* 1994). The idea to use polymers as dosimeters originated in 1954, when Alexander *et al* studied the effects of ionising radiation on polymethylmetacrylate (PMMA). In 1958, Hoecker and Watkins (1958) examined radiation induced polymerisation in liquids followed by Boni (1961) who investigated the degradation of polyacrylamide by X-rays and gamma irradiation. In 1992, Kennan *et al* demonstrated that MRI relaxation rates of irradiated solutions of Bis and agarose increased with absorbed doses (Kennan *et al* 1992). In the polymer gel dosimeter proposed by Maryanski in 1992, radiation induced radicals originating from the radiolysis of water initiate a polymerisation reaction between Aam and Bis forming a network of polymer. This polymer network is entangled in the gel matrix which results in a much more spatially stable dosimeter as compared to Fricke gel dosimeters. The polymer structures formed during the irradiation are shown to be best probed by MRI spin-spin relaxation rate ($R_2 = 1/T_2$) measurements. A strong focus on accuracy and precision of the dosimetric technique revealed the importance of several artefacts. An optimisation of the composition of the gel and the detailed fabrication procedure have led to the reduction of uncertainties associated with the fabrication (De Deene *et al* 2000d, 2002a, 2002b and 2007). An extensive investigation of the physico-chemical and radio-physical properties of the gel resulted in a more reliable gel dosimeter (Vergote *et al* 2004b, De Deene *et al* 2006a). Scrutinising the influence of MRI imaging revealed that dedicated strategies are vital to eliminated potential imaging artefacts such as eddy currents, B_1-field non uniformities and temperature drift during scanning (De Deene *et al* 2000a, De Deene *et al* 2000b, De Deene and De Wagter 2001). Finally, the optimal choice of the MRI imaging sequence and sequence parameters and post-processing calculations applied, significantly reduce the noise in the dose maps as mathematically and experimentally

shown in De Deene *et al* (1998a).

During the fabrication process, atmospheric oxygen needs to be removed from the gel solution as oxygen radicals are created during the irradiation and subsequently inhibit the radiation induced polymerisation processes. This is accomplished by manufacturing the gel in an oxygen free environment (such as a nitrogen-gas filled glove box). This procedure caused a significant limitation to the widespread dissemination of polymer gel dosimeters in clinical radiotherapy centres as the use of a glove box is both time consuming and labour intensive.

In 2001, a breakthrough in the development of more user-friendly gel dosimeter was made by introducing anti-oxidants to bind the oxygen present in a polymer gel dosimeter in a complex and thus eliminating the polymerisation inhibition (Fong *et al* 2001). These so-called "normoxic polymer gel dosimeters" could be manufactured on the laboratory bench-top under standard atmospheric conditions. Several antioxidants were proposed including ascorbic acid (used in a MAGIC gel) and tetrakis (hydroxymethyl) phosphonium sulphate (THPS) resulting in a normoxic gel dosimeter called PolyAcrylamide Gelatin gel fabricated at ATmospheric conditions (PAGAT, De Deene *et al* 2002a, Baldock 2006). Several other monomers have also been suggested as active components in normoxic polymer gel dosimeters such as: PABIG (using poly(ethylene glycol) diacrylate and bis), VIPAR (using N-vinylpyrrolidone and bis) and MAGAT (using methacrylic acid).

The normoxic polymer gel dosimeter used in the publications of this dissertation is PAGAT. The composition consists of a large fraction of deionised water (about 88 % w/w), the monomers acrylamide (about 2.5-3 % w/w) and Bis (about 2.5-3 % w/w) embedded in a gelatin matrix (about 6 % w/w). A small amount of the anti-oxidant THPS is added to inactivate the atmospheric oxygen (5 mM, about 0.3 % w/w) (Bayreder *et al* 2006).

Acrylamide and Bis (figure 1.4) are used to synthesize polyacrylamides which act as a thickener in for example gel electrophoresis (SDS-PAGE). Great care in handling these monomers is required as acrylamide is a well-known neurotoxin and carcinogen and Bis can cause irritations and is a suspected carcinogen.

In a PAGAT gel dosimeter, the dissolved monomers acrylamide and Bis are polymerised by high energy X-rays. This process starts with the dissociation of water molecules (radiolysis of water) in highly reactive radicals and ions characterised by a dissociation constant k_D (equation 1.1) (Baldock and De Deene *et al* 2010). These reactive particles (mostly e^-_{aq}, $OH^\bullet$, $H^\bullet$, also referred to as $R^\bullet$) initiate the polymerisation by reacting with available monomers (M) or with already formed polymer with n monomer units (M_n) (equation 1.2).

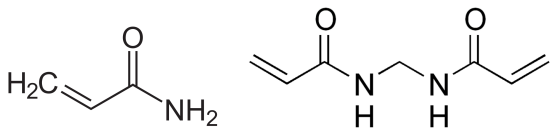

(a) (b)

Figure 1.4: *Molecular structure of acrylamide (a) and N,N'-methylene-Bis-acrylamide(b).*

$$H_2O \xrightarrow{k_D} 2R^{\bullet} \tag{1.1}$$

$$R^{\bullet} + M_n \xrightarrow{k_1(n)} RM_n^{\bullet} \tag{1.2}$$

This newly formed polymer radical will continue to grow and branch out by chain propagation reactions while reacting with other monomers or polymers chains (equation 1.3).

$$RM_n^{\bullet} + M_{(m)} \xrightarrow{k_p(nm)} RM_{(n+m)}^{\bullet} \tag{1.3}$$

Termination of the chain propagation reactions can occur by the reaction of two initiating radicals resulting in a stable initiator (I) (equation 1.4 - 1.6) or by disproportionation (equation 1.7) during which a hydrogen atom is transferred from one polymer radical to the other which corresponds to an oxidation of the donor and a reduction of the acceptor. Termination of the growing polymer chain can originate from transfer of the active radical group to other molecules (equation 1.8).

$$R^{\bullet} + R^{\bullet} \xrightarrow{k_{T1}} I \tag{1.4}$$

$$RM_n^{\bullet} + R^{\bullet} \xrightarrow{k_{T2}(n)} I + M_n \tag{1.5}$$

$$RM_n^{\bullet} + RM_m^{\bullet} \xrightarrow{k_{T3}(nm)} I + M_{n+m} \tag{1.6}$$

$$RM_n^{\bullet} + RM_m^{\bullet} \xrightarrow{k_{T4}(nm)} I + M_n + M_m \tag{1.7}$$

$$RM_n^{\bullet} + RM_m \xrightarrow{k_{trans}(nm)} RM_n + RM_m^{\bullet} \tag{1.8}$$

Finally, termination can also occur from reactions of the growing polymer chain with the gelatin matrix which is suggested by the finding that an increase of the gel fraction corresponds to a reduction of polymerisation reactions (Lepage *et al* 2001). The structure of the formed polymer depends on the type and ratio of monomers used in the gel dosimeter. The sole use of linear monomers (such as acrylamide) will result in a linear polymer. When a cross linker is added (such as Bis), a branched polymer is formed and depending on the ratio of linear monomer and cross linker, the degree of branching will be different (Baldock and De Deene *et al* 2010).

O_2 influences the propagation reactions via the formation of peroxide radicals (equation 1.9 and 1.10). The anti-oxidant THPS (figure 1.5) acts to capture atmospheric oxygen (O_2) in a complex to cancel its inhibitory effect on the propagation of the polymerisation reactions.

$$R^{\bullet} + O_2 \xrightarrow{k_{O1}} ROO^{\bullet} \tag{1.9}$$

$$RM_n^{\bullet} + O_2 \xrightarrow{k_{trans}(nm)} RM_nOO_m^{\bullet} \tag{1.10}$$

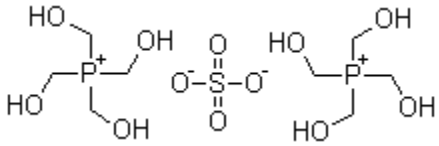

Figure 1.5: *Molecular structure of tetrakis (hydroxymethyl) phosphonium sulphate (THPS).*

These peroxide radicals will quickly react with other available radicals in the gel resulting in the termination of the chain propagation (equations 1.11 to 1.14).

$$ROO^{\bullet} + R^{\bullet} \xrightarrow{k_{R11}} ROOR \tag{1.11}$$

$$ROO^{\bullet} + RM_n^{\bullet} \xrightarrow{k_{R12}(n)} ROOM_nR \tag{1.12}$$

$$RM_nOO^{\bullet} + R^{\bullet} \xrightarrow{k_{R21}(n)} RM_nOOR \tag{1.13}$$

$$RM_nOO_n^{\bullet} + RM_m^{\bullet} \xrightarrow{k_{R22}(nm)} RM_nOOM_mR \tag{1.14}$$

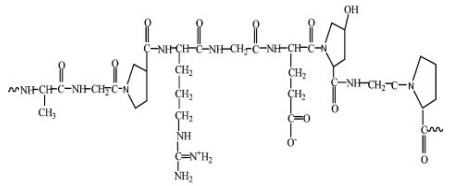

Figure 1.6: *Molecular structure of gelatin.*

The gelatin in polymer gel dosimeters is used to fix spatially the radiation-induced polymer chains. It is a biodegradable protein with an average molecular weight of 50-100 kDa. It is derived from acidic decomposed collagen from porcine skin. The charge on a gelatin molecule (figure 1.6) and its associated isoelectric point are primarily determined by the carboxyl, amino, and guanidino groups on the side chains. Gelatin has 78-80 mM of free carboxyl groups and an isoelectric point (pHi) of around 8.0. The generally accepted model for the gelatin molecule is a triple helix. The triple helix is stabilized by hydrogen bonds between the N-H groups of the gelatin backbone of one chain and C=O groups of a neighbouring chain. Water acts as an intermediary in inter-chain and intra-chain hydrogen bonding (Wustneck *et al* 1988, Fruhner and Kretzschmar 1989). For PAGAT gel dosimeters, a typical concentration of about 6 % (w/w) is used which is an optimum in terms of mechanical rigidity and dose sensitivity of the gel dosimeter (Vergote *et al* 2004b).

In dedicated research hospitals, the potential of polymer gel dosimeters in combination with MRI for dose verification was demonstrated for several radiotherapy treatment techniques (Ibbott *et al* 1997, Oldham *et al* 1998b, De Deene *et al* 1998b, Low *et al* 1999, Farajollahi *et al* 1999, McJury *et al* 1999, Hepworth *et al* 1999, Farajollahi *et al* 2000, Ertl *et al* 2000, De Deene *et al* 2000c, Hafeli *et al* 2000, Grebe *et al* 2001, Pappas *et al* 2001, De Deene *et al* 2001, Papagiannis *et al* 2001, Chan *et al* 2001, Novotny *et al* 2002, Scheib and Gianolini 2002, Vergote *et al* 2003, Duthoy *et al* 2003, Love *et al* 2003, Gustavsson *et al* 2003, Kipouros *et al* 2003, Amin *et al* 2003, Vergote *et al* 2004a, Duthoy *et al* 2004, Sandilos *et al* 2004, Fragoso *et al* 2004, Papagiannis *et al* 2005, Watanabe *et al* 2005, Karaiskos *et al* 2005, Baras *et al* 2005, Gifford *et al* 2005, Fearson *et al* 2005, Hurley *et al* 2006, Sandilos *et al* 2006a, Papagiannis *et al* 2006, Sandilos *et al* 2006b, Crescenti *et al* 2007, Isbakan *et al* 2007, Uusi-Simola *et al* 2007, Karlsson *et al* 2007, Boudou *et al* 2007, Björeland *et al* 2008, Pantelis *et al* 2008, Ceberg *et al* 2008, Pourfallah *et al* 2008, Pappas *et al* 2008, Baker *et al* 2009, Lin *et al* 2009, Pourfallah *et al* 2009, Moutsatsos *et al* 2009, Ceberg

et al 2010, Watanabe *et al* 2010, Deman *et al* 2011, Gopishankar *et al* 2011, Petrokokkinos *et al* 2011).

1.6.3 Radiochromic gel dosimeters

Radiochromic gels are a class of gel dosimeters that change colour upon irradiation allowing the deposited 3D dose information to be quantified using optical readout techniques. The first type of radiochromic dose measurement device was proposed by Day and Stein in 1950, where they added methylene blue to an agar gel. After irradiation of this methylene blue gel, the absorbed dose could be determined from the color changes. In 1958, Armstrong *et al* used the leuco-triarylmethane dye as a reporter molecule in combination with chlorinated halocarbons such as chloroform, carbon tetrachloride and trichloroethylene and an acid-base indicator.

In 2000, Bero *et al* suggested a modified version of the Fricke gel system (called FXG (Ferrous sulphate Xylenol Orange Gel)) in which gelatin gels are loaded with a modified Fricke solution that has pale orange colour prior to irradiation and changes to purple after irradiation. This FXG dosimeter allowed the deposited dose distribution to be quantified using spectrophotometric or other optical techniques. However, all Fricke gel dosimeters suffer from ion diffusion making them relatively unstable.

A new class of radiochromic dosimeters was introduced in 2003 in which an optically clear polyurethane matrix is loaded with a halogenated free radical initiator and a leucodye (Adamovics and Maryanski 2003). This dosimeter was patented under the name of Presage and has the advantage of being optically transparent allowing an optical transmission readout to analyse the 3D dose distribution. Upon irradiation, the halogenated hydrocarbons (initiators) dissociate to highly reactive free radicals. These free radicals react with the leucodye and oxidise it to its dye (coloured) form. The amount of radiation induced dye is dose dependent and can be measured using light transmission measurements (Adamovics and Maryanski 2006). The Presage dosimeter was developed in parallel with an optical CT scanner of which more details are given in section 1.6.4.3. The main disadvantage of Presage is the difficulty to manufacture the dosimeter in-house which makes the end user susceptible to random inter-batch variations in the radiation properties of the purchased Presage dosimeter. Some studies on the Presage dosimeter have shown it to be strongly dependent on temperature during irradiation and post-irradiation storage resulting in a non-linearity of the dose response (Skyt *et al* 2011, 2012). However, in Adamovics and Maryanski (2006) and Adamovics *et al* 2006, no non-linear effects were reported and thermal effects were found to be very small. These

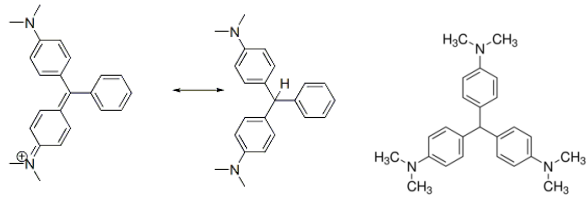

Figure 1.7: *Molecular structure of malachite green (a) which is the coloured form of leucomalachite green (b). In (c) the molecular structure of leucocrystal violet is shown.*

results suggest that different batches of Presage with different radio-physical properties have been distributed. Further optimisation and standardisation of Presage dosimeters should address inter-batch reproducibility in order for it to become a reliable dosimeter.

In 2009, Jordan and Avaakumov (2009) and Babic *et al* (2009b) suggested a similar dosimeter in which leucodyes (leucomalachite green (LMG) and leucocrystal violet (LCV), see figure 1.7) are dissolved in a gelatin gel. Because most leucodyes are hydrophobic, micelles were used to homogeneously dissolve the dye in the gel matrix. This type of gel dosimeter is therefore also called a micelle gel dosimeter. A micelle is a microscopic structure consisting of an aggregate of surface-active agents (Haldar *et al* 2001). These surfactants are amphiphilic which means that they both have a hydrophobic and a hydrophilic part. The hydrophobic (or lipophilic) part usually is made of a long hydrocarbon chain and is therefore also called the hydrophobic tail of the molecule. The head of the molecule possesses hydrophilic properties. When these molecules are mixed with water, aggregates of surfactants will be formed in which the hydrophilic heads will align themselves towards the water phase while the hydrophobic tails will align towards the middle of the structure which is called a micelle (figure 1.8a). This results in a spherical nanoparticle with the size of a few upto several hundred nanometres (Goyal and Aswal 2001). Water insoluble molecules can be encapsulated in the hydrophobic core of the micelles. The concentration of surfactant in water needs to be higher than the critical micelle concentration (CMC) to be able to form micelles. Different subsets of surfactants can be characterised. The hydrophilic head can be charged negatively (anionic surfactant, *e.g.* sodium dodecyl sulphate (SDS) see figure 1.8b) or positively (cationic surfactant, *e.g.* cetyl trimethylammonium bromide (CTAB)). Finally, non-ionic polar groups can serve as hydrophilic

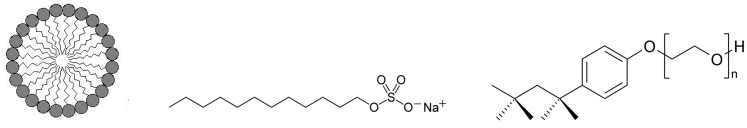

(a) (b) (c)

Figure 1.8: *A schematic representation of a micelle (a) and the molecular structure of sodium dodecyl sulphate (b) and triton X-100 (c).*

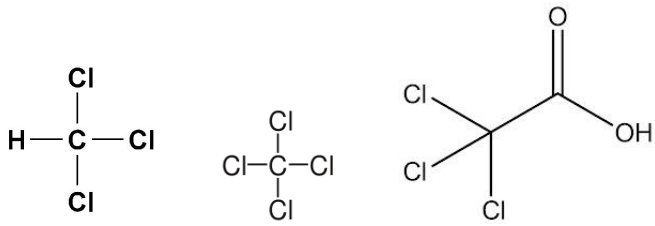

(a) (b) (c)

Figure 1.9: *Molecular structure of chloroform (a), carbon tetrachloride (b) and trichloroacetic acid (c).*

head groups such as in Triton-X-100 (figure 1.8c).

To oxidise the leucodye to its chromatic form, halogenated hydrocarbons are added to the radiochromic gel. They can be subdivided into two groups: the neutral halocarbons (*e.g.* chloroform ($CHCl_3$) and carbon tetrachloride (CCl_4)) and acidic halocarbons (trichloroacetic acid (CCl_3COOH)) (see figure 1.9). The halocarbons enhance the radiation sensitivity by interacting with the incident photons leading to the formation of oxidizing reagents (*e.g.* $OH^{\bullet}$, H_2O_2 and $Cl^{\bullet}$) which oxidise the leucodye to its chromatic structure (Ottolenghi and Stein 1961, Abramson and Firestone 1966, Baxter and Johnston 1968, Rezansoff *et al* 1970).

1.6.4 Imaging

Because of the range of different chemical principles upon which the functionality of gel dosimetry is based, several readout techniques have been used over the years. The most widely adopted readout technique has been magnetic resonance imaging (MRI) which probes nuclear magnetic resonance properties of the gel dosimeter. Recently with the introduction of radiochromic gel systems several optical readout techniques have been pro-

posed. Alternative readout techniques have also been developed such as X-ray CT imaging (Audet *et al* 2002, Jirasek *et al* 2012, Johnston *et al* 2012), Raman imaging (Baldock *et al* 1998b, Jirasek *et al* 2001) and ultrasound imaging (Mather and Baldock 2003) of which some have shown promising results but are not the subject of this dissertation.

1.6.4.1 MRI readout

The absorbed radiation dose distribution in a gel dosimeter has to be quantified to allow comparison between the planned radiation dose distribution and what is actually delivered. In polymer gel dosimeters, the amount of polymerisation is related to the absorbed radiation dose inside the gel, so a readout technique that is sensitive to the amount of polymer formed in a gel is needed. The polymerisation in a gel dosimeter affects an important contrast parameter in MRI namely the NMR spin-spin relaxation rate (R_2) which is the inverse of the spin-spin relaxation time, T_2. How the polymerisation causes a change in the R_2 relaxation is explained here.

The signal used to make MRI images originates from the atomic nuclei. In the human body (and in polymer gel dosimeters) hydrogen nuclei are the most abundant. The hydrogen nucleus consist of a proton which is characterised by basic physical properties such as mass, electric charge, magnetism and intrinsic spin. The proton in the nucleus of hydrogen atom has a spin angular momentum ($\vec{I}$) which arises from the intrinsic spin of the proton and induces a nuclear magnetic dipole momentum ($\vec{\mu}$) via the gyromagnetic ratio of protons (γ) (equation 1.15).

$$\vec{\mu} = \gamma \vec{I} \tag{1.15}$$

The spin angular momentum ($\vec{I}$) is characterised by the spin quantum number I. For the hydrogen proton, the spin quantum number amounts to $\frac{1}{2}$. Following the theory of quantum dynamics, the component of the spin angular momentum perpendicular to the magnetic field (I_z) is limited to $(2I+1)$ discrete values. Consequently, the nuclear magnetic dipole momentum along the z-axis is quantised and a measurement can only result in two possible states[1].

In an external magnetic field as applied in MRI, the nuclear magnetic dipole moment will posses a discretised potential energy (E, equation 1.16)

$$E = -\vec{\mu}\vec{B_0} = \begin{cases} +\frac{1}{2}\gamma\hbar B_0 & I_z = -\frac{1}{2}(spin\ down) \\ -\frac{1}{2}\gamma\hbar B_0 & I_z = +\frac{1}{2}(spin\ up) \end{cases} \tag{1.16}$$

[1]It should be noted that quantum mechanically, the angular momentum can have any linear combination of the eigenstates and is in a superposition of these eigenstates.

This is called the Zeeman-splitting of energy levels. For a proton to change energy state, a photon has to be absorbed with energy (equation 1.17)

$$\Delta E = \hbar\omega_L \tag{1.17}$$

in which ω_L is the angular frequency or Larmor frequency of the precessing nuclear magnetic dipole momentum (equation 1.18)

$$\omega_L = \gamma B_0 \tag{1.18}$$

A small fraction of the total amount of hydrogen protons will be at a lower energy state. The exact ratio of proton spins in the energy states is determined by the Boltzmann statistics and depends on the absolute temperature (T), the applied external magnetic field (B_0) and the Boltzmann constant (k) (equation 1.19). N_- is the spin population in the spin-down energy state while N_+ is the spin population in the spin-up energy state.

$$\frac{N_-}{N_+} = e^{-\frac{\Delta E}{kT}} = e^{-\frac{\gamma\hbar B_0}{kT}} \tag{1.19}$$

This small abundance of spins in a lower energy state creates a net macroscopic nuclear magnetic momentum and is referred to as a spin isochromat. This spin isochromat can be described in a classical way and is proportional to the external applied magnetic field strength (B_0) and the nuclear magnetic susceptibility (χ_n) (equation 1.20).

$$\vec{M} = \chi_n \vec{B_0} = N \tanh\left(\frac{\gamma\hbar B_0}{2kT}\right)\frac{\gamma\hbar}{2} \approx N\frac{\gamma^2\hbar^2 B_0}{4kT} \tag{1.20}$$

In MRI, radio-frequency (RF) pulses are applied (in which the magnetic field component is referred to as the B_1 field) perpendicular to the B_0 field to flip the macroscopic magnetisation over a flip angle θ (depending on the duration, τ, of the applied B_1 field) in a plane perpendicular to the applied magnetic field according to equation 1.21

$$\theta = \gamma B_1 \tau. \tag{1.21}$$

This induces a transverse macroscopic magnetisation of precessing spin isochromats in a plane perpendicular to the external B_0 field. This rotating magnetisation induces a current in coils placed in the proximity of the object which can then be measured. The transverse magnetisation originates from the partial alignment (phase) of spins perpendicular to the external applied magnetic field which will dephase after some time. Brownian motion of the molecules containing these protons and the vigorous molecular tumbling of

these molecules result in local magnetic field fluctuations (Bloembergen *et al* 1948). There are two contributions to T_2: static coupling and dynamic coupling. Lower frequency or static magnetic field differences between different protons lead to differences in the precession frequency. Magnetic field fluctuations at Larmor frequency cause spin flip-flop transitions. Both these processes lead to random variations in the precession frequency of the different spins. This dephasing of the spin isochromats results in an exponential decay of the signal and can be characterised by its time constant: the NMR spin-spin relaxation time (T_2) or the NMR spin-spin relaxation rate (R_2). The molecular environment strongly influences the "mobility" of the molecules that host the hydrogen protons and is responsible for a change in the spectral density of magnetic field fluctuations.

In an irradiated gel dosimeter different pools of protons are present which are characterised by their different relaxation rates. First, a large amount of mobile protons can be found in the gel associated with the free water molecules and small monomers. A second pool of protons is associated with the gelatin matrix which consists of both protons in the gelatin molecules itself and its hydration layer. The third proton pool can be found in the polymer chain created after irradiation and consists of protons in the polymer structure itself and the bound water molecules. As a result of rapid chemical exchange between the proton pools, the different relaxation rates of these pools manifest themselves in the resulting spin-spin relaxation. The MRI signal from unirradiated gel originates primarily from the first two pools. Upon irradiation, the fraction of protons in the third pool (polymer) increases while the first pool (monomers) will start to decrease. Because the mobility of the protons in branched polymer is decreased, T_2 is also decreased or R_2 is increased. Because the lifetimes of protons in the different pools are short compared to the relaxation times (*i.e.* fast exchange between water protons and polymer protons), the observed relaxation rate will be a weighted average of the relaxation rates of the different proton pools (Zimmerman and Brittin 1957). Otherwise a multi-exponential decay would be observed when the lifetimes of the different proton pools are long compared to the relaxation rates (*i.e.* slow exchange). Imaging sequences that measure the R_2 parameter are mainly used to quantify the amount of polymerisation and thus the absorbed dose in polymer gel dosimeters. The R_2 values in a gel dosimeter can be measured with several MRI imaging sequences (De Deene 2009). In this dissertation a multiple spin-echo sequence is used to measure a set of different T_2 weighted images (figure 1.10). This sequence was shown to be optimal from a signal-to-noise point-of-view (De Deene *et al* 1998a).

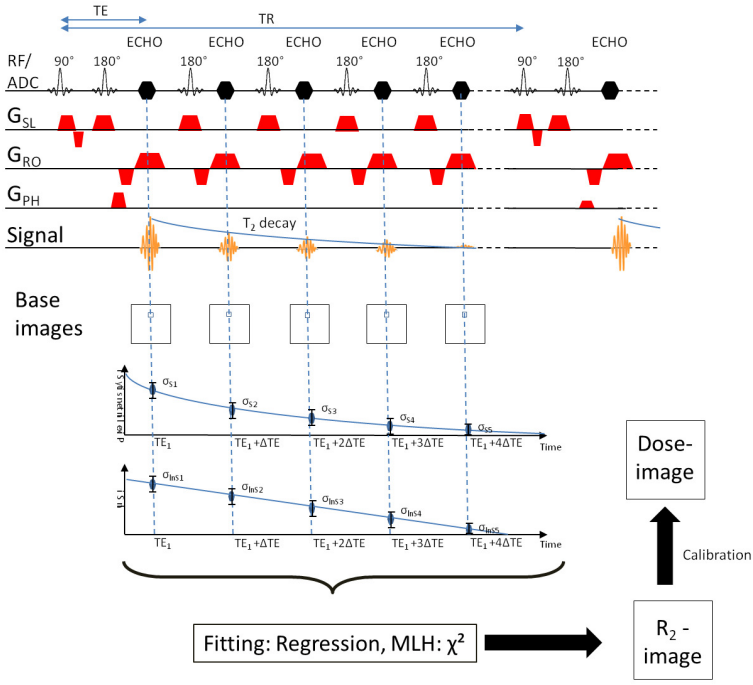

Figure 1.10: *A schematic overview of the measurement, MRI imaging sequence and calculation of R_2 images resulting in dose images for polymer gel dosimeters (Adapted from De Deene et al 1998a). Several base-images with different T_2-weighting are obtained with a multiple spin-echo sequence. The schematic sequence is displayed showing the radio-frequency (RF) pulses and analogue to digital converter (ADC) along with the separate lines for the slice selection gradient (G_{SL}), readout gradient (G_{RO}) and phase encoding gradient (G_{PH}). An R_2-image is calculated by fitting the pixel intensity of the base images against an exponential decay curve an a pixel-by-pixel basis. The R_2-images are converted to dose maps by applying a dedicated calibration.*

A fitting of the intensity of the equidistant consecutive T_2-weighted images to a mono-exponential decay using χ^2 minimalisation (based on Levenberg-Marquardt algorithm) is performed to obtain R_2 maps (De Deene *et al* 1998a).

To convert the MRI measured R_2 maps to dose maps a dedicated calibration strategy is needed. Several calibration methods have been proposed in the literature. The most frequently used calibration method is based on a dose-R_2 curve obtained from a series of calibration phantoms (*i.e.* set of test tubes filled with the same batch of polymer gel) irradiated to various well-defined doses (Baldock *et al* 1998a, 1999, De Deene *et al* 2000c, McJury *et al* 1999) or by use of a single calibration phantom with a well-defined dose distribution (Maryanski *et al* 1994, 1996, Oldham *et al* 1998a, 1998b, Olding *et al* 2011). Other calibration techniques make use of a plastic scintillator detector (Trapp *et al* 2009 and Tremblay *et al* 2011) or an ionisation chamber measurement inserted in the gel dosimeter (Björeland *et al* 2008). A Monte Carlo study showed that from an irradiation point-of-view the least accurate calibration method was that of long test tubes positioned coaxial with the beam (2 % dose error) as compared to large calibration phantoms and perpendicular test tubes (1 % dose error) (Taylor *et al* 2007).

To obtain a calibration curve, the mean R_2 values are calculated from the cross-sections of the calibration phantoms and these R_2 values are fitted against the radiation doses (D) given to the corresponding calibration phantoms using a mono-exponential function (equation 1.15)

$$R_2 = R_{2,sat} - \Delta R_2 \cdot e^{-\alpha \cdot D} \tag{1.22}$$

with $R_{2,sat}$, ΔR_2 and α the fit coefficients. This mono-exponential function is supported by the analysis on monomer consumptions (Jirasek *et al* 2001) and can be applied on the entire R_2 image to convert it to a dose map.

1.6.4.2 Optical readout

In conjunction to MRI readout techniques, other modalities have been developed (Doran and Krstajic 2006 and Doran 2009). The main principle on which optical scanning techniques are based, relies on the fact that incident light on a gel dosimeter is attenuated differently (usually more) by an irradiated dosimeter as compared to an unirradiated dosimeter. In a uniform medium with a linear attenuation coefficient μ, the transmitted light intensity from a sample with thickness d is given by the Beer-Lambert law (equation 1.23)

$$I(d) = I_0 \cdot exp(-\mu d) \tag{1.23}$$

in which I_0 is the intensity of the incident light and $I(d)$ is the intensity of the transmitted light.

In polymer gel dosimeters, the attenuation is based on scattering of the light by the radiation-induced polymers while in radiochromic gel dosimeters attenuation results from absorption of the light by the radiation-induced dye molecules. To obtain spatial dose information from an irradiated dosimeter, several optical scanners were developed that can probe the attenuation coefficient spatially throughout the dosimeter. Two main configurations of optical readout systems have been proposed using a laser beam and using an image sensor. Of each configuration several optical scanner types have been proposed in the scientific literature. Gore *et al* (1996), Maryanski *et al* (1996) and Tarte and van Doorn (1993) demonstrated the potential of optical readout systems (figure 1.11a). In this set-up, a laser beam is mechanically moved by two mirrors aimed at a photodiode detector to scan the dosimeter in a step by step fashion. This resulted in a commercially available system called the OCTOPUS scanner proposed by MGS Inc and tested by several groups (Islam *et al* 2003, Xu and Wuu 2004 and Lopatiuk-Tirpak *et al* 2008, Zeidan *et al* 2010). A major drawback of this first generation laser scanner is the slow scanning speed (multiple hours for 3D dose information). The introduction of a rotating mirror to sweep the laser beam in one dimension along the gel phantom to replace the mechanically translating laser beam was a major step forward (Wuu *et al* 2003, Van Doorn *et al* 2005 and Conklin *et al* 2006). The most sophisticated system up to date was proposed by Krstajic and Doran 2007 and uses two rotating mirrors in combination with two paraboloidal mirrors to sample a gel phantom in two dimensions to significantly reduce the scan time (figure 1.11b). Laser CT scanners although being relative slow, have good signal-to-noise ratios (high intensity laser beam), and are also much less susceptible to scattering artefacts because only one point is being measured at the same time. Optical readout of gel dosimeters is performed in an aquarium which is filled with a refractive index matching solution to avoid that the laser beam is deflected at the surface of the gel phantom resulting in artefacts. Recently Ramm *et al* proposed a dry in air scanner to eliminate the use of an aquarium (Ramm *et al* 2012).

An alternative method to deal with slow scan times was to use pixelated detectors such as CMOS and CCD detectors to acquire a set of "photographs" of the gel dosimeter at each rotational increment. This method allows for very fast acquisition of a 3D dose distribution (10 to 30 minutes for 3D dose information). Two configurations of image sensor based scanners have been proposed using a parallel geometry of the light path and a cone-beam geometry. In the parallel beam geometry, a homogeneous plane

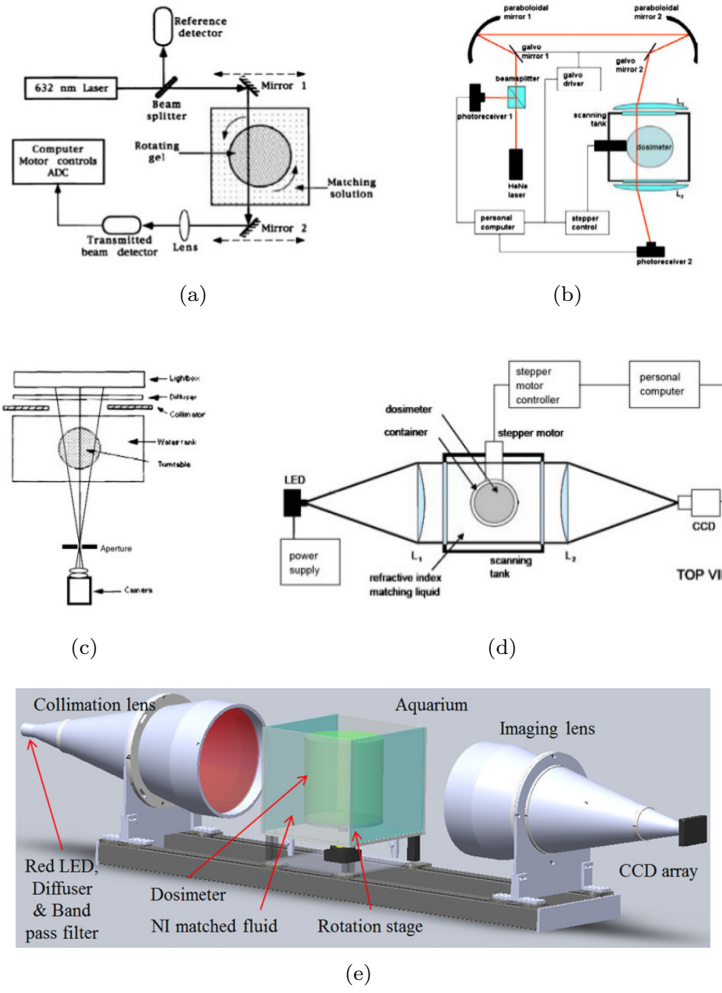

Figure 1.11: *Schematic overview of several different types of optical scanners for gel dosimetry: (a) the first generation laser scanner proposed by Gore et al (1996), (b) the most sophisticated laser scanning system up to date proposed by Krstajic and Doran (2007), (c) the cone beam geometry proposed by Wolodzoko et al (1999) and (d) a parallel beam CCD scanner (Krstajic and Doran 2006). In (e) a telecentric lens configuration is shown from the Duke large field of view optical CT scanner (Thomas et al 2011b).*

of parallel travelling light rays is created to illuminate the gel dosimeter (Doran *et al* 2001). This can be achieved by using a set of two planoconvex lenses in between a light source and camera (figure 1.11d Krstajic and Doran 2006) or by using dedicated telecentric lenses (Sakhalkar and Oldham 2008, Thomas *et al* 2011a, Thomas *et al* 2011b, figure 1.11e).

The cone-beam geometry (figure 1.11c, Wolodzko *et al* 1999) uses a diffuse light source to illuminate the gel phantom and a camera behind a pinhole collimator. This geometry is able to scan large objects while keeping the apparatus compact without significantly increasing the cost. A version has been commercialised by Modus Medical Devices under the trade name VISTA scanner. Both types of pixelated detectors are prone to scattered light created in the gel dosimeter.

Two systems have recently been proposed using a design that incorporates properties of laser CT scanners and pixelated scanners and uses line-beams to illuminate the gel samples (Papadakis *et al* 2011 and Cheng *et al* 2011). The group of Jirasek (Jirasek *et al* 2009 and Campbell *et al* 2013) developed a fan-beam optical CT scanner and adds physical collimation to allow imaging of both absorption-based and scatter-based samples of high opacities. This type of scanner could find a balance between speed of scans and versatility of dosimeter type but more work is needed to address image noise.

1.6.4.3 Optoscan

At the Ghent University, an optical laser CT scanner was built and optimised under the name, Optoscan (figure 1.12, Vandecasteele and De Deene 2009a and 2009b). The Optoscan scanner was used to perform all optical readout experiments of micelle gel dosimeters in this dissertation. The Optoscan is composed of a 633 nm 2 mW HeNe laser (model 1122p, JDS Uniphase) which is projected towards a rotating galvano-mirror (model QS-7, Nutfield). This galvano-mirror sweeps the laser beam along a dual lens configuration mounted in a cubic poly-methyl-methacrylate (PMMA) reservoir filled with a refractive index matching solution (9 % propylene glycol in water). The planoconvex lenses (custom made by Melles Griot) assure that the laser beam travels in parallel paths through the reservoir perpendicular to the walls and is finally focused onto a large area photodiode receiver (Model 2307, New Focus). A cylindrical gel dosimeter is attached to a rotating and vertically translating stage above the reservoir. This stage lowers the phantom into the reservoir at well-defined depths and allows transmission profiles to be acquired from multiple angles. A transmission profile is recorded onto a computer after each sweep of the laser beam. The set of transmission profiles is saved as function of the angle at which it was

recorded (sinogram). Alongside a sinogram, dark values (without any light reaching the detector) and a blank scan (without the phantom in the laser beam) are acquired to correct for a detector offset and any non-uniformities in the transmission profiles. Each transmission profile in the sinogram is corrected using the following equation

$$OD(x,\theta) = -log_{10}\left(\frac{S_{irr}(x,\theta) - S_{dark}}{S_{blank}(x) - S_{dark}}\right) \tag{1.24}$$

in which OD is the optical density, S_{irr} the transmitted light intensity profile, S_{dark}, the dark value and S_{blank} the profile without any phantom. This OD sinogram is then converted into a two dimensional (2D) image using a filtered back projection with a Hann filter.

1.7 Objectives

By the end of the 1990's, gel dosimetry had shifted from radiochromic dosimeters such as Fricke gel to polymer gel dosimeters to overcome the spatially unstable dose distribution due to ion diffusion within the irradiated dosimeter. Polymer gel dosimeters became infamous as a dosimetry technique because of several limitations: highly labour intensive, low accuracy and precision and very time-demanding. The introduction of normoxic polymer gel dosimeters was a first step forward to increase the user-friendliness. A lack of confidence in the dosimetric accuracy of these three dimensional (3D) dosimeters resulted in only a few clinics worldwide able to incorporate it in their QA programs. The first objective of this work was to validate the dosimetric accuracy and precision of normoxic polymer gel dosimeters with MRI readout. An analysis of chemical and radio-physical characteristics of the gel and the influence of readout related uncertainties was performed. This research assured that accurate and precise 3D dosimetry was available against which all newer 3D dosimetry systems such a radiochromic gel dosimeters and optical readout techniques could be validated.

To date, most gel dosimetry has used MRI as a way to obtain a quantitative dose distribution from an irradiated dosimeter. This readout technique yields excellent results provided sufficient attention is taken to characterise the MRI scanner and implement the necessary imaging sequences. These measures are imperative to obtain a clinical acceptable level of accuracy and are responsible for the limited usage of the technique. As a result, research was directed on making 3D dosimetry more accessible to a broader clinical radiotherapy usage. We envisaged the use of optical computed tomography (optical CT) technology to deal with some of the drawbacks of MRI. In conjunction, alternative gel formulations were developed which are

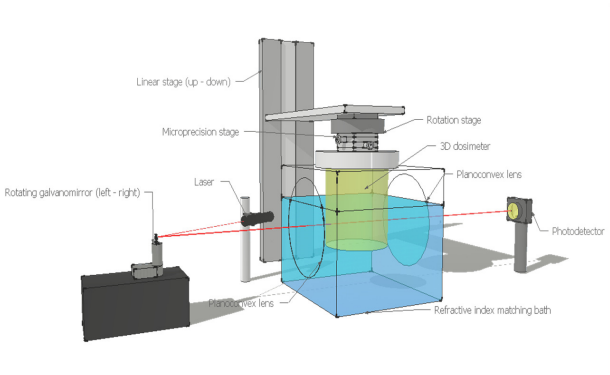

(a)

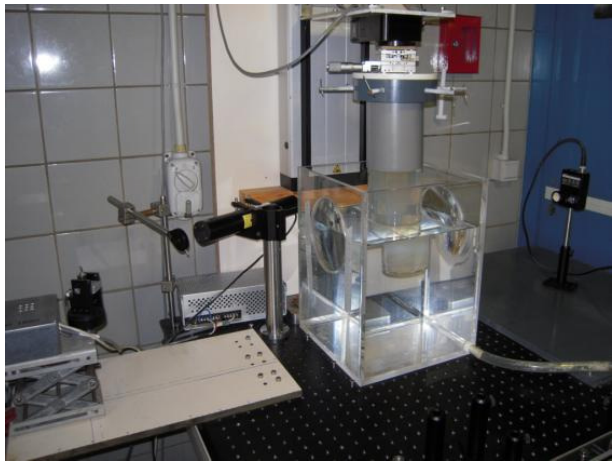

(b)

Figure 1.12: *Schematic overview of the in-house built optical CT laser scanner (a) and a photograph (b). A laser beam is projected towards a rotating galvano-mirror which sweeps the laser beam along a dual lens configuration mounted in a cubic PMMA reservoir filled with a refractive index matching solution. The planoconvex lenses assure that the laser beam travels in parallel paths through the reservoir perpendicular to the walls and is finally focused onto a large area photodiode receiver. A cylindrical gel dosimeter is attached to a rotating and vertically translating stage above the reservoir. This stage lowers the phantom into the reservoir at well-defined depths and allows transmission profiles to be acquired from multiple angles.*

more optimised for optical readout. The development of easy-to-fabricate radiochromic gels, along with the development of a fast and compact optical laser scanner, is suspected to advance the routine use of full 3D dosimetry techniques in a broad radiotherapy setting.

1.8 Outline

The validity of MRI polymer gel dosimeters was assessed in 3D by performing a reproducibility study and is presented in Chapter 2. Both the intra- and inter-batch precision was found to be very high notwithstanding a poor dosimetric accuracy. The calibration method was identified in both experiments as the origin of inaccuracy as temperature variations between calibration phantoms and volumetric phantoms were shown to be the major cause of dosimetric deviations. The effect of dose scaling strategies using an independent ion chamber dose measurement is discussed in small and large volume gel dosimeters.

Chapter 3 summarises the influences of several physico-chemical factors on the uncertainties in polymer gel dosimetry. The sensitivity of polymer gels to temperature changes before, during and after irradiation was quantified. Experiments to test the effects of post-irradiation oxygen exposure and the recipient wall effects were studied. None of the investigated physico-chemical effects were found responsible for the significant discrepancies discussed in Chapter 3, however they are important factors that should be addressed to reach a clinical acceptable dosimetric accuracy.

In Chapter 4, the relative contribution of important sources of uncertainty in MR scanning to the overall accuracy and precision of 3D MRI polymer gel dosimetry is quantified. The performance in terms of signal-to-noise and imaging artefacts was evaluated on three different MRI scanners (two 1.5 T scanners and a 3 T scanner). These include: B_0- field inhomogeneity, B_1-field inhomogeneity, dielectric effects such as losses and standing waves and temperature inhomogeneity during scanning. Spatial and temporal temperature inhomogeneities were identified as the origin of major dose deviations and temperature stabilisation strategies are proposed.

In Chapter 5, a new radiochromic gel formulation is presented which uses micelles to dissolve a leucodye in a gelatin matrix. The composition of this leucodye micelle gel dosimeter was optimised and all important radiophysical characteristics were investigated: the dose sensitivity, dose rate dependency, energy dependency, temperature during irradiation and optical readout, spatial integrity and tissue equivalence. The radiochromic gel was found to have a significant dose rate dependency, however the experimental results indicate that there is a potential for improvement.

A comparison between polymer gel dosimetry with MRI and radiochromic gel dosimetry with an optical laser scanner was made in Chapter 6. Firstly, a simple square beam depth dose distribution was used to benchmark both dosimeters. Secondly, both dosimeters were subjected to a full 3D dose verification of a brain tumour IMRT treatment. Experimental results illustrate the strengths and weaknesses of both dosimetry systems.

An overview of all important random and systematic uncertainties affecting the dosimetric and geometric accuracy of radiochromic and polymer gel dosimetry are discussed in Chapter 7. Both dosimeters are compared and some perspectives for future studies are proposed.

Finally, in Chapter 8, the main conclusion of this work are summarised.

2

On the validity of 3D polymer gel dosimetry: I. Reproducibility study

---

Jan Vandecasteele and Yves De Deene
Both authors contributed equally to this study.

Manuscript on which this chapter is based:
Physics in Medicine and Biology **58** (2013) 19-42

On the validity of 3D polymer gel dosimetry: I. Reproducibility study*

Jan Vandecasteele[1] **and Yves De Deene**[1,2]

[1] Department for Radiation Oncology and Experimental Cancer Research, Ghent University, De Pintelaan 185, 9000 Gent, Belgium
[2] Institute of Medical Physics, School of Physics, University of Sydney, Sydney NSW 2006, Australia

E-mail: Jan.Vandecasteele@UGent.be

Received 7 Februari 2012, in final form 28 Augustus 2012
Published 6 December 2012
Online at stacks.iop.org/PMB/58/19

Abstract. The intra- and inter-batch accuracy and precision of MRI (polyacrylamide gelatin gel fabricated at atmospheric conditions) polymer gel dosimeters are assessed in full 3D. In the intra-batch study, eight spherical flasks were filled with the same polymer gel along with a set of test tubes that served as calibration phantoms. In the inter-batch study, the eight spherical flasks were filled with a different batch of gel. For each spherical phantom a separate set of calibration phantoms was used. The spherical phantoms were irradiated using a three-field coplanar beam configuration in a very reproducible manner. The calibration phantoms were irradiated to known doses to obtain a dose-R_2 calibration plot which was applied on the corresponding R_2 maps of all spherical phantoms on an individual basis. The intra-batch study showed a high dosimetric precision (3.1%) notwithstanding poor accuracy (mean dose discrepancies up to 13.0%). In the inter-batch study, a similar dosimetric precision (4.3%) and accuracy (mean dose discrepancies up to 13.7%) were found. The poor dosimetric accuracy was attributed to a systematic fault that was related to the calibration method. Therefore, the dose maps were renormalised using an independent ion chamber dose measurement. It is illustrated that with this renormalisation, an excellent agreement between the gel measured and TPS calculated 3D dose maps is achievable: 97% and 99% of the pixels meet the 3%/3mm criteria for the intra- and inter-batch experiment respectively. However renormalisation will result in significant dose deviations inside a realistically-sized anthropomorphic phantom as will be shown in a concurrent paper.

*Both authors contributed equally to this study

1. Introduction

Normoxic polymer gel dosimeters have been proposed as a user-friendly 3D gel dosimeter (*e.g.* Fong *et al* 2001, De Deene *et al* 2002a, 2006, Gustavsson *et al* 2003, Hurley *et al* 2005, 2006, Venning *et al* 2005, Jirasek *et al* 2006, Senden *et al* 2006, Luci *et al* 2007, Björeland *et al* 2008, Hill *et al* 2008). So far, clinical dissemination of normoxic polymer gel dosimeters however has been limited, partially because of a lack of confidence in the dosimetric accuracy of these new 3D dosimeters. In this study, the intra- and inter-batch accuracy and precision of normoxic polymer gel dosimeters based on acrylamide and N,N'-methylene-bis-acrylamide are assessed.

Several calibration methods have been proposed in the literature. The most frequently used method is based on a dose-R_2 curve obtained from a series of calibration phantoms irradiated to various doses (Baldock *et al* 1998, 1999, De Deene *et al* 2000c, McJury *et al* 1999) or by use of a single calibration phantom with a well-defined dose distribution (Maryanski *et al* 1994, 1996, Oldham *et al* 1998a, 1998b, Olding and Schreiner 2011). Other calibration techniques make use of a plastic scintillator detector (Trapp *et al* 2009 and Tremblay *et al* 2011) or an ionisation chamber measurement inserted in the gel dosimeter (Björeland *et al* 2008). A Monte Carlo study showed that from an irradiation point of view the least accurate calibration method was that of long test tubes coaxial with the beam (2% dose error) as compared to large calibration phantoms and perpendicular test tubes (1% dose error) (Taylor *et al* 2007). The technique of irradiating calibration phantoms perpendicular to the beam's axis was therefore applied throughout this study.

The calibration technique is essential to obtain an 'absolute' dose verification. Here, 'absolute' refers to the independent calibration of the experimentally derived dose maps, in contrast to a relative calibration of the R_2 maps with respect to the 100% isodose in the TPS calculation or normalisation of the dose maps. In the past, several authors have found discrepancies between the gel measured dose and the TPS calculated dose values which are not attributed to TPS related errors (Low *et al* 1999, Cosgrove *et al* 2000, Cardenas *et al* 2002, Watanabe *et al* 2005, Crescenti *et al* 2007). These discrepancies were attributed to volumetric effects (MacDougall *et al* 2008, Dumas *et al* 2006, Xu *et al* 2010, De Deene *et al* 2002b, Vergote *et al* 2004), cooling history (De Deene *et al* 2007), temperature during irradiation (Salomons *et al* 2002, Sedaghat *et al* 2010, Sedaghat *et al* 2011b), oxygen contamination effects (Hepworth *et al* 1999, Sedaghat *et al* 2011a) and imaging artefacts (De Deene *et al* 2000a, 2000b, De Deene and De Wagter 2001).

The aim of this study is to analyse the contribution of all relevant factors in the overall accuracy of the normoxic 3D gel dosimeter. Unique in our approach is that a full 3D polymer gel dosimetry experiment was repeated eight times and that the reproducibility was assessed. From an intra- and inter-batch reproducibility study, two classes of error sources were isolated. In the intra-batch reproducibility study, variations related to the fabrication process as potential cause of dosimetric errors were excluded while in the inter-batch reproducibility study both chemical and scanning related sources

could be investigated as the potential sources of discrepancies between the different measured dose distributions. The TPS calculated dose map, which was independently validated by ion chamber dose measurements, was compared against all gel measured dose maps.

2. Materials and Methods

2.1. Gel fabrication

The normoxic polymer gel dosimeters used in this study have acrylamide (Aam) and N,N'-methylene-bis-acrylamide (Bis) as active components (PolyAcrylamide Gelatin gel fabricated at ATmospheric conditions, PAGAT). This type of dosimeter was chosen because of its superior characteristics in terms of dose rate dependence (De Deene *et al* 2006, Karlsson *et al* 2007) and dependence on cooling rate (De Deene *et al* 2007). The PAGAT dosimeter used in this study, is composed of gelatin (6% w/w), Aam (2.5% w/w), Bis (2.5% w/w) and 5 mM Bis[tetrakis(hydroxymethyl)phosphonium]sulphate (THPS) as antioxidant. The polymer gel was fabricated according to a procedure described elsewhere (De Deene *et al* 2006). The gel was at 32 °C when it was poured in 19 test tubes and eight similar spherical flasks. The test tubes are made out of borosilicate glass (Pyrex®) and have a length of 10.0 cm, an inner diameter of 12.4 mm, an outer diameter of 15.0 mm and a wall thickness of 1.3 mm. The spherical flasks are also composed of borosilicate glass and have an outer diameter of 8.50 cm, a wall thickness of 2 mm and a volume of 250 ml. The test tubes served as calibration phantoms while the spherical flasks served as volumetric gel dosimeter phantoms.

Two experiments were performed on separate dates. First, the intra-batch reproducibility was investigated by fabricating a large quantity of gel (3 l) in one batch and dividing it over the eight spherical flasks and nineteen test tubes (figure 1), *i.e.* one set of calibration phantoms. Secondly, an inter-batch experiment was performed in which 0.6 l of normoxic gel was fabricated eight times and, each batch, divided over a spherical flask and 19 test tubes. The eight volumetric phantoms were always scanned together with calibration phantoms of the corresponding batch.

2.2. Storage

After filling, all phantoms were placed in a large reservoir that was filled with 60 l of water at 32 °C to assure a similar cooling trajectory in calibration phantoms and volumetric gel dosimeter phantoms (De Deene *et al* 2007). The water and phantoms were allowed to cool down at normal atmospheric conditions (*i.e.* 20°C-22°C) for approximately 22 h. The phantoms were taken out of the reservoir 60 min prior to irradiation.

2.3. Treatment planning

Helical computerised tomography (CT) scanning (Toshiba Aquilion LB) of a spherical phantom filled with 6% gelatin gel (G2500, Sigma Aldrich type A gelatin, 300 bloom) placed upon a dedicated holder was performed (figure 1a). Sixty-five slices were acquired with following scanning parameters: slice thickness: 3 mm, energy: 120 KVp, exposure: 250 mAs, matrix size (MS): 512 × 512 and field of view (FOV): 256 × 256 mm^2. Subsequently, the images were sent to the treatment planning system (TPS) and planning was performed with Pinnacle^{TM} 8.0 m. The dose grid resolution was set to 1.0 × 1.0 × 1.0 mm^3 in a dose computation grid size of 100 × 100 × 100 pixels. A heterogeneous density correction was used with the collapsed cone convolution dose engine.

The irradiation set-up was composed of three separate beams with gantry positioned at 180° (525 monitor units (MU)), 60° (150 MU) and -60° (375 MU) respectively. For all beams the same parameters were chosen: field size: 3.2 × 3.2 cm^2, collimator angle: 0°, energy: 6 MV and dose rate: 400 cGy min^{-1} at reference depth of 10 cm. This resulted in a total dose of 11.24 Gy at the centre of the spherical phantom according to the TPS.

A reference measurement was performed in the centre of the spherical flask filled with a 6% gelatin gel using a small volume ionisation chamber (PTW semiflex 31010) (figure 1b). The measured dose in the centre of the spherical phantom amounted to 11.28 Gy which corresponds with a dose difference of 0.41% with the TPS.

2.4. Irradiation

All irradiation procedures were performed on a clinical linear accelerator (linac) Elekta Synergy (Elekta Oncology Systems, Crawley, UK) equipped with an Elekta Beam Modulator^{TM}.

Each individual calibration phantom was irradiated perpendicular to the beam's axis in a large cubic water phantom (32 × 32 × 20 cm^3) with the longitudinal axis of the test tube positioned at a depth of 10 cm and with a source-to-surface distance (SSD) of 90 cm. The linear accelerator was calibrated so that, for a 6 MV photon beam with a field size of 9.6 × 9.6 cm^2, 1 monitor unit (MU) corresponds to a dose of 1 cGy at the isocentre. The calibration phantoms were irradiated to different well-defined doses (0 Gy up to 15 Gy). This irradiation set-up was thoroughly validated by pinpoint ion chamber measurement assuring the accuracy of the procedure. Furthermore, Taylor *et al* (2007) showed that using a thin test tube (length: 10 cm, inner diameter: 10 mm, wall thickness: 1 mm) with its axis perpendicular to the beam axis results in dose values that match those to water within half a per cent.

A dedicated phantom holder was constructed in polymethylmethacrylate (PMMA) to place the spherical phantoms in a highly reproducible irradiation and read-out position (figure 1a). The phantom holder is composed of a positioning plate with circular cut-out which allows the passage of the upward radiation beam without any

Table 1. Overview of scanning parameters that were used to obtain the 2D and 3D quantitative R_2 maps.

Scanning parameters	2D scan intra-batch	2D scan inter-batch	3D scan
Repetition time [ms]	3000	3000	10 000
Echo time [ms]	40	40	40
In-plane resolution [mm×mm]	0.5 × 0.5	1 × 1	1 × 1
Slice thickness [mm]	10	10	5
Receiver bandwidth [Hz/pixel]	130	130	130
# of acquisitions [-]	1	2	1
# of spin echoes [-]	32	32	32
# phase encoding steps	256	136	150
Total scan time	12 m 48 s	13 m 36 s	49 m 50 s

perturbation by the holder (gantry angle 180°). All phantoms were irradiated without any repositioning of the holder. This way, any set-up errors related to phantom positioning were minimized. The same phantom holder is also used during MR scanning.

2.5. Scanning

Each of the eight sets of the irradiated spherical phantoms and calibration phantoms were positioned in a clinical NMR scanner (Siemens Avanto 1.5 T) using the same dedicated phantom holder used during irradiation. The phantoms were subsequently scanned one after the other. Quantitative NMR spin-spin relaxation rate images (R_2-maps) were acquired in a transverse plane (2D) through the isocentre in a transmit-receive CP head coil using a multiple spin-echo sequence with a maximum number of spin-echoes of 32. Scanning parameters are listed in table 1. The calibration phantoms were inserted in a dedicated polystyrene holder and placed in the scanner around the spherical phantom holder. The longitudinal axis of the calibration phantoms was positioned along the main magnetic field. A transverse slice was recorded perpendicular to the calibration phantom's axis approximately 2 cm from the bottom of the calibration phantom. The position of this transverse slice corresponds to the location of the irradiation isocentre.

For the intra-batch experiment, 2D measurements for all eight phantoms were repeated at times 6, 30 and 54 h post-irradiation. For the inter-batch experiment, 2D measurements were acquired 19 and 43 h post-irradiation. In addition, full 3D R_2 distributions (ten adjoined slices) of all eight phantoms were acquired 92 h post-irradiation for the intra-batch and 85 h post-irradiation for the inter-batch experiment.

2.6. Data processing

A fitting of the intensity of 31 equidistant consecutive base images to a mono-exponential decay using χ^2 minimalisation (based on Levenberg-Marquardt algorithm) was performed to obtain R_2 maps (De Deene *et al* 1998). The mean R_2 values and

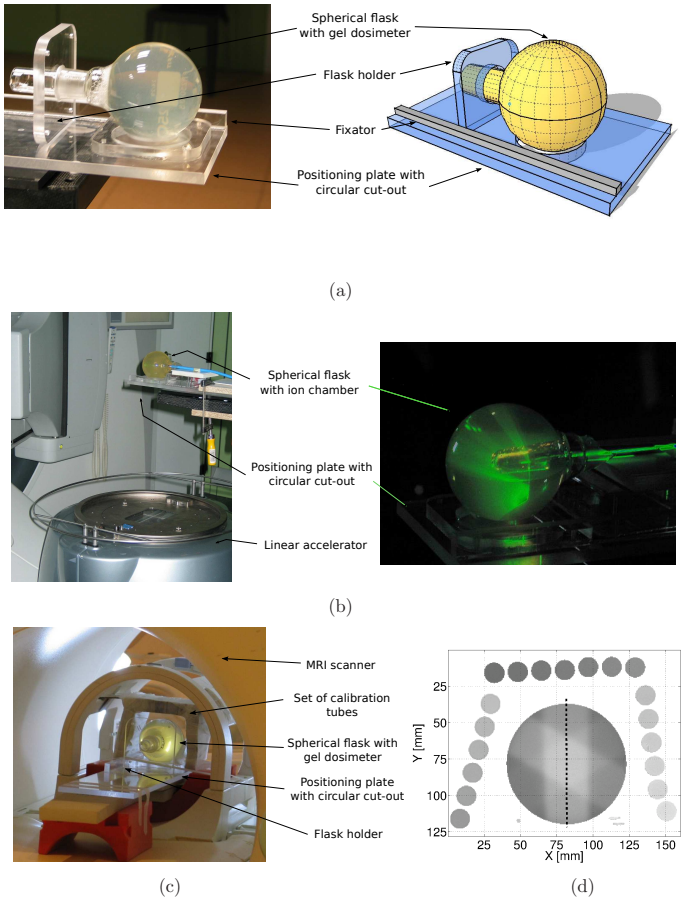

Figure 1. A photographic and schematic representation of the phantom holder used to fixate the spherical flasks during irradiation (a). A circular cut-out is present in the positioning plate to allow the radiation beam to pass. The fixator bar restricts the positioning of the phantom in the horizontal direction. A reference measurement was performed with a semiflex ion chamber positioned inside a similar spherical flask filled with gelatin gel (b). The same dedicated phantom holder was also used during scanning on the MR scanner (c). The set of calibration phantoms is placed around the spherical phantom. A transverse plane (2D) through the isocentre of the spherical phantom and set of calibration phantoms is shown in (d).

standard deviations were extracted from the calibration phantoms in these R_2 maps using circular regions of interest (ROIs) of 50 mm^2 corresponding to the cross-sections of the calibration phantoms. For each ROI, the mean and standard deviation of the R_2 value were calculated for that particular calibration phantom. This procedure was repeated for all calibration phantoms. An R_2-dose calibration plot was used to derive the mean R_2 values from the calibration phantoms in function of dose (D). These points were fitted against a mono-exponential function (1)

$$R_2 = R_{2,sat} - \Delta R_2 \cdot e^{-\alpha \cdot D} \tag{1}$$

with $R_{2,sat}$, ΔR_2 and α the fit coefficients. More intuitive parameters were extracted from these fit parameters:

$$slope = \Delta R_2 \cdot \alpha \tag{2}$$

$$R_{2,0} = R_{2,sat} - \Delta R_2 \tag{3}$$

The slope was defined as the derivative at 0 Gy. $R_{2,0}$ was defined as the intersection with the y-axis and $R_{2,sat}$ was defined as the saturation R_2 value. R_2 range was defined as the R_2 increase resulting from a irradiation dose of 12 Gy at 30 h post-irradiation.

The resolution of the intra-batch MRI scans was 0.5×0.5 mm^2. In order to compare the gel data to the planning data, a rescaling was performed on a 2 x 2-pixel averaging basis which resulted in a theoretical doubling of the signal-to-noise-ratio (SNR).

To investigate the influence of the calibration procedure on the reproducibility of the gel dosimetry experiment, four different calibration procedures were considered. The main focus is on the traditional method of calibrating the irradiated phantom with small test tubes 'homogeneously irradiated' with a well-defined dose. Many other authors however have applied relative calibrating methods. Three different rescaling techniques were implemented in correspondence with rescaling methods applied elsewhere (*e.g.* Low *et al* 1999, Gustavsson *et al* 2003, Love *et al* 2003, Fragoso *et al* 2004, Ceberg *et al* 2008, Björeland *et al* 2008, Ceberg *et al* 2010, Watanabe and Gopishankar 2010, Tremblay *et al* 2011). It should be emphasized that an independent dose measurement with an ion chamber in the volumetric phantom was performed in order to avoid masking of the acquired dose deviations.

(i) First, the calibration plot was applied without any renormalisation to calibrate the R_2 maps to dose maps (*calibration method 1*).

(ii) Secondly, a linear fit was made between the R_2 value of the non-irradiated calibration phantom (0 Gy) and the R_2 value measured at the isocentre of the spherical phantom where also the ion chamber measurement was performed (11.24 Gy) (*calibration method 2*). The radius of the ROI in which the mean R_2 value was calculated, corresponds with the radius of the active volume of the ion chamber.

(iii) The third calibration method was based on a linear renormalisation of the calibration function. Two ROIs are selected in the planned dose distribution: one ROI in a low-dose region and one ROI in a high-dose region. The corresponding R_2

values in the measured dose distributions are then determined in the same ROIs. From equation 1 the fit coefficient α is saved. Using equations 4 and 5 the new fit coefficients $\Delta R_2'$ and $R_{2,sat}'$ are calculated:

$$\Delta R_2' = \frac{R_{2,2} - R_{2,1}}{exp(-\alpha_1 \cdot D_2) - exp(-\alpha_1 \cdot D_1)} \tag{4}$$

$$R_{2,sat}' = R_{2,1} - \Delta R_2' \cdot exp(-\alpha_1 \cdot D_1) \tag{5}$$

where $\Delta R_2'$ and $R_{2,sat}'$ are the new fit coefficients for equation 1. $R_{2,1}$ and $R_{2,2}$ are the R_2 values corresponding to a low dose and high dose region. D_1 and D_2 are the planned dose values corresponding to the R_2 values. Using these new calibration functions, renormalised dose maps were calculated. This renormalisation procedure uses dose data from the dose distribution which is actually being verified to calibrate the dosimeter's response. However, if the two dose points are measured with an independent dosimeter, this could still be used as an independent dose verification technique. This renormalisation procedure will further be referred to as *calibration method 3*.

(iv) A fourth renormalisation procedure was evaluated in which the slope of the original calibration fit was adjusted to match the R_2 value at the isocentre while maintaining the R_2 value at 0 Gy. This method is described in Tremblay *et al* (2011). This renormalisation procedure will be further referred to as *calibration method 4*.

2.7. Gamma map analysis

Quantitative comparison between the planned dose distribution and the measured dose distribution was performed by calculation of the 3D γ analysis index (Low *et al* 1998). The γ analysis was calculated with in house developed Matlab^{TM} software. The MR measurement data was chosen as reference data and the noise-free TPS data was chosen as the evaluated distribution (Low and Dempsey 2003). If noisy data (*i.e.* MR) were to be chosen as the evaluated distribution, this would lead to a reduction in the value of γ linearly proportional to the noise. This corresponds to an overestimation of the accuracy of the measured dose distribution. Additionally, the 2D gel measured dose maps are the sparsest data set which makes the gel measurements the reference dose distribution.

The 3D planned dose distribution and the 2D gel-measured dose distributions (acquired at 6, 30 and 54 h post-irradiation for the intra-batch experiment and acquired at 19 and 43 h post-irradiation for the inter-batch experiment) were interpolated to a grid of 0.25 $\times$ 0.25 mm^2 in order to obtain more accurate γ values. The 3D planned dose distribution and 3D gel-measured dose distributions (acquired 92 h post-irradiation for the intra-batch experiment and 85 h post-irradiation for the inter-batch experiment) were evaluated with a grid size of 1 $\times$ 1 $\times$ 1 mm^3.

The γ analysis was calculated for the criteria of 3% dose difference and 3 mm distance to agreement (DTA) (3%/3 mm).

Table 2. The maximum difference in slope (Δslope_{max}), $R_{2,intercept}$ ($\Delta\text{intercept}_{max}$) and $R_{2,sat}$ (Δsat_{max}) are listed for each scan in absolute values and in per cent relative to the mean value. Maximum dose difference (ΔD_{max}) are also shown that would result from calibrating the same measured R_2 value with the two most diverging calibration curves.

Calibration parameters at	6 h	30 h	54 h	92 h
Mean slope $[\times 10^{-2} s^{-1} Gy^{-1}]$	6.48	7.24	7.20	7.41
Δslope_{max} $[\times 10^{-2} s^{-1} Gy^{-1}$ (%)]	0.499 (7.7%)	0.221(3.1%)	0.079 (1.1%)	0.166 (2.2%)
Mean intercept $[s^{-1}]$	1.06	1.22	1.29	1.26
$\Delta\text{intercept}_{max}$ $[\times 10^{-2} s^{-1}$ (%)]	3.12 (2.9%)	0.84 (0.7%)	1.52 (1.2%)	1.33 (1.0%)
Mean saturation $[s^{-1}]$	1.875	1.993	2.105	1.979
Δsat_{max} $[s^{-1}$ (%)]	0.172 (9.2%)	0.247(12.4%)	0.233 (11.1%)	0.174 (8.8%)
ΔD_{max} [Gy (%)]	1.75 (14.6%)	0.164 (1.4%)	0.541 (4.5%)	0.517 (4.3%)

2.8. Dose resolution

The experimental dose resolution $D_{\Delta}^{95\%}$ (Baldock *et al* 2001), defined as the minimal separation at which two doses can be distinguished with a given level of confidence (95%), was calculated from the calibration phantom measurements as an indication of the uncertainty of the measured dose. The minimal detectable dose was also derived by calculating the dose resolution at 0 Gy.
A comparison was made with the theoretical dose resolution (De Deene *et al* 1998) from which the same parameters were calculated.

3. Results

3.1. Intra-batch reproducibility study

3.1.1. Dose-R_2 calibration One set of calibration phantoms was used in the intra-batch study. The set was irradiated with doses between 0 and 15 Gy. Thereafter, the calibration phantoms were scanned together with the volumetric phantoms in 4 scan sessions: 6 h, 30 h, 54 h and 92 h post-irradiation. During each scan session, each of the eight phantoms was scanned together with the set of calibration phantoms. From this study, the long term response stability of the gels was assessed. All dose-R_2 calibration plots were found to be well fitted by a mono-exponential function (figure 2). From the fit parameters, more intuitive parameters were calculated: slope, $R_{2,intercept}$ and $R_{2,sat}$. Table 2 summarises these results.

The trend in slopes, $R_{2,intercept}$ and $R_{2,sat}$ can be observed in figure 3.

For each scan session, the maximum dose difference was calculated that would result from calibrating the same measured R_2 value with the two most divergent calibration curves. This resulted in a 'worst-case' dose difference of 1.75 Gy, 0.164 Gy, 0.541 Gy and 0.517 Gy for the measurements performed at 6 h, 30 h, 54 h and 92 h post-irradiation

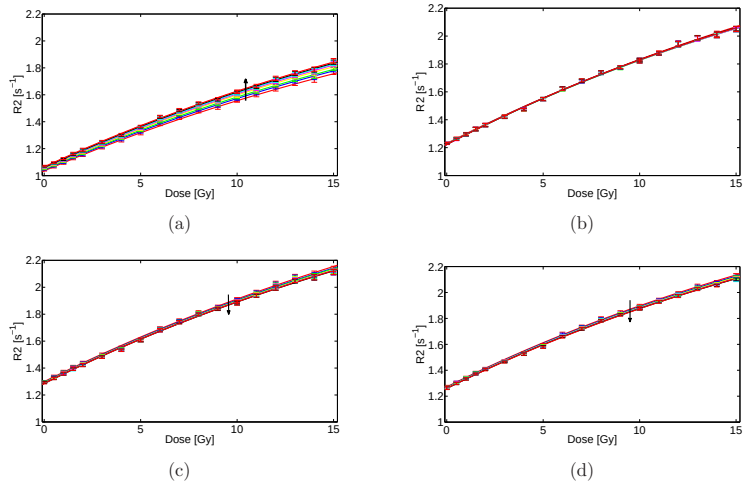

Figure 2. Dose-R_2 plots of the intra-batch reproducibility study recorded at 6 h (a), 30 h (b), 54 h (c) and 92 h (d) post-irradiation. At each scan session, eight consecutive scans were acquired which were all fitted against a mono-exponential function. The arrow indicates the direction of consecutive scans.

respectively on a total dose of 12 Gy. These numbers are a measure of the maximum dose deviation resulting from the calibration curve: 14.6%, 1.4%, 4.5% and 4.3% respectively.

The dose resolution (minimal separation between two absorbed doses such that they may be distinguished with a given level of confidence of 95%) as a function of absorbed dose was determined for the intra-batch reproducibility experiment and displayed in figure 4. The minimal detectable dose is the dose resolution as the dose approaches zero and was determined to be 0.31 Gy. The mean dose resolution in a dose interval between 0 and 10 Gy amounts to 0.38 Gy while the maximum dose resolution in this dose interval amounts to 0.46 Gy.

3.1.2. Volumetric measurements For each scan session, the maximum R_2 difference at the isocentre between the eight phantoms was calculated. These values amount to 0.054 s^{-1}, 0.021 s^{-1}, 0.014 s^{-1} and 0.036 s^{-1}. With an R_2 range of 0.65 s^{-1}, these R_2 differences amount to 8.3%, 3.2%, 2.2% and 5.5%.

In figure 5a, 5d, 5g and 5j R_2 profiles are shown of the transverse measurements in a vertical plane through the isocentre. In figure 1d a dashed line is drawn, indicating the location of the profile according to the phantom. Good agreement between the R_2 values of all phantoms can be observed in measurements 30 h (figure 5d) and 54 h (figure 5g) post-irradiation.

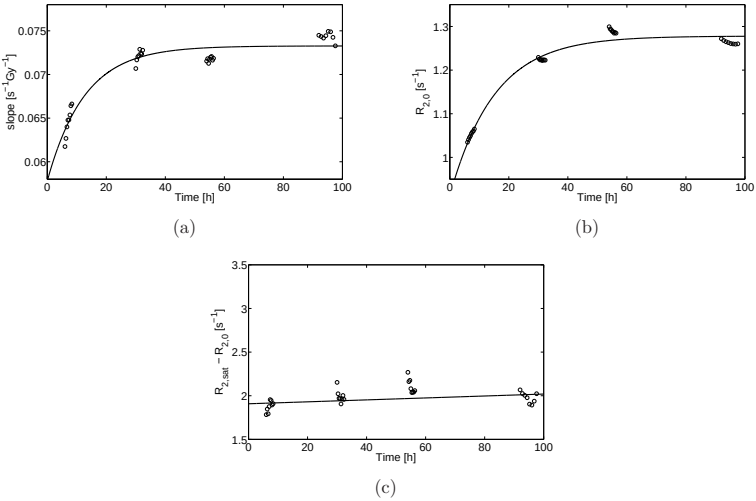

Figure 3. The slope (a), $R_{2,intercept}$ (b) and $R_{2,sat}$ (c) of the dose-R_2 plots derived from the dose-R_2 response as shown in figure 2. An exponential fit in (a) and (b) and a linear fit in (c) is shown as a guide to the eye.

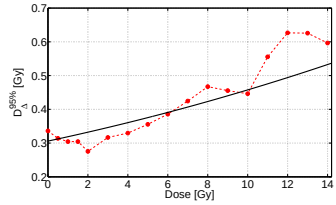

Figure 4. Experimental dose resolution $D_{\Delta}^{95\%}$ as a function of absorbed dose is compared to the theoretical dose resolution (full line).

Subsequently, the R_2 maps were calibrated to dose maps using the dose-R_2 relation derived from the calibration phantoms (calibration method 1). The deviation between the TPS calculated dose and the mean dose of the eight gel measured dose maps at the isocentre was determined. This average deviation amounted to 2.7% at 6 h, 9.0% at 30 h, 9.9% at 54 h and 13.0% at 92 h post-irradiation. The standard deviation of the mean dose difference amounts to 2.9% at 6 h, 1.4% at 30 h, 1.8% at 54 h and 3.1% at 92 h post-irradiation. These standard deviations correspond to the dosimetric precision

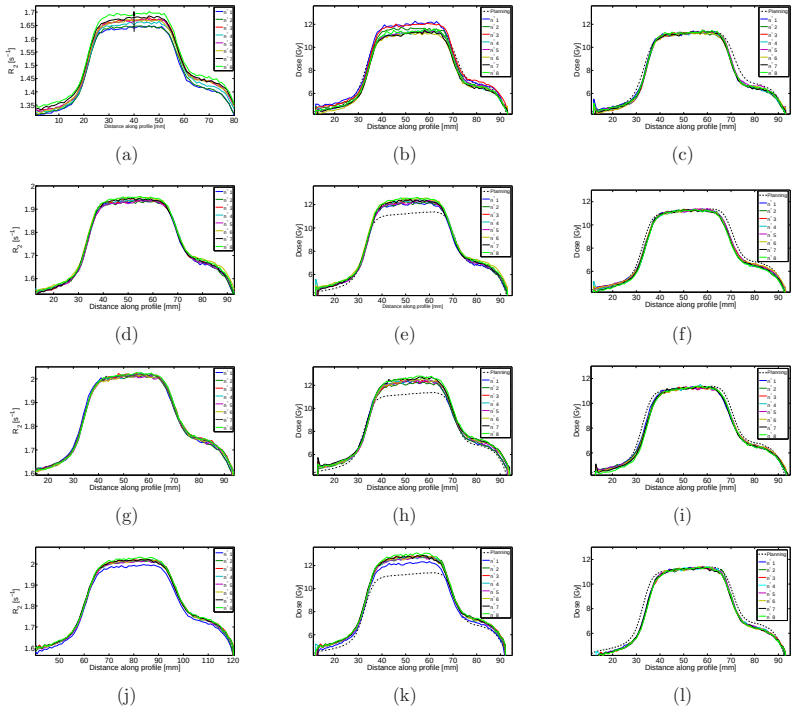

Figure 5. Profiles in the anterior-posterior direction (y-direction in figure 6) are shown of transverse measurements in a vertical plane through the isocentre of the data acquired in scan sessions at 6 h (a,b,c) 30 h (d,e,f), 54 h (g,h,i) and 92 h (j,k,l) post-irradiation. Graph a, d, g and j show profiles through R_2 maps of all eight phantoms. Graph b, e, h and k show profiles through the eight gel measured dose maps calibrated with the calibration phantoms (calibration method 1) compared to a corresponding profile through the TPS calculated dose map. The large dose deviation can be clearly seen. Finally, graph c, f, i and l show profiles through renormalised gel measured dose maps (using calibration method 3) compared to a profile through the TPS calculated dose map.

of the intra-batch experiment. The dose differences are shown for all phantoms in table 3. In figure 5b, 5e, 5h and 5k dose profiles are shown of the transverse measurements in a vertical plane through the isocentre. The dose offset between all phantoms and the planned dose profile (dashed line) can be clearly seen.

To investigate the origin of the large dose deviations between the TPS calculated and gel measured dose distributions, the calibration function was renormalised for all gel phantoms individually (calibration methods 2, 3 and 4). These new calibration

Table 3. For each phantom the dose difference in per cent relative to the ion chamber recorded dose at the isocentre is shown for each scan session of the intra-batch reproducibility study (calibration method 1). The phantoms are numbered in order of scanning (*i.e.* phantom number 1 was scanned first and phantom number 8 was scanned last). The average dose differences and standard deviations (dosimetric precision) are also given.

	2D scan at 6 h	2D scan at 30 h	2D scan at 54 h	Full 3D scan at 92 h
No 1	6.9%	7.8%	7.3%	6.2%
No 2	3.7%	7.5%	7.4%	11.4%
No 3	7.0%	8.8%	9.8%	13.5%
No 4	0.9%	9.3%	10.4%	13.0%
No 5	0.5%	7.5%	10.2%	13.6%
No 6	0.3%	10.3%	10.7%	14.5%
No 7	0.1%	9.4%	11.4%	15.5%
No 8	1.8%	11.5%	12.3%	16.2%
Mean	2.7%	9.0%	9.9%	13.0%
σ	2.9%	1.4%	1.8%	3.1%

Table 4. Overview of γ analysis results for 3%/3 mm for scan session 4 (92 h) comparing the different calibration methods. In this table the percentage in agreement ($\gamma \leq 1$) are given for all phantoms.

Intra-batch γ	Method 1	Method 2	Method 3	Method 4
No 1	93.3%	96.4%	98.0%	98.3%
No 2	85.4%	89.2%	96.2%	97.8%
No 3	76.3%	85.5%	96.3%	97.9%
No 4	76.2%	82.3%	96.5%	97.9%
No 5	75.3%	81.8%	95.7%	97.7%
No 6	70.8%	81.3%	95.9%	97.4%
No 7	68.2%	81.3%	95.6%	97.0%
No 8	62.3%	82.5%	96.3%	96.4%
Mean	76.0%	85.0%	96.3%	97.6%

functions were then used to recalculate dose maps. In figure 6, an overview is given of the eight transverse dose maps obtained by using calibration method 3 and acquired 54 h post-irradiation. The planned dose distribution is shown in figure 6a.

3D γ maps between gel-measured and calculated dose distributions were calculated. The different calibration methods are compared for the full 3D scan (92 h) in table 4 using a γ analysis of 3%/3 mm. In table 4 calibration method 1 and 2 show a large percentage of pixels failing the γ criteria. Calibration methods 3 and 4 result in a better match between the gel measured dose distribution and the TPS calculated dose distribution and will therefore be the only two calibration methods further compared in this paper.

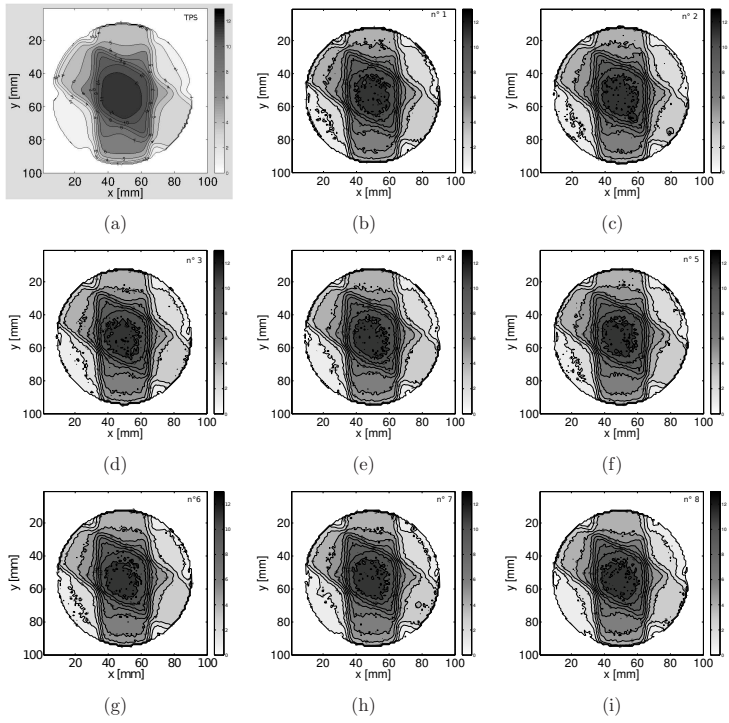

Figure 6. An overview of the eight gel measured transverse dose maps acquired 54 h post-irradiation (b-i) calibrated using method 3 compared to the TPS calculated dose distribution in (a). The units of the colorbar are expressed in Gy.

An overview of the number of pixels passing the γ criteria after renormalisation using method 3 and 4 for all phantoms is given in table 5. For a 3%/3 mm γ evaluation 97.9%, 96.9%, 96.3% and 96.3% of the pixels passes the criteria at 6 h, 30 h, 54 h and 92 h respectively for method 3. For calibration method 4, these numbers amount to 97.0%, 96.5%, 96.5% and 97.6%.

The highest number of pixels passing the γ criteria were found in phantom number 1(figure 7a and 7b) and the lowest number of pixels passing were found in phantom number 7 (7c and 7d). In phantom number 7 small air bubbles were formed after fabrication causing a higher percentage of pixels failing the γ criteria.

Table 5. Overview of γ analysis results for 3%/3 mm on dose maps of the intra-batch reproducibility study. In this table the percentage of pixels in agreement ($\gamma \leq 1$) are given for all phantoms and all measurements. Calibration method 3 and 4 are compared to each other.

	2D scan at 6 h		2D scan at 30 h		2D scan at 54 h		3D scan at 92 h	
Renormalisation method:	3	4	3	4	3	4	3	4
No 1	98.7%	97.5%	96.5%	97.1%	94.8%	97.1%	98.0%	98.3%
No 2	97.6%	95.9%	95.5%	93.9%	96.0%	96.7%	96.2%	97.8%
No 3	98.0%	94.5%	97.1%	97.2%	96.4%	96.8%	96.3%	97.9%
No 4	97.0%	97.3%	97.6%	97.0%	96.1%	96.1%	96.5%	97.9%
No 5	97.7%	97.3%	96.0%	96.2%	97.0%	97.3%	95.7%	97.7%
No 6	97.8%	98.3%	97.3%	96.7%	97.0%	97.0%	95.9%	97.4%
No 7	98.6%	97.5%	97.5%	96.9%	95.9%	95.9%	95.6%	97.0%
No 8	97.6%	97.3%	97.9%	97.1%	96.8%	95.2%	96.3%	96.4%
Mean	97.9 %	97.0%	96.9%	96.5%	96.3%	96.5%	96.3%	97.6%

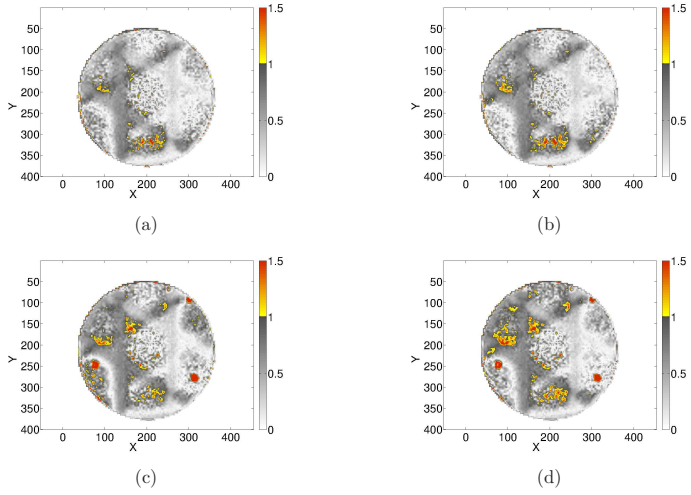

Figure 7. γ evaluation map (3%/3 mm) of phantom number 1 (a,b) and number 7 (c,d) calculated after calibration with method 3 (a,c) and method 4 (b,d) showing the regions where the $\gamma > 1$ in color. In phantom number 7, small air bubbles occurred after fabrication causing a higher percentage of pixels failing the γ criteria. The units of the colour bar are γ values.

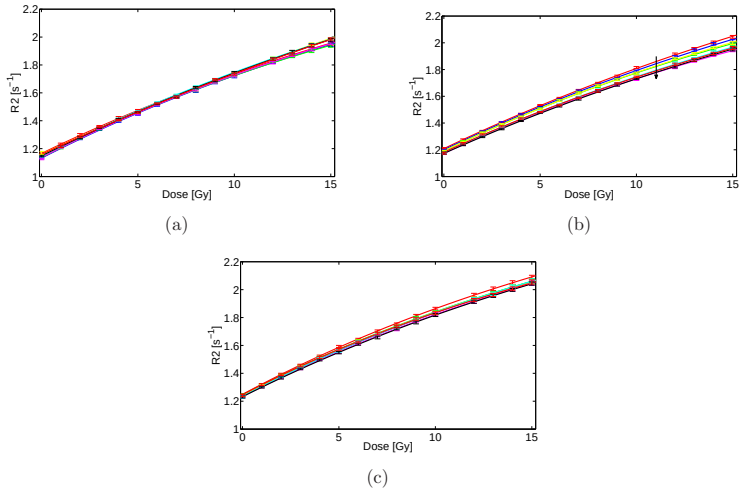

Figure 8. Dose-R_2 plots of the inter-batch reproducibility study recorded at 19 h (a), 43 h (b) and 85 h (c) post-irradiation. At each time point eight consecutive scans were acquired which were all fitted against a mono-exponential function. The arrow in (b) indicates the direction of the effect of increasing post-irradiation time. In (a) and (c), no directional effect of increasing post-irradiation time was found, explaining the absence of an arrow in these figures. The different time points correspond to the data points in figure 9.

3.2. Inter-batch reproducibility study

The inter-batch reproducibility study also includes chemical variations which are typical for a repeated fabrication of a gel dosimeter. First, the reproducibility of the dose-R_2 response of the calibration phantoms will be addressed. Secondly, the 2D and 3D measurements performed at 19 h, 43 h and 85 h post-irradiation will be discussed.

3.2.1. Dose-R_2 calibration Eight sets of calibration phantoms were fabricated and irradiated along with the corresponding spherical phantom. All sets were irradiated with doses ranging between 0 and 15 Gy. Thereafter, the calibration phantoms were scanned at 3 occasions: 19 h, 43 h and 85 h post-irradiation. All dose-R_2 calibration plots were found well-fitting to a mono-exponential function (figure 8).

From the fit parameters the slope, $R_{2,intercept}$ and $R_{2,sat}$ were calculated which are summarised in table 6.

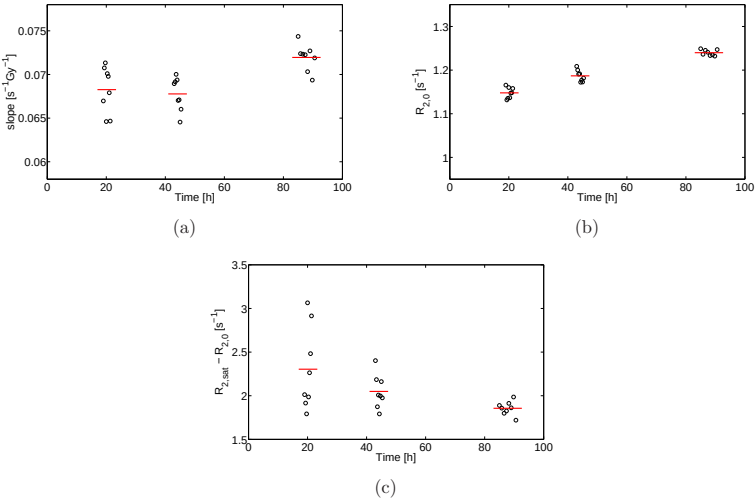

Figure 9. The slope (a), $R_{2,intercept}$ (b) and $R_{2,sat}$ (c) of the dose-R_2 plots derived from the dose-R_2 response as shown in figure 8. Note the scale is identical to figure 3. The red bars represent the mean values of all eight phantoms for each measurement.

Table 6. The maximum difference in slope ($\Delta slope_{max}$), $R_{2,intercept}$ ($\Delta intercept_{max}$) and $R_{2,sat}$ (Δsat_{max}) are listed for each scan in absolute values and in per cent relative to the mean value. Maximum dose difference (ΔD_{max}) are also shown that would result from calibrating the same measured R_2 value with the two most diverging calibration curves.

Calibration parameters at	19 h	43 h	85 h
Mean slope $[\times 10^{-2} s^{-1} Gy^{-1}]$	6.79	6.80	7.23
$\Delta slope_{max}$ $[\times 10^{-2} s^{-1} Gy^{-1}$ (%)]	0.67(9.9%)	0.55 (8.0%)	0.50 (6.9%)
Mean intercept $[s^{-1}]$	1.15	1.18	1.24
$\Delta intercept_{max}$ $[\times 10^{-2} s^{-1}$ (%)]	8.2 (7.1%)	4.1 (3.5%)	1.7 (1.4%)
Mean saturation $[s^{-1}]$	2.30	2.05	1.86
Δsat_{max} $[\times 10^{-2} s^{-1}$ (%)]	1.27 (55.2%)	0.61 (29.8%)	0.27 (14.3%)
ΔD_{max} [Gy (%)]	0.608(5.1%)	1.63(13.6%)	1.00(8.3%)

The relation between all slopes, $R_{2,intercept}$ and $R_{2,sat}$ can be observed in figure 9.

For each scan session, the maximum dose difference was calculated that would result from calibrating the same measured R_2 value with the two most divergent calibration curves. Note that here the calibration curves were acquired from eight different batches of gel. Therefore larger differences are expected. This resulted in a dose difference of 0.608 Gy (5.1%), 1.63 Gy (13.6%) and 1.00 Gy (8.3%) for the measurements performed

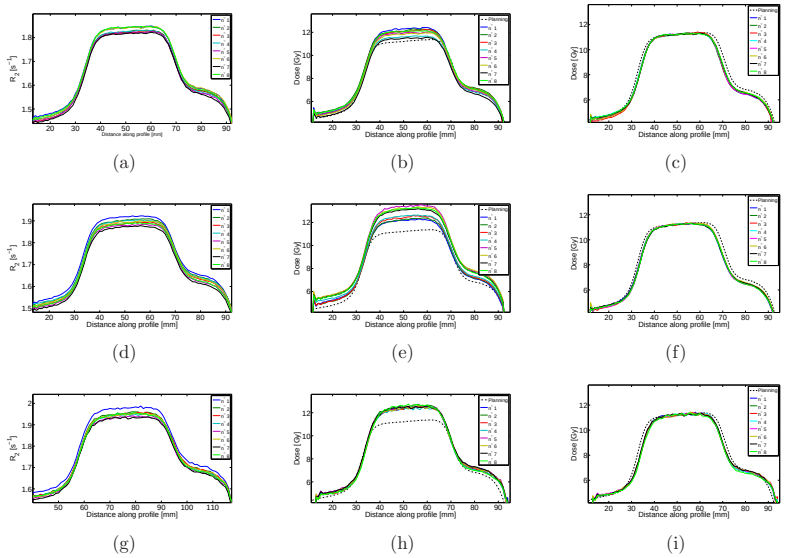

Figure 10. Profiles in anterior-posterior direction are shown of transverse measurements in a vertical plane through the isocentre of the data acquired at 19 h (a,b,c) 43 h (d,e,f) and 85 h (g,h,i) post-irradiation (inter-batch reproducibility experiment). Graph a, d and g show profiles through R_2 maps of all eight spherical flasks. Graph b, e and h show profiles through the eight gel-measured dose maps calibrated with the calibration phantoms compared to a profiles through the TPS calculated dose map. Finally graph c, f and i show profiles through linearly renormalised gel measured dose maps compared to a profile through the TPS calculated dose map.

at 19 h, 43 h and 85 h post-irradiation respectively on a total dose of 12 Gy (table 6).

3.2.2. Volumetric measurements For each scan session, the maximum R_2 difference at the isocentre between the eight phantoms (each of a different batch) was calculated. These values amount to 0.027 s^{-1}, 0.045 s^{-1} and 0.051 s^{-1}. Relative to an R_2 range of 0.65 s^{-1} this amounts to 4.2%, 6.9% and 7.9% maximum difference in R_2 value at the isocentre of the phantom. In figure 10a, 10d and 10g R_2 profiles are shown of the 2D transverse measurements in a vertical plane through the isocentre.

The R_2 maps were calibrated to dose using the dose-R_2 relationship derived from the corresponding calibration curves (calibration method 1). The deviation between the TPS calculated dose and the mean dose of the eight gel phantoms was determined in the isocentre. The dose differences are listed for all phantoms in table 7. The dosimetric

Table 7. For each phantom the dose difference in per cent relative to the ion chamber measured dose in the isocentre is shown for each scan session of the inter-batch reproducibility study. The phantoms are numbered in order of scanning (*i.e.* phantom number 1 was scanned first and phantom number 8 was scanned last). The average dose differences and corresponding standard deviations (dosimetric precision) are also given.

Inter-batch	2D scan at 19 h	2D scan at 43 h	Full 3D scan at 85 h
No 1	9.7%	8.4%	9.8%
No 2	8.0%	9.1%	11.0%
No 3	7.3%	10.3%	9.8%
No 4	3.1%	11.8%	9.8%
No 5	6.3%	19.2%	10.8%
No 6	5.5%	17.4%	10.0%
No 7	2.6%	16.4%	10.9%
No 8	7.6%	17.1%	12.2%
Mean	6.3%	13.7%	10.6%
σ	2.4%	4.3%	0.8%

Table 8. Overview of γ analysis results for 3%/3 mm.The percentage in agreement ($\gamma \leq 1$) is given for all phantoms for all measurements. Calibration method 3 and 4 are compared with each other.

	2D scan at 19 h		2D scan at 43 h		3D scan at 85 h	
Renormalisation method:	3	4	3	4	3	4
No 1	99.5%	98.5%	97.9%	99.3%	95.9%	98.0%
No 2	99.5%	99.0%	98.9%	99.4%	96.6%	98.5%
No 3	99.1%	99.3%	98.8%	99.1%	96.5%	97.3%
No 4	99.1%	99.3%	98.3%	99.4%	96.5%	97.6%
No 5	99.2%	99.4%	97.5%	98.9%	96.8%	98.2%
No 6	99.2%	98.8%	96.7%	97.9%	95.7%	97.8%
No 7	99.4%	99.5%	98.5%	98.9%	96.7%	98.6%
No 8	98.3%	95.7%	98.1%	98.7%	92.3%	92.4%
Mean	99.2 %	98.7%	98.1%	99.0%	95.9%	97.3%

precision of the inter-batch experiment is defined as the standard deviation of the mean dose deviation between the gel measured and TPS calculated dose maps and amounts to 2.4%, 4.3% and 0.8% for the measurements performed at 19 h, 43 h and 85 h post-irradiation, respectively.

In figure 10b and 10e, anterior-posterior dose profiles through the isocentre are shown. The dose offset between all phantoms and planned dose profile (dashed line) can be observed.

3D γ maps between gel-measured (calibrated using method 3 and 4) and TPS calculated dose distributions were constructed. An overview of the number of pixels passing the γ analysis criteria for all phantoms is given in table 8.

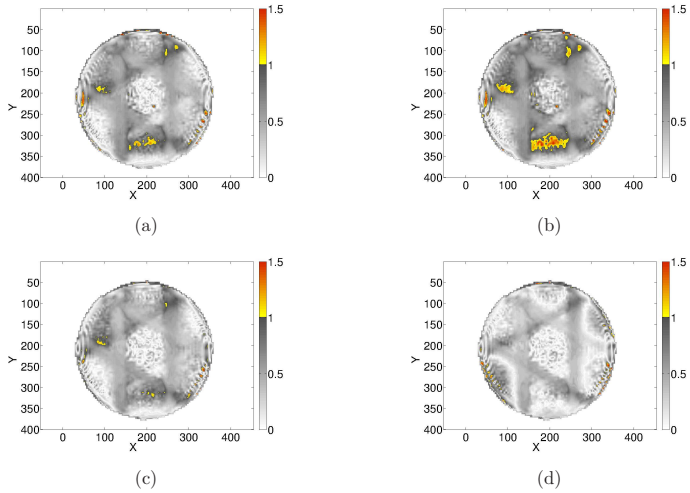

Figure 11. γ evaluation map (3%/3 mm) of phantom number 8 (a,b) and number 1 (c,d) calculated after renormalisation with method 3 (a,c) and method 4 (b,d) showing the regions where $\gamma > 1$ in color. The units of the colour bar are γ values.

In figure 11, the 2 renormalisation methods are compared for the γ maps with the lowest (a and b) and the highest (c and d) percentage of pixels ≤ 1.

4. Discussion

4.1. Intra-batch reproducibility study

The intra-batch reproducibility study, of which the results are presented in this work, is used to evaluate the validity of gel dosimetry without the influence of variations in chemical composition or fabrication procedure. Furthermore, great care was taken to ensure that the irradiation and read-out positioning was performed in a highly reproducible manner to minimise the influence of set-up errors.

4.1.1. Dose-R_2 calibration The theoretical dose resolution ($D_{\Delta}^{95\%}$) for this experiment demonstrated a maximum uncertainty of 0.46 Gy and an average uncertainty of 0.38 Gy for the dose range 0-10 Gy, which corresponds to a maximum uncertainty of 4.1% and an average uncertainty of 3.4% compared to the isocentre dose.

Four scan sessions of eight phantoms and 19 calibration phantoms were performed at 6 h, 30 h, 54 h and 92 h after irradiation. Each of the eight phantoms was scanned together with the corresponding set of calibration phantoms. During the

first measurement (6 h post-irradiation) large variations between consecutive scans are attributed to well-described chemical instabilities. As also shown by De Deene *et al* (2006), the slope and, to a lesser extent, the intercept significantly increase the first hours post-irradiation. In this study the slope and intercept change with respectively 0.00205 s^{-1} Gy^{-1} h^{-1} and 0.0116 s^{-1} h^{-1}.

The maximum dose difference in the other sessions *i.e.* acquired at 30 h, 54 h and 92 h post irradiation, obtained by using the most deviating calibration curves, would amount to 1.4% (30 h), 4.5% (54 h) and 4.3% (92 h). The smallest difference in calibration curves in scan session 2 (30 h) is also apparent from figure 2b. For scan sessions 3 (figure 2c) and 4 (figure 2d) a small but steady downwards shift in calibration curves appears over the eight measurements as indicated by the direction of the arrow. We attribute these small differences to temperature variations during scanning. This is also apparent from a variation in the intercept of the calibration curves which can be observed in figure 3b. As shown in a Vandecasteele and De Deene (2013b) a decrease in intercept of 0.02 s^{-1} is estimated to be caused by a temperature increase of $0.6°C$ between the first and the last scan in the scan session. It is noted that no significant correlation with changes in slope and $R_{2,sat}$ are found.

4.1.2. Volumetric phantoms A comparison was made between all R_2 maps of the phantoms. Again, significant deviations in R_2 occur during scan session 1 (6 h) because of chemical instabilities during the first hours post-irradiation (figure 5a). This is indicated by the arrow showing the direction of increasing post-irradiation time. For scan session 2-4 (acquired at 30 h, 54 h and 9 2h post-irradiation), the maximum R_2 difference measured at the isocentre between all eight phantoms during each measurement amounted to 5.5%. It is noted that the maximum difference of 5.5% is caused by a single measurement outlier (*i.e.* first measurement at 92 h post-irradiation, figure 5j). This deviation corresponds to a $1°C$ higher temperature in phantom number 1 as compared to the other phantoms. The maximum difference between the other seven scans performed in the same scan session is 2.9%. This significant deviation in R_2 for a $1°C$ temperature variation illustrates the high sensitivity to temperature during scanning. All phantoms were stored in a corner of the MRI scanning room. We found that temperature differences between the scanner bore and the scanner room may easily amount to 1 to $2°C$ which also depends on the ventilation of the scanner bore and the scanner load of that day (Vandecasteele and De Deene 2013b). Ignoring the measurement on phantom number 1 in scan session 4 (92 h), the maximum R_2 uncertainty amounts to 3.2% (maximum difference occurred at 30 h post-irradiation).

This result also implies that a calibration of a volumetric phantom performed with a volumetric calibration phantom (containing a similar volume of the same batch of gel) would result in a minimum dose uncertainty of 3.2%. The calibration method using small calibration phantoms results in a higher minimal dose uncertainty (4.5%). As will be proven in Vandecasteele and De Deene (2013b), small calibration phantoms are more easily influenced by small temperature variations. These small variations will result in

significant dose variations. Larger volumetric phantoms exhibit more thermal inertia.

The calibration of the R_2 maps to dose maps using the measured dose-R_2 relationship (calibration method 1) was found to result in large mean dose deviations up to 13.0% and thus a poor accuracy. The dosimetric precision of the intra-batch experiment was defined as the maximum standard deviation of the mean dose difference between the gel measured dose and ion chamber recorded dose for all measurements and amounted to 3.1% (92 h post-irradiation).

We furthermore observe that there is a trend towards larger dose deviations in the scans acquired later within each scan session (see table 3). In the specific case of the measurement performed 6 hours post-irradiation, measurements 1, 2 and 3 result in large dose discrepancies of approximately 4% - 7% (table 3). Thereafter, the next five measurements are within 1% - 2% of the ion chamber dose value indicating that some time was needed to equilibrate the gel phantoms to the MRI scanner room.

Ideally, gel dosimetry should be applied as an absolute dosimetry technique. Therefore the main focus is on the traditional method of calibrating the irradiated phantom with small test tubes 'homogeneously irradiated' with a well-defined dose (calibration method 1). Because calibration method 1 resulted in large dose inaccuracies, three renormalisation methods were tested to investigate the origin of the dose discrepancies. The renormalisation methods are intended to rescale the gel measured dose maps using independent dose measurements. In this study we used the ion chamber measurement as independent dose verification technique. Method 2 was based on a linear fit between the R_2 value of the non-irradiated calibration phantom and the R_2 value measured at the isocentre of the volumetric phantom. The results show an increase in slope as compared to calibration method 1. From the γ evaluation results, it can be concluded that this renormalisation technique meets the criteria of 3%/3 mm for only (on average) 85% of the pixels which is almost 10% higher than using method 1 but also 10% lower than method 3 and 4. Method 3 uses two independently determined dose points to linearly renormalise the calibration curve while the shape of the calibration plot is maintained. Method 4 uses only one independently determined dose point to adjust the slope of the calibration curve obtained from the calibration phantoms. Method 4 was previously described by Tremblay *et al* (2011) where in the gel plastic scintillating detectors (PSD) are used to measure the dose. We have measured the dose indirectly by use of a pinpoint ion chamber inserted into a spherical phantom. The renormalised dose maps using calibration methods 3 and 4 show a good agreement with the planning data. The γ criterion of 3%/3 mm was passed for on average 97% of the pixels in calibration methods 3 and 4. In one of the phantoms air bubbles were formed after fabrication. In these regions the γ criteria were not reached as can be seen in figure 7. Both method 3 and method 4 achieve the same level of accuracy. Method 4 can be considered as the preferred method because only one independently determined dose point is required which can be obtained by ion chamber or PSD measurement.

4.2. Inter-batch reproducibility study

Any variations in the fabrication of the gel dosimeter also emerge in the accuracy and precision of the inter-batch reproducibility study.

4.2.1. Dose-R_2 calibration Three scan sessions of the eight phantoms and eight sets of calibration phantoms were acquired at 19 h, 43 h and 85 h after irradiation. The maximum dose deviation that corresponds to the two most divergent calibration curves amounted to 5.1% (19 h), 13.6% (43 h) and 8.3% (85 h). As within scan session 2 (43 hours post-irradiation), a continuous trend in the variation of the dose-R_2 calibration plots is observed (indicated by the direction of the arrow in figure 8b), the large variations in dose-R_2 of 13.6% are also attributed to temperature fluctuations. Probably, the variations occurring at 85 hours post-irradiation are more representative for the maximum dose deviation.

4.2.2. Volumetric phantoms A comparison was made between all R_2 maps of the spherical phantoms. An anterior-posterior profile through the R_2 maps for all measurements is shown in figure 10a, 10d and 10g. The maximum difference measured at the isocentre between all eight spherical flask during each measurement amounted to 7.9%. This is in the same order of magnitude as the 8.3% precision obtained for the calibration phantoms. As the maximum inter-batch deviation in R_2 amounts to 7.9%, it is advisable to use the same batch of gel to calibrate volumetric phantoms to dose where a dose uncertainty of 3.2% is achievable.

The dose differences show an initial increase up to 43 hours post-irradiation followed by a decrease of the dose difference at 85 hours post-irradiation.

In figure 10c and figure 10f the lower part of the dose profile presents a dose offset, however in figure 10i this offset is eliminated. Again the randomness of temperature fluctuations during scanning is suggested by these results causing spatial dose variations inside the gel dosimeter.

When dose calibration of the R_2 maps is performed on the basis of small calibration phantoms, large mean dose deviations up to 13.7% are found. Remarkably, a very low variability is observed in scan session 3 (85 h post-irradiation) as can be seen in figure 10h and in table 7.

The gel measured dose profiles are 1.5 mm narrower than the profiles obtained from the TPS which can be observed in figure 10c, 10f and 10i. This is a cumulative effect of uncertainties of three intersecting beams. This discrepancy between the treatment planning system and the linac at our department results from poor modelling of small fields.

Overall the mean dose accuracy obtained in the inter-batch reproducibility study using an absolute calibration (method 1) is similar to the mean accuracy obtained in the intra-batch study. This is also in accordance with the hypothesis that the discrepancy between calibration phantoms and large phantoms lies at the origin of the

dose discrepancies.

To investigate the origin of the large mean dose discrepancies, the gel measured dose maps were rescaled. The renormalised dose maps using methods 3 and 4 show a good agreement with the planning data. Almost 99% of the pixels pass the γ criterion of 3%/3 mm. A higher success rate of the γ criterion 3%/3 mm was achieved during the inter-batch study compared to the intra-batch study. This can be explained by the fact that the SNR is higher in the inter-batch study. Both method 3 and method 4 achieve the same level of accuracy. No additional dose discrepancies were found inside the volumetric phantoms compared to the TPS after renormalisation suggesting the validity of the renormalisation technique for small volume phantoms. However, for realistically-sized anthropomorphic polymer gel phantoms renormalisation will not suffice because of large temperature differences inside the phantom as shown in a concurrent paper (Vandecasteele and De Deene 2013b).

Further investigations into physico-chemical effects and MR imaging artefacts were performed to determine the relative contribution of other causes of inaccuracies in two companion papers (Vandecasteele and De Deene 2013a and 2013b).

5. Conclusions

The aim of this study was to evaluate the validity of 3D dosimetry using normoxic polymer gel dosimeters. Both the intra-batch and inter-batch accuracy and precision were evaluated.

The results of the intra-batch study showed a high dosimetric precision (3.1%) notwithstanding a poor dosimetric accuracy (mean dose discrepancies up to 13.0%). For the inter-batch experiment a similar precision was found (4.3%) along with a poor dosimetric accuracy (mean dose discrepancies up to 13.7%). The calibration method was identified in both experiments as the origin of inaccuracies. Further experiments to reveal the exact causes of these inaccuracies are performed in two companion papers (Vandecasteele and De Deene 2013a and 2013b). The dose resolution demonstrated a maximum uncertainty of 4.1% for the dose range between 0 and 10 Gy within a level of confidence of 95%. The effect of different renormalisation procedures of the dose-R_2 calibration curve using an independent ion chamber dose measurement on the dosimetric accuracy and precision was also investigated to seek the origin of the large mean dose discrepancies. Applying a two-point renormalisation, an excellent agreement between the gel measured and TPS calculated 3D dose maps is achievable: 97% and 99% of the pixels meet the 3%/3mm criteria respectively for the intra- and inter-batch experiment.

It is therefore concluded that polymer gel dosimetry of small volumetric phantoms can be performed with a high dosimetric precision and accuracy when a renormalisation is performed using independent dose measurements. For realistically-sized anthropomorphic polymer gel phantoms renormalisation will not suffice because of large temperature differences inside the phantom (Vandecasteele and De Deene 2013b). The implementation of dedicated artefact compensation strategies are therefore

required. Temperature variations between calibration and volumetric phantoms are shown to be the major cause of dosimetric inaccuracy when MRI polymer gel dosimetry is performed in an 'absolute' way.

Acknowledgments

This research is supported by the Institute for the Promotion of Innovation though Science and Technology in Flanders (IWT -Vlaanderen). The authors would like to thank Bart Truyens for constructing dedicated equipment that was indispensable in the experimental set-up.

References

Baldock C, Burford R P, Billingham N, Wagner G S, Patval S, Badawi R D and Keevil S F 1998 Experimental procedure for the manufacture and calibration of polyacrylamide gel (PAG) for magnetic resonance imaging (MRI) radiation dosimetry *Phys. Med. Biol.* **43** 695-702

Baldock C, Lepage M, Bck S Å J, Murry PJ, Jayasekera P M, Porter D and Kron T 2001 Dose resolution in radiotherapy polymer gel dosimetry: effect of echo spacing in MRI pulse sequence. *Phys. Med. Biol.* **46** 449-60

Baldock C, Murry P and Kron T 1999 Uncertainty analysis in polymer gel dosimetry. *Phys. Med. Biol.* **44** N243-6

Björeland A, Lindvall P, Karlsson A, Gustavsson H, Bäck S Å J, Karlsson M and Bergenheim T A 2008 Liquid ionization chamber calibrated gel dosimetry in conformal stereotactic radiotherapy of brain lesions *Acta. Oncol.* **47** 1099-109

Cardenas R L, Cheng K H, Verhey L J, Xia P, Davis L and Cannon B 2002 A self consistent normalized calibration protocol for three dimensional magnetic resonance gel dosimetry *Magn. Reson. Imaging* **20** 667-79

Ceberg S, Gagne I, Gustafsson H, Scherman J B, Korreman S S, Kristoffersen F K, Hilts M and Bäck S Å J 2010 RapidArc treatment verification in 3D using polymer gel dosimetry and Monte Carlo simulation *Phys. Med. Biol.* **55** 4885-98

Ceberg S, Karlsson A, Gustavsson H, Wittgren L and Bäck S Å J 2008 Verification of dynamic radiotherapy: the potential for 3D dosimetry under respiratory-like motion using polymer gel *Phys. Med. Biol.* **53** N387-N396

Cosgrove V P, Murphy P S, McJury M, Adams E J, Warrington A P, Leach M O and Webb S 2000 The reproducibility of polyacrylamide gel dosimetry applied to stereotactic conformal radiotherapy *Phys. Med. Biol.* **45** 1195-210

Crescenti R A, Scheib S G, Schneider U and Gianolini S 2007 Introducing gel dosimetry in a clinical environment: customization of polymer gel composition and magnetic resonance imaging parameters used for 3D dose verifications in radiosurgery and intensity modulated radiotherapy *Med. Phys.* **34** 1286-97

De Deene Y 2004 Fundamentals of MRI measurements for gel dosimetry *J. Phys. Conf. Ser.* **3** 87-114

De Deene Y and De Wagter C 2001 Artifacts in multi-echo T2 imaging for high-precision gel dosimetry: III. Effects of temperature drift during scanning *Phys. Med. Biol.* **46** 2697-711

De Deene Y, De Wagter C and De Neve W 2000a Artifacts in multi-echo T2 imaging for high-precision gel dosimetry: II. Analysis of B1 field inhomogeneity *Phys. Med. Biol.* **45** 1825-39

De Deene Y, De Wagter C, De Neve W and Achten E 2000b Artifacts in multi-echo T2 imaging for high-precision gel dosimetry: I. Analysis and compensation of eddy currents *Phys. Med. Biol.* **45** 1807-23

De Deene Y, De Wagter C, Van Duyse B, Derycke S, Mersseman B, De Gersem W, Voet T, Achten E and De Neve W 2000c Validation of MR-based polymer gel dosimetry as a pre-clinical 3D verification tool in conformal radiotherapy: comparison with film dosimetry and computer planning *Magn. Reson. Med.* **43** 116-125

De Deene, Y, Hurley C, Venning A, Vergote K, Mather M, Healy B and Baldock C 2002a A basic study of some normoxic polymer gel dosimeters *Phys. Med. Biol.* **47** 3441-63

De Deene Y, Pittomvils G and Visalatchi S 2007 The influence of cooling rate on the accuracy of normoxic polymer gel dosimeters *Phys. Med. Biol.* **52** 2719-28

De Deene Y, Van de Walle R, De Wagter C and Achten E 1998 Mathematical analysis and experimental investigation of noise in quantitative magnetic resonance imaging applied in polymer gel dosimetry *Signal Process.* **70** 85-101

De Deene Y, Venning A, Hurley C, Healy B J and Baldock C 2002b Dose-response stability and integrity of the dose distribution of various polymer gel dosimeters *Phys. Med. Biol.* **47** 2459-70

De Deene Y, Vergote K, Claeys C and De Wagter 2006 The fundamental radiation properties of normoxic polymer gel dosimeters: a comparison between a methacrylic acid based gel and acrylamide based gels *Phys. Med. Biol.* **51** 653-73

Dumas E M, Leclerc G and Lepage M 2006 Effect of container size on the accuracy of polymer gel dosimetry *J. Phys.: Conf. Ser* **56** 239-41

Fong P M, Keil D C , Does M D and John C Gore 2001 Polymer gels for magnetic resonance imaging of radiation dose distributions at normal room atmosphere *Phys. Med. Biol.* **46** 3105-13

Fragoso M, Love P A , Verhaegen F , Nalder C, Bidmead A M, Leach M and Webb S 2004 The dose distribution of low dose rate Cs-137 in intracavitary brachytherapy: comparison of Monte Carlo simulation, treatment planning calculation and polymer gel measurement *Phys. Med. Biol.* **49** 5459-74

Gustavsson H, Karlsonn A, Bäck S *Å* J and Olsson L E 2003 Magic-type polymer gel for three-dimensional dosimetry: Intensity-modulated radiation therapy verification *Med. Phys.* **30** 1264-71

Hepworth S J, Leach M O and Doran S J 1999 Dynamics of polymerization in polyacrylamide gel (PAG) dosimeters: (II) modeling oxygen diffusion *Phys. Med. Biol.* **44** 1875-84

Hill B, Venning A J and Baldock C 2008 Polymer gel dosimetry on a multislice computed tomography scanner: effect of changing parameters on CTDI *Phys. Med.* **24** 149-58

Hurley C, McLucas C, Pedrazzini G and Baldock C 2006 High-resolution gel dosimetry of a HDR brachytherapy source using normoxic polymer gel dosimeters: Preliminary study *Nucl. Instr. Meth. Phys. Res.* A **565** 801-11

Hurley C, Venning A and Baldock C 2005 A study of a normoxic polymer gel dosimeter comprising methacrylic acid, gelatin and tetrakis (hydroxymethyl) phosphonium chloride (MAGAT). *Appl. Radiat. Isot.* **63** 443-56

Jirasek A, Hilts M, Shaw C and Baxter P 2006 Investigation of tetrakis hydroxymethyl phosphonium chloride as an antioxidant for use in x-ray computed tomography polyacrylamide gel dosimetry *Phys. Med. Biol.* **51** 1891-906

Karlsson A, Gustavsson H, Mnsson S, McAuley K B and Bäck S *Å* J 2007 Dose integration characteristics in normoxic polymer gel dosimetry investigated using sequential beam irradiation. *Phys. Med. Biol.* **52** 4697-706

Love P A, Evans PM, Leach M O and Webb S 2003 Polymer gel measurement of dose homogeneity in the breast: comparing MLC intensity modulation with standard wedged delivery *Phys. Med. Biol.* **48** 1065-74

Low D A and Dempsey J F 2003 Evaluation of the gamma dose distribution comparison method *Med. Phys.* **30** 2455-64

Low D A, Dempsey J F, Venkatesan R, Mutic S, Markman J, Mark Haacke E and Purdy A 1999 Evaluation of polymer gels and MRI as a 3-D dosimeter for intensity-modulated radiation therapy *Med. Phys.* **26** 1542-51

Low D A, Harms W B, Mutic S and Purdy J A 1998 A technique for the quantitative evaluation of

dose distributions *Med. Phys.* **25** 656-61
Luci J J, Whitney H M and Gore J C 2007 Optimization of MAGIC gel formulation for three-dimensional radiation therapy dosimetry *Phys. Med. Biol.* **52** N241-8
MacDougall N D, Miquel M E and Keevil S F 2008 Effects of phantom volume and shape on the accuracy of MRI BANG gel dosimetry using BANG3 *Br. J. Radiol.* **81** 46-50
Maryanski M J, Schulz R J, Ibbott G S, Gatenby J C, Xie J, Horton D and Gore J C 1994 Magnetic resonance imaging of radiation dose distributions using a polymer-gel dosimeter *Phys. Med. Biol.* **39** 1437-55
Maryanski M J, Zastavker Y Z and Gore J C 1996 Radiation dose distributions in three dimensions from tomographic optical density scanning of polymer gels: II. Optical properties of the BANG polymer gel *Phys. Med. Biol.* **41** 2705-17
McJury M, Tapper P D, Cosgrove V P, Murphy P S, Griffin S, Leach M O, Webb S, and Oldham M 1999 Experimental 3D dosimetry around a high-dose-rate clinical 192Ir source using a polyacrylamide gel (PAG) dosimeter *Phys. Med. Biol.* **44** 2431-44
Oldham M, Baustert I B, Lord C, Smith T A R, McJury M, Leach M O, Warrington A P and Webb S 1998a An investigation into the dosimetry of a 9 field tomotherapy irradiation using BANG-gel dosimetry *Phys. Med. Biol.* **43** 1113-32
Oldham M, McJury M, Baustert I B, Webb S and Leach M O 1998b Improving calibration accuracy in gel dosimetry *Phys. Med. Biol.* **43** 2709-20
Olding T and Schreiner L J 2011 Cone-beam optical computed tomography for gel dosimetry II: imaging protocols *Phys. Med. Biol.* **56** 1256-79
Salomons G J, Park Y S, McAuley K B and Schreiner L J 2002 Temperature increases associated with polymerization of irradiated PAG dosimeters *Phys. Med. Biol.* **47** 1435-48
Sedaghat M, Bujold R and Lepage M 2010 Effect of the exothermal polymerization reaction on polymer gel dosimetric measurements *J. Phys.: Conf. Ser.* **250** 012018
Sedaghat M, Bujold R and Lepage M 2011a Severe dose inaccuracies caused by an oxygen-antioxidant imbalance in normoxic polymer gel dosimeters *Phys. Med. Biol.* **56** 601-25
Sedaghat M, Bujold R and Lepage M 2011b Investigating potential physicochemical errors in polymer gel dosimeters *Phys. Med. Biol.* **56** 6083-107
Senden R J, De Jean P, McAuley K B and Schreiner L J 2006 Polymer gel dosimeters with reduced toxicity: a preliminary investigation of the NMR and optical dose-response using different monomers *Phys. Med. Biol.* **51** 3301-15
Taylor M L, Franich R D, Johnston P N, Millar R M and Trapp J V 2007 Systematic variations in polymer gel dosimeter calibration due to container influence and deviations from water equivalence *Phys. Med. Biol.* **52** 3991-4005
Trapp J V, Kairn T, Crowe S and Fielding A 2009 Internal calibration of gel dosimeters: A feasibility study *J. Phys.: Conf. Ser.* **164** 012014
Tremblay N M, Hubert-Tremblay V, Bujold R, Beddar A S, Beaulieu L and Lepage M 2011 Accurate calibration of a polymer gel dosimeter with a plastic scintillation detector. *Med. Phys.* **38** 2754-61
Vandecasteele and De Deene 2013a On the validity of 3D polymer gel dosimetry: II. Physico-chemical effects *Phys. Med. Biol* **58** 43-61
Vandecasteele and De Deene 2013b On the validity of 3D polymer gel dosimetry: III. MRI related error sources *Phys. Med. Biol* **58** 63-85
Venning A J, Hill B, Brindha S, Healy B J, Baldock C 2005 Investigation of the PAGAT polymer gel dosimeter using magnetic resonance imaging. *Phys Med Biol.* **50** 3875-88
Vergote K, De Deene Y, Vanden Bussche E and De Wagter C, 2004 On the relation between the spatial dose integrity and the temporal instability of polymer gel dosimeters *Phys. Med. Biol.* **49** 4507-22
Watanabe Y, Akimitsu T, Hirokawa Y, Mooij R B and Perera G M 2005 Evaluation of dose delivery accuracy of Gamma Knife by polymer gel dosimetry *J. Appl. Clin. Med. Phys.* **6** 133-42
Watanabe Y, Gopishankar N, 2010 Three-dimensional dosimetry of TomoTherapy by MRI-based polymer gel technique *J. Appl. Clin. Med. Phys.* **12** 3273

Xu Y, Wuu C S and Maryanski M J 2010 Sensitivity calibration procedures in optical-CT scanning of BANG 3 polymer gel dosimeters *Med. Phys.* **37** 861-8

3

On the validity of 3D polymer gel dosimetry: II. Physico-chemical effects

---

Jan Vandecasteele and Yves De Deene
Both authors contributed equally to this study.

Manuscript on which this chapter is based:
Physics in Medicine and Biology **58** (2013) 43-61

On the validity of 3D polymer gel dosimetry: II. Physico-chemical effects*

Jan Vandecasteele[1] **and Yves De Deene**[1,2]

[1] Department for Radiation Oncology and Experimental Cancer Research, Ghent University, De Pintelaan 185, 9000 Gent, Belgium
[2] Institute of Medical Physics, School of Physics, University of Sydney, Sydney, NSW 2006, Australia

E-mail: Jan.Vandecasteele@UGent.be

Received 8 Februari 2012, in final form 28 Augustus 2012
Published 6 December 2012
Online at stacks.iop.org/PMB/58/43

Abstract. This study quantifies some major physico-chemical factors that influence the validity of MRI (PAGAT) polymer gel dosimetry: temperature history (pre-, during and post-irradiation), oxygen exposure (post-irradiation) and volumetric effects (experiment with phantom in which a small test tube is inserted).Present results confirm the effects of thermal history prior to irradiation. By exposing a polymer gel sample to a linear temperature gradient of ~2.8°C/cm and following the dose deviation as a function of post-irradiation time new insights into temporal variations were added. A clear influence of the temperature treatment on the measured dose distribution is seen the first hours post-irradiation (resulting in dose deviations up to 12%). This effect diminishes to 5% after 54 h post-irradiation. Imposing a temperature offset (maximum 6°C for 3 h) during and following irradiation on a series of calibration phantoms results in only a small dose deviation of maximum 4%. Surprisingly, oxygen diffusing in a gel dosimeter up to 48 h post-irradiation was shown to have no effect. Volumetric effects were studied by comparing the dose distribution in a homogeneous phantom compared to the dose distribution in a phantom in which a small test tube was inserted. This study showed that the dose measured inside the test tube was closer to the ion chamber measurement in comparison to the reference phantom without test tube by almost 7%. It is demonstrated that physico-chemical effects are not the major causes for the dose discrepancies encountered in the reproducibility study discussed in the concurrent paper (Vandecasteele and De Deene 2013a *Phys. Med. Biol.* **58** 19-42). However, it is concluded that these physico-chemical effects are important factors that should be addressed to further improve the dosimetric accuracy of 3D MRI polymer gel dosimetry.

*Both authors contributed equally to this study

1. Introduction

Previously, mean dose deviations up to 13.7% were found when small calibration phantoms were used to calibrate larger volumetric phantoms (Vandecasteele and De Deene 2013a). In the aforementioned study, it was also shown that calibrating large volumetric phantoms with similar-sized calibration phantoms would result in a significant lower dose uncertainty in comparison to using small calibration phantoms. To elucidate the origins of these dose discrepancies caused by the calibration using small calibration phantoms, several experiments were set up to investigate possible physico-chemical effects that may influence the accuracy of polymer gel dosimetry. Several hypotheses were already proposed in the scientific literature for these differences (MacDougall *et al* 2008, Dumas *et al* 2006, Xu *et al* 2010, De Deene *et al* 2007, Salomons *et al* 2002, Sedaghat *et al* 2010, Hepworth *et al* 1999, Sedaghat *et al* 2011a, 2011b). These hypotheses included the effect of inhomogeneous distribution of oxygen before irradiation (Sedaghat *et al* 2011a, 2011b) and temperature effects before and during irradiation (Cosgrove *et al* 2000, Salomons *et al* 2002, De Deene *et al* 2006, De Deene *et al* 2007, Sedaghat *et al* 2010). In this part of the study, following effects on the accuracy and precision are investigated: temperature history (pre-, during and post-irradiation), oxygen exposure (post-irradiation) and volumetric effects (phantom in which a small test tube is inserted). A polyacrylamide gelatin gel with the anti-oxidant tetrakis-hydroxyphosphonium chloride (PAGAT) gel dosimeter was selected on the basis of its optimal performance in terms of reported radiation properties: chemical stability, temperature insensitivity, dose rate independence, energy independence and tissue equivalence (De Deene *et al* 2006).

2. Materials and Methods

2.1. Gel fabrication and storage

The normoxic acrylamide polymer gel dosimeters (PAGAT) were composed of gelatin (6% w/w), acrylamide (2.5% w/w), N,N'-methylene-bis-acrylamide (2.5% w/w) and 5 mM Bis[tetrakis(hydroxymethyl)phosphonium]sulphate (THPS) as antioxidant.

The polymer gels were fabricated according to a procedure as described elsewhere (De Deene *et al* 2006). The gel was approximately at 32 °C when it was poured in the recipients.

2.2. Effects of temperature history

2.2.1. Effect of a pre-irradiation temperature gradient Large phantoms are expected to cool down non-uniformly. De Deene *et al* (2007) found a dose deviation of 7% caused by significant pre-irradiation temperature differences of approximately 20°C for approximately 7 h in PAGAT-type dosimeters. It can therefore be speculated that spatial temperature differences during cooling may obscure the measured dose

distributions.

To investigate the influence of an inhomogeneous temperature distribution within a gel dosimeter during storage, a temperature gradient was artificially induced in a box-shaped phantom. This is achieved by positioning the phantom between two water perfused plates. The top plate was perfused with hot water while the bottom plate was perfused with cold water creating a temperature gradient of ~2.8°C/cm resulting in a maximum temperature difference of 16.8°C. The four other surfaces of the box-shaped phantom were thermally isolated with styrofoam.

In a first experiment, the evolution of the temperature distribution in the box-shaped gel phantom (8% gelatin gel with 0.5% NaN_3 added as fungicide) was assessed by use of a fiber optic temperature measurement system (Reflex 4, Neoptix, Québec, Canada, nominal accuracy: 0.3°C) equipped with four fibre optic temperature probes. Three of those probes were inserted in the gel along the central longitudinal axis of the phantom (see figure 1f). The box-shaped Barex phantom measured 6.0 cm × 6.0 cm × 6.8 cm with a Barex wall thickness of 4 mm.

In a second experiment, the effect of a pre-irradiation temperature gradient on an unirradiated box-shaped phantom filled with PAGAT gel was experimentally investigated. This phantom was exposed to the temperature gradient for 14 h. Afterwards, the unirradiated phantom was scanned in a clinical NMR scanner (Siemens Avanto 1.5 Tesla) 24 h after fabrication (and 10 h after exposure to the temperature gradient). During scanning, the phantoms were positioned in a cylindrical recipient that was filled with a GdDTPA-doped solution to avoid imaging artefacts caused by B_0 magnetic field distortions. Following imaging parameters were used: pixel size 1 × 1 × 5 mm^3, repetition time (TR) = 4000 ms, number of equidistant echoes = 32, echo time range (TE) = 40 ms - 1280 ms, NEX = 4 and total scan time = 1 h 3 m 7 s.

In a third experiment, the effect of a pre-irradiation temperature gradient was investigated on two box-shaped Barex phantoms filled with PAGAT gel. One phantom was exposed to the temperature gradient for 14 h while the other phantom was allowed to cool down at 20°C-22°C for approximately 22 h in a large water reservoir (60 l). A set of fourteen test tubes were filled from the same batch of gel and allowed to cool down in the large water reservoir. These test tubes are made out of borosilicate glass (Pyrex®) and have a length of 10.0 cm, inner diameter of 12.4 mm, outer diameter of 15.0 mm and a wall thickness of 1.3 mm.

Afterwards, both box-shaped phantoms were irradiated from the side (*i.e.* perpendicular to the axis of the temperature gradient) with a square 4 cm × 4 cm photon beam (6 MV; SSD = 100 cm; Output = 900 MU) with a clinical linear accelerator (linac) Elekta Synergy (Elekta Oncology Systems, Crawley, UK) equipped with an Elekta Beam Modulator^{TM}. The calibration phantoms were irradiated with known doses between 0 and 15 Gy (detailed irradiation protocol is described in Vandecasteele and De Deene (2013a)).

An MR scan was acquired along the direction of the temperature gradient for both irradiated phantoms 6h post-irradiation. During this scan session six measurements

Table 1. Thermal properties of the different materials that occur in the box-shaped Barex gel phantom.

Material	mass density (ρ)	specific heat capacity (c)	thermal conductivity (k)	Reference
Gel (PAGAT)	1050 kg m^{-3}	3780 J kg^{-1} K^{-1}	0.56 W K^{-1} m^{-1}	Chen and Vyazovkin 2009, Sakiyama *et al* 1991
Barex wall	1110 kg m^{-3}	410 J kg^{-1} K^{-1}	0.25 W K^{-1} m^{-1}	Ineos Barex USA 2006
Styrofoam	200 kg m^{-3}	1130 J kg^{-1} K^{-1}	0.033 W K^{-1} m^{-1}	

were performed using the same imaging parameters and positioning protocol as describe above for the unirradiated box-shaped phantom. Other scan sessions were performed at 30 h and 54 h post-irradiation with the same imaging parameters.

From the set of base images excluding the first echo, R_2 maps were calculated. An R_2-dose calibration plot was derived by extracting the mean R_2 values from the calibration phantoms as function of dose. These points were fitted against a mono-exponential function (equation 1). This procedure is described in more detail elsewhere (De Deene *et al* 1998, Vandecasteele and De Deene 2013a).

$$R_2 = R_{2,sat} - \Delta R_2 \cdot e^{-\alpha \cdot D} \tag{1}$$

with $R_{2,sat}$, ΔR_2 and α the fit coefficients.

In a fourth experiment, a reference dose measurement was performed in a similar box-shaped Barex phantom (filled with 8% gelatin gel doped with 0.5% NaN_3) in which a cavity was made for placement of a small volume ionisation chamber (PTW pinpoint 31006). The dose in the centre of the phantom amounted to 10.29 Gy.

In addition, the evolution of the temperature distribution was also calculated by solving the heat equation numerically using a finite difference time domain scheme (FDTD). A Douglas-Gunn alternating direction implicit (ADI) method was implemented in three spatial dimensions and time (Douglas and Gunn 1964). The computer program is developed in house and is written in ansi C. The calculated temperature distribution is displayed using Matlab routines. The box-shaped Barex gel phantom was thermally modelled using literature values of thermal conductivity and specific heat capacity (see table 1) that were allocated to each voxel.

The calculation took approximately 8 h on a laptop equipped with an Intel Core (i7) processor (1.6 GHz) and 4 GB memory for a spatial voxel size of 0.8 mm $\times$ 0.8 mm $\times$ 0.8 mm resulting in 480000 voxels. Although the ADI method is unconditionally stable, it was found that a time increment of 0.1 s was required to give reliable results because the time increment is proportional to the mesh size.

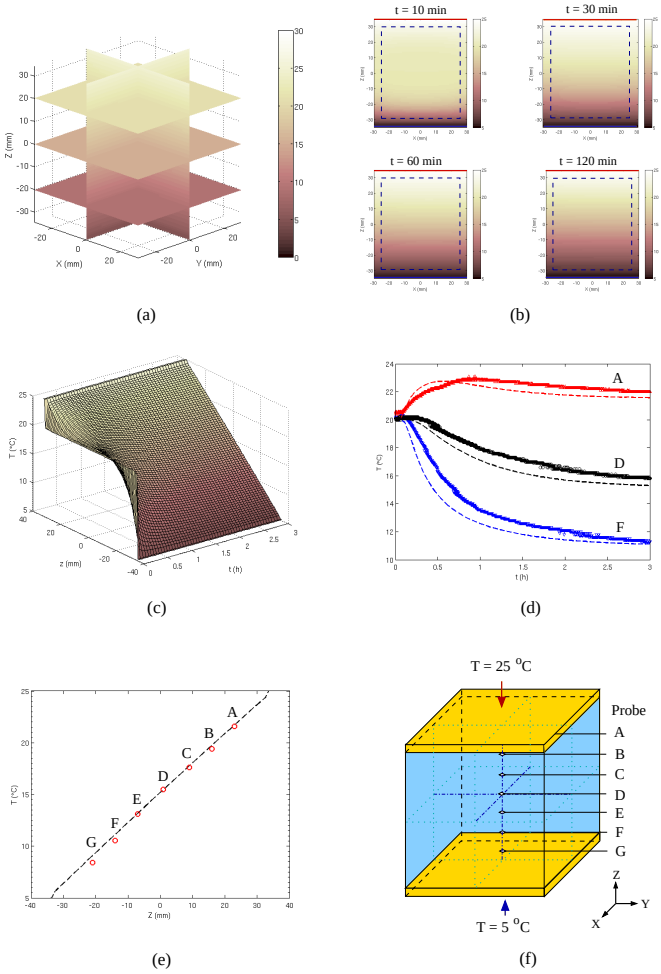

Figure 1. Temperature distribution in a cubic Barex gel phantom of which the upper and lower surface are exposed to a hot (25°C) surface and cold surface (5°C). Orthogonal cross-sections through the simulated temperature distribution in the steady state (a) and longitudinal cross-sections at various time points during the build-up of the gradient (b). The change in temperature gradient along the longitudinal axes of the phantom over time is shown in (c). Temperature recordings at three locations (symbols) over time show a fair correspondence with the simulated temperature course (dashed line) in the transient regime (d) and in the steady state regime (after 10 h) (e). The temperature recordings in (d) and (e) correspond with the probe positions indicated in (f).

2.2.2. Effect of temperature differences during and following irradiation Following the studies of Cosgrove *et al* (2000), Salomons *et al* (2002) and Sedaghat *et al* (2010) where they show that an exothermal polymerisation reaction causes a temperature increase during irradiation, it was hypothesized that this temperature increase remains present for a longer time in large phantoms in comparison to small phantoms because of thermal inertia. This temperature increase in larger phantoms may affect the polymerisation reaction dynamics or polymer morphology which results in a higher R_2 value for the same dose. The calibration method using calibration phantoms of a small volume would therefore be inaccurate since the small volume would not experience the same temperature changes as the larger volume of interest.

An initial experiment was set-up to determine the increase in temperature and the duration of this increase upon irradiation of a spherical gel phantom and a standard calibration phantom due to polymerisation induced heat with optical temperature sensors. Two sensors were placed in the spherical phantom. One sensor was located at the centre of the phantom while the other sensor was located near the outer glass wall of the phantom. The recorded temperature increase and the difference in duration at which the temperature in the spherical phantom was higher compared to the small calibration phantom served as a guideline for the artificially imposed temperature history in the following experiment.

Next, an experiment was set-up in which standard calibration phantoms were irradiated at three different temperatures and afterwards stored at these elevated temperatures during different amounts of time. This experiment simulates an irradiation of a larger gel phantom in which the temperature history during and immediately after irradiation is imposed artificially causing a *temporal* temperature difference.

Six sets of nine test tubes were filled with the same batch of PAGAT gel (dimensions of test tubes are given in section 2.2.1). The first set was irradiated at $22°C$ and was stored at $22°C$ during 4h. This set served as a reference. Two sets were irradiated at $25°C$ ($\Delta T = +3°C$) and stored at that temperature for 1h and 3h respectively. Another two sets were irradiated at $28°C$ ($\Delta T = +6°C$) and stored at that temperature for 1h and 3h respectively. The last set of calibration phantoms was irradiated at $28°C$ and stored at $22°C$ and served as a control set to investigate the effect of a higher temperature during irradiation on the reaction dynamics. The temperature history imposed on different phantom sets is shown schematically in figure 2.

All phantoms were scanned in three scan sessions: 4h after induced temperature offset (7h post-irradiation), 16 h post-irradiation and 40 h post-irradiation with the body coil using the following imaging parameters: pixel size $1 \times 1 \times 10$ mm^3, TR = 3000 ms, echoes = 32, TE = 40 ms - 1280 ms, NEX = 2 and total scan time = 25 m 39 s. The slice location was perpendicular to the axis of the test tube phantoms approximately 2-3 cm from the bottom of the test tubes.

R_2 maps of all measured base images, excluding the first echo, were calculated and the dose-R_2 relation was determined for all sets of small calibration phantoms. All dose-R_2 calibration plots were fitted by a mono-exponential function. For each scan session,

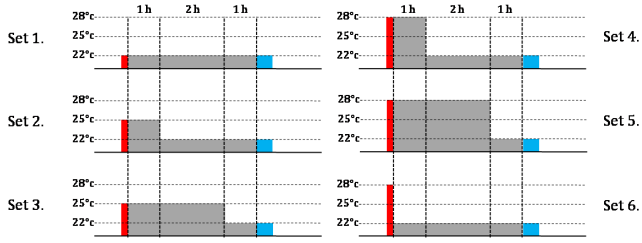

Figure 2. Schematical representation of the temperature protocol used for the different sets of calibration phantoms. Set n°1 was irradiated (red bar) and stored (gray bar) at 22°C and served as a reference. The MRI read-out was performed at 22°C for all calibration sets (blue bar). Sets n°2 and n°3 were irradiated at 25°C and stored at that temperature for 1h and 3h respectively. Sets n°4 and n°5 were irradiated at 28°C and stored at that temperature for 1h and 3h respectively. The last set n°6 was irradiated at 28°C and stored at 22°C.

all calibration curves were compared to the reference calibration function (irradiated at 22°C and stored at 22°C during 4 h). The maximum dose difference was calculated that would result from calibrating the same measured R_2 value with the reference set versus the experimental sets. This resulted in a 'worst-case' dose difference. Furthermore, slope and intercept were derived from the fit parameters (equations 2 and 3).

$$slope = \Delta R_2 \cdot \alpha \tag{2}$$

$$R_{2,0} = R_{2,sat} - \Delta R_2 \tag{3}$$

The slope was defined as the derivative at 0 Gy and $R_{2,0}$ was defined as the intersection with the y-axis.

2.3. Oxygen effects

In the intra-batch reproducibility study discussed in Vandecasteele and De Deene (2013a) the dose difference between gel and ion chamber measurements tends to increase as function of time when the gel phantoms are calibrated to dose using calibration phantoms. The time scale on which the increase took place suggested that it would be caused by a slow physico-chemical process. A reasonable hypothesis was that 3 to 4 days post irradiation slowly diffusing oxygen molecules could affect the smaller calibration phantoms. This is reflected by a change in R_2 values, caused by post-irradiation oxygen influx that reacts with long-lived polymer radicals in the gel after irradiation. The oxygen diffuses through the seal of the calibration phantoms or comes from residual air above the gel. The diffusion coefficient of oxygen in gel amounts to $8 \pm 2 \cdot 10^{-6} cm^2 s^{-1}$ (Hepworth *et al* 1999) which could explain the chances in R_2 occurring over a time period of 92 h. Using equation 4 the mean oxygen displacement can be calculated:

$$x = \sqrt{6Dt}, \tag{4}$$

with x the mean displacement from the starting point in 3D after time interval t (in seconds) and diffusion coefficient D (in $cm^2\ s^{-1}$). The mean oxygen displacement after 92 h amounts to $\sim$ 4 cm. Long-lived macroradicals are known to be present in polymer gel dosimeters and are held responsible for dose overshoots and dose overestimation in irradiated PAG gels at sufficiently high doses (De Deene *et al* 2002a, Vergote *et al* 2004). Furthermore, Hepworth *et al* (1999), De Deene *et al* (2006) and Sedaghat *et al* (2011a) have already shown that oxygen contamination in PAGAT gel dosimeters *before* irradiation affects the amount of polymerisation upon irradiation due to chemical reactions of the oxygen with radiation induced radicals. The following experiment was set-up to investigate potential oxygen effects occurring after irradiation of the gel dosimeters.

Three sets of 5 small glass test tubes (inner diameter: 9 mm, outer diameter: 13 mm, length: 45 mm) were filled with PAGAT gel. After filling of the test tubes, the air above the gel was carefully removed by conical shaped glass stoppers. Each set of phantoms was irradiated with their longitudinal axis perpendicular to the axis of the radiation beam at reference conditions where 1 monitor unit corresponds with 1 cGy to doses of 0 Gy, 1 Gy, 5 Gy, 10 Gy and 15 Gy. Of the three sets of test tubes, set n° 1 served as a reference in which no oxygen diffusion was allowed. In set n° 2 and set n° 3 the glass stopper was intentionally replaced by Parafilm (Novolab, Geraardsbergen, Belgium) 24 h and 48 h prior to the MRI scan, respectively, to allow oxygen infiltration while minimising drying of the gel (Bemis company, Inc 2010). Fresh oxygen penetrated the gel and could interact with long-lived radicals. An MRI scan was performed 48 h post-irradiation in which the R_2 value was determined on a plane along the length of the phantoms. A dedicated phantom holder was constructed in polystyrene to position the small phantoms parallel to each other in a reproducible read-out position.

Scan parameters were as follows: pixel size 0.6 $\times$ 0.6 $\times$ 5 mm^3, TR = 4650 ms, echoes = 32, TE = 20-640 ms, NEX = 1 and total scan time = 11 m 44 s.

2.4. Volumetric effects: test tube inside spherical phantom

The measured R_2 difference of up to 14% reported in Vandecasteele and De Deene (2013a) between small calibration phantoms and large volumetric phantoms was further investigated with following experiment. Two spherical glass flasks (250 ml) were filled with PAGAT gel. The first phantom was completely filled with gel and served as a reference. In the second phantom, a test tube similar to the calibration phantoms was inserted in the centre of the volumetric phantom (figure 3). Both the spherical container and the inserted test tube were filled with the same gel. In addition, fourteen standard sized test tubes (for dimensions see section 2.2.1) were filled with gel and served as calibration phantoms.

The spherical phantoms were irradiated 24h after fabrication. The irradiation set-up is identical to the set-up used in Vandecasteele and De Deene (2013a), where it is discussed in more detail. This resulted in a total dose of 11.24 Gy at the centre of

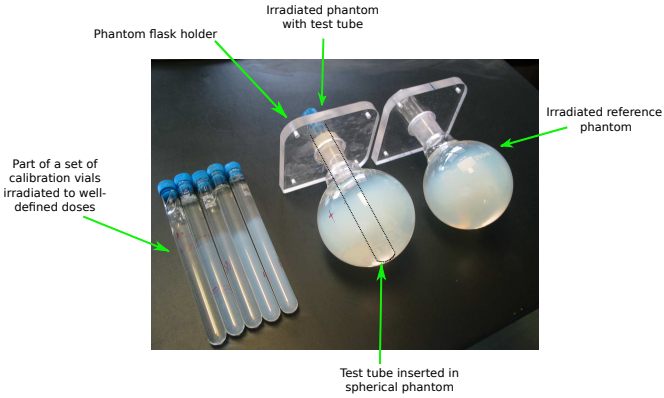

Figure 3. A photographic representation of the spherical phantoms along with a part of the set of calibration phantoms. The calibration phantoms are shown on the left irradiated to well-defined radiation doses. The top parts of the calibration phantoms are not polymerised due to the irradiation set-up. In the middle the irradiated spherical phantom is show which has a test tube inserted through the isocentre. The position of the test tube is highlighted by the dashed line. On the right hand side the irradiated reference phantom is shown which has no test tube inserted. The phantom flask holder limits the movement of the spherical flask which makes this set-up very reproducible for irradiation and read-out.

both spherical phantoms (with and without test tube) as verified with pinpoint ion chamber measurements. The calibration phantoms were positioned in a large cubic water phantom ($32 \times 32 \times 20$ cm^3) with their longitudinal axis perpendicular to the beam axis at 10 cm depth corresponding to the reference depth for a 6 MV photon beam using a polystyrene holder. This irradiation set-up was experimentally validated (Vandecasteele and De Deene 2013a). The samples were irradiated with photon beams (10×10 cm^2) delivered by the linac.

The two irradiated spherical phantoms and corresponding calibration phantoms were scanned subsequently 24 h and 48 h after irradiation in a clinical NMR scanner (Siemens Avanto 1.5 Tesla) using the same dedicated phantom holder as was used for irradiation. Imaging parameters were identical to the ones reported in Vandecasteele and De Deene (2013a).

The R_2 maps were calibrated to dose maps using the dose-R_2 relationship extracted from the calibration phantoms. The 2D dose distribution in a transverse plane through the isocentre of the two spherical phantoms was compared with the TPS calculated dose distribution. Anterior-posterior R_2 profiles and dose profiles were acquired in both phantoms.

The temperature history in the spherical phantom with test tube was also recorded to investigate the influence of the test tube on the temperature distribution. The

temperature was measured inside the test tube and immediately outside the test tube close to the centre of the phantom. This continuous measurement was performed immediately after fabrication and also during and following irradiation.

3. Results

3.1. Effect of a pre-irradiation temperature gradient

Numerical simulations of the thermal distribution within the Barex phantom are in good agreement with point measurements performed with a Fabry-Perot optical thermometry system (figure 1). The temperature gradient induced by the hot (25°C) and cold (5°C) plate element reached a steady state regime after approximately 1.5 h (figures 1(c) and 1(d)) and a uniform temperature distribution was obtained at approximately 0.5 h after removal of the hot and cold plate elements (figure 4). The time difference can be attributed to the fact that more sides of the phantom are exposed to the intended temperature while equilibrating to the surrounding temperature as compared to the situation in which a temperature gradient in the phantom was induced from only two sides by the cooling/heating elements placed on top of and below the phantom. The temperature distribution in the gel phantom remains uniform (within 0.2°C) in sections perpendicular to the temperature gradient during the complete experiment (figures 1(b) and 4(a)-(c)).

The effect of a temperature gradient on the R_2 distribution in an unirradiated box-shaped phantom filled with PAGAT gel can be observed in figure 5 (measured 10 h after exposure and 24 h after fabrication). The R_2 map shows a maximum R_2 variation of 0.07 s^{-1} (6.3% relative to the mean R_2 value of 1.12 s^{-1}). This is illustrated by figure 5b in which a lateral profile through the R_2-map is shown (left y-axis in red). The data of the profile was calculated by averaging 20 pixels along the y-axis. To correlate the R_2 profile to the temperatures that were induced during storage, the right black y-axis was added which marks the position of the temperature points along the temperature gradient during steady state.

A comparison of the effect of a pre-irradiation temperature gradient was made over time (post-irradiation stability) between an irradiated box-shaped phantom, exposed to a temperature gradient and a box-shaped phantom that was stored under normal atmospheric conditions (20-22°C) prior to irradiation (figure 6). The corresponding calibration curves shown in figure 6(a) (measured at 6, 7, 8, 9, 10, 11, 3h and 54 h post-irradiation) were used to calibrate the R_2 maps (of which lateral profiles can be observed in figure 6(b)) to dose maps (of which lateral profiles can be observed in figure 6(c)). Note that the gel measured dose values in the reference phantom (*not* exposed to the temperature gradient) where maximum 3.7% higher compared to the ion chamber dose recording (10.29 Gy).

The dose and R_2 uncertainty (expressed in percent relative to the R_2 range (0.65 s^{-1})) are plotted for the region exposed to the heating element (figure 7(a)) (located

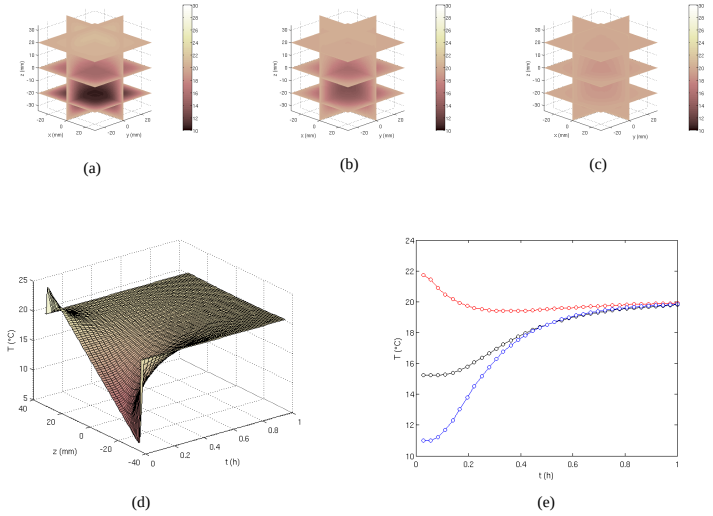

Figure 4. Simulated temperature distribution in a cubic Barex gel phantom after the induction of a temperature gradient (i.e. when the hot and cold element are removed). Temperature distribution at 10 minutes (a), 20 minutes (b) and 30 minutes (c) after removing the hot and cold element. Change in the temperature gradient along the central longitudinal axis of the Barex gel phantom (d) and at the same three probe locations (A, D and F) as in figure 3(e).

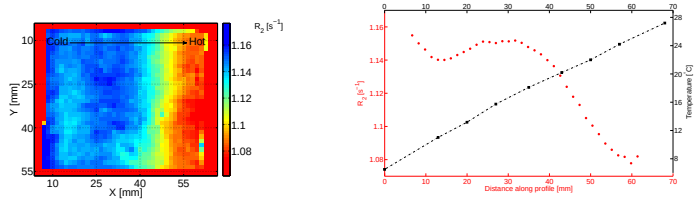

Figure 5. An R_2 map acquired along the direction of the temperature gradient of an unirradiated box-shaped PAGAT gel dosimeter (a). The cooling element was placed at the left side of the phantom, the heating element was placed at the right side. In b a lateral profile through the R_2 map is shown in red corresponding to the red left y-axis. To correlate the measured R_2 values to the induced temperature gradient, the right (black) y-axis was added which marks the position of the temperature points measured along the temperature gradient.

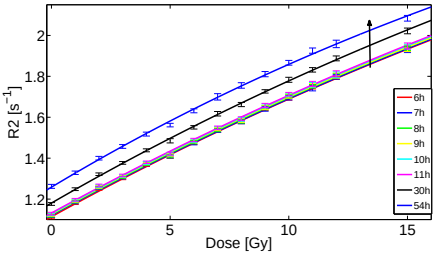

(a)

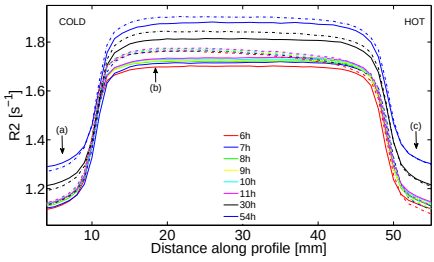

(b)

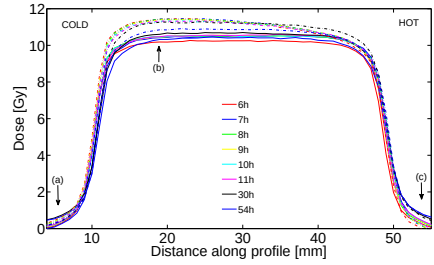

(c)

Figure 6. Dose-R_2 plots of the 'temperature-during-storage'-study recorded at 6h, 7h, 8h 9h, 10h, 11h, 30h and 54h post-irradiation (a). All dose-R_2 plots were fitted against a mono-exponential function. The arrow indicates the direction of the effect of increasing post-irradiation time. Graph b shows lateral profiles through R_2 maps of the phantom exposed to a temperature gradient (dashed line) and the reference phantom (full line). The orientation of the heating and cooling elements are shown in the graph. The arrows (a), (b) and (c) indicate the position of the calculated dose deviation relative to the ion chamber recorder dose plotted in figure 7. Graph c shows lateral profiles through the gel measured dose maps of the phantom exposed to the temperature gradient (dashed line) and the reference phantom (full line).

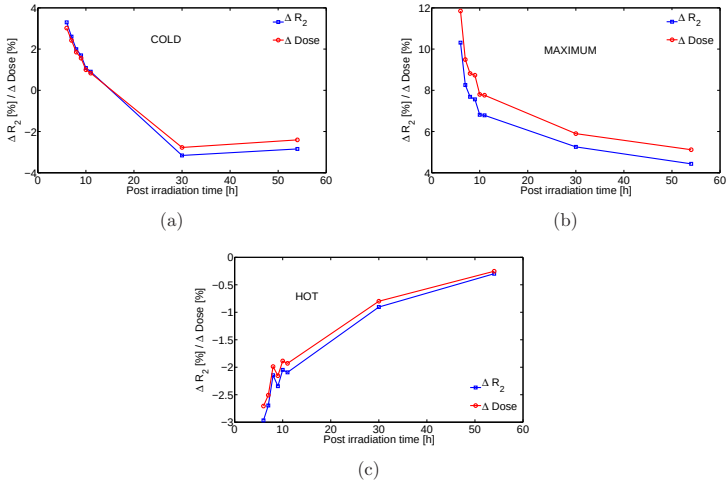

Figure 7. The dose deviation expressed in percentage relative to the ion chamber recorded dose (10.27 Gy) in the isocentre and R_2 deviation expressed in percent relative to the R_2 range (0.65 s^{-1}) are plotted for the region exposed to the cooling element (located in figure 6 at 3 mm along the profile) (a), the region of maximum dose and R_2 deviation (located in figure 6 at 18 mm along the profile) (b) and the region exposed to the heating element (located in figure 6 at 56 mm along the profile) (c).

in figure 6 at 56 mm along the profiles), for the region exposed to the cooling element (figure 7(c)) (located in figure 6 at 3 mm along the profiles) and the region of the maximum dose and R_2 deviation (figure 7(b)) (located in figure 6 at 18 mm along the profiles). The graphs (a) and (c) in figure 7 are determined in the low dose regions, while graph (b) is acquired in the high dose region.

3.2. Effect of temperature differences during and following irradiation

The increase in temperature and the duration of the increase in a spherical phantom filled with PAGAT gel upon irradiation were quantified. The temperatures at the centre and the inner wall of a spherical phantom were compared to the temperature in a small volume calibration phantom (figure 8). The maximum temperature difference between wall and centre amounts to approximately 2°C. This temperature difference decreased over time to a value of 0.2°C after 5 h (nominal accuracy = 0.3°C). The maximum temperature difference between the centre of a large spherical phantom and a small volume calibration phantom amounts to approximately 1°C. The temperature in the calibration phantom reaches equilibrium approximately 2 h faster than the temperature in the spherical phantom. This recorded temperature increase and the difference in

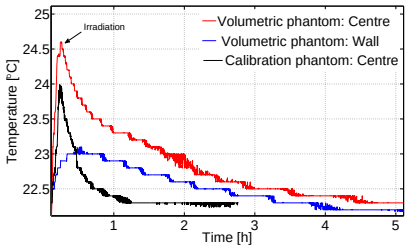

Figure 8. The temperature increase upon irradiation was quantified in a PAGAT gel. 'Wall' stands for the temperature probe located near the inner wall of the spherical volumetric phantom. 'Centre' stands for the temperature measurement performed at the centre of the spherical phantom. A third measurement was performed at the centre of a small volume calibration phantom.

duration at which the temperature in the spherical phantom was higher compared to the small calibration phantom served as a guideline for the artificially imposed temperature history in the following experiment.

Six sets of nine small calibration phantoms were exposed to different temperatures during and following irradiation for different amounts of times. The dose-R_2 response curves were fitted against a mono-exponential function (figure 9).

A comparison was made between the different calibration curves relative to the reference set (irradiated at 22 °C). The maximum dose deviation resulting from the different calibration curves amounted to 3.8% relative to the reference set. No trend could be established.

3.3. Oxygen effects

The effect of post-irradiation oxygen diffusion in a gel dosimeter was examined. R_2 profiles were acquired along the length of the small phantoms to measure a possible change in R_2 because of post-irradiation oxygen infiltration. The gel was exposed to oxygen at different time points after irradiation so that the oxygen diffusion front was located at different depths in the phantoms at the moment of scanning. The vertical lines in figures 10a and 10b indicate the mean displacement of the oxygen front inside the phantom after 24 h and 48 h. Large fluctuations in R_2 values were measured, originating from oxygen contamination occurring prior to irradiation at the top of the phantoms (between 0 and 10 mm along the x-axis in figure 10a and 10b). Upon irradiation, this infiltrated oxygen results in an inhibition region within the first centimeter from the top of the phantom. Furthermore, in the first 1 mm to 2 mm from the top, a sharp increase in R_2 values is seen originating from dehydration of the gel. No differences in R_2 are found between the different sets of phantoms resulting from post-irradiation oxygen diffusion within the uncertainty of the measurement at larger distances.

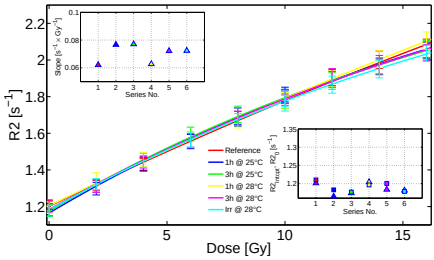

(a)

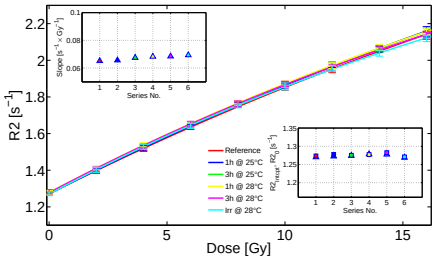

(b)

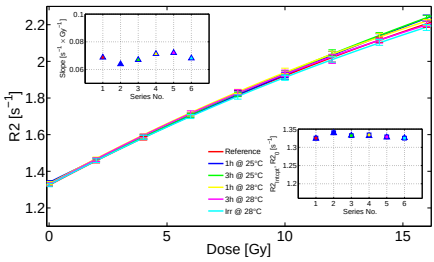

(c)

Figure 9. Dose-R_2 plots with mono-exponential fits of the 'temperature-post-irradiation'-study recorded at 7h (a), 16h (b) and 40h (c) post-irradiation. During each scan session six consecutive scans were acquired. The inset figures in the top left and bottom right show the variation in slope and the variations in $R_{2,intcpt}$ and $R_{2,0}$ respectively.

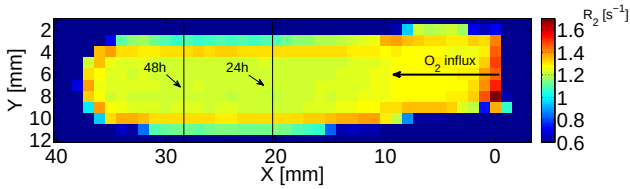

(a)

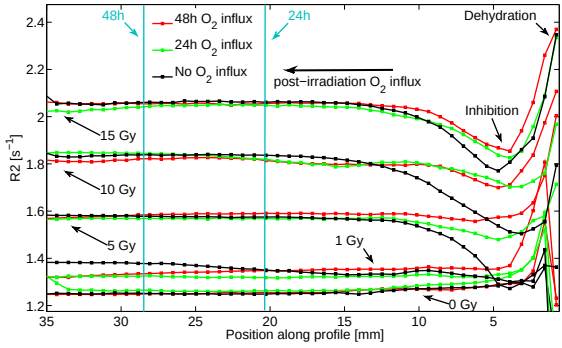

(b)

Figure 10. An R_2 map of a small unirradiated phantom. The position of the expected oxygen diffusion fronts after 24 h (2.04 cm) and 48 h (2.88 cm) are indicated. The oxygen diffused into the irradiated gel from the opened top as indicated by the direction of the arrow. R_2 profiles were acquired 48 h post-irradiation along the axis of the small phantoms.

3.4. Volumetric effects: test tube inside spherical phantom.

The dose distributions in two spherical phantoms with and without test tube were compared.

The temperature difference between the gel inside the test tube and the gel located outside the test tube in the spherical gel phantom after fabrication and also during and following irradiation was found to be negligible (data not shown). This was investigated

Table 2. R_2 and dose values acquired at the isocentre of the two spherical phantoms. The percentage values between brackets next to the dose value indicate the dose difference relative to the ion chamber measurement. $Phantom_{ref}$ stands for the reference phantom (without test tube inserted). $Phantom_{tt}$ stands for the phantom with the test tube inserted through the isocentre. The absolute and relative dose difference ΔD between both phantoms at the isocentre is listed.

	24h	48h
$R_2(Phantom_{ref})$ [s^{-1}]	1.866	1.991
$R_2(Phantom_{tt})$ [s^{-1}]	1.842	1.954
$D(Phantom_{ref})$ [Gy]	12.45 (+10.8%)	12.49 (+11.1%)
$D(Phantom_{tt})$ [Gy]	11.97 (+6.5%)	11.73 (+4.4%)
ΔD [Gy]	0.48 (4.3%)	0.76 (6.7%)

to exclude temperature differences during and following irradiation originating from the glass test tube inserted in the larger volumetric phantom as origin for any discrepancies. In addition, the effect of a test tube inside a volumetric phantom on the dose distribution was verified via a pinpoint ion chamber measurement. The dose with or without test tube was found to be identical within the uncertainties of the measurement (0.2%) assuring the validity of the irradiation set-up.

The dose-R_2 relationships from the calibration phantoms were fitted by a mono-exponential curve and displayed in figure 11d. A 2D transverse R_2 map of a homogeneous spherical phantom with an inserted test tube both filled with GdDTPA-doped gelatin gel is shown in figure 11a. The R_2 maps acquired 48h post-irradiation are shown in figure 11b and 11c. The position of the test tube can be clearly seen in 11a and 11c.

In figure 11e dose profiles are shown comparing all measurements. The significant dose overestimation between all phantoms and the TPS calculated dose profile (blue dashed line) can be clearly seen. The R_2 values and dose values were determined at the isocentre and are listed in table 2.

4. Discussion

4.1. Effect of a pre-irradiation temperature gradient

The effect of a temperature gradient on the R_2 distribution in an unirradiated box-shaped phantom filled with a PAGAT gel can be observed in figure 5. It should be noted that the box-shaped phantom was fully acclimatised to normal room temperature prior to MR image acquisition. The R_2 map shows an R_2 variation of 10.9% (relative to an R_2 range of 0.65 s^{-1}) originating from a temperature difference of 16.8°C. Higher measured R_2 values are correlated to an exposure to colder temperature. A relative homogeneous region in R_2 values (maximum variation is 2.3%) is observed in the region exposed between 8°C and 20°C. Towards the higher temperatures (between 20°C and 25°C) an inverse linear relation between R_2 and temperature is observed, with a slope of approximately -0.01 s^{-1}/°C (= -1.5%/°C). To investigate whether the gelation process

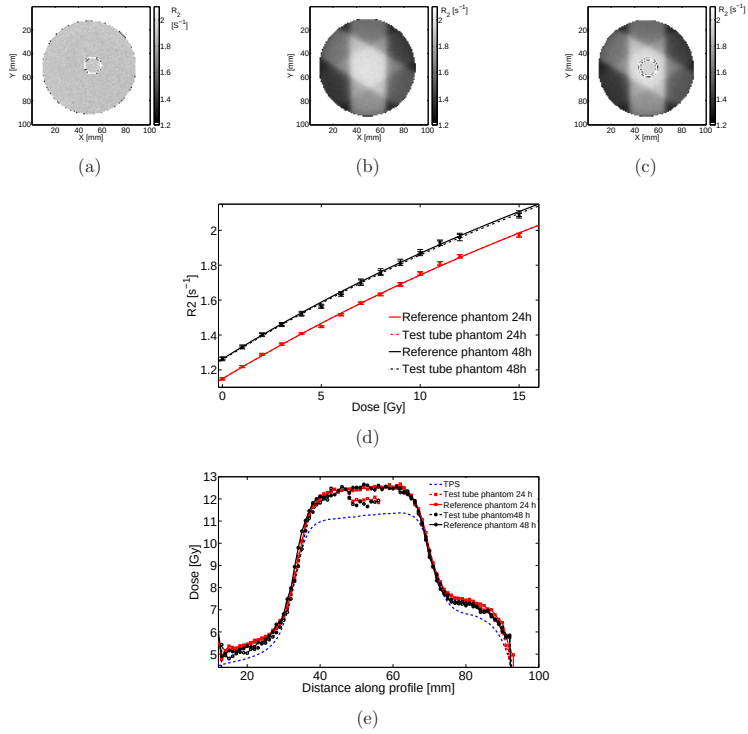

Figure 11. Dose-R_2 plots of the 'volumetric effect'-study recorded at 24 h and 48 h post-irradiation (d). During each scan session two consecutive scans were acquired which were fitted against a mono-exponential function. R_2 map of a spherical phantom filled with gelatin gel is shown in (a) to rule out potential susceptibility artefacts. R_2 maps acquired 48h post-irradiation of the irradiated reference spherical phantom (b) and the spherical phantom in which a test tube was inserted (c). The position of the test tube can be easily seen in figures (a) and (c) by the ring shaped signal void corresponding with the test tube's glass wall. Graph (e) shows lateral profiles through the gel measured dose maps of the reference phantom (full line) and the phantom in which a test tube was inserted (dashed line) at 24 h (red) and 48 h (black) post-irradiation. The dose profiles are compared to the TPS calculated dose profile shown in blue (dashed line). The large dose deviation from the TPS can be clearly seen.

is responsible for this increase in R_2, a homogeneous gelatine phantom was also exposed to the same temperature gradient (data not shown). No significant change in R_2 was measured in contrast to an unirradiated PAGAT phantom. An interaction between the antioxidant THPS and gelatin is presumed to be responsible for the measured effect in an unirradiated PAGAT gel dosimeter.
Under normal circumstances, temperature differences in the order of 16.8°C will never be encountered inside a gel dosimeter when a dedicated cooling protocol is used as suggested by De Deene *et al* (2007). However it should be noted that these temperature differences may occur between large phantoms and small phantoms or even within large phantoms when a refrigerator is used to cool down the gel phantoms after fabrication. In addition this experiment was performed to maximise possible discrepancies.

After irradiation of the box-shaped phantom with a square radiation field perpendicular to the temperature gradient, the plateau of the dose profile of the box-shaped phantom exposed to a temperature gradient is tilted during the first 11 h compared to the reference phantom (figure 6b and 6c). It was determined by independent temperature measurements that the box-shaped phantom was at thermal equilibrium during irradiation and scanning. During scan sessions acquired 30 h and 54 h post-irradiation, this tilt diminishes. However, a dose offset of 0.52 Gy remains. The maximum dose deviation of 12% is located at the side of the box-shaped phantom that was exposed to the cooling element. The temperature history prior to irradiation is known to affect the polymerisation dynamics or the polymer morphology as shown by De Deene *et al* (2007). In that study it was shown that for a temperature offset of 18°C for approximately 7 h, the maximum dose deviation for a PAGAT gel dosimeter amounted to 7%. In our recent measurement performed 30 h post-irradiation, a comparable dose deviation of 6% was found for an induced temperature difference of 8°C for 14 h. In this recent study, we discovered that the dose deviation changes over time which can be attributed to a changing macromolecular environment (THPS and gelatin) in a polymer gel dosimeter after irradiation.

In figure 7, the dose deviations and R_2 deviations are also plotted in the region exposed to the cooling and heating element. Small variations in the order of 3% (∼0.31 Gy relative to 10.27 Gy) are measured in the low dose regions (∼0.6 Gy). These can be considered not significant because the dose resolution for this type of dosimeter amounts to 0.46 Gy (Vandecasteele and De Deene 2013a).

4.2. Effect of temperature differences during and following irradiation

To evaluate the influence of a temperature increase induced by the polymerisation process, the maximum temperature difference between the centre of a large volumetric phantom and the centre of a small calibration phantom was measured. The temperature was found to be approximately 1°C higher in the volumetric phantom compared to the calibration phantom. Although a larger phantom is associated with a higher heat capacity and therefore a lower temperature increase for the same amount of

polymerisation-induced heat is expected, this effect is not prevailing. It should be noted, however, that the small calibration phantom was irradiated in water which extracts the generated heat from the polymerisation reaction quickly, therefore reducing the total temperature increase and the cool-down time. Furthermore, as was suspected, calibration phantoms were shown to cool down much faster compared to the larger volumetric phantom. These temperature differences and especially the extent of time at which the larger phantoms remain at a higher temperature were suspected to be the origin of dose overestimations in Vandecasteele and De Deene 2013a. However, our experiment shows that the maximum dose deviation for all calibration sets exposed to various temperatures post-irradiation is within 4% which is just within the maximum dose uncertainty. Therefore it can be concluded that temperature differences due to polymerisation exothermia upon irradiation do not influence the reaction dynamics or polymer morphology in PAGAT gel dosimeters as suggested earlier by Salomons *et al* 2002. These results were recently confirmed by Sedaghat *et al* 2011b. Based on these results, the calibration with small volume calibration phantoms can not be advised against. It can also be concluded that temperature differences in large phantoms as a result of an inhomogeneous dose distribution will not cause significant dose deviations.

4.3. Oxygen effects

The experiment to investigate potential *post-irradiation* oxygen effects in gel dosimeters could not establish significant differences in R_2 between the different sets of phantoms. In the first centimeter, dehydration resulted in an R_2 increase and pre-irradiation oxygen contamination resulted in an inhibition region. This inhibition region originates from small amounts of oxygen already present in the gel prior to irradiation causing an inhibition of free radical polymerisation reactions in the polymer gel dosimeter (De Deene *et al* 2002b). The trend towards increasing dose differences as function of time between gel and ion chamber dose measurements in the intra-batch reproducibility study of Vandecasteele and De Deene (2013a) is presumed to be not systematic.

4.4. Volumetric effects: test tube inside spherical phantom.

This experiment was set-up to expose any physico-chemical factors that affect the calibration of volumetric phantoms using small calibration phantoms. The dose distributions in two spherical phantoms (in which in one phantom a test tube was inserted) were compared. Both phantoms were irradiated with a well defined treatment plan of which the dose in the isocentre was verified via an ion chamber measurement. Both phantoms were calibrated with the traditional calibration method using a set of small calibration phantoms. This way a set of 'free' test tubes could be compared to a test tube inserted inside a spherical phantom.

In accordance with Vandecasteele and De Deene (2013a) large dose deviations with the ion chamber recorded dose were found up to 10.8% (24h) and 11.1% (48h). A remarkable reduction in this dose deviation was found in the gel inside the inserted test

tube. The dose difference was reduced to 6.5% (24h) and 4.4% (48h).
It was experimentally refuted that the measured difference could be attributed to a temperature difference pre- or post-irradiation. It was also excluded that the effect could be attributed to any imaging artefacts (*e.g.* magnetic susceptibility) by acquiring an R_2 map of a homogeneously filled phantom in which a test tube was inserted. Also the irradiation set-up of the calibration phantoms was thoroughly validated by pinpoint ion chamber measurement assuring that the test tube did not have a significant effect on the dose. However, it should be noted that this effect is also too small to be responsible for the large dose discrepancies found between small volume calibration phantoms and larger volumetric phantoms (Vandecasteele and De Deene (2013a)).

While thermal effects (pre- and post-irradiation), irradiation set-up and imaging artefacts can be excluded as a possible explanation for the measured dose deviations between both phantoms, the exact origin of the dose deviations remains unclear. Temperature differences in the order of 0.3°C to 0.4°C between the gel in the embedded test tube and outside the test tube during MR image acquisition are a possible hypothesis as suggested by a concurrent paper (Vandecasteele and De Deene 2013b). This needs to be further investigated.

5. Conclusions

This study quantifies some major physical (temperature) and chemical (oxygen) factors that influence the accuracy and precision of MRI polymer gel dosimetry.
The effect of the thermal history prior to irradiation is revisited. By exposing a polymer gel sample to a linear temperature gradient of ~2.8°C/cm (amounting to a total temperature difference of 16.8°C) new insights into temporal variations were added. A clear influence of the temperature on the resulting dose is seen the first h post-irradiation (resulting in dose errors up to 12%). Remarkably, these measured dose deviations decrease to 5% after 54 h post-irradiation.
Furthermore, the dose deviation resulting from imposing a temperature offset during and following irradiation resulted in only a small dose deviation of maximum 4%.
The effect of oxygen infiltration in a gel dosimeter after 48 h post-irradiation was shown to have no significant effect.
Finally, a study in which a small test tube was inserted inside a larger spherical phantom (and compared to the same spherical phantom but without test tube) demonstrated a volumetric effect (in the order of 6.7%) that could not be attributed to differences in thermal history; irradiation set-up or imaging artefacts. This volumetric effect however, could not explain the more pronounced measured dose difference between gel dosimeter and ion chamber dose measurements in Vandecasteele and De Deene (2013a).
From this study, it can be concluded that the investigated physico-chemical effects in the PAGAT gel dosimeter are not responsible for the significant dose discrepancies between gel dosimeter and ion chamber dose measurements in Vandecasteele and De Deene (2013a).

Acknowledgments

This research is supported by the Institute for the Promotion of Innovation though Science and Technology in Flanders (IWT -Vlaanderen). The authors would like to thank Bart Truyens for constructing dedicated equipment that was indispensable in the experimental set-up.

References

Bemis Company, Inc (2010), Floral tape and parafilm products, available at http://www.parafilm.com (last accessed on 1 June 2012)

Chen K and Vyazovkin S 2009 Temperature Dependence of sol-gel conversion kinetics in gelatin-water system *Macromol. Biosci.* **9** 383-92

Cosgrove V P, Murphy P S, McJury M, Adams E J, Warrington A P, Leach M O and Webb S 2000 The reproducibility of polyacrylamide gel dosimetry applied to stereotactic conformal radiotherapy *Phys. Med. Biol.* **45** 1195-210

De Deene Y, Hurley C, Venning A, Vergote K, Mather M, Healy B J and Baldock C 2002a A basic study of some normoxic polymer gel dosimeters *Phys. Med. Biol.* **47** 3441-3463

De Deene Y, Pittomvils G and Visalatchi S 2007 The influence of cooling rate on the accuracy of normoxic polymer gel dosimeters *Phys. Med. Biol.* **52** 2719-28

De Deene Y, Van de Walle R, De Wagter C and Achten E 1998 Mathematical analysis and experimental investigation of noise in quantitative magnetic resonance imaging applied in polymer gel dosimetry *Signal Process.* **70** 85-101

De Deene Y, Venning A, Hurley C, Healy B J and Baldock C 2002b Dose-response stability ans integrity of the dose distribution of various polymer gel dosimeters *Phys. Med. Biol.* **47** 2459-70

De Deene Y, Vergote K, Claeys C and De Wagter 2006 The fundamental radiation properties of normoxic polymer gel dosimeters: a comparison between a methacrylic acid based gel and acrylamide based gels *Phys. Med. Biol.* **51** 653-73

Douglas J and Gunn J E 1964 A general formulation of alternating direction methods: Part I. Parabolic and hyperbolic problems *Numerische Mathematik* **6** 428-53

Dumas E M, Leclerc G and Lepage M 2006 Effect of container size on the accuracy of polymer gel dosimetry *J. Phys.: Conf. Ser* **56** 239-241

Ineos Barex®USA 2006 Barex®218 Extrusion Grade: Typical physical properties available at http://www.ineosbarex.com/files/upload/Barex218E_06_06.pdf

Hepworth S J, Leach M O and Doran S J 1999 Dynamics of polymerization in polyacrylamide gel (PAG) dosimeters: (II) modeling oxygen diffusion *Phys. Med. Biol.* **44** 1875-84

MacDougall ND, Miquel ME and Keevil SF 2008 Effects of phantom volume and shape on the accuracy of MRI BANG gel dosimetry using BANG3 *Br. J. Radiol.* **81** 46-50

Sakiyama T, Han S, Torii A, Miyawaki O and Yano T 1991 Intrinsic thermal conductivity of gelatin estimated independently of heat conduction models *Agric. Biol. Chem.***55** 487-92

Salomons G J, Park Y S, McAuley K B and Schreiner L J 2002 Temperature increases associated with polymerization of irradiated PAG dosimeters *Phys. Med. Biol.* **47** 1435-48

Sedaghat M, Bujold R and Lepage M 2010 Effect of the exothermal polymerization reaction on polymer gel dosimetric measurements *J. Phys.: Conf. Ser.* **250** 012018

Sedaghat M, Bujold R and Lepage M 2011a Severe dose inaccuracies caused by an oxygen-antioxidant imbalance in normoxic polymer gel dosimeters *Phys. Med. Biol.* **56** 601-25

Sedaghat M, Bujold R and Lepage M 2011b Investigating potential physicochemical errors in polymer gel dosimeters *Phys. Med. Biol.* **56** 6083-6107

Vandecasteele and De Deene 2013a On the validity of 3D polymer gel dosimetry: I. Reproducibility study *Phys. Med. Biol* **58** 19-42

Vandecasteele and De Deene 2013b On the validity of 3D polymer gel dosimetry: III. MRI related error sources *Phys. Med. Biol* **58** 63-85

Vergote K, De Deene Y, Vanden Bussche E and De Wagter C, 2004 On the relation between the spatial dose integrity and the temporal instability of polymer gel dosimeters *Phys. Med. Biol.* **49** 4507-22

Xu Y, Wuu C S and Maryanski M J 2010 Sensitivity calibration procedures in optical-CT scanning of BANG 3 polymer gel dosimeters *Med. Phys.* **37** 861-8

4

On the validity of 3D polymer gel dosimetry: III. MRI related error sources

---

Jan Vandecasteele and Yves De Deene
Both authors contributed equally to this study.

Manuscript on which this chapter is based:
Physics in Medicine and Biology **58** (2013) 63-85

On the validity of 3D polymer gel dosimetry: III. MRI related error sources*

Jan Vandecasteele[1] **and Yves De Deene**[1,2]

[1] Department for Radiation Oncology and Experimental Cancer Research, Ghent University, De Pintelaan 185, 9000 Gent, Belgium
[2] Institute of Medical Physics, School of Physics, University of Sydney, Sydney NSW 2006, Australia

E-mail: Jan.Vandecasteele@UGent.be

Received 8 Februari 2012, in final form 28 Augustus 2012
Published 6 December 2012
Online at stacks.iop.org/PMB/58/63

Abstract. In MRI (PAGAT) polymer gel dosimetry, there exists some controversy on validity of 3D dose verifications of clinical treatments. The relative contribution of important sources of uncertainty in MR scanning to the overall accuracy and precision of 3D MRI polymer gel dosimetry is quantified in this study. The performance in terms of signal-to-noise and imaging artefacts was evaluated on 3 different MR scanners (two 1.5 T and a 3 T scanner). These include: (1) B_0-field inhomogeneity, (2) B_1-field inhomogeneity, (3) dielectric effects (losses and standing waves) and (4) temperature inhomogeneity during scanning. B_0-field inhomogeneities that amount to maximum 5 ppm result in dose deviations of up to 4.3% and deformations of up to 5 pixels. Compensation methods are proposed. B_1-field inhomogeneities were found to induce R_2 variations in large anthropomorphic phantoms both at 1.5 T and 3 Ta. At 1.5 T these effects are mainly caused by the coil geometry resulting in dose deviations of up to 25%. After correction of the R_2 maps using a heuristic flip angle-R_2 relation, these dose deviations are reduced to 2.4%. At 3 T, dielectric properties of the gel phantoms are shown to strongly influence B_1-field homogeneity, hence R_2 homogeneity, especially of large anthropomorphic phantoms. The low electrical conductivity of polymer gel dosimeters induces standing wave patterns resulting in dose deviations up to 50%. Increasing the conductivity of the gel by adding NaCl reduces the dose deviation to 25% after which the post-processing is successful in reducing the remaining inhomogeneities caused by the coil geometry to within 2.4%. The measurements are supported by computational modelling of the B_1-field. Finally, temperature fluctuations of 1°C frequently encountered in clinical MRI scanners result in dose deviations up to 15%. It is illustrated that with adequate temperature stabilisation, the dose uncertainty is reduced to within 2.58%.

*Both authors contributed equally to this study

1. Introduction

The amount of polymer created in a polymer gel can be directly related to the amount of radiation dose deposited inside a gel. The amount of polymerisation is spatially measured by means of magnetic resonance imaging (MRI). To generate dose information from the R_2-maps an adequate calibration technique is needed. In Vandecasteele and De Deene (2013a) is shown that the calibration process using small volume calibration phantoms results in unacceptably large mean dose deviations up to 13.7% relative to an ion chamber measurement. In the described experiment, a normalisation of the dose-R_2 relationship against an independent ion chamber measurement was required to bring the dose deviations down to acceptable levels. However, the origins of the reported dose discrepancy between volumetric phantoms and calibration phantoms were still not found and this results in a lack of confidence in the validity of polymer gel dosimetry. In Vandecasteele and De Deene (2013b) different physico-chemical origins were explored but these could not explain the dose discrepancies in the order of 13.7%.

In this study, the relative contribution of MR imaging artefacts on the 3D dose distribution is quantified so that the traditional method for calibration using small calibration phantoms could be reinstated as the standard technique. Former studies already investigated the effects of eddy currents in a multiple spin-echo sequence (De Deene *et al* 2000a), B_1-field inhomogeneity (De Deene *et al* 2000b) and temperature during scanning (De Deene and De Wagter 2001) on the dose maps. This study quantifies the relative contribution of these error sources on the overall inaccuracy of 3D polymer gel dosimetry and is also extended to higher magnetic field strengths. Other groups previously reported on polymer gel dosimetry using higher magnetic fields of 3 T or above (Ertl *et al* 2000, Berg *et al* 2001, Heufelder *et al* 2003, Berg *et al* 2004, Bayreder *et al* 2006, Seimenis *et al* 2009, Gopishankar *et al* 2011, Wong *et al* 2009, Xuanfeng *et al* 2010, Deman *et al* 2011). However, an assessment of the 3D dose accuracy at these higher field strengths is lacking, especially for realistically sized anthropomorphically shaped phantoms. The influences of spatial inhomogeneities of the static magnetic field (B_0-field) and radio frequency field (B_1-field) on the dose accuracy are examined for different geometrically shaped phantoms at different field strengths. It is shown that at higher field strengths, the dielectric properties of the polymer gel dosimeters have a significant influence on the B_1-field homogeneity in realistically sized phantoms and hence on the dose maps. Ultimately, the effect of temperature fluctuations during scanning is revisited using experiments and simulations.

2. Materials and Methods

2.1. Gel fabrication and storage

The PAGAT gel dosimeter (PolyAcrylamide Gelatin gel fabricated at ATmospheric conditions) used in this study is composed of gelatin (6% w/w), acrylamide (2.5% w/w), N,N'-methylene-bis-acrylamide (2.5% w/w) and 5 mM

Bis[tetrakis(hydroxymethyl)phosphonium]sulphate (THPS) as antioxidant. The polymer gels were fabricated according to a procedure as described elsewhere (De Deene *et al* 2006).

2.2. Dose-R_2 relationship as a function of B_0-field strength

PAGAT gel was divided over 10 standard sized Pyrex® test tubes (height: 10.0 cm, inner radius: 6.2 mm and wall thickness of 1.3 mm) and 10 small glass test tubes (height: 18 cm, inner radius: 5.0 mm and wall thickness 0.7 mm). The samples were irradiated 24 h post fabrication with a clinical linear accelerator (Elekta Synergy) to a well-defined dose, ranging between 0 Gy and 18 Gy in steps of 2 Gy. This procedure is described in more detail elsewhere (Vandecasteele and De Deene 2013a). The R_2 values were subsequently measured in the small size test tubes with a 0.5 T benchtop relaxometer (Brüker Minispec^{TM} mq20) using a multiple spin echo CPMG sequence at a temperature of 21°C (20 hours post irradiation) with following imaging parameters: τ = 0.5 s, total measuring time = 3s and # of data points = 3000.

The standard sized test tubes were scanned on a Siemens Magnetom Avanto (1.5 T) and a Siemens Magnetom Trio (3 T) scanner with following imaging parameters: TR = 3000 ms, TE = 40-1280 ms, matrix size = 0.5×0.5×10 mm^3, BW = 130 Hz/pixel, NEX = 2, contrast = 32 and total scan time = 10 m 47 s. The R_2 values were calculated as described before (De Deene *et al* 1998). The dose-R_2 response data points were fitted against a mono-exponential function (equation 1) from which the slope (at 0 Gy) and the intercept were extracted (explained in more detail in Vandecasteele and De Deene 2013a).

$$R_2 = R_{2,sat} - \Delta R_2 \cdot e^{-\alpha \cdot D} \tag{1}$$

2.3. Volumetric R_2 homogeneity study

Scanning was performed on three different MR scanners: Siemens Magnetom Trio (3 T), Magnetom Avanto (1.5 T) and Magnetom Symphony (1.5 T). The mean R_2 and standard deviation were determined in a region of interest (ROI) for several gel dosimetry test phantoms filled with 8% gelatin gel doped with NaN_3 (0.5% was added as fungicide): a box-shaped phantom (0.25 l), a spherical phantom (0.25 l) and an anthropomorphically shaped head-and-neck phantom (9 l). The polygonal ROI was chosen in the centre of the respective phantom excluding a margin of minimal 2 pixels from the edge of the phantom. This ROI included approximately 80% of the measured MRI slice inside the phantom. Of this selected ROI, the mean R_2 value and the standard deviation was calculated. The box-shaped phantom and the spherical phantom were scanned in circularly polarised (CP) head coil while the head-and-neck phantom was scanned in the CP body coil. A multiple spin echo sequence was used along three orthogonal slice orientations with following imaging parameters for all slice orientations and all phantoms: TR = 3000 ms, TE = 40-1280 ms, BW = 130 Hz/pixel, NEX = 1, contrast

= 32 and slice thickness 10 mm. Other imaging parameters were chosen depending on the phantom and slice orientation and are listed in table 1.

2.4. B_0-field mapping

B_0-field maps of different volumetric test phantoms and at the different scanners were acquired by use of a susceptibility weighted echo-time encoding (SWEET) technique (Park et al 1988, De Deene and De Wagter 1999, De Deene *et al* 2001). Two spin-echo phase images were recorded with an echo time of 20 ms but in which the refocusing pulse was shifted towards the frequency encoding gradient with, respectively, 1 ms and 4 ms. Phase difference images were calculated from the corresponding phase images after phase unwrapping using the 2D Goldstein algorithm (Goldstein *et al* 1988).

2.5. B_1-field mapping and simulation

The apparent B_1-field homogeneity was investigated for the same volumetric test phantoms and scanners using the double angle method with reference flip angle (FA)= 30° (Insko and Bolinger 1992).

In 3D polymer gel dosimetry large anthropomorphically shaped phantoms are often used. These phantoms are composed of a hydrogel in which monomers are dissolved. The dielectric properties of these media may have a significant influence on the apparent B_1-field homogeneity inside the phantom. If the wavelength of the RF field is comparable to the geometric dimensions of the scanned object, constructive or destructive interference of the transmitted RF waves may occur (Tofts 1994). These standing waves are strongly dependent on the dielectric constant of the bulk medium of the phantom. Therefore, the effect on the homogeneity of the B_1-field distribution inside a phantom was investigated as a function of phantom diameter, scanner frequency and electrical conductivity of the medium.

The electrical conductivity (σ) and permittivity (ϵ') as a function of frequency were determined for polymer gels and NaCl solutions: distilled water, distilled water + 1% NaCl, 8% gelatin gel, 8% gelatin gel + 1% NaCl, unirradiated PAGAT and irradiated PAGAT (20 Gy). A coaxial impedance probe was connected to a network analyser (HP 8754A Network analyser) and the probe was inserted in 2 ml of the examined medium (Clerjona *et al* 2003, Venkatesh and Raghavan 2005).

The B_1-field in polymer gel dosimeters was calculated for different MR resonance frequencies by algebraically solving the Maxwell equations for a cylinder (Tofts (1994) and Jin (1998)):

$$B_1 = \sqrt{2} \cdot \frac{Ai}{2\omega} \cdot \left(\frac{J_1(k_d \rho)}{\rho} + J_1'(k_d \rho) \cdot k_d \right) \tag{2}$$

Table 1. Overview of isotropic in-plane resolution (Res in mm^2), phase encoding steps (PES) and total scan time (TST) that were used for scanning three different gel phantoms on three Siemens MR scanners.

		Box-shaped			Spherical			Head-and-neck		
		Tra	Cor	Sag	Tra	Cor	Sag	Tra	Cor	Sag
Avanto	Res [mm^2]	0.25	0.25	0.25	0.25	0.25	0.25	1	1	1
	# PES [-]	64	64	64	88	88	88	256	320	240
	TST	3m12s	3m12s	3m12s	4m24 s	4m24 s	4m24s	12m48s	16m	12m
Symphony	Res [mm^2]	0.25	0.25	0.25	0.25	0.25	0.25	1	1	1
	# [-]	136	136	136	192	176	176	256	256	384
	TST	6m48s	6m48s	6m48s	9m36s	8m48 s	8m48s	12m48 s	12m48 s	19m12s
Trio	Res [mm^2]	0.25	0.25	0.25	0.25	0.25	0.25	1	1	1
	# [-]	128	128	128	192	192	192	256	448	260
	TST	6m24s	6m24s	6m24s	9m36s	9m36s	9m36s	12m48s	22m24s	13m

where

$$A = \frac{b}{a}\frac{J_1(k_0 b)Y_1(k_0 c) - J_1(k_0 c)Y_1(k_0 b)}{k_d J_1'(k_d a)F(k_0,a,c) - k_0 J_1(k_d a)G(k_0,a,c)} \tag{3}$$

in which

$$F(k_0,a,c) = J_1(k_0 a)Y_1(k_0 c) - J_1(k_0 c)Y_1(k_0 a) \tag{4}$$

$$G(k_0,a,c) = J_1'(k_0 a)Y_1(k_0 c) - J_1(k_0 c)Y_1'(k_0 a) \tag{5}$$

with a the cylindrical phantom radius, b the coil radius, c the RF shield radius. In the above, $k_0 = \omega\sqrt{\mu_0\epsilon_0}$ represents the free space wave number and $\epsilon_c = \epsilon_r + i\sigma/\omega\epsilon_0$, with ϵ_r and σ being the relative permittivity and conductivity of the dielectric cylinder. Furthermore, $k_d = k_0\sqrt{\epsilon_c}$ and J_1 and Y_1 denote the first order Bessel functions of the first and second kind. A CP body coil and an infinitely long cylinder were assumed.

2.6. Temperature drift during MR scanning

Temperature fluctuations during MR scanning are known to have a significant influence on the dose accuracy (De Deene *et al* 2006). The hypothesis was tested whether this effect could account for mean dose deviations up to 13.7%. Firstly, the temperature fluctuations occurring in an MR scanner room were measured. The temperature history in an MRI scanner room (Siemens Magnetom Avanto) was recorded over a period of seven days by use of a fiber optic temperature measurement system (Reflex 4, Neoptix, Québec, Canada, nominal accuracy: 0.3°C) equipped with two fibre optic temperature probes. One probe was inserted inside a spherical flask (300 ml) filled with an 8 % gelatin gel doped with NaN_3 while the other probe was left in air. The temperature in air was also recorded at five different locations inside the scanner room and one location inside the scanner bore. Each temperature measurement was recorded over a time period of approximately 3 min to make sure that no temperature changes were occurring during the measurement. This set of measurements was repeated at two separate occasions two weeks apart.

The temperature sensitivity of the dose response during MR imaging was determined to investigate the influence of temperature fluctuations during scanning on the dose accuracy. Eight standard sized test tubes (see section 2.2) were filled with the same batch of PAGAT gel. The small phantoms were irradiated on a clinical linear accelerator (Elekta Synergy) 24 h post fabrication with well defined doses between 0 Gy and 14 Gy in steps of 2 Gy. The irradiation set-up was thoroughly validated as described in Vandecasteele and De Deene 2013a. Another 24 hours later, the test tubes were scanned on the Siemens Avanto 1.5 T scanner. During scanning, the test tubes were positioned in a cylindrical recipient that was perfused with a GdDTPA-doped water solution (T_1 and T_2 lower than 60 ms) to avoid imaging artefacts caused by motion of the circulating water. The cylindrical recipient was connected to a temperature controlled water bath. The temperature inside the recipient was recorded by use of a fiber optic temperature measurement system. Scans were acquired at eight different

water temperatures. Sufficient time (∼20 minutes) was allowed to equilibrate the temperature of the calibration phantoms inside the water filled cylindrical recipient. This was also verified using the fiber optic temperature measurement system. The following temperatures were induced: 8.0°C, 8.9°C, 12°C, 15°C, 20°C, 25°C, 30°C and 35°C. The following imaging parameters were used: pixel size 0.78 × 0.78 × 10 mm^3, TR = 3000 ms, number of equidistant echoes = 32, TE = 40 ms - 1280 ms and NEX = 1. R_2 maps were calculated as described elsewhere (Vandecasteele and De Deene 2013a). The dose-R_2 relations recorded at different temperatures were fitted against a mono-exponential saturation function (equation 1). The dose error induced by a temperature difference between calibration phantom and volumetric phantom (previously reported in De Deene *et al* 2006) was derived as

$$\frac{\partial D}{\partial T} = \frac{-\frac{\partial R_{2,sat}}{\partial T} \cdot e^{\alpha \cdot D} + \frac{\partial \Delta R_2}{\partial T} - \Delta R_2 \cdot D \cdot \frac{\partial \alpha}{\partial T}}{\alpha \cdot \Delta R_2} \tag{6}$$

Ultimately, to experimentally validate the influence of temperature fluctuations during scanning on the dose accuracy, an experiment in a temperature controlled environment was performed. A set of fifteen calibration phantoms and one spherical phantom were fabricated and irradiated according to the protocol used in Vandecasteele and De Deene (2013a). The phantom and calibration phantoms were scanned in the Siemens Avanto 1.5 T MR scanner in a closed cylindrical water recipient that was perfused with a GdDTPA-doped water solution connected to a temperature controller. The temperature was monitored by four fiber optic temperature measurement probes. The first probe was inserted in the water solution, the second and third probes were inserted inside calibration phantoms and the fourth probe was inserted in the centre of the spherical phantom. The following imaging parameters were used for all image acquisitions: pixel size 0.52 × 0.52 × 10 mm^3, TR = 3000 ms, number of equidistant echoes = 32, TE = 40 ms - 1280 ms and NEX = 1. Three MR scans were acquired at a temperature equilibrium of ≈ 22.4°C. Each acquired R_2 map was calibrated to dose with the dose-R_2 relationship derived from the calibration phantoms scanned at the same time. The gel measured isocentre dose in the spherical phantom is extracted from each of the dose maps and compared to the ion chamber recorded dose at the same location.

To investigate how much the temperature can fluctuate in a polymer gel dosimeter phantom, the evolution of the temperature distribution in several phantoms was calculated by analytically solving the heat equation (Carslaw and Jaeger, 1959).

The temperature trajectories in a small cylindrical calibration phantom, a small spherical phantom (250 ml) and a large spherical phantom (4.5 l, simulating a realistically sized human head phantom) were compared. The calibration phantom was represented by a finite hollow cylinder of glass filled with gel at an initial temperature of 20°C moved to an ambient temperature of 22°C. The spherical phantoms were represented by a hollow glass sphere filled with gel in the same temperature conditions as described above (Carslaw and Jaeger, 1959).

All these phantoms were exposed to a sudden temperature increase of 2°C. This particular situation occurred when phantoms were moved from their storage locations

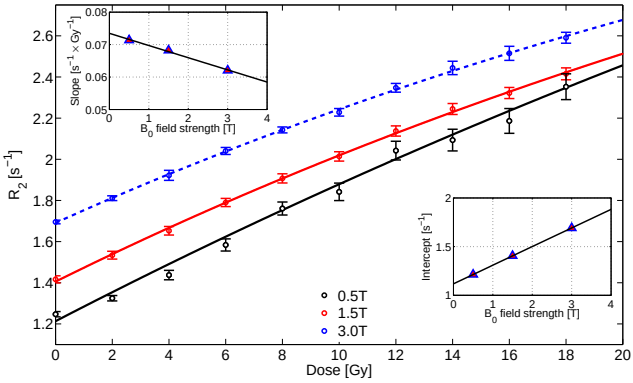

Figure 1. Dose-R_2 curves for the same samples of PAGAT gel measured at 0.5 T, 1.5 T and 3 T. The errorbars in the 1.5T and 3T data are the standard deviations of the regions of interest in which the mean R_2 values are calculated. The errorbars in the 0.5T data represent the uncertainty of the exponential decay fit. The inset figures display the linear evolution of the slope and intercept as function of field strength.

in the scanner room from outside to inside the scanner bore where they were scanned.

Finally, it should be noted that in all MRI measurements no use of centric k-space reordering was made although suggested by De Deene and De Wagter (2001). Centric k-space reordering is important to minimize the influence of temperature changes due to RF deposition during scanning. A measurement of the temperature inside a gel phantom did not show any effects of RF induced temperature changes. However centric k-space reordering is recommended when scanning large phantoms in which large amounts of RF energy are deposited. At the start of the MRI acquisition, the temperature between the calibration phantoms and volumetric phantom should be equilibrated.

3. Results

3.1. Dose-R_2 relationship as a function of B_0-field strength

The R_2-intercept increases by approximately 0.19 s^{-1} per T. In addition, the dose sensitivity decreases by approximately 0.0038 s^{-1} Gy^{-1} per T. The dose-R_2 curves are displayed in figure 1.

3.2. B_0-field homogeneity

The R_2 maps and B_0-field maps were acquired for a box-shaped, spherical and head-and-neck phantom. From all R_2 maps the mean value and standard deviation were extracted.

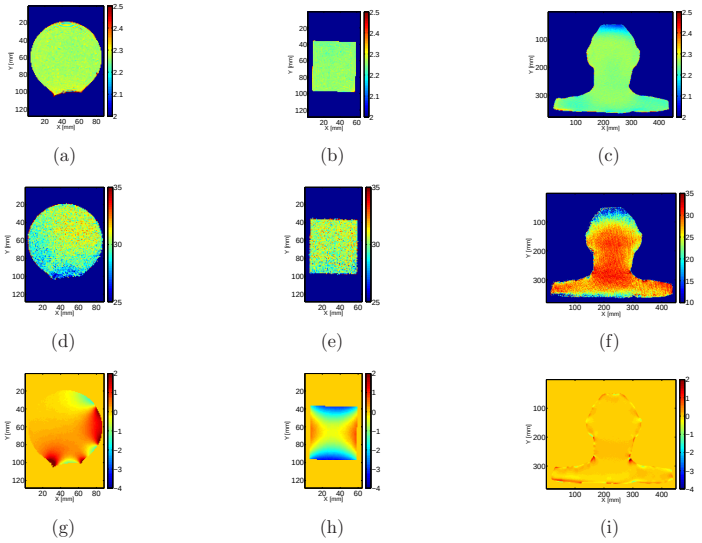

Figure 2. An overview is given of R_2 maps (a, b and c, expressed in s-1), FA maps (d, e and f, expressed in degrees) and B_0-field maps (g, h and i, expressed in ppm) measured with a 1.5 T Siemens avanto MR scanner acquired of a spherical phantom (a, d and g), a box-shaped phantom (b, e and h) and a head-and-neck phantom (c, f and i).

Figure 2 displays the R_2 maps (in a, b and c) and B_0 maps (in g, h and i) of the different phantoms acquired with the Siemens Avanto 1.5 T scanner. Table 2 lists the mean R_2 values and standard deviation along with the B_0 variation range acquired for all test phantoms with the Siemens Avanto, Symphony and Trio scanners, respectively. Notice the global B_0 variations in the spherical phantom where the dedicated PMMA phantom holder (Vandecasteele and De Deene 2013a) is located (figure 2g). These larger B_0 inhomogeneities in the order of 5 ppm (spread out along the entire phantom) result in an R_2 variation of approximately 0.024 s^{-1}. In the box-shaped phantom, an excellent R_2 homogeneity (maximum σ_{R_2} = 1.6% of mean R_2 value) was found although global B_0 variations are present in the order of 3 ppm. In the head-and-neck phantom local B_0 deviations in the order of 5 ppm are measured, resulting in a small local R_2 increase in the order of 0.028 s^{-1}. These deviations occur at the outer edge of the gel phantom near sharp transitions of air and phantom wall (*e.g.* transition between shoulder and neck region in figure 2i). With an R_2 range of 0.65 s^{-1}, these deviations correspond to a dose uncertainty of approximately 4.3%.

Table 2. Overview of the mean R_2, mean FA values and B_0 range along with the standard deviation expressed in percent relative to the mean value of a box-shaped, spherical and head-and-neck phantom scanned along three orthogonal orientations: transversal (T), Coronal (C) and Sagittal (S) with a Siemens Magnetom Avanto (1.5 T), Symphony (1.5 T) and Trio (3 T) MR scanner.

		Box-shaped			Spherical			Head-and-neck		
		Tra	Cor	Sag	Tra	Cor	Sag	Tra	Cor	Sag
Siemens Avanto	Mean R_2 [s^{-1}]	2.26	2.25	2.26	2.26	2.26	2.26	2.22	2.25	2.21
	σ_{R_2} [%]	1.1	1.4	1.6	1.1	1.5	1.5	0.7	**2.1**	**2.9**
	Mean FA [°]	28.1	30.1	30.3	30.3	30.4	29.9	28.5	27.8	27.0
	σ_{FA}[%]	11.3	9.9	10.2	8.0	8.9	8.7	8.7	**18.4**	**21.9**
	ΔB_0 [ppm]	1.36	2.75	2.72	1.10	3.24	3.78	0.96	5.17	4.92
Siemens Symphony	Mean R_2 [s^{-1}]	2.29	2.29	2.30	2.24	2.29	2.25	1.85	1.85	1.85
	σ_{R_2} [%]	1.1	1.3	1.2	0.9	1.0	1.0	0.7	**1.4**	**2.1**
	Mean FA [°]	27.6	28.7	28.1	29.4	28.9	28.8	29.3	28.0	28.1
	σ_{FA}[%]	10.6	9.5	10.2	7.1	7.4	7.3	5.9	**11.4**	**13.0**
	ΔB_0 [ppm]	1.33	2.89	3.27	1.29	5.50	5.47	1.14	3.17	2.33
Siemens Trio	Mean R_2 [s^{-1}]	2.45	2.41	2.43	2.43	2.42	2.44	1.81	1.81	1.80
	σ_{R_2} [%]	0.7	0.6	0.7	0.7	0.5	0.5	**1.8**	**2.2**	**1.6**
	Mean FA [°]	28.3	29.9	27.4	28.1	27.1	26.7	27.1	29.7	27.6
	σ_{FA} [%]	5.0	4.4	4.6	5.7	4.3	5.3	**11.4**	**16.0**	**9.7**
	ΔB_0 (ppm)	1.18	2.69	2.74	4.92	5.76	5.21	1.17	3.22	3.67

3.3. B_1-field homogeneity

In the small volume test phantoms (box-shaped and spherical phantom) no correlation between R_2 and the flip angle could be established as the B_1 inhomogeneity was very low. The coronal and sagittal R_2 maps of the head-and-neck-phantom scanned at 1.5 T and the transverse, coronal and sagittal maps scanned at 3 T showed substantially higher standard deviations (highlighted in table 2).

At 1.5 T these deviations originate from a drop in the R_2 value in the order of 10% of the mean R_2 value near the upper and lower edge of the head-and-neck-phantom (figure 2c). These inhomogeneities result in a dose deviation of approximately 25%. A correlation between the inhomogeneity in the R_2 and the inhomogeneity in the flip angle map (figure 2f) was found as shown in figure 3a. FA maps were smoothed using a Wiener filter (Lim 1990). The flip angle-R_2 relationship could be used to compensate the inhomogeneous R_2 maps as previously shown by Vergote *et al* 2004a. The standard deviation in the corrected R_2 maps is reduced to 1% of the mean R_2 value after correction and the R_2-signal drop near the upper and lower edges was compensated (figure 3b). This results in a dose uncertainty within 2.4%.

At 3 T, a drop in the mean R_2 value in the order of 19% can be seen near the centre of the phantom (figure 4a and 4c). A correction of these large R_2 inhomogeneities using the

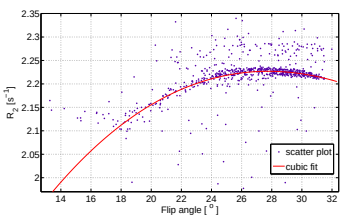

(a)

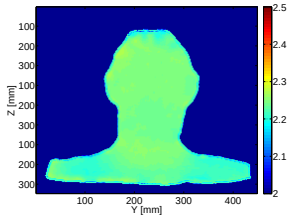

(b)

Figure 3. Flip angle-R_2 relation for the coronal slice of a head-and-neck phantom acquired with the Siemens Avanto MR scanner (a). A third-order polynomial fit is applied. A corrected coronal R_2 map (expressed in s-1) is displayed in b using the FA-R_2 relation. In figure 2c the uncorrected image is shown.

Table 3. Experimentally determined electrical conductivity and relative permittivity of several media.

	Electrical conductivity (σ, S $\cdot$m^{-1})	Relative Permittivity (ϵ')
H_2O	10^{-5}	81
H_2O + 1% NaCl	1.564	75
8% Gelatin gel	0.079	69
8% Gelatin gel + 1% NaCl	1.554	71
PAGAT (0 Gy)	0.101	86
PAGAT (20Gy)	0.104	80

measured FA-R_2 relationship was attempted. However, after correction inhomogeneities in R_2 remained in the order of 8% of the mean value. These R_2 inhomogeneities can result in dose deviations of approximately 25%. These artefacts were attributed to dielectric properties of the gel phantoms. The electrical conductivity and relative permittivity of several media were measured as listed in table 3. The addition of 1% NaCl to water or gelatin gel has a strong influence on the electrical conductivity of the medium. No large variations in dielectric permittivity between the different media were found. No significant variations in dielectric properties of unirradiated and irradiated PAGAT gel were found and were also very similar to these of pure gelatin gel.

The head-and-neck phantom was refilled with a gelatin gel in which 1% NaCl was added. The corresponding R_2 maps showed R_2 signal variations in the order of 10% of the mean value similar to the R_2 variations measured at 1.5 T (figure 4e and 4g). This inhomogeneity results in a dose uncertainty in the order of 25%. Correction of the remaining inhomogeneities in the R_2 maps was performed using the measured FA-R_2 relationship resulting in a standard deviation within 1% of the mean R_2 value.

Proof of the effect of the dielectric properties on the B_1-field homogeneity is

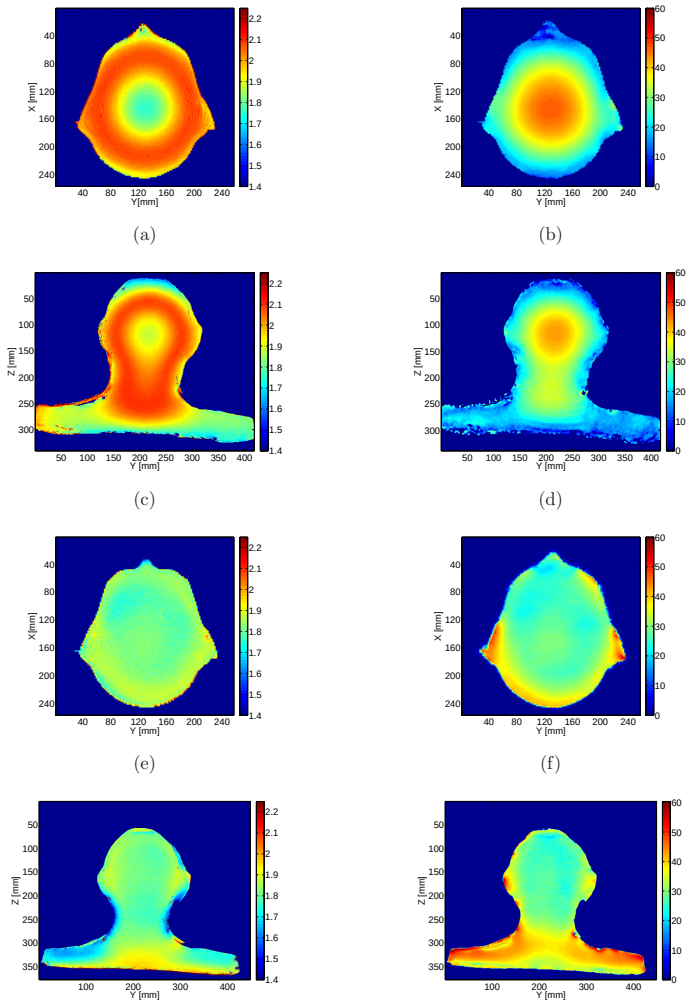

Figure 4. Transverse (a, b, e and f) and coronal (c, d, g and h) acquired images of a head-and-neck phantom measured at 3 T. R_2 maps (expressed in s-1) are shown in a, c, e and g along with their corresponding FA maps (expressed in degrees) in b, d, f and h. The phantom was filled with a low conducting medium (8% gelatin gel) in a, b, c and d, while in e, f, g and h the phantom was filled with conducting medium (8% gelatin gel doped with 1% NaCl).

provided by computational modelling of the B_1-field. A clear trend in B_1 inhomogeneity as a function of phantom size is demonstrated for the same electrical conductivity. Furthermore, in highly conducting media (*e.g.* gelatin gel doped with NaCl) the RF waves are attenuated leading to a signal void towards the centre of the phantom (figure 5b) compared to low conducting media (water, pure gelatin gel, PAGAT) where standing waves become apparent (figure 5a). These effects become much more pronounced at higher field strengths (figure 5c and 5d). For smaller sized test phantoms, these effects are less pronounced, even at 3 T (figure 5e and 5f). A good correspondence between simulations and measurements can be seen when comparing figure 5c - 4b and 5d - 4f.

3.4. Temperature drift during MR scanning

The maximum temperature difference over a period of seven days amounts to 1.1°C (figure 6).

The temperature was recorded at different locations inside the same scanner room. This measurement was repeated at two separate occasions two weeks apart. During each of these measurements, the temperature difference *around* the MR scanner among the five measurement locations did not differ by more than 0.3°C. However, the temperature *inside* the scanner bore was 2.4°C and 1.0°C higher than the temperature around the scanner during the first and second measurement respectively.

The sensitivity of the dose-R_2 response to temperature during MR imaging was measured using a set of PAGAT calibration phantoms. The phantoms were scanned at different temperatures between 8°C and 35°C. The calibration curves are displayed in figure 7a. The slope of the dose-R_2 response changed at a rate of -0.0023 $s^{-1}Gy^{-1}$ per °C (figure 7b) while the intercept changed by -0.0328 s^{-1} per °C (figure 7c).

Using the aforementioned temperature dependence of the dose-R_2 response curves, dose deviations can be calculated originating from temperature fluctuations during scanning. A dose-R_2 calibration function acquired at 20°C was compared to the calibration function acquired at 21°C (shown in figure 8a) for two gel compositions: 5% total monomer concentration and 6% total monomer concentration derived from De Deene *et al* (2006). From the difference between these two calibration functions, the resulting dose deviation could be calculated. This simulation suggests that a temperature offset of 1°C at 20°C results in 1.76 Gy (15.6%) dose overestimation for a 5%T PAGAT composition compared to 0.97 Gy (8.6%) overestimation for a 6%T PAGAT. The estimated dose deviation induced by a temperature difference between calibration and volumetric phantoms was derived using equation 6 and is plotted as a function of dose in figure 8b. This results in a similar dependence of relative dose deviation per °C.

To experimentally validate the influence of temperature fluctuations during scanning on the dose accuracy, an experiment in a temperature controlled environment was performed (figure 9a). The dose deviation at thermal equilibrium between calibration phantoms and spherical phantom amounted to 2.58% compared to the ion

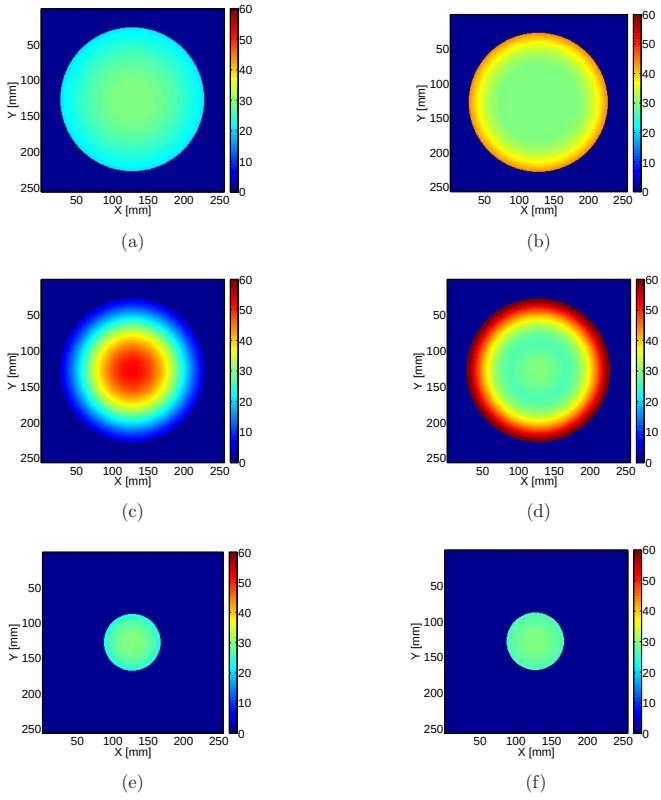

Figure 5. Simulated FA maps (expressed in degrees) are shown in a, b, c and d of a spherical geometry of comparable size as the transverse measurement of the head-and-neck phantom displayed in figure 4. In e and f, a small spherical phantom was simulated with a comparable size of the gel dosimeter used in Vandecasteele and De Deene (2013a). In a, c and e the FA map was calculated for a low conducting medium. In b, d and f a high electrical conductivity was assumed. In a and b the field strength was set to 1.5 T, while in c, d, e and f simulations were performed for a magnetic field strength of 3 T. A good correspondence between simulations and measurements can be seen when comparing figure 5c - 4b and 5d - 4f, respectively.

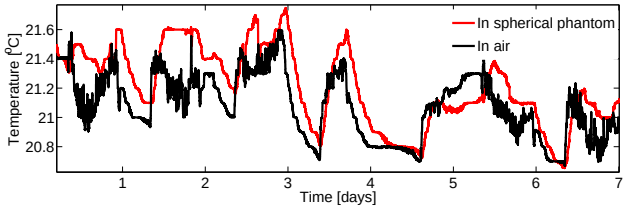

Figure 6. Temperature fluctuations inside an MR scanner room (Avanto) recorded over a period of seven days in a spherical phantom (red) and in air (black). High frequency temperature fluctuations in air are dampened in the spherical phantom.

chamber reference dose (figure 9b).

As shown previously in this section, a temperature difference of 1°C to 2°C is frequently encountered between the phantoms storage location around the MRI scanner and the scanner bore. Computational modelling of the temperature history in a small calibration phantom and large volumetric phantoms was performed after a sudden exposure to a temperature increase of 2°C. In figure 10a the absolute temperature in the centre and at the surface of both simulated phantoms as a function of time is plotted. Also the temperature history of the small calibration phantom is shown. The large temperature difference between the calibration phantom and the large phantom can be clearly seen after 1 hour. A quantification of the differences between the surface and central temperature in the spherical phantoms as well as the differences between the central temperatures between the spherical phantoms and calibration phantom is shown in figure 10b. The transfer of the phantoms from their storage location around the scanner to the scanner bore results in temperature differences between calibration phantoms and large phantoms upto 1.5 to 2 °C. In addition, a temperature difference inside the volumetric phantoms of upto 1.2°C can be seen in figure 10b.

4. Discussion

4.1. Dose-R_2 relationship as a function of B_0-field strength

The dose sensitivity as a function of field strength of the PAGAT polymer gel dosimeter decreases by approximately 8% per T. In addition the R_2 intercept increases by approximately 15% per T. Similar observations in both polymer gel dosimetry and protein relaxometry were reported in Koenig and Brown III 1990, Henckelman *et al* 1993 and Lepage *et al* 2001. Moving from 1.5 T to 3 T in polymer gel dosimetry will decrease the dose sensitivity by approximately 12%. An increase in SNR of 50% is however expected. This is shown in table 2 where the standard deviation values in the images acquired at 3 T are approximately half of those acquired at 1.5 T.

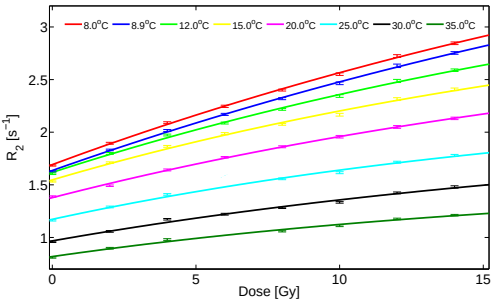

(a)

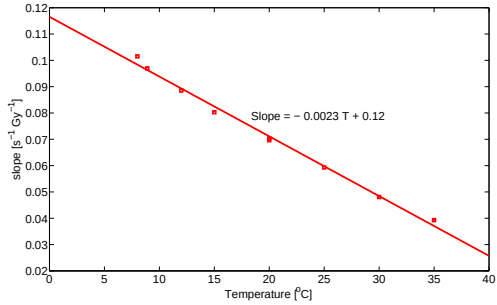

(b)

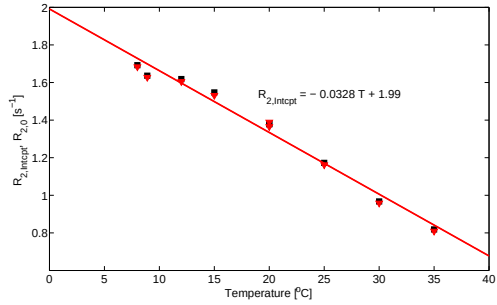

(c)

Figure 7. Dose-R_2 response curves, recorded at different temperatures (in °C) during MR image acquisition (a). The slope (b) and intercept (c) are plotted as function of temperature. A linear fit is shown from which the rate of change of the slope and intercept as function of temperature can be deduced. In (c) the black squares are the $R_{2,intcpt}$ and the red triangles are $R_{2,0}$.

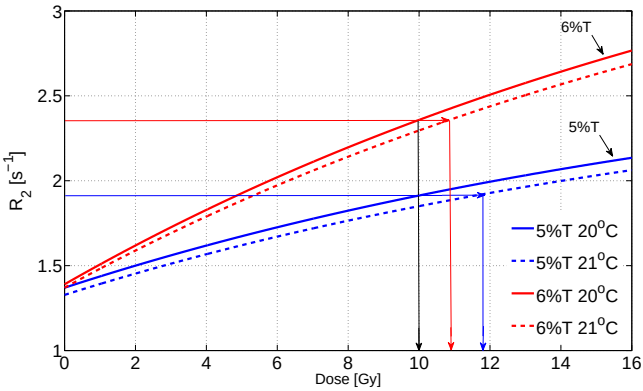

(a)

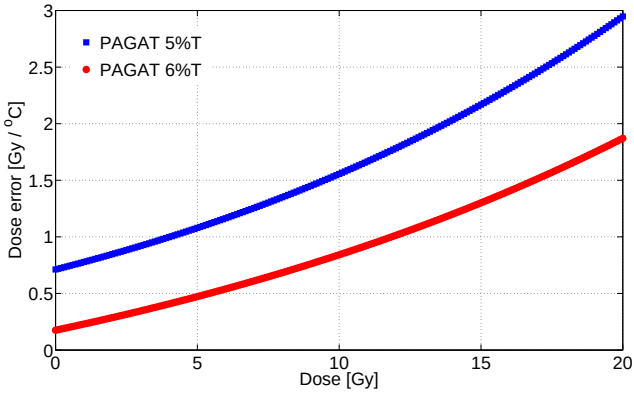

(b)

Figure 8. Simulation of the effect of temperature on the dose response curve for a 5%T PAGAT gel and a 6%T PAGAT gel (De Deene *et al* 2006) in a. The arrows suggest the dose deviation resulting from a temperature difference of 1°C at 20°C. In b the dose error induced by a temperature difference derived from equation 6 is plotted as function of dose for the 5%T PAGAT and 6%T PAGAT.

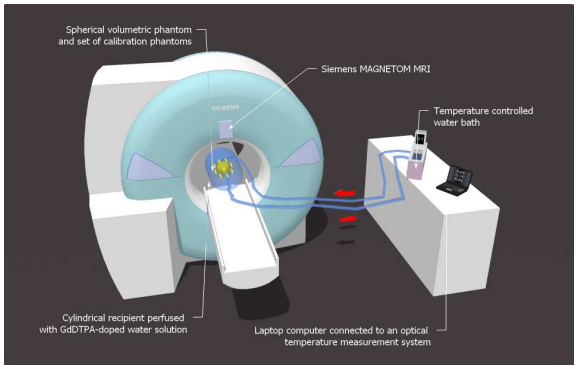

(a)

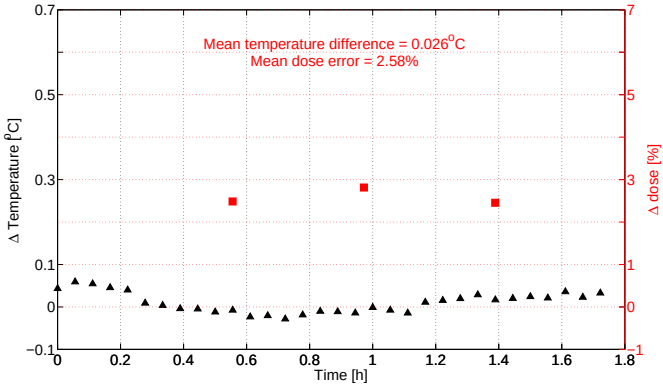

(b)

Figure 9. A schematic representation of a 3D polymer gel dosimetry experiment of a spherical volumetric phantom and calibration phantoms under temperature controlled conditions (a). The phantoms were placed inside a cylindrical recipient perfused with GdDTPA-doped water solution of which the temperature was controlled by a water bath and an optical temperature measurement system. The dose deviation at the centre of a spherical phantom calibrated with small volume calibration phantoms is shown in b. The temperature difference between calibration phantoms and the centre of the spherical phantom (left y-axis) is plotted against the percentage dose deviation relative to the ion chamber reference dose (right y-axis).

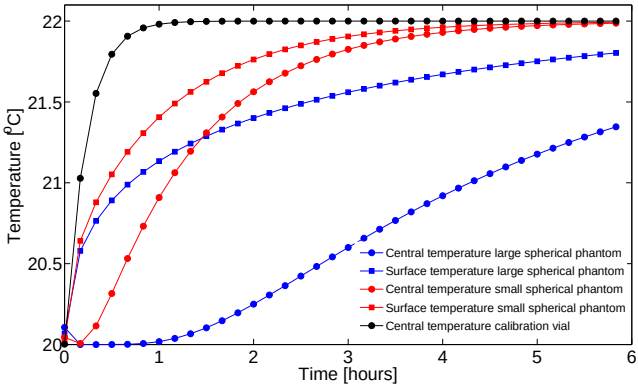

(a)

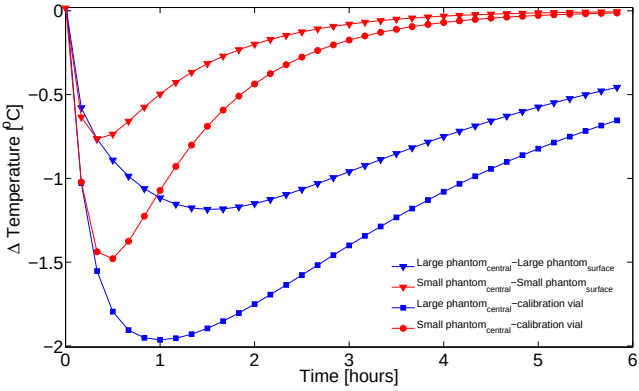

(b)

Figure 10. Temperature distribution as a function of time is simulated in several phantoms (a). A comparison is made between the central temperature and surface temperature of a small spherical phantom (0.25 l) and a large spherical phantom (4.5 l) and compared to the temperature of a calibration phantom all exposed to a sudden temperature increase of 2°C. In b the temperature difference is plotted between the central temperature and surface temperature of the different phantoms. Also the temperature difference between large phantoms and the calibration phantom is displayed.

4.2. B_0-field homogeneity

The B_0-field maps were acquired for a box-shaped, spherical and head-and-neck phantom with the Siemens Avanto, Symphony and Trio scanners respectively. In the box-shaped phantom, no significant variations in R_2 were found. R_2 variations in the spherical phantom amounted to 0.024 s^{-1} resulting from B_0 variations in the order of 5 ppm. This is correlated with a dose uncertainty of approximately 3.7%. These B_0 variations are caused by the PMMA holder on which the phantom was positioned during scanning. The magnetic susceptibility (χ_m) of PMMA is close to that of water (Leach *et al* 1995). Susceptibility effects at PMMA-water boundaries are negligible and thus placing the spherical phantom in a water container would significantly reduce the B_0-field inhomogeneities inside the phantom. Without the use of a water container, careful phantom construction is important to minimize sharp boundaries between air and PMMA to avoid susceptibility artefacts.

R_2 variations in the head-and-neck phantom amounted to 0.028 s^{-1} resulting from local B_0 variations in the order of 5 ppm. These R_2 variations result in dose deviations in the order of 4.3% and occur at the outer Barex^{TM}-air boundaries of the anthropomorphic gel phantom near sharp transitions of air and phantom wall. Because the use of anthropomorphically shaped phantoms is one of the big advantages of polymer gel dosimetry, compensation of these susceptibility artefacts can not always be accomplished by shaping the phantom to avoid sharp edges. These susceptibility artefacts can however be easily minimized by placing the whole gel phantom in a water container. Decreasing the T_1 and T_2 values of the water to within 40 ms by use of a paramagnetic contrast agent (*e.g.* GdDTPA or $CuSO_4$) is recommended to minimize motion artefacts and to keep the field-of-view and thus the imaging time within reasonable limits.

B_0 inhomogeneities inside gel phantoms up to 5 ppm are expected to result in pixel shift artefacts. Theoretically, this B_0 inhomogeneity results in a frequency shift in the order of 319.3 Hz and 638.6 Hz for 1.5 T and 3 T respectively. In polymer gel dosimetry, the receiver bandwidth per pixel (rBW) is chosen as low as possible in order to maximise the signal-to-noise-ratio (SNR). A typical rBW value of 130 Hz per pixel results in approximately 2.5 and 5 pixels shift respectively. By increasing the bandwidth to 260 Hz per pixel these shifts are reduced to 1.25 and 2.5 pixels for 1.5 T and 3 T respectively at the cost of a reduction in SNR by a factor of $\sqrt{2}$. The loss in SNR as a result of an increase in rBW can be compensated by increasing the number of acquisitions at the cost of total measurement time.

4.3. B_1-field homogeneity

The effect of an inhomogeneous B_1 field on the dose maps is quantified using the same gel phantoms (box-shaped, spherical and head-and-neck) and at the same field strengths. At 1.5 T, no significant B_1 effects were found in the smaller spherical and box-shaped phantoms. However, in the larger head-and-neck phantom significant variations in the R_2 maps in the order of 10% near the upper and lower edges of the phantom were

correlated to inhomogeneous flip angles originating from the coil geometry. These effects would result in a dose deviation of approximately 25%. The FA-R_2 relation is approximated by a third-order polynomial, which allows easy correction of the R_2 image. It should be noted that using a FA map to correct the R_2-maps may add additional noise to the measured dose distribution. As such, low signal-to-noise-ratio in FA maps will result in noisy (less precise) dose maps. Therefore, FA maps were filtered from Gaussian noise by applying a Wiener filter (Lim 1990). This is justified by the fact that B_1-fields in general do not contain high-frequency spatial components. After correction of the R_2 map using the FA-R_2 relation, the dose deviations were suppressed to within 2.4%. Similar results were previously reported in Vergote *et al* 2004a.

At 3 T, again no significant B_1 effects were found in the smaller spherical and box-shaped phantoms. In the head-and-neck phantom, a FA-related dose deviation of approximately 50% is observed. Performing corrections based on the measured FA-R_2 relation were not sufficient because inhomogeneities still result in dose deviations in the order of 25%. These remaining R_2 inhomogeneities originate from close to zero FA values near the edges of the phantom (figure 4b and 4d). In these regions no clear FA-R_2 correlation could be extracted.

These FA inhomogeneities originate from the fact that the effective wavelength of the B_1-field at 3 T is comparable to the dimension of the human body. This gives B_1 standing wave effects and consequently the B_1-field homogeneity can be strongly degraded (Alecci *et al* 2001, Dietrich *et al* 2008). The effective B_1 wavelength depends on the dielectric properties of the phantom (electrical conductivity and relative permittivity). The addition of NaCl will strongly influence the electrical conductivity of the medium as shown in table 3. It was shown experimentally that 1% NaCl in a gel reduced the maximum dose deviation down to 25% before post-processing correction as shown in figure 4 which was further reduced to 2.4% after correction for the coil geometry. In the corresponding FA maps a decrease in FA amplitude is present towards the centre of the phantom (figure 4f and 4h). This effect can be explained from the fact that a higher electrical conductivity results in an electrical field component which is responsible for a decrease in FA towards the centre of the phantom.

The influence of dielectric properties of the gel on the B_1-field homogeneity are illustrated by computational modelling. An increase in B_1 inhomogeneity as a function of phantom size is demonstrated for gel phantoms with the same electrical conductivity. Also, these effects become more pronounced at higher field strengths. Scanning of realistically sized low conducting gel dosimeters at 3 T will result in large dose inaccuracies (up to 50%) as illustrated by measurements and calculations which are difficult to be compensated by post-processing (still 25% dose deviation). Increasing the conductivity of the gel by adding NaCl, however, reduces the B_1 inhomogeneity after which the post-processing is successful in reducing the remaining inhomogeneities to an acceptable level for clinical 3D radiation dosimetry. It is beyond the scope of this study to investigate the influence of NaCl on the radio-physical properties of the polymer gel dosimeter.

B_1-field inhomogeneities can originate from both the coil geometry and the dielectric properties of the phantom. In this study, no significant effects of the coil geometry on B_1 inhomogeneity were measured. However, it should be noted that scans of the large head-and-neck phantom were acquired in a body coil for which the distance between coil elements and phantom is relatively large. Therefore, in this study, the B_1 field homogeneity was mainly determined by the dielectric properties of the gel phantom.

In summary, the results on B_0 and B_1 inhomogeneities illustrate the importance of acquiring an R_2 data set of an unirradiated blank polymer gel phantom before the actual dosimetry experiment. Any inhomogeneities in B_0 or B_1 affecting R_2 can be adequately accounted for by acquiring B_0 and B_1-field maps. Standardisation of all imaging protocols using dedicated phantoms of which all properties have been thoroughly investigated is highly recommended.

4.4. Temperature drift during MR scanning

The maximum temperature variation in our MR scanner room between the bore and the scanner room amounts to +2.4°C. Although the magnitude of the temperature difference varied between repeated experiments (between +1°C and +2.4°C), the temperature recorded in the scanner bore was always *higher* than in the surrounding scanner room. This trend in temperature difference between the scanner bore and scanner room probably depends on the ventilation of the scanner bore and intensity of scanner usage of that day. The maximum temperature range in the scanner room was found to be within 1.1°C over a course of seven days. We assume that these recorded temperature fluctuations are typical for intensively used clinical MRI scanners.

The temperature sensitivity of the dose-R_2 response was determined and a dose deviation of up to 15.6% per °C difference was deduced.

From the intra-batch and inter-batch experiment discussed in Vandecasteele and De Deene 2013a, absolute mean dose deviations of up to 13.7% were measured relative to the ion chamber reference dose. Repetitive measurements on different days revealed that these dose deviations were not reproducible in amplitude (ranging between 2.7% and 13.7%) but they were reproducible in sign. In all experiments, the dose in the 3D gel measurements was overestimated. This study shows that the dose overestimation is mainly attributed to calibration of a volumetric phantom with calibration phantoms that are at a higher temperature as compared to the volumetric phantom. Based on the similarity between the measured dose deviations in Vandecasteele and De Deene 2013a and temperature measurements in this study, a reproducibility experiment was repeated under temperature controlled conditions. In this experiment was shown that the dose deviation at thermal equilibrium between calibration phantoms and volumetric phantom was limited to 2.58% compared to the ion chamber reference dose. From this study it is concluded that the main source of dose inaccuracies in polymer gel dosimetry when calibrating with small calibration phantoms is related to temperature differences between volumetric phantoms and small calibration phantoms during scanning. It is

shown that absolute 3D radiation dosimetry by use of external calibration phantoms is possible to within an accuracy of 2.58% in dose when an active temperature stabilisation to within 0.2°C is performed.

Computational simulations of the effect of temperature variations on the dose deviation suggest that a temperature discrepancy in the order of 1°C between calibration and experimental phantoms results in a dosimetric uncertainty in the order of 15% at a dose of 10 Gy with a 5% total monomer concentration (T) gel (figure 8). This temperature dependency seems to be proportional to the dose: by doubling the dose, the dose deviation doubles. However, the maximum dose given to a PAGAT gel dosimeter should be limited to approximately 15 Gy to preserve spatial dose-integrity that originates from diffusing monomers (De Deene *et al* 2002, Vergote *et al* 2004b). Using a higher concentration of monomers (*e.g.* 6%T in De Deene *et al* 2006) results in a 13% higher dose sensitivity compared to the 5%T, but the temperature dependence still remains significant. A temperature discrepancy of 1°C is still correlated to a dose deviation of approximately 9%. It is concluded that a temperature stabilisation technique is needed to compensate for temperature variations in the order of 2°C that frequently occur in a clinical MR scanner. In this work a lower concentration of 5%T was chosen to avoid incompletely dissolved monomers.

By computational modelling, a sudden temperature increase of 2°C was simulated in different sized gel phantoms caused by moving them from their storage location in the MRI scanner room to the scanner bore. After one hour, a temperature difference of approximately 1.1°C between the centre and the surface of a large phantom (figure 10b) is calculated. This temperature difference results in a dose deviation of 16%. Even after six hours, a temperature difference of 0.5°C is still present corresponding to a dose deviation of approximately 8%. At that same moment, the temperature difference between the large volumetric phantom and calibration phantoms still amounts to 0.6°C (dose deviation of 9%).
A small spherical phantom takes almost one and a half hours to homogenise to within 5% dose uncertainty while at that time a temperature offset of 0.7°C is still present between the phantom and the calibration phantoms resulting in a dose overestimation of approximately 10% over the entire volume. These results clearly show that a passive temperature homogenisation by keeping calibration and experimental phantoms together at all time so that all phantoms reach thermal equilibrium before scanning is not feasible due to the large amounts of time needed to reach thermal equilibrium.

Temperature experiments and computational modelling demonstrated the extreme sensitivity of the calibration procedure using small calibration phantoms to these temperature fluctuations. In a temperature controlled environment dose uncertainty was minimised to within 2.58%. It is therefore suggested that MR scanning of polymer gel dosimeters should be performed in a water container with an active temperature stabilisation to within 0.2°C. An additional advantage of this approach is that B_0 and B_1 artefacts can also be minimised.

5. Conclusions

In this study, the relative contributions of error sources during scanning of polymer gel dosimeters are quantified. The static magnetic B_0-field inside three different gel phantoms is assessed: a spherical, a box-shaped and an anthropomorphic head-and-neck phantom for magnetic field strengths of 1.5 T and 3 T. The maximum B_0-field variations amounted to approximately 5 ppm which results in a dose deviation of approximately 4.3% located near the phantom edges. Additionally, this causes a pixel shift of approximately 2.5 to 5 pixels at 1.5 T and 3 T respectively. Scanning inside a water container can reduce these effects significantly.

The effect of an inhomogeneous radio-frequency (B_1) field on the dose maps is quantified using the same gel phantoms at the same field strengths. It is shown that B_1-field inhomogeneities originate from both the coil geometry and the dielectric properties of the phantom. At 1.5 T, significant variations in the R_2 maps in the order of 10% near the upper and lower edges of the large head-and-neck phantom were correlated to an inhomogeneous flip angle distribution resulting in a dose deviation of approximately 25%. Applying a post-processing correction of the R_2 maps on the basis of the FA-R_2 correlation enabled suppression of the dose deviations to within 2.4%. In the smaller spherical and box-shaped phantoms, no significant B_1 effects were found. At 3 T, a dose deviation of approximately 50% is measured in the realistically sized head-and-neck phantom. These artefacts were attributed to standing waves that are related to the low electrical conductivity of polymer gel dosimeters which could be solved by adding 1% NaCl to the gel.

The sensitivity of the dose-R_2 response of the polymer gel dosimeter to temperature fluctuations during MR imaging was confirmed. Temperature variations in the MR scanner room of 1°C were measured and were estimated to contribute to a dose deviation of 15%. Temperature experiments and computational modelling demonstrated the extreme sensitivity of the calibration procedure using small calibration phantoms to these temperature fluctuations. This study reveals that the main source of dose inaccuracies in polymer gel dosimetry with small calibration phantoms is related to temperature differences between volumetric phantoms and small calibration phantoms during scanning. Moreover, it is shown that absolute 3D radiation dosimetry by use of external calibration phantoms is possible with a dose uncertainty within 2.58% when an active temperature stabilisation to within 0.2°C is performed. For large polymer gel dosimeters compensation of the B_0-field and B_1-field inhomogeneity may be required. The need for B_0 or B_1 correction can be assessed by scanning a 'blank' gel phantom.

Acknowledgments

This research is supported by the Institute for the Promotion of Innovation though Science and Technology in Flanders (IWT -Vlaanderen). The authors would like to thank Bart Truyens for constructing dedicated equipment that was indispensable in the

experimental set-up.

References

Alecci M, Collins C M, Smith M B, Jezzard P 2001 Radio frequency magnetic field mapping of a 3 T birdcage coil: Experimental and theoretical dependence on sample properties *Magnet reson med* **46** 379-385

Bayreder C, Georg D, Moser E and Berg A 2006 Basic investigations on the performance of a normoxic polymer gel with tetrakis-hydroxy-methyl-phosphonium chloride as an oxygen scavenger: reproducibility, accuracy, stability, and dose rate dependence *Med. Phys.* **33** 2506-18

Berg A, Ertl A and Moser E 2001 High-resolution polymer gel dosimetry by parameter selective MR-micro imaging on a whole body scanner at 3 T *Med. Phys.* **28** 833-43

Berg A, Pernkopf M, Fellner C, Schmidt W, Moser E 2004 High resolution MR based polymer dosimetry versus film densitometry: a systematic study based on the modulation transfer function approach *Phys. Med. Biol.* **49** 4087-108

Carslaw H S and Jaeger J C 1959 Conduction of Heat in Solids, 2nd edn. Oxford: Clarendon Press.

Clerjona S, Daudina JD, Dameza JL 2003 Water activity and dielectricproperties of gels in the frequency range 200 MHz-6 GHz *Food Chem* **82** 87-97

De Deene Y and De Wagter C 1999 Gel dosimetry in conformal radiotherapy: Validation, optimization and MR artifacts *Proc. 1st International Workshop on Radiation Therapy Gel Dosimetry (Lexington, Kentucky)* ed L J Schreiner pp 75-89

De Deene Y and De Wagter C 2001 Artifacts in multi-echo T2 imaging for high-precision gel dosimetry: III. Effects of temperature drift during scanning *Phys. Med. Biol.* **46** 2697-2711

De Deene Y, De Wagter C and De Neve W 2000b Artifacts in multi-echo T2 imaging for high-precision gel dosimetry: II. Analysis of B1 field inhomogeneity *Phys. Med. Biol.* **45** 1825-39

De Deene Y, De Wagter C, De Neve W and Achten E 2000a Artifacts in multi-echo T2 imaging for high-precision gel dosimetry: I. Analysis and compensation of eddy currents *Phys. Med. Biol.* **45** 1807-23

De Deene Y, Reynaerdt N and De Wagter C 2001 On the accuracy of monomer/polymer gel dosimetry in the proximity of a high-dose-rate 192-Ir source *Phys. Med. Biol.* **46** 2801-25

De Deene Y, Van de Walle R, De Wagter C and Achten E 1998 Mathematical analysis and experimental investigation of noise in quantitative magnetic resonance imaging applied in polymer gel dosimetry *Signal Process.* **70** 85-101

De Deene Y, Venning A, Hurley C, Healy B J and Baldock C 2002 Dose-response stability ans integrity of the dose distribution of various polymer gel dosimeters *Phys. Med. Biol.* **47** 2459-70

De Deene Y, Vergote K, Claeys C and De Wagter 2006 The fundamental radiation properties of normoxic polymer gel dosimeters: a comparison between a methacrylic acid based gel and acrylamide based gels *Phys. Med. Biol.* **51** 653-73

Deman P, Vautrin M, Stupar V, Barbier E L, Elleaume H, Esteve F and Adam J F 2011 Monochromatic minibeam radiotherapy: theoretical and experimental dosimetry for preclinical treatment plans *Phys. Med. Biol.* **56** 4465-80

Dietrich O, Reiser M F, Schoenberg S O 2008 Artifacts in 3-Tesla MRI: Physical background and reduction strategies *Eur J Radiol* **65** 29-35

Ertl A, Berg A, Zehetmayer M and Frigo P 2000 High-resolution dose profile studies based on MR imaging with polymer BANG(TM) gels in stereotactic radiation techniques *Magn. Reson. Imaging* **18** 343-9

Goldstein R M, Zebken H A, and Werner C L 1988 Satellite radar interferometry:Two-dimensional phase unwrapping *Radio Sci.* **23** 713-720

Gopishankar N, Watanabe Y and Subbiah V 2011 MRI-based polymer gel dosimetry for validating plans with multiple matrices in Gamma Knife stereotactic radiosurgery *J. Appl. Clin. Med. Phys.* **12** 133-145

Henkelman R M, Huang X, Xiang Q-S, Stanisz G J, Swanson S D and Bronskill M J 1993 Quantitative interpretation of magnetization transfer *Magn. Reson. Med.* **29** 759-66

Heufelder J, Stiefel S, Pfaender M, Ludemann L, Grebe G and Heese J 2003 Use of BANG polymer gel for dose measurements in a 68 MeV proton beam *Med. Phys.* **30** 1235-40

Insko EK, Bolinger L. 1992 B1 mapping *Proceedings of the 11th Annual Meeting of SMRM, Berlin, Germany* p. 4302.

Jin J 1988 *Electromagnetic analysis and design in magnetic resonance imaging* (Boca Raton, Fl: CRC Press) p 213

Koenig S H and Brown III R D 1990 *Field-cycling relaxometry of protein solutions and tissue: implications for MRI* (*Prog. NMR Spectr. vol 22*) (Oxford: Pergamon) pp 487-567

Leach MO, Collins DJ, Keevil S, Rowland I, Smith MA, Henriksen O, Bove WM and Podo F 1995 Quality assessment in in vivo NMR spectroscopy: III. Clinical test objects: design, construction, and solutions. *Magn. Reson. Imaging* **13** 131-7

Lepage M, Whittaker A K, Rintoul L, Back S and Baldock C 2001 The relationship between radiation-induced chemical processes and transverse relaxation times in polymer gel dosimeters *Phys. Med. Biol.* **46** 1061-74

Lim J S 1990 Two-Dimensional Signal and Image Processing Englewood Cliffs, NJ, Prentice Hall, p. 548

Park H W, Ro Y M and Chot Z H 1988 Measurement of the magnetic susceptibility effect in high-field NMR imaging *Phys. Med. Biol.* **33** 339-349

Seimenis I, Moutsatsos A, Petrokokkinos L, Kantemiris I, Benekos O, Efstathopoulos E, Papagiannis P, Spevacek V, Semnicka J and Dvorak P. 2009 The use of high field strength and parallel imaging techniques for MRI-based gel dosimetry in stereotactic radiosurgery. *J. Instr.* **4** P07004

Tofts P S 1994 Standing Waves in uniform water phantoms *J. Magn. Res. Ser. B* **104** 143-7

Vandecasteele and De Deene 2013a On the validity of 3D polymer gel dosimetry: I. Reproducibility study *Phys. Med. Biol.* **58** 19-42

Vandecasteele and De Deene 2013b On the validity of 3D polymer gel dosimetry: II. Physico-chemical effects *Phys. Med. Biol.* **58** 43-61

Venkatesh MS and Raghavan GSV 2005 An overview of dielectric properties measuring techniques *Can. Biosys. Eng.* **47** 7.15-7.30

Vergote K, De Deene Y, Duthoy W, De Gersem W, De Neve W, Achten E and De Wagter C 2004a Validation and application of polymer gel dosimetry for the dose verification of an intensity-modulated arc therapy (IMAT) treatment *Phys. Med. Biol.* **49** 287-305

Vergote K, De Deene Y, Vanden Bussche E and De Wagter C, 2004b On the relation between the spatial dose integrity and the temporal instability of polymer gel dosimeters *Phys. Med. Biol.* **49** 4507-22

Wong C J, Ackerly T, He C, Patterson W, Powell C E, Qiao G, Solomon D H, Meder R and Geso M 2009 Small field size dose-profile measurements using gel dosimeters, gafchromic films and micro-thermoluminescent dosimeters *Radiat. Meas.* **44** 249-56

Xuanfeng Ding, Olsen J, Best R, Bennett M, McGowin I, Dorand J, Link K and Bourland JD 2010 High resolution polymer gel dosimetry for small beam irradiation using a 7T micro-MRI scanner *J. Phys.: Conf. Ser.* **250** 012094

5

Radio-physical properties of micelle leucodye 3D integrating gel dosimeters

---

Jan Vandecasteele, Sara Ghysel, Steven Baete and Yves De Deene

Manuscript on which this chapter is based:
Physics in Medicine and Biology **56** (2011) 627-651

Radio-physical properties of micelle leucodye 3D integrating gel dosimeters

J Vandecasteele[1], S Ghysel[1], SH Baete[1] and Y De Deene[1,2]

[1] Department of Radiation Oncology and Experimental Cancer Research, Ghent University Hospital, De Pintelaan 185, 9000 Ghent, Belgium.
[2] Department of Nuclear Medicine and Radiobiology, University of Sherbrooke, 12^{th} Avenue North 3001, Sherbrooke QC, Canada.

E-mail: Jan.Vandecasteele@UGent.be

Received 9 June 2010, in final form 2 December 2010
Published 10 Januari 2011
Online at stacks.iop.org/PMB/56/627

Abstract. Recently, novel radiochromic leucodye micelle hydrogel dosimeters were introduced in the literature. In these studies, gel measured electron depth dose profiles were compared with ion chamber depth dose data, from which it was concluded that leucocrystal violet type dosimeters were independent of dose rate. Similar conclusions were drawn for leucomalachite green type dosimeters, only after pre-irradiating the samples to a homogeneous radiation dose. However, in our extensive study of radio-physical properties of leucocrystal violet and leucomalachite green type dosimeters, a significant dose rate dependency was found. For a dose rate variation between $50\,cGy\,min^{-1}$ and $400\,cGy\,min^{-1}$, a maximum difference of 75 % was found in optical dose sensitivity for the leucomalachite green type dosimeter. Furthermore, the measured optical dose sensitivity of the leucomalachite green type dosimeter was 4 times lower than the value previously reported in the literature. For the leucocrystal violet type dosimeter, a maximum difference in optical dose sensitivity of 55 % was found between $50\,cGy\,min^{-1}$ and $400\,cGy\,min^{-1}$. A modified composition of leucomalachite green type dosimeter is proposed. This dosimeter is composed of gelatin, sodium dodecyl sulphate, chloroform, trichloroacetic acid and leucomalachite green. The optical dose sensitivity amounted to $4.375 \cdot 10^{-5} cm^{-1} cGy^{-1}$ (dose rate $400\,cGy\,min^{-1}$). No energy dependence for photon energies between 6 MV and 18 MV was found. No temperature dependence during readout was found notwithstanding a temperature dependence during irradiation of 1.90 cGy per °C increase on a total dose of 100 cGy. The novel gel dosimeter formulation exhibits an improved spatial stability ($2.45 \times 10^{-7} cm^2 s^{-1}$ ($= 0.088\,mm^2 h^{-1}$)) and good water/soft tissue equivalence. Nevertheless, the novel formulation was also found to have a significant, albeit reduced, dose rate dependence, as a maximum difference of 33% was found in optical dose sensitivity when the dose rate varied between $50\,cGy\,min^{-1}$ and $400\,cGy\,min^{-1}$. By pre-irradiating the novel leucomalachite green type dosimeter to 500 cGy, the apparent difference in dose response between $200\,cGy\,min^{-1}$ and $400\,cGy\,min^{-1}$ was eliminated, similar to earlier findings. However, a dose response difference of 38 % between $50\,cGy\,min^{-1}$ and $200\,cGy\,min^{-1}$ was still measured. On the basis of these experimental results it is concluded that the leucodye micelle gel

dosimeter is not yet optimal for dose verifications of high precision radiation therapy treatments. This study however, indicates that the dose rate dependence has a potential for improvement. Future research is necessary to further minimize the dose rate dependency through extensive chemical analysis and optimization of the gel formulation. Some insights in the physicochemical mechanisms were obtained and are discussed in this paper.

1. Introduction

The goal of modern radiation therapy is to eradicate cancerous cells by delivering a cytotoxic dose of radiation while minimizing the effect on healthy tissue. Various technologies have been developed to achieve this goal (such as intensity modulated radiation therapy (IMRT), Intensity Modulated Arc Therapy (IMAT) and stereotactic radiosurgery) and are now widely available. These conformal radiation delivery techniques require a higher degree of confidence in software calculations and equipment as compared to conventional radiation therapy. Radiation physicists and radiation oncologists urge for more sophisticated quality assurance tools to monitor the complex treatment chain of patients and to verify the delivered radiation dose distribution in three dimensions (3D).

3D integrating radiation dosimetry is capable of monitoring the whole treatment chain (patient scanning, treatment planning, treatment delivery) and obtaining a quantitative radiation dose distribution in 3D (De Deene *et al* 2000, Duthoy *et al* 2003, Vergote *et al* 2004, Baldock *et al* 2010). An important obstacle however for the implementation of 3D integrating radiation dosimetry in any radiotherapy site involves the readout technique. The most frequently used readout technique for 3D dosimeters in the past was magnetic resonance imaging (MRI) (De Deene *et al* 2000, Duthoy *et al* 2003, Vergote *et al* 2004). For many clinical sites however, there is limited accessibility to MR scanners and the required know-how on quantitative MRI is often lacking. In order to overcome this impediment, alternative scanning techniques have been investigated of which the most promising is optical computerized tomography (optical CT) (Doran 2009). The introduction of optical CT scanning is expected to increase the accessibility of this 3D dose verification technique in radiation therapy centres. Concomitantly, the introduction of optical CT scanners stimulated the development of 3D dosimeters that remain transparent after irradiation and therefore suffer less from light scatter as compared to polymer gel systems (Oldham 2006).

Radiochromic dosimeters change colour upon irradiation. The radiochromic dosimeter investigated in this study changes colour upon irradiation due to the oxidation of leucodyes by halogen radicals. In commercially available products like Presage^{TM}, the leucodyes and halogens are dissolved in a polyurethane matrix (Adamovics and Maryanski 2006). In recently published papers by Jordan and Avvakumov (2009) and Babic *et al* (2009) another approach was taken: in their proposed dosimeter the colour dye and halogen are dissolved in a gelatin gel. As the colour dye and halogen

do not readily dissolve in the gelatin hydrogel, the dye and halogen are embedded in micelles. The advantage of these micelle gels in comparison to the polyurethane dosimeters is their tissue equivalence over a wide range of photon energies. In addition, the fabrication procedure of gelatin-based chemical dosimeters is less complicated than of polyurethane-based dosimeters for which dedicate equipment (special containers, pressure vessel) is needed and is therefore more practical to implement in a clinical environment. The absence of an exothermic reaction during fabrication results in a better optical homogeneity (*i.e.* Schliere artefacts are eliminated) (Doran 2008).

Dosimetric quality assurance should meet certain radio-physical specifications to assure a reliable clinical verification (De Deene *et al* 2006). A high spatial resolution in 3D is required to clearly display the high dose gradients that are typical for conformal radiation therapy. Also, the spatial integrity of the 3D dosimeter is very important to accurately record and preserve the dose information between the irradiation and readout of the 3D dosimeter. The complex dose distribution achieved with conformal radiation therapy also corresponds with a non-uniform distribution of dose rate in the 3D dosimeter. To obtain a reliable dose map from the 3D dosimeter, the dose reading of optical density should therefore be independent of the dose rate. This is not evident as reaction rates of active components in these dosimeters are strongly influenced by diffusion controlled processes.

Jordan and Avvakumov (2009) and Babic *et al* (2009) described the radio-physical properties of micelle gel dosimeters based on leucomalachite green and leucocrystal violet respectively. Jordan and Avvakumov found that an electron depth dose curve measured with a leucomalachite green doped dosimeter showed a 2 mm depth offset in comparison to the ion chamber based measurement. This misalignment was eliminated by pre-irradiating the samples with an uniform dose to shift the measurement in the linear region of the dose response curve. The authors conclude that the gel response was independent of dose rate after pre-irradiating the gel to a homogeneous radiation dose. Babic *et al* also conclude that the leucocrystal violet micelle gel dosimeter is a potential 3D dosimeter that has no dose rate dependence and good spatial stability. The authors conclusion on dose rate dependence was also based on a comparison of the shape of a gel measured dose depth curve for electron beams and a dose depth curve acquired with an ion chamber. In our study, the radio-physical properties of the leucodye micelle gel were investigated independently with photon beams and a significant dose rate dependence was found. The radio-physical properties of different kinds of leucodye gel dosimeters were investigated, including the gel dosimeter proposed by Jordan and Avvakumov (2009). A modified leucodye gel dosimeter is proposed that has a similar dose sensitivity and improved spatial integrity and dose rate dependence as compared to the composition proposed by Jordan and Avvakumov (2009). Some insights into the chemical basis of the dose rate dependence are provided.

Table 1. Overview of various dosimeter systems investigated in this study. LMD1 corresponds with the composition described by Jordan and Avvakumov (2009). The newly proposed composition is referred to as LMD2. The optimized composition in terms of optical dose sensitivity is indicated in bold. LMD3 corresponds with a dosimeter doped with LCV. LCS refers to a solution of LMG in chloroform.

	LMD1	LMD2	LMD3	LCS
LMG [mM]	0.3	**0.37**, 1, 10, 45	-	0.4, 1, 10, 45
LCV [mM]	-	-	1	-
$CHCl_3$ [mM]	-	0, 40, **80**, 100	-	100%
CCl_4 [mM]	-	0, 20	-	-
CCl_3COOH [mM]	16	0, **5**	25	-
H_2SO_4	-	**0**, match pH CCl_3COOH	-	-
SDS [mM]	-	0, 20, **50**, 100	50	-
Triton X-100 [mM]	7	**0**, 7	-	-
Gelatin [% (w/w)]	4	0, 4, **6**, 8,10	4	-

2. Materials and methods

2.1. Gel fabrication

The radiation sensitive leucodye micelle gel dosimeter proposed by Jordan and Avvakumov (2009) (further referred to as LMD1) consists of five key components: a gelling agent (gelatin), a leucodye (leucomalachite green (LMG)), a radiation sensitizer (trichloroacetic acid (CCl_3COOH)) and a surfactant (Triton X-100) all dissolved in deionized water (LMD1 in table 1). The radio-physical properties of LMD1 are compared against the radiation dosimeter proposed in this paper (further referred to as LMD2). The chemical concentrations of the various components of LMD2 were optimized in terms of sensitivity (LMD2 in table 1).

To further investigate dose rate effects on other leucodyes, a gel dosimeter doped with leucocrystal violet (LCV) was fabricated. The composition was based on the dosimeter proposed by Babic *et al* 2009. The composition used in this paper was identical, only the surfactant was changed to sodium dodecyl sulphate (SDS) in contrast to Triton X-100 used by Babic *et al* (2009). This dosimeter will be referred to as LMD3.

In order to isolate the dose rate dependence effect caused by the reaction kinetics of the leucodye from additional effects by other chemicals, solutions of different concentrations of LMG in chloroform ($CHCL_3$) were prepared (LCS in table 1).

The final composition of LMD2 gel used in further radio-physical experiments consist of gelatin, $CHCl_3$, SDS, CCl_3COOH, LMG and deionized water. Gelatin is dissolved in 37 % (w/w) of total water volume at room temperature and is left to swell for 10 minutes. The remaining 55 % of total water volume is used to dissolve SDS and CCl_3COOH. $CHCl_3$ is used to dissolve LMG after which this solution is carefully

added to the water-SDS-CCl_3COOH-solution. The solution is covered to minimize the evaporation of $CHCl_3$ and stirred for 5 minutes. Additionally, the solution is wrapped in aluminium foil to minimize any photochemical induced reaction. After cooling the gelatin-water solution to approximately 35°C, the two solutions are added together and stirred for 20 minutes in a dark room at 35°C. Finally the gel is poured into small cuvettes ($1 \times 1 \times 4.5\,cm^3$, PMMA, Sigma Aldrich) unless stated otherwise. These cuvettes are further referred to as spectroscopic samples.

Besides cuvettes, a small PMMA phantom (dimensions $1 \times 1 \times 8\,cm^3$) and a large PMMA phantom (dimensions $1 \times 1 \times 40\,cm^3$) were filled with LMD2. After filling, all phantoms were placed in a refrigerator over night at 4°C. The following radio-physical properties were investigated for LMD2 type dosimeters: optical dose sensitivity, dose rate dependence, energy dependence, temperature dependence during irradiation and readout, spatial integrity and tissue equivalence.

The LMD1 dosimeter was fabricated according to the fabrication procedure described in the publication by Jordan and Avvakumov (2009) and poured into small cuvettes. The following radio-physical properties were investigated for LMD1 type dosimeters: optical dose sensitivity, dose rate dependence, energy dependence, temperature dependence during irradiation and tissue equivalence.

The LMD3 dosimeter was fabricated by dissolving gelatin in 37 % water at room temperature and is left to swell for 10 minutes. The remaining 55 % of total water volume is used to dissolve SDS, CCl_3COOH and LCV. Triton X-100 failed to completely dissolve the leucodye (LCV) in the gel without precipitation in the concentration as proposed by Babic *et al* (2009). Therefore, SDS was used as a surfactant in the LMD3 type dosimeter. The two solutions (water-gelatin and surfactant-leucodye solution) are added together at approximately 35°C, and stirred for 20 minutes in a dark room. Finally, the gel is poured into small cuvettes. The following radio-physical properties were investigated for LMD3 type dosimeters: optical dose sensitivity and dose rate dependence.

2.2. Optimization of the composition of LMD2 in terms of dose sensitivity

The composition of the LMD2 type dosimeter was optimized in terms of optical dose sensitivity. The optimization took into account the leucodye, initiator, surfactant and gelatin concentrations (table 1) as well as the transparency of the resulting system.

2.2.1. Initiator. The initiators used in this study are halogenated hydrocarbons. They can be subdivided into two groups: the neutral halocarbons (chloroform ($CHCl_3$) (Sigma Aldrich) and carbon tetrachloride (CCl_4) (Sigma Aldrich)) and the acidic halocarbons (trichloroacetic acid (CCl_3COOH) (Sigma Aldrich)). The halocarbons enhance the radiation sensitivity by interacting with the incident photons leading to the formation of oxidizing reagents (*e.g.* $OH^\bullet$, H_2O_2 $Cl^\bullet$) which oxidize LMG to its chromatic quinonoid structure MG^+ (Ottolenghi and Stein 1961, Abramson and Firestone 1966, Baxter and Johnston 1968, Rezansoff *et al* 1970, Kosobutskii 2001). However, studies reported

additional effects of the acid HCl as a sensitizer (Mai *et al* 2008). To isolate the effect of the $Cl^{\bullet}$ radicals from effects of pH, H_2SO_4 (Sigma Aldrich) was added in replacement of CCl_3COOH. The dose sensitivity in a liquid environment (no gelatin added) was investigated in both scenarios.

Gels were fabricated using neutral halocarbon $CHCl_3$ in concentrations 0 mM, 40 mM, 80 mM and 100 mM and CCl_4 in concentrations 0 mM and 20 mM in 6 % gelatin, 5 mM CCl_3COOH and 0.37 mM LMG. All chemicals were dissolved in de-ionized water. Aqueous solutions of H_2SO_4 in various concentrations added to solutions doped with SDS [50 mM] and LMG [0.37 mM] were fabricated and poured into small cuvettes. The pH of each batch was measured using a pH electrode (multiline P4, WTW, Weilheim Germany). The experiment was repeated for a similar composition in which H_2SO_4 was replaced with CCl_3COOH in concentration matching the pH of the dosimeter.

2.2.2. Leucodye. LMG was dissolved in $CHCl_3$ in concentrations of 0.37 mM, 1 mM, 10 mM and 45 mM. Additionally, SDS - gelatin gels were prepared using $CHCl_3$ and CCl_3COOH as initiator with LMG in different concentrations (0.37 mM and 1 mM).

2.2.3. Surfactant. To obtain a better understanding in the chemical structure of the leucodye micelle gel dosimeter, the interactions between gelatin and SDS were investigated. The chemical structure is believed to be of great importance for the radiophysical behaviour of the gel dosimeter and as a result also for the radiation properties. Sodium dodecyl sulphate (SDS) is chosen in this work since it is widely used and may be considered as a generic surfactant. SDS binds to gelatin very strongly at a pH below the isoelectric pHi of gelatin at which the gelatin molecule becomes positively charged (Griffiths *et al* 1997). The binding of SDS to gelatin is considered as a beneficial mechanism that limits the diffusion of micelles in the gel. Additionally a positively charged dye molecule will interact very strongly with the oppositely charged surfactant molecules of SDS limiting the diffusion of dye molecules outside the micelles (Bielska 2009). SDS was tested in concentrations 0 mM, 20 mM, 50 mM and 100 mM. The non-ionic surfactant Triton X-100 was tested as alternative for SDS in a concentration of 7 mM as used by Jordan and Avvakumov (2009).

2.2.4. Gelatin. Gelatin used in this study is a biodegradable protein with an average molecular weight of 50-100 kDa. It is derived from acidic decomposed collagen from pig skin (G2500, Sigma Aldrich type A gelatin, 300 bloom). The charge on a gelatin molecule and its associated isoelectric point are primarily determined by the carboxyl, amino, and guanidino groups on the side chains. Gelatin has 78-80 mM of free carboxyl groups per 100 g of protein and an isoelectric point (pHi) of around 8.0. The generally accepted model for the gelatin molecule is a triple helix. The triple helix is stabilized by hydrogen bonds between the N-H groups of the gelatin backbone of one chain and C=O groups of a neighbouring chain. Water acts as an intermediary in inter-chain and intra-chain hydrogen bonding (Wustneck *et al* 1988, Fruhner and Kretzschmar 1989).

Gelatin was chosen in this study because of its superb optical characteristics. Gelatin, in combination with SDS, will form a complex of negatively charged head groups and hydrophobic tails of SDS bound to the positively charged and hydrophobic gelatin maze (Fruhner H and Kretzschmar 1992, Griffith *et al* 1996, Griffith *et al* 1997, Onesippe and Lagerge 2009). The impact of gelatin concentration on the dosimeter optical dose sensitivity was tested in concentrations 0 %, 4 %, 6 %, 8 % and 10 % (w/w).

2.3. Irradiation procedure

All irradiations were performed on a clinical linear accelerator (Elekta SL*i*, Stockholm, Sweden). The spectroscopic samples were irradiated in a cylindrical water container (radius 17 cm, height 27 cm). The influence of the container on the absorbed dose in the gel has already been thoroughly investigated. Studies by Baldock *et al* 1998, Baldock *et al* 1999, Taylor *et al* 2007 and Taylor *et al* 2009a have shown that such cross-talk effects are minimal. The samples were positioned at a water-depth of 5 cm and a source-to-surface-distance (SSD) of 95 cm. For irradiation, a 6 MV photon beam at a dose rate of 400 $cGy\,min^{-1}$ was used with a field size of $10 \times 10\,cm^2$, unless stated otherwise.

2.4. Optical measurement

2.4.1. Spectroscopic measurements. All spectroscopic samples were taken out of the refrigerator about 45 minutes prior to readout and left to equilibrate at room temperature (19°C - 21°C). Subsequently, the spectroscopic samples were placed in a cuvette holder with temperature stabilization (Ocean Optics, Dunedin, USA) and read out by an USB 4000 fiber optic spectrometer (Ocean Optics) using a in-house constructed white led light source. The readout parameters for LMD1 and LMD2 were: 100 ms integration time, 50 averages over 629 nm - 636 nm (maximum absorption peak of LMD1 and LMD2 was located at 635 nm). For LMD3, the maximum absorption peak was located at 602 nm. All LMD3 data however, was averaged over 587 nm - 594 nm to simulated the readout with a yellow light emitting diode. From the spectra of blank spectroscopic samples and irradiated spectroscopic samples an optical density difference (ΔOD) was calculated.

2.4.2. Diffusion measurements. The spatial stability of the LMD2 type dosimeter is verified by measuring profiles through a half irradiated spectroscopic sample using an in-house build optical laser CT scanner (Vandecasteele and De Deene 2009). A spectroscopic sample was half irradiated with a 6 MV photon beam to a total dose of 200 Gy. Attenuation profiles of a half irradiated spectroscopic sample, an unirradiated spectroscopic sample and a homogeneously irradiated spectroscopic sample (200 Gy) were subsequently recorded over a period of approximately 24 h. Every 10 minutes an attenuation profile was recorded by the optical CT scanner using a red laser source (633 nm). The ambient temperature in the room during the measurement was 25°C. The recorded profiles were processed using in-house written Matlab scripts (The Mathworks,

Inc., Natick, USA). The optical density difference profiles (ΔOD(x)) were constructed for each measured attenuation profile (equation 1).

$$\Delta OD(x) = -log_{10}\left(\frac{S_{irr}(x)}{S_{blank}(x)}\right) \tag{1}$$

with $S_{irr}(x)$ the signal intensity in the profile of the half irradiated phantom and $S_{blank}(x,y)$ the pixel intensity in the profile of the non-irradiated phantom. ΔOD profiles at 130 time points were fitted against an algebraic diffusion function derived from equation 2 with starting conditions given in equation 3 and boundary conditions given in equation 4. The solution of equation 2 takes the form of a infinite sum of error functions (equation 5).

$$\frac{\delta C}{\delta t} = D \cdot \frac{\delta^2 C}{\delta^2 x} \tag{2}$$

$$t = 0 : \begin{cases} C = C_{max} & if \; -h < x < 0 \\ C = 0 & if \quad 0 < x < h \end{cases} \tag{3}$$

$$\frac{\delta C}{\delta x} = 0 : \begin{cases} x = \quad h \\ x = -h \end{cases} \tag{4}$$

$$C = \frac{1}{2} \cdot C_0 \cdot \sum_{n=-\infty}^{\infty} \left(erf\left(\frac{h + 2nl + x}{2\sqrt{Dt}}\right) + erf\left(\frac{h - 2nl + x}{2\sqrt{Dt}}\right)\right) \tag{5}$$

with C the concentration related to ΔOD, C_0 the initial concentration, h the half width of the profile, l the total width of the profile, D the diffusion coefficient, t the time increment and x the position along the profile. The infinite sum is approximated by three terms.

2.4.3. Depth dose profiles. Depth dose profiles were measured with the LMD2 type dosimeter for electron beams of 6 MeV at an SSD of 95 cm and field size $10 \times 10\,cm^2$ (using an electron applicator and appropriate cut-out) for dose rates set at $400\,cGy\,min^{-1}$, $200\,cGy\,min^{-1}$ and $50\,cGy\,min^{-1}$ at isocentre. The central axis of the PMMA phantoms was positioned along the beam direction. Jordan and Avvakumov suggested to pre-irradiate LMD1 dosimeters with a dose of 500 cGy in order to compensate for a systematic 2 mm depth offset in electron depth dose curves which was related with a non linear dose response (Jordan and Avvakumov 2009). Similar to the method suggested by Jordan and Avvakumov, a 500 cGy pre-irradiation dose was also delivered using two 6 MV, $30 \times 30\,cm^2$ opposing photon beams to three spectroscopic samples of LMD2 dosimeters. Another three LMD2 dosimeters (small PMMA phantoms, 8 cm length) were not pre-irradiated. Measured depth dose profiles were rescaled to the dose maximum for the PMMA phantom irradiated at $400\,cGy\,min^{-1}$. Ion chamber measurements for a $10 \times 10\,cm^2$ electron field of 6 MeV were electronically available in-house. These ion chamber depth dose profiles were compared with depth dose profiles acquired with the gel dosimeter.

Depth dose profiles were measured with the LMD2 type dosimeter for photon beams of 6 MV at an SSD of 95 cm and field size $10 \times 10\,cm^2$ for a dose rate set at $400\,cGy\,min^{-1}$ at isocentre. The central axis of the large PMMA phantom (40 cm length) was positioned along the beam direction. Measured depth dose profiles were rescaled to dose maximum. Ion chamber measurements are performed with a 0.016 cm^3 pinpoint ion chamber (PTW 31016) and an automated water phantom (PTW). Ion chamber depth dose profiles were compared with depth dose profiles acquired with the gel dosimeter.

All PMMA phantoms were read out with the USB4000 fiber optic spectrometer along the depth of the recorded dose distribution in steps of 1 mm using a linear stage (PTW, Freiburg, Germany) which travelled in spacial increments of 1 mm. From all measured spectral data, optical density difference (ΔOD) data (equation 1) were calculated with Matlab scripts.

2.5. Characterisation of dosimetric properties

2.5.1. Dose sensitivity. Dose sensitivity was investigated for the LMD1 type, LMD2 type and LMD3 type dosimeters. Spectroscopic samples of LMD1 and LMD2 were irradiated with doses ranging between 0 cGy and 6000 cGy in steps of 500 cGy and between 6000 cGy and 10000 cGy in steps of 1000 cGy. Spectroscopic samples of LMD3 were irradiated with doses ranging between 0 cGy and 3000 cGy in steps of 1000 cGy. Subsequently, all spectroscopic samples were placed in a refrigerator over night at 4°C. The spectroscopic samples were read out approximately 12 h post irradiation by use of the USB4000 spectrometer. Cuvettes stored in the dark at ambient temperature show a linear increase in dose sensitivity of 0.44 %/h due to chemical auto-oxidation. Cuvettes stored in a refrigerator show an increase in optical dose sensitivity of 0.042 %/h during the first 15 h which justifies the storage over 12 h post irradiation. The ΔOD dose plots (calculated at 633 ± 3 nm for LMD1 and LMD2 and at 590 ± 3 nm for LMD3) was fitted against a linear function (in Matlab) and the slope was used in further comparisons.

2.5.2. Dose rate dependence. A clinical linear accelerator generates bursts of electrons that exit the accelerator tube in multiple pulses. When the photon beam pulsation rate is increased the time span between two pulses is decreased, resulting in more closely packed bursts of photons. Alternatively the dose rate can be increased by decreasing the distance between the source and the measuring point (SSD). In this case the time span between two pulses remains identical, however the amount of photons reaching the measuring point increases during one pulse resulting in more radiation interactions. The dose rate dependence for the LMD1 type, LMD2 type (0 %, 6 % and 10 % (w/w) gelatin) and LMD3 type dosimeter was investigated using the same two irradiation set-ups as stated above for photon beams of 6 MV. In a first procedure the dose rate was varied by changing the photon beam pulsation rate. Spectroscopic samples were irradiated at dose rate $400\,cGy\,min^{-1}$, $200\,cGy\,min^{-1}$, $100\,cGy\,min^{-1}$ and $50\,cGy\,min^{-1}$ at isocentre. In a second procedure the dose rate was varied by changing the SSD to 100 cm, 136 cm,

195 cm and 277 cm and choosing an appropriate field size. The cuvettes were positioned at a depth of 5 cm. The dose rates at this depth were verified with a 0.6 cm^3 Farmer ion chamber (PTW).

$CHCl_3$ - LMG (4 mM) solutions (LCS) poured in test tubes were irradiated in a box-shaped standard dosimetry water phantom tilted at 90° to position the test tubes vertically in the centre of the irradiation field. LCS was irradiated with the following parameters: SSD 95 cm, energy 6 MV, depth 5 cm, field size $10 \times 10\,cm^2$ and dose rate set at 600 $cGy\,min^{-1}$, 400 $cGy\,min^{-1}$, 200 $cGy\,min^{-1}$, 100 $cGy\,min^{-1}$ and 50 $cGy\,min^{-1}$ at isocentre.

2.5.3. Energy dependence. For the energy dependence study, three spectroscopic samples filled with the LMD1 type dosimeter were irradiated at 5 cm depth using 6 MV energy photons to a dose of 30 Gy (field size 10 × 10 cm^2, SDS 95 cm). Subsequently three spectroscopic samples (from the same batch) were irradiated at 10 cm depth using 18 MV energy photons to a dose of 30 Gy (field size 10 × 10 cm^2, SDS 90 cm). All spectroscopic samples were read out and compared to verify the energy dependence. The same procedure was performed to test the energy dependence of the LMD2 type dosimeter, except that the spectroscopic samples were irradiated to a dose of 10 Gy.

2.5.4. Temperature dependence during irradiation. The influence of temperature variations during irradiation on the optical dose response (ΔOD versus dose) was determined for the LMD1 type and LMD2 type dosimeter. Spectroscopic samples were placed in a cylindrical water bath (volume 6.12 l). The deionized water in the water bath was cooled to different temperatures in a thermostatic bath (Ecoline E100, Lauda, Knigshofen, Germany). The temperature of the spectroscopic samples was allowed to equilibrate to the water temperature for 10 minutes prior to irradiation. Temperature was monitored before and after irradiation. Different temperatures were used during irradiation of the cuvettes: 13°C, 16°C, 20°C, 23°C and 26°C. The temperature variation in the spectroscopic samples during irradiation was less than 2°C.

2.5.5. Temperature dependence during readout. The influence of temperature variations on the optical dose response during readout of the LMD2 type dosimeter were investigated using a cuvette holder with temperature stabilization connected to a circulating thermostatic bath. Optical densities were measured at temperatures: 5°C, 10°C, 15°C, 20°C and 25°C. Exothermic changes in the gel during or after irradiation are suspected to be very small and were not measured.

2.5.6. Tissue equivalence. The soft-tissue equivalence of the LMD1 type and LMD2 type dosimeter was determined theoretically by calculating the mass density (ρ), relative electron density (ρ_e^w), the effective atomic number (Z_{eff}) and mass attenuation coefficients (μ/ρ). The mass density is defined as the mass per unit volume. The

relative electron density of the leucodye micelle gel dosimeter is defined as the ratio of the electron density of the dosimeter and the electron density of water:

$$\rho_e^w = \frac{\rho N_A}{\rho_{ew}} \sum_i f_i \left(\frac{Z}{A}\right)_i \tag{6}$$

where N_A is Avogadro's number ($6.022 \times 10^{23} mol^{-1}$), ρ_{ew} the electron density of water, f_i the elemental fraction of atom i and $\left(\frac{Z}{A}\right)_i$ the ratio of atomic number Z and atomic mass A for atomic element i.

The mass attenuation coefficient (μ/ρ) for energies between 0.01 MeV and 100 MeV was calculated using the Xcom database (Berger *et al* 2005). The average mass attenuation coefficients were spectrum-weighted for a 6 MV photon beam. The beam data was obtained from the treatment planning system (Pinnacle version 8.0m). The effective atomic number (Z_{eff}) was derived from cross-section data of the constituent elements and spectrum-weighted for the 6 MV photon beam. This method is described in Thirumala *et al* 1985, Parthasaradhi *et al* 1989 and Taylor *et al* 2008, 2009b.

3. Results

3.1. Optimization of the composition of LMD2 in terms of dose sensitivity

An overview of the results can be found in table 2. In LMD2 type dosimeters, the maximum optical dose sensitivity was obtained for 0.37 mM LMG concentration. When higher concentrations of LMG were used in the formulation, there was an extensive background colouration present resulting in a lower dose sensitivity.

The concentration of gelatin resulting in the highest dose sensitivity ($4.375 \times 10^{-5} cm^{-1} cGy^{-1}$) amounted to 4-6 %. This corresponds to the value of 4 % as mentioned by Jordan and Avvakumov (2009). The optical dose sensitivity was found to decrease with gelatin concentration above 6 %. The decrease in optical dose sensitivity amounts to 6.3 % for the 8 % gelatin formulation and 23.1 % for the 10 % gelatin formulation relative to the 4-6 % gelatin formulation. When gelatin was omitted, the optical dose sensitivity decreased approximately 7-fold to $0.57 \times 10^{-5} cm^{-1} cGy^{-1}$.

A decrease in optical dose sensitivity was seen when the surfactant SDS was replaced by Triton X-100: $4.375 \times 10^{-5} cm^{-1} cGy^{-1}$ for SDS (50 mM) versus $1.030 \times 10^{-5} cm^{-1} cGy^{-1}$ for Triton X-100 (7 mM). The concentrations of SDS and Triton X-100 are both in the range above their critical micelle concentration ($CMC_{TritonX-100}$ = 0.2 mM, CMC_{SDS} = 8 mM).

The optical dose sensitivity of a LMD2 dosimeter without initiators CCl_4, $CHCl_3$ and CCl_3COOH amounts to $1.253 \times 10^{-5} cm^{-1} cGy^{-1}$. When 20 mM CCl_4 is added, the optical dose sensitivity increases to $3.438 \times 10^{-5} cm^{-1} cGy^{-1}$. However, extensive precipitation of leucodye molecules is seen. The addition of 80 mM $CHCl_3$ results in an optical dose sensitivity of $3.231 \times 10^{-5} cm^{-1} cGy^{-1}$. When 5 mM CCl_3COOH is added, the optical dose sensitivity increases to $2.792 \times 10^{-5} cm^{-1} cGy^{-1}$ (a small amount

Table 2. Comparison of different gel compositions based on their optical dose sensitivity.

Gelatin	Initiator [mM]	Surfactant [mM]	Optical dose sensitivity ($\times 10^{-5} cm^{-1} cGy^{-1}$)
6 %	-	SDS [50]	1.253
	H_2SO_4	SDS [50]	2.450
	CCl_4 [20]	SDS [50]	3.438
	$CHCl_3$ [80]	SDS [50]	3.231
	CCl_3COOH [5]	SDS [50]	2.792
	$CHCl_3$ [80], CCl_3COOH [5]	SDS [50]	4.375
	$CHCl_3$ [80], CCl_3COOH [5]	Triton [7]	1.030
0 %	$CHCl_3$ [80], CCl_3COOH [5]	SDS [50]	0.570
4 %	$CHCl_3$ [80], CCl_3COOH [5]	SDS [50]	4.369
8 %	$CHCl_3$ [80], CCl_3COOH [5]	SDS [50]	4.099
10 %	$CHCl_3$ [80], CCl_3COOH [5]	SDS [50]	3.364

of precipitating dye is seen in this formulation). Replacing CCl_3COOH by H_2SO_4 (concentrations adapted to match the pH value of the standard gel dosimeter) resulted in a 56% less sensitive dosimeter. When $CHCl_3$ [80 mM] and CCl_3COOH [5 mM] are both added, the optical dose sensitivity amounts to $4.375 \times 10^{-5} cm^{-1} cGy^{-1}$.

The composition of LMD2 gel used in further radio-physical experiments consisted of gelatin [6 %w/w], $CHCl_3$ [80 mM], SDS [50 mM], CCl_3COOH [5 mM], LMG [0.37 mM] and deionized water [approximately 92 % (w/w)]. This formulation is indicated in bold in table 1.

3.2. Characterisation of dosimetric properties

3.2.1. Dose sensitivity. The dose sensitivity of the optimized LMD2 dosimeter amounted to $4.375 \times 10^{-5} cm^{-1} cGy^{-1}$ (at a dose rate of $400\, cGy\, min^{-1}$). The dose sensitivity curve shows a linear dependence (figure 1). The dose sensitivity of the LMD1 dosimeter (fabricated according to the recipe described by Jordan and Avvakumov (2009)) amounted to $1.031 \times 10^{-5} cm^{-1} cGy^{-1}$ (at a dose rate of $400\, cGy\, min^{-1}$). The dose sensitivity of LMD3 (which is doped with LCV) amounted to $6.216 \times 10^{-5} cm^{-1} cGy^{-1}$ (at a dose rate of $400\, cGy\, min^{-1}$).

The intra-batch reproducibility of all gel systems is within 1.9 %. However data on inter-batch reproducibility shows that the dose sensitivity can vary between batches up to 22.1 %. These differences have only been measured when batches of different volumes are compared (*i.e.* 0.1 l versus 3 l of gel). When the same volume of gel is fabricated, the maximum inter-batch difference in dose sensitivity amounts to 8.9 %. This is probably due to the higher amount of evaporation of chloroform when fabricating

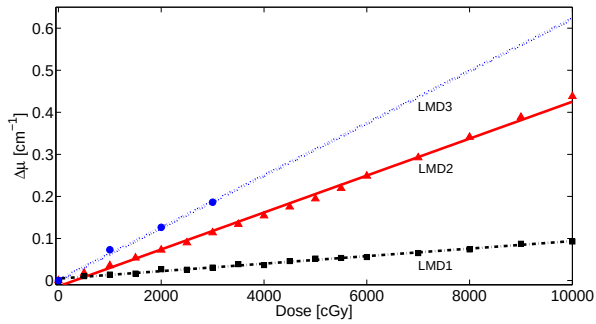

Figure 1. Dose response for LMD1(■), LMD2 type gel (▲) and LMD3 type gel (●) irradiated at $400\,cGy\,min^{-1}$. A linear fit is shown as a dot-dashed line for LMD1, as a full line for LMD2 and as a dotted line for LMD3.

large volumes of gel in comparison to small volumes of gel. Large volumes of gel also take longer to cool down in ambient temperatures (up to 6 h) which negatively influences the dose sensitivity. It is therefore suggested to keep gels in a refrigerator immediately after fabrication to minimize chemical auto-oxidation. However, the inter-batch reproducibility is still an issue that remains unsolved.

3.2.2. Dose rate dependence. A clear dose rate dependence is seen for all radiochromic dosimeters investigated in this study. As described in paragraph 2.5.2, the dose rate was varied by changing either the photon beam pulsation rate or the SSD. Identical results were obtained for both irradiation set-ups. Figure 2 shows that the deviation in optical dose sensitivity between $50\,cGy\,min^{-1}$ and $400\,cGy\,min^{-1}$ of LMD1 (4 % gelatin (w/w)) reached 74.6 % relative to the optical dose sensitivity at $400\,cGy\,min^{-1}$ as compared to 33.7 % for the LMD2 type dosimeter (6 % gelatin (w/w)) and 54.8 % for the LMD3 type dosimeter (4 % gelatin (w/w).

The dose rate dependence was also investigated for LMD2 type dosimeters with various concentrations of gelatin (0 %, 4 %, 6 %, 8 % and 10 % (w/w)). The optical dose sensitivity difference between $50\,cGy\,min^{-1}$ and $400\,cGy\,min^{-1}$ amounted to 70.2 % (0 % gelatin), 33.7 % (4 % gelatin), 29.2 % (6 % gelatin), 25.6 % (8 % gelatin) and 27.8 % (10 % gelatin) relative to $400\,cGy\,min^{-1}$. It should be noted that the uncertainty on the measurement of the dose rate dependence of 0 % gelatin is relatively high due to the low dose sensitivity.

The dose rate dependence of LCS was investigated for dose rates between $50\,cGy\,min^{-1}$ and $600\,cGy\,min^{-1}$. Figure 3 shows the ratio of the optical dose sensitivity at different dose rates over the optical dose sensitivity at $400\,cGy\,min^{-1}$. The optical dose sensitivity of LCS irradiated at $50\,cGy\,min^{-1}$ amounted to $4.829 \times 10^{-4} cm^{-1} cGy^{-1}$.

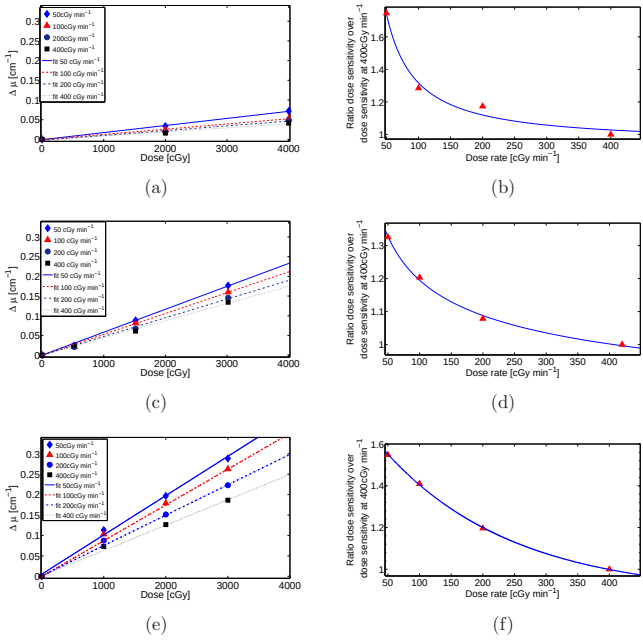

Figure 2. Comparison of dose response for LMD1 (a), LMD2 (c) and LMD3 dosimeter (e) irradiated at different dose rates ($50\,cGy\,min^{-1}$ (♦——), $100\,cGy\,min^{-1}$ (▲- - - -), $200\,cGy\,min^{-1}$ (● — · —), $400\,cGy\,min^{-1}$(■· · · · · ·)). Plot (b), (d) and (f) show the dose sensitivity as function of dose rate relative to $400\,cGy\,min^{-1}$. An exponential fit is shown as a full line as a guide to the eye.

Depth dose profiles of 6 MeV electron beams were measured at different dose rates by varying the linac pulsation rate. In figure 4(a) and figure 4(b), electron depth dose profiles were measured with the LMD2 dosimeter without a homogeneous pre-irradiation dose. The maximum ΔOD between $50\,cGy\,min^{-1}$ and $400\,cGy\,min^{-1}$ amounted to 33.1 %; a similar relation between the ΔOD and the dose rate was found in the case of photons. In figure 4(c) and figure 4(d), electron depth dose profiles were recorded following a homogeneous irradiation of the phantom with a pre-irradiation dose of 500 cGy. These results show that no significant deviation in ΔOD between $200\,cGy\,min^{-1}$ and $400\,cGy\,min^{-1}$ was found. However, a difference in ΔOD of 38 % was still present between $50\,cGy\,min^{-1}$ and $200\,cGy\,min^{-1}$. In figure 4(b) and 4(d) the depth dose profiles are individually normalized to the maximum dose demonstrating the high apparent correspondence between the three curves.

Additionally, in figure 5(a) and 5(b) simulated depth dose profiles are shown

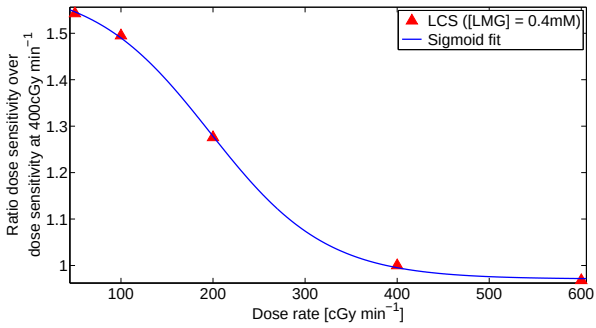

Figure 3. Dose rate dependence of LCS solutions containing 4 mM LMG relative to dose sensitivity at $400\,cGy\,min^{-1}$. A sigmoid fit is shown as a full line as a guide to the eye.

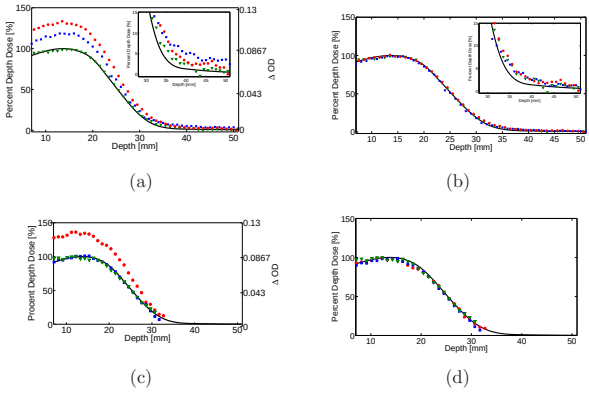

Figure 4. Electron depth dose profile (6 MeV) measured with the LMD2 type dosimeter at three dose rates: $50\,cGy\,min^{-1}$ (●), $200\,cGy\,min^{-1}$ (■), $400\,cGy\,min^{-1}$ (▼) compared with an ionisation chamber measured PDD (——). The measuring uncertainty in the data points amounted to 0.56%. Plot (a) and (b) shows the recorded electron beam with a non-pre-irradiated LMD2 dosimeter. The inset figures show a detail in the tail region of the electron depth dose curves. Plot (c) and (d) shows the recorded electron beam with the homogeneously pre-irradiated LMD2 dosimeter with a dose of 500 cGy. The PDD's are scaled with the same normalisation factor for the PDD recorded at $400\,cGy\,min^{-1}$ in (a and c). The PDD's are scaled with their individual normalization factor in (b and d). The missing depth dose data beyond 30 mm in (c) and (d) is due to the use of a 4.5 cm length cuvette (and not 8 cm length that was used to collect the data shown in (a) and (b)).

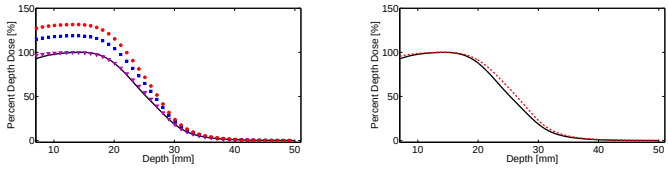

(a) (b)

Figure 5. A simulation of the influence of measured dose rate dependence at three dose rates: $50\,cGy\,min^{-1}$ (●), $200\,cGy\,min^{-1}$ (■) and $400\,cGy\,min^{-1}$ (▼) for electrons upon the depth dose profile (- - - -) compared to a PDD recorded with an ionisation chamber (——). The PDD's are scaled with the same normalisation factor for the PDD recorded at $400\,cGy\,min^{-1}$ in (a). The dose rate dependent electron depth dose curve is shown compared to the ion chamber measurement in (b).

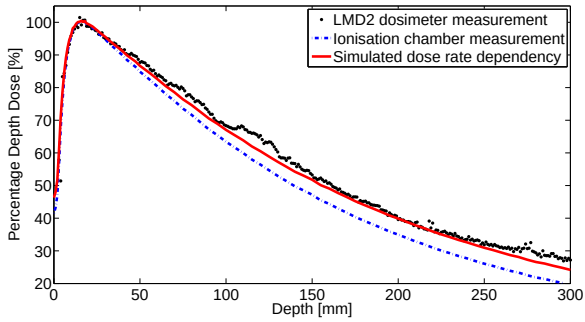

Figure 6. Comparison of PDD profiles for LMD2 type dosimeter (·····) versus ionisation chamber measurements (— · —) of 6 MV photon beams. The ——line represents the simulated dose rate dependent PDD curve as calculated from the measured dose rate dependence of the LMD2 type dosimeter.

as calculated from an ionisation chamber measured depth dose distribution. These simulations account for the measured dose rate dependence for electrons.

Additionally, a 6 MV photon beam depth dose distribution was recorded with the LMD2 type dosimeter. Deviations up to 4.9 % relative to the dose maximum are found for the LMD2 type dosimeter (figure 6). A dose rate dependent PDD is also simulated based on the measured dose rate dependence of the LMD2 type dosimeter. The results are consistent with a measured PDD.

3.2.3. Energy dependence. The mean optical density of the LMD1 type dosimeter irradiated with 6 MV photons to a dose of 30 Gy amounted to $2.633 \pm 0.220 \times 10^{-2} cm^{-1}$.

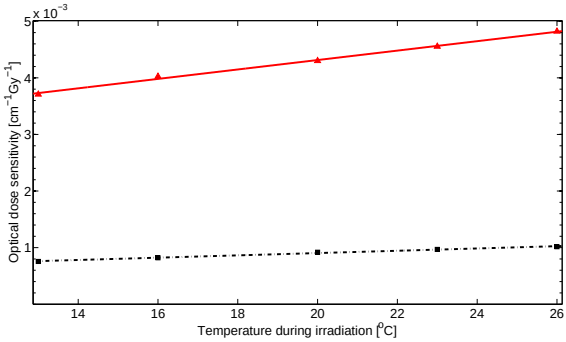

Figure 7. Temperature dependence during irradiation for LMD1(■) and LMD2 type gel (▲) irradiated between 13°C and 26°C. A linear fit is shown as a dot-dashed line for LMD1 and as a full line for LMD2. Note the significantly higher sensitivity of LMD2, hence the breaks in the vertical scale.

The mean optical density amounted to $2.484 \pm 0.250 \times 10^{-2} cm^{-1}$ for LMD1 type dosimeter irradiated with 18 MV photons to a dose of 30 Gy.

For the LMD2 type dosimeter irradiated with 6 MV photons to a dose of 1000 cGy, the mean optical density amounted to $4.154 \pm 0.037 \times 10^{-2} cm^{-1}$ for LMD2 type dosimeter. The mean optical density amounted to $4.164 \pm 0.086 \times 10^{-2} cm^{-1}$ for LMD2 type dosimeter irradiated with 18 MV photons to a dose of 10 Gy.

Within uncertainty there is no observable energy dependence between 6 MV and 18 MV for the LMD1 and LMD2 type dosimeter.

3.2.4. Temperature dependence during irradiation. The influence of temperature on the dose sensitivity during irradiation was assessed between 13°C and 26°C (figure 7). For the LMD1 type dosimeter, a linear correspondence was found between the measurements with a slope of $2.034 \times 10^{-7} cm^{-1} cGy^{-1}$ °C^{-1}. Also for the LMD2 type dosimeter, a linear correspondence was found between the measurements with a slope of $8.332 \times 10^{-7} cm^{-1} cGy^{-1}$ °C^{-1}.

3.2.5. Temperature dependence during readout. The influence of temperature on the dose sensitivity of LMD2 type dosimeter during scanning was evaluated between 5 °C and 25 °C (figure 8). Maximum optical dose sensitivity was recorded at 5 °C-10 °C ($4.487 \times 10^{-5} cm^{-1} cGy^{-1}$) after which there is a linear decrease of $7.808 \times 10^{-8} cm^{-1} cGy^{-1}$ °C^{-1}. This parameter was not evaluated for LMD1 type dosimeter.

3.2.6. Spatial integrity. Spatial integrity is of great importance for the accurate recording of steep dose gradients with a 3D dosimeter. The diffusion coefficient of the

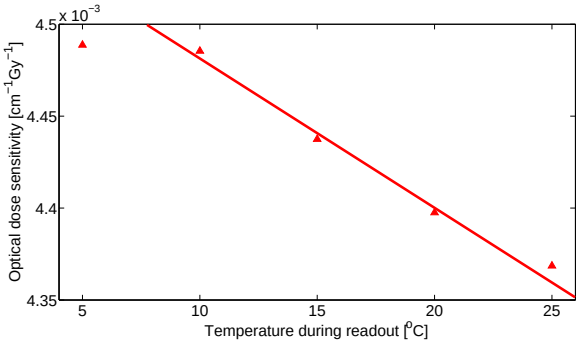

Figure 8. Temperature dependence during readout for LMD2 type dosimeter (▲) measured between 5°C and 25°C. A linear fit of the data points between 10°C and 25°C is shown as a full line as a guide to the eye.

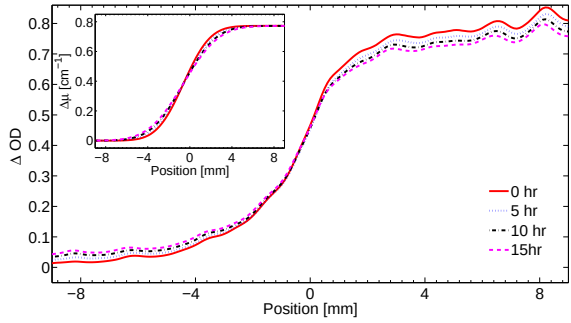

Figure 9. Optical density profiles through a half irradiated plan-parallel perspex phantom. A profile is plotted at 0 h (——), 5 h (· · · · · ·), 10 h (— · —) and 15 h (- - - -). The inset figure shows the fitted analytical diffusion profiles at the corresponding time points.

LMD2 dosimeter is derived by fitting an analytical diffusion function to measured optical density profiles (figure 9). The diffusion coefficient amounted to $2.45 \times 10^{-7} cm^2 s^{-1}$ ($= 0.088\, mm^2 h^{-1}$). The calculation of the diffusion coefficient was based upon measurements performed at an ambient temperature of 27°C. During the measurement, a chemical auto-oxidation reaction resulted in a linear offset in optical density as a function of time ($5.01 \times 10^{-5} cm^{-1} h^{-1}$) which results in an apparent dose increase of 0.875 cGy/h. Therefore, the optical density profiles had to be rescaled in order to fit the measured profiles to an algebraic diffusion function.

Table 3. The mass density ρ, relative electron density ρ_e^w, spectrum-weighted effective atomic number Z_{eff}, spectrum-weighted mass attenuation coefficient μ/ρ for 6 MeV energy and composition by elemental percentage mass of LMD1 type and LMD2 type dosimeters in comparison to water and soft tissue (ST, Jayachandran 1971)) are shown (calculated at room temperature ($\pm$ 20°C)).

					Elemental fraction f_i						
	ρ (g cm^{-3})	ρ_e^w	Z_{eff}	μ/ρ ($g^{-1}cm^2$)	H	C	N	O	S	Na	Cl
LMD1	1.015	1.0158	3.364	0.07262	0.1104	0.0229	0.0001	0.8649	-	-	0.0017
LMD2	1.012	1.0107	3.393	0.07255	0.1087	0.0379	0.0001	0.8414	0.0011	0.0016	0.0091
H_2O	0.998	1.0000	3.367	0.07275	0.1110	-	-	0.8890	-	-	-
ST	1.07	0.9919	3.468	0.07194	0.1002	0.1495	0.0353	0.7150	-	-	-

3.2.7. Tissue equivalence. The elemental atomic composition, mass density, relative electron density, spectrum-weighted effective atomic number and spectrum-weighted mass attenuation coefficient of the LMD1 and LMD2 type dosimeter are shown in table 3. Since the composition of the organic gelling agents can vary slightly, an average structural atomic composition was used for gelatin ($C_{3.44}NO_{2.22}H_{6.9}$). No effects of dissolved gasses in the gel were incorporated. In table 3, the spectrum-weighted effective atomic number and the mass attenuation coefficients of the different gels correspond very well to the values for water for 6 MeV nominal energy photon beams (mean photon energy: 1.41 MeV). To compare the different gels over a larger range of photon energies the mass attenuation coefficient was computed (figure 10). The mass attenuation coefficient for soft tissue and water is also plotted. The inset figure shows the mass attenuation coefficients relative to water. For a 6 MV photon beam, the spectrum-weighted effective atomic number amounts to 3.364 and 3.393 for the LMD1 and LMD2 type dosimeter, respectively. The spectrum-weighted mass attenuation coefficient amounts to 0.07262 and 0.07255, respectively.

4. Discussion

4.1. Optimization of the composition of LMD2 in terms of dose sensitivity

4.1.1. Initiator. The optimal gel composition in terms of optical dose sensitivity contains 80 mM $CHCl_3$ and 5 mM CCl_3COOH. Experimental results show that the addition of CCl_3COOH (5 mM) to the gel (composition: H_2O, 6 % gelatin (w/w), 50 mM SDS and 0.37 mM LMG) results in a 2.2 fold increase of optical dose sensitivity. Furthermore, the optical dose sensitivity is increased by 2.6 fold when $CHCl_3$ (80 mM) is added. The addition of both halocarbons results in a 3.5 fold increase in optical dose sensitivity. The large difference in concentration between CCl_3COOH and $CHCl_3$ added to the gel dosimeter results in only a small variation in optical dose sensitivity. An attempt to increase the concentration of CCl_3COOH did not result in a higher sensitivity and reduced the optical transparency. The addition of CCl_4 (20 mM) resulted in a 2.7 fold increase in optical dose sensitivity. This is the highest optical dose sensitivity

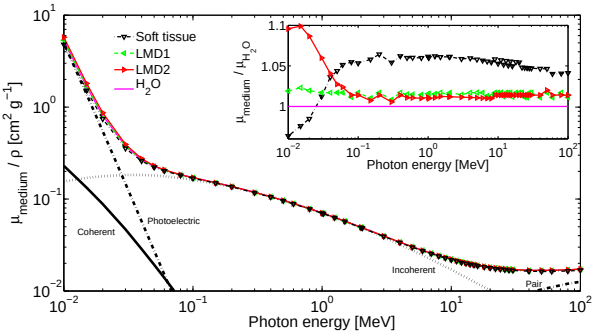

Figure 10. Mass attenuation coefficient as a function of photon energy for the different gel systems (LMD1 and LMD2), water (H_2O) and soft tissue. The different interaction contributions are shown in dashed lines. The inset figure shows the attenuation coefficient for the different gel dosimeters relative to water.

obtained by an individual initiator. In CCl_4 the bond between C and Cl has the lowest bond energy of all tested initiators, leading to the rapid formation of $Cl^{\bullet}$ radicals upon irradiation. Despite this high optical dose sensitivity, extensive precipitation of the leucodye is seen when CCl_4 is used. Therefore, CCl_4 was eliminated in further formulations.

The increase in optical dose sensitivity can be explained by radiation induced decomposition of $CHCl_3$ and CCl_3COOH (Ottolenghi and Stein 1961, Werner and Firestone 1965, Abramson and Firestone 1966, Rezansoff *et al* 1970, Mai *et al* 2008) resulting in the formation of Cl atoms (amongst others) which contribute to the oxidation of LMG to its chromatic form.

4.1.2. Leucodye. The optimal gel composition in terms of dose sensitivity contains 0.37 mM LMG. This corresponds with the value of 0.3 mM reported by Jordan and Avvakumov (2009). The decreased dose sensitivity at larger LMG concentrations can be partially explained by a significant increased background colour caused by the presence of small traces of MG^+ among LMG. These colour particles can be eliminated by recrystallisation of the leucodye. It is expected that this will improve the optical dose sensitivity.

4.1.3. Surfactant. The optimal gel composition in terms of optical dose sensitivity contains 50 mM SDS (critical micelle concentration of 7 mM). The use of SDS results in a 4 times higher sensitivity as compared to Triton X-100. The exact origin of this increase in sensitivity is not known. It can be speculated that the radiochemical conversion efficacy of LMG molecules in the presence of anionic surfactant molecules (SDS) is

improved. SDS at a concentration of 50 mM will adhere strongly to the gelatin strand and form surfactant aggregates with negligible free SDS micelles. These micelles were found to be larger in the presence of gelatin than in the absence of gelatin (Griffith *et al* 1996). In contrast, Triton X-100 exhibits little hydrophobic binding to gelatin (Saxena *et al* 1998). It is hypothesized that the larger micelles of SDS-gelatin will lead to a closer packing of LMG and $CHCl_3$ which will result in more interactions between LMG and radiation induced reaction products of $CHCl_3$. The use of SDS resulted in a homogeneous surfactant-dye solution without precipitation of dye molecule within seconds. The ease of fabrication was an additional advantage of the use of SDS over Triton X-100 as Triton X-100 resulted in an extended mixing time (30-45 min) at elevated temperature (30°C) before all LMG dye precipitation was dissolved.

4.1.4. Gelatin. The presence of 4 - 6 % gelatin results in a 7 fold increase of the optical dose sensitivity. Jordan and Avvakumov (2009) also noticed a threefold increase of the optical dose sensitivity in a micelle gel containing 4 % gelatin. Their explanation was that gelatin is able to scavenge OH radicals and also provides a source of organic peroxides. OH radicals are able to oxidize the newly formed MG^+, causing a decrease in optical dose sensitivity. When the concentration of gelatin is increased from 6 % to 10 % a decrease of 23 % in optical dose sensitivity is observed.

4.2. Characterisation of dosimetric properties

4.2.1. Dose sensitivity. The maximum optical dose sensitivity for LMD2 was $4.375 \times 10^{-5} cm^{-1} cGy^{-1}$ (dose rate $400\, cGy\, min^{-1}$) which is 5% lower than the value of the leucodye dosimeter proposed by Jordan and Avvakumov (2009) ($4.6 \times 10^{-5} cm^{-1} cGy^{-1}$). In order to compare the characteristics of the LMD2 dosimeter, the leucodye dosimeter proposed by Jordan and Avvakumov (2009) (LMD1) was fabricated according to an identical fabrication procedure as described in their publication. The maximum optical dose sensitivity for LMD1 amounted to $1.031 \times 10^{-5} cm^{-1} cGy^{-1}$ (dose rate $400\, cGy\, min^{-1}$) which is four times lower than the value reported by Jordan and Avvakumov (2009). A substantial increase of the background colour is seen during the first hour post fabrication although the dosimeter was stored in a refrigerator at 4 °C. Attempts to reduces this background colour by fabricating the gel in a dark room have not been successful. A possible explanation for this increased background colour is the slightly higher mixing temperature as compared to Jordan and Avvakumov. However lowering this temperature resulted in a substantial amount of air bubbles trapped inside the gel phantom.

The maximum optical dose sensitivity of LMD3 type dosimeter amounted to $6.216 \times 10^{-5} cm^{-1} cGy^{-1}$ (dose rate $400\, cGy\, min^{-1}$). Babic *et al* proposed a LCV type dosimeter which is 17 % more sensitive and uses Triton X-100 in stead of SDS (Babic *et al* 2009). SDS was favoured above Triton X-100 because it was more successful in producing a optical clear gel without precipitation of dye molecules. Leucodyes are

notorious for impurities which are suspected to be the underlying cause of discrepancies between our results and those of Babic *et al* (2009).

4.2.2. Dose rate dependence. In contemporary high precision radiation therapy the dose rate varies depending on the spatial location in the patient. It is therefore crucial that dosimeters are dose rate independent. It is shown that LMD1 type, LMD2 type and LMD3 type dosimeters depend strongly on the dose rate.

For LMD2 type dosimeters without gelatin the maximum difference in optical dose sensitivity at different dose rates amounts to approximately 70 %. The addition of 4-6 % of gelatin results in a optical dose sensitivity difference of 33 % between $50\,cGy\,min^{-1}$ and $400\,cGy\,min^{-1}$. For a gelatin concentration of 10 % the optical dose sensitivity difference amounts to 27.8 %. It was therefore conjectured that gelatin could influence the dose rate dependence possibly due to its buffer capacity. Armstrong 1958 and Armstrong and Grant 1958 showed that dose rate effects are known to be related to pH in water-saturated chlorinated hydrocarbons. Mai *et al* 2008 also have reported the effect of HCl (newly formed during radiation) to induce an accelerated colour change of the leucodye. The presence of gelatin has a major effect on the dose sensitivity and dose rate dependence, nevertheless changing the gelatin concentration between 4 % and 10 % has only minor effects on the dose rate dependence.

To illustrate the effect of the dose rate dependence on a dose distribution, a PDD of a 6 MeV electron beam was recorded with a LMD2 type dosimeter irradiated at different dose rates. The influence of a homogeneous pre-irradiation dose was also investigated. It is clear from figure 4a that, in the case of a non-pre-irradiated dosimeter, lower dose rate regimes result in higher dose sensitivity. However, when a pre-irradiation dose of 500 cGy was delivered in the phantoms, no significant deviation was found in the electron depth dose curves irradiated at $200cGy\,min^{-1}$ and $400cGy\,min^{-1}$ (figure 4c). Jordan and Avvakumov have found a small over-response of the LMD1 dosimeter at low dose rates. By depositing a pre-irradiation dose of 500 cGy in the gel, they initiate the measurement in the linear part of the dose response curve. They argue that the pre-irradiation dose effectively eliminated a species responsible for the initial over-response. Although the over-response is a plausible hypothesis for Jordan and Avvakumov (2009), this is not apparent from our data. In our experiments, for the LMD2 dosimeter, a small under-response of the dose response curve was detected. An explanation for the coincidence of the depth dose curves measured at $200cGy\,min^{-1}$ and $400cGy\,min^{-1}$ is not known. It can be hypothesised that new chemical species are formed after the initial exposure to a pre-irradiation dose. These species are responsible for a dose rate independent response between $200cGy\,min^{-1}$ and $400cGy\,min^{-1}$. Further work either through chemical modelling or experiment, is needed to explain this phenomenon of which the underlying mechanism is not yet understood.

When all measured depth dose attenuation coefficients are normalized to their individual dose maximum value (d_{max}) no significant deviation from the ion chamber measurement is seen (figure 4(b) and figure 4(d)).

The dose rate dependence effects were also simulated on a depth dose distribution measured with an ion chamber (figure 5(a)). The maximum deviation between the dose rate dependent and independent PDD amounts to 8% of dose maximum between 20 and 30 mm depth (figure 5(b)). However a positional shift of 0.9 mm results in an almost complete correspondence of both curves between dose maximum and 5 cm depth indicating that this method of identifying dose rate dependence is very sensitive to positional errors.

To extend the previous results, the effects of the dose rate dependent optical dose response is also investigated for photon beams. Deviations up to 4.9 % relative to the dose maximum are found for the LMD2 type dosimeter (figure 6). To accurately assess dose rate dependence of a gel dosimeter, PDD's of photon beams should be measured up to a minimum depth of 20 cm to reveal any dose rate dependency of importance to conformal radiation therapy treatments.

To further our understanding into the radio-physical mechanisms of the dose rate dependence, solutions of LMG dissolved in $CHCl_3$ (LCS) were irradiated. The results suggest a sigmoid relation between radiochromic yield and dose rate in the range between $50\,cGy\,min^{-1}$ and $600\,cGy\,min^{-1}$ (figure 3). For dose rates exceeding $600\,cGy\,min^{-1}$ fading of the gel colour is observed which can be attributed to long lived oxidising species that destroy the MG^+ molecules. This is in accordance with observations by Armstrong (1958) and Armstrong and Grant (1958) who found a colour fading at dose rates above $400\,cGy\,min^{-1}$ in liquid leucodye based dosimeter systems. The sigmoid relationship between $50\,cGy\,min^{-1}$ and $600\,cGy\,min^{-1}$ can be interpreted as the combined effect of diffusion and recombination of radiolytic species. However, there may be other factors that influence the dose rate dependence. Armstrong (1958) and Armstrong and Grant (1958) investigated the radiation chemistry of solutions of water, $CHCl_3$, initiators and leucodyes. In such systems, dose rate effects occur above $400\,cGy\,min^{-1}$, resulting in a fading of the dye to a maximum of 8 %. In our dosimeter systems however, deviations up to 33 % for LMD2 and 75 % for LMD1 type dosimeters were measured between $50\,cGy\,min^{-1}$ and $400\,cGy\,min^{-1}$. The major difference between the LMD type dosimeters and the solutions of Armstrong (1958) and Armstrong and Grant (1958) can be attributed to the presence of gelatin and surfactants in the former type. These two components induce many other chemical reactions that have an effect on the formation and destruction of dye molecules. The predominant chemical that influences the dose rate dependence is believed to be the surfactant because of three reasons. Firstly, omitting gelatin from the dosimeter formulation does not avoid a dose rate dependence. Secondly, changing the leucodye does not influences the dose rate dependency significantly and thirdly, changing the concentration and type of surfactant (SDS versus Triton X-100) results in substantial differences in dose rate dependence. The large number of chemical components and the chemical heterogeneity of the micelles in the LMD type dosimeters results in a high complexity of radiation induced reaction kinetics which can not be completely disentangled.

Although pre-exposing a dosimeter to a radiation dose sheds some light onto

the radio-physical properties of chemical dosimeters, this technique can result in uncertainties when it is used without a thorough understanding of the chemical basis. By giving a pre-dose, the total scanned gel volume is assumed to have a uniform linear dose response. The chemical basis of the dose rate dependency is not yet fully unravelled which makes an inhomogeneous pre-exposure to eliminate (or form) the necessary chemical species result in possible regional differences in dose response and dose rate dependency. These effects need to be further investigated in large phantoms. Furthermore, by pre-exposing a gel to a large pre-dose will decrease the dynamic range and in turn will limit the amount of dose that can be delivered to a gel system.

Dumas *et al* 2006, MacDougall *et al* 2008 and Xu *et al* 2010 have shown that discrepancies in dose response can occur between different volumes of the same gel. All the results presented in this study were obtained in small recipients. The volume of the test phantoms can therefore be regarded as a possible influencing factor on the presented dose sensitivity and dose rate data. Further research using larger volumes is suspected to shed some light on these issues.

4.2.3. Energy dependence. No energy dependence for LMD1 or LMD2 type dosimeters has been found for photon energies of 6 MV and 18 MV.

4.2.4. Temperature dependence during irradiation. A linear correspondence was found between the optical dose sensitivity and the temperature during irradiation for both the LMD1 and LMD2 type dosimeters. For the LMD1 type dosimeter, this results in a slope of $2.033 \times 10^{-7} cm^{-1} cGy^{-1}$ $^{\circ}C^{-1}$. For the LMD2 type dosimeter, the temperature dependence during irradiation was shown to be $8.332 \times 10^{-7} cm^{-1} cGy^{-1}$ $^{\circ}C^{-1}$. Consequently, a change of 1°C during irradiation will result in a deviation of 2.28 cGy on a total dose of 100 cGy for LMD1 and 1.90 cGy on a total dose of 100 cGy for LMD2. Therefore, the need for temperature stabilisation during irradiation is shown to be of importance for both types of dosimeters.

4.2.5. Temperature dependence during readout. For LMD2, a minimal temperature dependent dose response during readout was found between 5 °C and 25 °C with a maximum optical dose sensitivity of $4.487 \times 10^{-5} cm^{-1} cGy^{-1}$ at 5-10 °C. The dose sensitivity decreased by 2.7 % at a temperature of 25 °C. Consequently, a temperature change of 1 °C during readout will cause a deviation of 0.18 cGy on a total dose of 100 cGy. The need for temperature stabilisation during readout is not of importance for the LMD2 type dosimeter.

4.2.6. Spatial integrity. Upon irradiation LMG is oxidized to MG^{+}. The diffusion of these dye molecules inside the gelatin matrix causes a loss of spatial information. The spatial integrity over time was examined by optical diffusion measurements. The calculated diffusion coefficient of LMD2 type dosimeter measured $0.088\, mm^2/h$. After 100 minutes the root mean square displacement of MG^{+} amounts $0.94\, mm$. A time

window of 100 minutes is the time needed to scan a typical radiation dosimeter (cylinder of radius 6 cm and height 8 cm at a resolution of $0.4 \times 0.4 \times 2\,\mathrm{mm}^3$) with the in-house build fast laser scanning optical CT scanner (OptoScan, Vandecasteele and De Deene 2009). This does not result in a quantifiable influence on the optically measured dose distributions. The LMD2 type dosimeters can be scanned immediately after irradiation (the shortest time span between irradiation and readout was 5 minutes). A linear increase in optical dose sensitivity of 0.44 %/hr due to chemical auto-oxidation has been observed but this linear increase can be corrected.

In comparison to Fricke gel dosimeters ($D = 0.81\,mm^2/h$, Pederson *et al* 1997) the diffusion coefficient of LMD2 type is approximately 10-fold lower. Jordan and Avvakumov (2009) have measured the diffusion coefficient of the LMD1 type dosimeter to be a 3-fold lower than Fricke gel dosimeters ($D = 0.14\,mm^2/h.$). Changing the surfactant from Triton X-100 to SDS results in a 1.6 fold improvement of the spatial integrity. The conjecture that the anionic surfactant (SDS) decreases the diffusion rate of the cationic dye molecule (MG^+) is supported by this result. Babic *et al* 2009 have measured the diffusion coefficient of a low diffusion leucocrystal violet containing micelle gel dosimeter. Their gel was found to have a 25-fold lower diffusion coefficient in comparison to Fricke gel dosimeters ($D = 0.036\,mm^2/h$, Babic *et al* 2009). The crystal violet molecule is more hydrophobic than the malachite green molecule (a diamino triphenylmethane dye) which can explain the 2-fold increase of spatial integrity over the LMD2 type dosimeter (De *et al* 2002). Changing the surfactant in the leucocrystal violet containing gel dosimeter is suspected to improve the spatial stability even further. However further experiments are necessary to validate this hypothesis.

4.2.7. Tissue equivalence. In terms of spectrum-weighted mean Z_{eff} values (6 MV), the difference between LMD1 and water amounts to 0.1 %. For LMD2 this amounts to 0.8 %. In terms of spectrum-weighted mean mass attenuation coefficients (6 MV) the difference between LMD1 and water amounts to 0.2 % and between LMD2 and water to 0.3 %. At high photon energies the relative electron and mass densities of LMD1 and LMD2 type dosimeters can be considered as water-soft tissue equivalent.

5. Conclusions

The increasing need for dedicated 3D quality assurance tools in modern radiation therapy is the main motivation behind the development of accurate and user-friendly 3D dosimetry tools. This development consist of two major parts: the development of optical CT readout systems which is expected to facilitate the usability of 3D dosimeters by radiotherapy centres. Secondly the development of accurate and reliable 3D dosimeters able to record the radiation dose distribution. Recently, novel radiochromic leucodye micelle hydrogel dosimeters were introduced in the literature. In these studies, gel measured electron depth dose profiles were compared with ion chamber depth dose data, from which it was concluded that leucocrystal violet type dosimeters were

independent of dose rate. Similar conclusions were drawn for leucomalachite green type dosimeters, only after pre-irradiating the samples to a homogeneous radiation dose. However, in our extensive study of radio-physical properties of leucocrystal violet and leucomalachite green type dosimeters, a significant dose rate dependency was found. A modified composition of leucomalachite green type dosimeter is proposed. This dosimeter is composed of gelatin, sodium dodecyl sulphate, chloroform, trichloroacetic acid and leucomalachite green. This modified radiochromic dosimeter has comparable radio-physical properties as the dosimeters proposed in the literature: *i.e.* no energy dependence, a minimum temperature dependence, good water/soft tissue equivalence and an improved spatial integrity. Nevertheless, the novel formulation was also found to have a significant, albeit reduced, dose rate dependency. By pre-irradiating the novel leucomalachite green type dosimeter to 500 cGy, the apparent difference in dose response between $200\,cGy\,min^{-1}$ and $400\,cGy\,min^{-1}$ was eliminated, similar to earlier findings. However, a dose response difference between $50\,cGy\,min^{-1}$ and $200\,cGy\,min^{-1}$ was still measured. It can therefore be concluded that all existing radiochromic gel dosimeters still show some shortcomings for high precision clinical radiation therapy dose verifications. Radiochromic gel dosimeters are promising candidates for dosimetric quality assurance of complex radiation treatments because of the ease of fabrication, low cost and quick readout possibilities. In this study, the dose rate dependence is shown to have a potential for improvement. Therefore, future research should focus on trying to eliminate the dose rate dependence through extensive chemical analysis and optimization of the formulation.

Acknowledgments

This research is supported by the Institute for the Promotion of Innovation though Science and Technology in Flanders (IWT -Vlaanderen). The authors would like to thank Bart Truyens for constructing dedicated equipment that was indispensable in the experimental set-up.

References

Abramson F P and Firestone R F 1966 Combined effects of dose rate and temperature in the radiolysis of liquid chloroform. Application of homogeneous kinetics to the radiolytic system *J Phys. Chem.* **70** 3596–605

Adamovics J and Maryanski M J 2006 Characterisation of Presage: a new 3D radiochromic solid polymer dosemeter for ionizing radiation *Radiat. Prot. Dosim.* **120** 107–12

Armstrong W A 1958 Radiation chemistry of solutions I. Use of leuco trialrylmethane compounds for chemical dosimetry *Radiat. Res.* **8** 375–87

Armstrong W A and Grant G A 1958 Radiation chemistry of solutions II. Dose-rate, energy and temperature dependence of a leuco triarylmethane dosimeter solution *Can. J. Chem.* **36** 1398–404

Babic S, Battista J, Jordan K 2009 Radiochromic leuco dye micelle hydrogels: II. Low diffusion rate leuco crystal violet gel *Phys. Med. Biol.* **54** 6791–808

Baldock C, Buford R P, Billingham N, Wagner G S, Patval S, Badawi R D and Keevil S F 1998

Experimental procedure for the manufacture and calibration of polyacrylamide gel (PAG) for magnetic resonance imaging radiation dosimetry *Phys. Med. Biol.* **43** 695–702

Baldock C, Murry P and Kron T 1999 Uncertainty analysis in polymer gel dosimetry *Phys. Med. Biol.* **44** N243–6

Baldock C, De Deene Y, Doran S, Ibbot G, Jirasek A, Lepage M, McAuley K B, Oldham M and Schreiner L J 2010 Polymer gel dosimetry *Phys. Med. Biol.* **55** R1–R63

Baxter J N and Johnston F J 1968 Gamma radiolysis studies of the chloroacetic acids *Radiat. Res.* **33** 331–24

Berger M J, Hubbell J H, Seltzer S M, Chang J, Coursey J S, Sukumar R and Zucker D S 2005 XCOM: photon cross section database (version 1.3) [Online] Available: http://physics.nist.gov/xcom. National Institute of Standards and Technology, Gaithersburg, MD.

Bielska M, Sobczynska A and Prochaska K 2009 Dye-surfactant interactions in aqueous solutions *J. Dye. Pig.* **80** 201–5

De S, Girigoswami A, Mandal S 2002 Enhanced fluorescence of triphenylmethane dyes in aqueous surfactant solutions at supramicellar concentrations–effect of added electrolyte *Spectrochimica Acta A* **58** 2547–55

De Deene Y, De Wagter C, Van Duyse B, Derycke S, Mersseman B, De Gersem W, Voet T, Achten E and De Neve W 2000 Validation of MR-based polymer gel dosimetry as a preclinical three-dimensional verification tool in conformal radiotherapy *Magn. Reson. Med.* **43** 116-25

De Deene Y, Vergote K, Claeys C and De Wagter C 2006 The fundamental radiation properties of normoxic polymer gel dosimeters: a comparison between a methacrylic acid based gel and acrylamide based gels *Phys. Med. Biol.* **51** 653-73

Doran S 2009 The history and principles of optical computed tomography for scanning 3D radiation dosimeters: 2008 update *J. Phys.: Conf. Ser.* **164** 012020

Dumas E-M, Leclerc G, Lepage M 2006 Effect of container size on the accuracy of polymer gel dosimetry *J. Phys.: Conf. Ser.* **56** 239–41

Duthoy W, De Gersem W, Vergote K, Coghe M, Boterberg T, De Deene Y, De Wagter C, Van Belle S and De Neve W 2003 Whole abdominal radiotherapy (WAPRT) using intensity-modulated arc therapy (IMAT): First clinical experience *Int. J. Radiat. Oncol. Biol. Phys.* **57** 1019-32

Fruhner H and Kretzschmar G 1989 Effect of pH on the binding of alkyl sulphates to gelatin *Colloid Polym. Sci.* **267** 839–43

——1992 The interaction of anionic surfactants with gelatin *Colloid Polym. Sci.* **270** 177–82

Griffiths P, Rowlands C, Goyffon P, Howe A and Bales B 1997 EPR insights into aqueous solutions of gelatin and sodium dodecyl sulfate *J. Chem. Soc., Perkin Trans.* **2** 2473–7

Griffiths P, Stilbs P, Howe A and Cosgrove T 1996 A self-diffusion study of the complex formed by sodium dodecyl sulfate and gelatin in aqueous solutions *Langmuir* **12** 2884–93

Jayachandran C A 1971 Calculated effective atomic number and kerma values for tissue equivalent and dosimetry materials *Phys. Med. Biol.* **16** 617–23

Jordan K and Avvakumov N 2009 Radiochromic leuco dye micelle hydrogels: I. Initial investigation *Phys. Med. Biol.* **56** 141–53

Kosobutskii V S 2001 Radiation-initiated dehalogenation of trichloroacetic acid in aqueous solutions *High Energy Chem.* **35** 202–3

MacDougall N D, Miquel M E, Keevil S F 2008 Effects of phantom volume and shape on the accuracy of MRI BANG gel dosimetry using BANG3$\langle TM \rangle$ *Br. J. Radiol.* **81** 46–50

Mai H H, Solomon H M, Taguchi M and Kojima T 2008 Polyvinyl butyral films containing leuco-malachite green as low dose dosimeters *Radiat. Phys. Chem.* **77** 457–62

McCullough and Holmes 1985 Acceptance testing of computerized radiation therapy treatment planning systems: Direct utilization of CT scan data *Med. Phys.* **12** 237–42

Oldham M 2006 3D dosimetry by optical-CT scanning *J. Phys.: Conf. Ser.* **56** 58–71

Onesippe C and Lagerge S 2009 Study of complex formation between sodium dodecyl sulphate and gelatin *Colloids Surf.,*A **337** 61–6

Ottolenghi M and Stein G 1961 The radiation chemistry of chloroform *Radiat. Res.* **14** 281–90

Parthasaradhi K, Mallikarjuna Rao B and Guru Prasad S 1989 Effective atomic numbers of biological materials in the energy region 1 to 50 MeV for photons, electrons and He ions *Med. Phys.* **16** 653–4

Pederson T V, Olsen D R and Skretting A 1997 Measurement of ferric diffusion coefficient in agarose and gelatin gels by utilisation of the evolution of a radiation induced edge as relaxation rate images *Phys. Med. Biol.* **42** 1575–85

Rezansoff B J, McCallum K J and Woods R J 1970 Radiolysis of aqueous chloroform solutions *Can. J. Chem.* **48** 271–6

Saxena A, Antony T and Bohidar H B 1998 Dynamic light scattering study of gelatin-surfactant interactions *J. Phys. Chem.*,B **102** 5063–8

Taylor M L, Franich R D, Johnston P N, Millar R M, Trapp J V 2007 Systematic variations in polymer gel dosimeter calibration due to container influence and deviations from water equivalence *Phys. Med. Biol.* **52** 3991–4005

Taylor M L, Franich R D, Trapp J V and Johnston P N 2008 The effective number of dosimetric gels *Australas. Phys. Eng. Sci.* **31** 131–8

——2009 Electron interaction with gel dosimeters: Effective atomic numbers for collisional, radiative and total interaction processes *Radiat. Res.* **171** 123–6

——2009 A comparative study on the effect of calibration conditions on water equivalence of a range of gel dosimeters *Trans. Nucl. Sci.* **56** 429–36

Thirumala Rao B V, Raju M L N, Narasimham K L, Parthasaradhi K and Mallikarjuna Rao B 1985 Interaction of low energy photons with biological materials and the effective atomic number *Med. Phys.* **12** 745–8

Vandecasteele J and De Deene Y 2009 Optimization of a fast optical CT scanner for nPAG gel dosimetry *J. Phys.: Conf. Ser.* **164** 012024

Vergote K, De Deene Y, Duthoy W, De Gersem W, De Neve W, Achten E and De Wagter C 2004 Validation and application of polymer gel dosimetry for the dose verification of an intensity-modulated arc therapy (IMAT) Phys. Med. Biol. **49** 287-305

Werner H R and Firestone R F 1965 Kinetics of γ-ray-induced decomposition of chloroform *J. Phys. Chem.* **69** 840–9

Wustneck R, Wetzel R, Buder E and Hermel H 1988 The modification of the triple helical structure of gelatin in aqueous solution I. The influence of anionic surfactants, pH-value, and temperature *Colloid Polym. Sci.* **266** 1061–7

Xu Y, Wuu C-H and Maryanski M 2010 Sensitivity calibration procedures in optical-CT scanning of Bang3 polymer gel dosimeters *Med.Phys.* **37** 861–8

6

Evaluation of radiochromic gel dosimetry and polymer gel dosimetry in a clinical dose verification

---

Jan Vandecasteele and Yves De Deene

Manuscript on which this chapter is based:
Physics in Medicine and Biology **58** (2013) 6241-6262

Evaluation of radiochromic gel dosimetry and polymer gel dosimetry in a clinical dose verification

Jan Vandecasteele[1] **and Yves De Deene**[1,2]§

[1] Department for Radiation Oncology and Experimental Cancer Research, Ghent University, De Pintelaan 185, 9000 Gent, Belgium
[2] Institute of Medical Physics, School of Physics, University of Sydney, Sydney NSW 2006, Australia

E-mail: Jan.Vandecasteele@UGent.be

Received 6 May 2013, in final form 10 July 2013
Published 22 August 2013
Online at stacks.iop.org/PMB/58/6241

Abstract. A quantitative comparison of two full three-dimensional (3D) gel dosimetry techniques was assessed in a clinical setting: radiochromic gel dosimetry with an in-house developed optical laser CT scanner and polymer gel dosimetry with MRI. To benchmark both gel dosimeters, they were exposed to a 6 MV photon beam and the depth dose was compared against a diamond detector measurement that served as golden standard. Both gel dosimeters were found accurate within 4 % accuracy. In the 3D dose matrix of the radiochromic gel, hotspot dose deviations up to 8 % were observed which are attributed to the fabrication procedure. The polymer gel readout was shown to be sensitive to B_0 field and B_1 field non-uniformities as well as temperature variations during scanning. The performance of the two gel dosimeters was also evaluated for a brain tumour IMRT treatment. Both gel measured dose distributions were compared against treatment planning system predicted dose maps which were validated independently with ion chamber measurements and portal dosimetry. In the radiochromic gel measurement, two sources of deviations could be identified. Firstly, the dose in a cluster of voxels near the edge of the phantom deviated from the planned dose. Secondly, the presence of dose hotspots in the order of 10 % related to inhomogeneities in the gel limit the clinical acceptance of this dosimetry technique. Based on the results of the micelle gel dosimeter prototype presented here, chemical optimisation will be subject of future work. Polymer gel dosimetry is capable of measuring the absolute dose in the whole 3D volume within 5 % accuracy. A temperature stabilisation technique is incorporated to increase the accuracy during short measurements, however keeping the temperature stable during long measurement times in both calibration phantoms and the volumetric phantom is more challenging. The sensitivity of MRI readout to minimal temperature fluctuations is demonstrated which proves the need for adequate compensation strategies.

§ Present address: Institute of Medical Physics, School of Physics, University of Sydney, Sydney NSW 2006, Australia

1. Introduction

Polymer gel dosimetry using a PolyAcrylamide Gelatin gel fabricated at ATmspheric conditions (PAGAT) and magnetic resonance imaging (MRI) has been studied for over a decade (Baldock *et al* 2010 and references herein). Only recently, a study demonstrated that PAGAT polymer gel dosimetry can reach a clinical acceptable level of accuracy (Vandecasteele and De Deene 2013c). A very strict protocol is required to achieve this, which results in a reduced feasibility of the use of 3D dosimetry in clinical practice. Many radiotherapy clinics do not have the manpower or resources to perform polymer gel dosimetry to verify clinical dose distributions. Nevertheless, these advanced dosimetry techniques are indispensable as radiation treatments have become more and more complex. To provide more user-friendly and accessible 3D dosimetry, a radiochromic gel dosimeter was developed in combination with an optical readout system. This system has several advantages: small and inexpensive readout device, fast throughput and a reduced toxicity. An optical readout system was developed that could accommodate the needs of radiotherapy clinics. However, radiochromic gel dosimetry needs to be validated against a gold standard dosimeter for a realistic irradiation treatment.

In the present study, a quantitative comparison between radiochromic gel dosimetry and polymer gel dosimetry was performed. Firstly, the two dosimetric techniques are benchmarked using a well defined depth dose irradiation protocol. Secondly, the performance of the two dosimeters was evaluated for a brain tumour IMRT treatment. For this second study, a head phantom was constructed with a cylindrical cavity for the 3D gel dosimeters. Both gels were chosen because of their superior radio-physical properties: the leucomalachite green micelle gel has the best spatial stability and dose rate dependence characteristics (Jordan and Avaakumov 2009, Vandecasteele et al 2011) and the PAGAT gel has no dose rate dependency and the lowest temperature dependency during storage and irradiation as compared to other polymer gel systems (De Deene et al 2006a, De Deene et al 2007, Vandecasteele and De Deene 2013a,b,c). Furthermore, both gels were chosen because of their compatibility with the readout system. The polymer gel dosimeter was read out with an MRI scanner while the radiochromic gel dosimeter was read out with an optical laser CT scanner. The measured dose distributions were compared against treatment planning system (TPS) predicted dose maps.

2. Materials and Methods

2.1. Gel fabrication

2.1.1. Radiochromic gel dosimeter (RGD) The radiochromic micelle gel consists of 6 % (w/w) gelatin, 80 mM chloroform ($CHCl_3$), 50 mM sodium dodecyl sulphate (SDS), 5 mM trichloroacetic acid (CCl_3COOH) and 0.37 mM leucomalachite green (LMG) all dissolved in deionised water (Vandecasteele *et al* 2011). The fabrication protocol was slightly modified as compared to Vandecasteele *et al* 2011. The total gel composition consists of 92 % (w/w) deionised water. Gelatin is dissolved in two-third of this water

volume at room temperature and is left to swell for 10 minutes. Thereafter the gelatin-water solution is heated to 45°C. The remaining one-third of the water volume is used to dissolve in the following order SDS, CCl_3COOH, $CHCl_3$ and LMG. The solution is stirred for 30 minutes until all LMG is completely dissolved. After cooling down the gelatin-water solution to approximately 40°C, the two solutions are added together and stirred for 30 minutes in a dark room. The gel is poured into a cylindrical fluorinated-ethylene-propylene (FEP, Teflon^{TM}) recipient (Holscot, Grantham, UK) with wall thickness 0.1 cm, outer diameter 9.6 cm and height 30.0 cm. This material was chosen because of its similar refractive index (R.I. = 1.344) as the gel which results in smaller refraction errors near the edges of the phantom during scanning.

After filling, the phantom was placed in a refrigerator at 4°C overnight. The phantom was taken out of the refrigerator 3 hours prior to irradiation and allowed to thermally equilibrate at room temperature (approximately 22°C) in a dark room.

2.1.2. Polymer gel dosimeter (PGD) The PAGAT dosimeter (PolyAcrylamide Gelatin gel fabricated at ATmspheric conditions) consisted of 6 % (w/w) gelatin, 3 % (w/w) acrylamide (Aam), 3 % (w/w) N,N'-methylene-bis-acrylamide (bis) and 5 mM bis[tetrakis(hydroxymethyl)phosphonium]sulphate (THPS). The PAGAT gel was fabricated following a procedure described in De Deene *et al* 2006a. The gel is poured into a cylindrical borosilicate glass flask with wall thickness 0.4 cm, outer diameter 10.4 cm and height 40 cm. Additionally, small borosilicate glass test tubes were also filled with the same batch of gel and served as calibration phantoms. The wall thickness of the test tubes measured 0.1 cm, outer diameter 1.5 cm and length 10.0 cm. The calibration vials were irradiated to well defined doses. Borosilicate glass was chosen because it avoids infiltration of oxygen through the walls into the gel.

After the cylindrical phantom and calibration phantoms were filled with gel, they were placed in a large reservoir that was filled with 60 l of water at 32 °C to assure a similar cooling trajectory in calibration phantoms and volumetric gel dosimeter phantoms (De Deene *et al* 2007, Vandecasteele and De Deene 2013b). The water and phantoms inside the reservoir were allowed to cool down at normal atmospheric conditions and stored at room temperature (22°C) before the irradiation. The phantoms were taken out of the reservoir 60 minutes prior to irradiation and stored in a dark room at the same room temperature. The temperature during the actual irradiation experiment was also 22°C.

2.2. Depth dose measurement

2.2.1. Irradiation set-up Depth dose profiles were measured with a radiochromic gel (in FEP container) and polymer gel (in borosilicate glass container) for a photon beam of 6 MV at an SSD of 90 cm and field size 4×4 cm^2 for a dose rate of 400 cGy min^{-1} at the isocentre delivered by a clinical linear accelerator (linac) Elekta Synergy (Stockholm Sweden). The central axis of the cylindrical phantoms was positioned along the beam

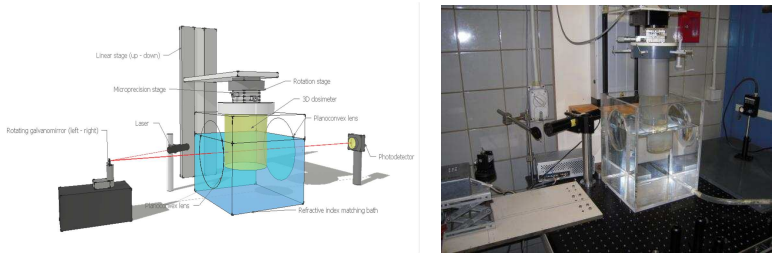

(a) (b)

Figure 1. Schematic overview of the in-house built optical CT laser scanner (a) and a photograph (b). A laser beam is projected towards a rotating galvano-mirror which sweeps the laser beam along a dual lens configuration mounted in a cubic PMMA reservoir filled with a refractive index matching solution. The planoconvex lenses assure that the laser beam travels in parallel paths through the reservoir perpendicular to the walls and is finally focused onto a large area photodiode receiver. A cylindrical gel dosimeter is attached to a rotating and vertically translating stage above the reservoir. This stage lowers the phantom into the reservoir at well-defined depths and allows transmission profiles to be acquired from multiple angles.

direction.

2.2.2. Radiochromic gel dosimetry readout The dose distribution in the radiochromic gel was read out with an in-house built optical laser CT scanner, the Optoscan (figure 1, Vandecasteele and De Deene 2009).

The Optoscan is composed of a 633 nm 2 mW HeNe laser (model 1122p, JDS Uniphase) which is projected towards a rotating galvano-mirror (model QS-7, Nutfield). This galvano-mirror sweeps the laser beam along a dual lens configuration mounted in a cubic poly-methyl-methacrylate (PMMA) reservoir filled with a refractive index matching solution (9 % propylene glycol in water). The planoconvex lenses (custom made by Melles Griot) assure that the laser beam travels in parallel paths through the reservoir perpendicular to the walls and is finally focused onto a large area photodiode receiver (Model 2307, New Focus). A cylindrical gel dosimeter is attached to a rotating and vertically translating stage above the reservoir. This stage lowers the phantom into the reservoir at well-defined depths and allows transmission profiles to be acquired from multiple angles. A transmission profile is recorded onto a computer after each sweep of the laser beam. The set of transmission profiles is saved as function of the angle at which it was recorded (sinogram). Alongside a sinogram, dark values (without any light reaching the detector) and a blank scan (without the phantom in the laser beam) are acquired to correct for a detector offset and any non-uniformities in the transmission profiles. Each transmission profile in the sinogram is corrected using the following

equation

$$OD(x,\theta) = -log_{10}\left(\frac{S_{irr}(x,\theta) - S_{dark}}{S_{blank}(x) - S_{dark}}\right) \quad (1)$$

in which OD is the optical density, S_{irr} the transmitted light intensity profile, S_{dark}, the dark value and S_{blank} the profile without any phantom. This OD sinogram is then converted into a two dimensional (2D) image using a filtered back projection with a Hann filter.

The irradiated radiochromic gel dosimeter was scanned using the following scanning parameters: angular range 360°, angular resolution 2°, profile resolution 0.2 mm, 24 slices at 5 mm interleaves. The laser vertical size amounted to 1.27 mm as measured in Vandecasteele and De Deene 2009. The optical readout was repeated twice: starting at 19 minutes and 21 hours post-irradiation. After the first measurement, the gel dosimeter was stored in a refrigerator over night at 4°C. The next day, the same gel was rescanned after being thermally equilibrated to room temperature for 3 hours (in total 21 hours post irradiation).

Measured optical density values are calibrated to dose values using ion chamber measured doses in an unirradiated region and the region of dose maximum.

A region of interest (ROI) of 1 cm × 1 cm from all the axial measured slices in the centre of the irradiated region was averaged to generate a depth dose profile. From this ROI, the mean value, structural, stochastic and total noise were calculated in all slices. The ROI's were subdivided into square regions of 3-by-3-voxels. In each of the square regions, the mean value and the standard deviation was calculated. The structural noise is then defined as the standard deviation of all mean values in the different regions. The stochastic noise is defined as the mean of all standard deviations in all regions (De Deene *et al* 2000).

2.2.3. Polymer gel dosimetry readout The irradiated polymer gel along with calibration phantoms were scanned at a 1.5 T MRI scanner (Magnetom Avanto, Siemens). Quantitative NMR spin-spin relaxation images (R_2 maps) were acquired in transverse planes through the cylindrical phantom and calibration phantoms in a transmit-receive circularly polarised (CP) head coil using a multiple spin-echo sequence (Vandecasteele and De Deene 2013a).

A dedicated temperature stabilisation protocol was adopted to minimise the temperature drift between the large phantom and the calibration phantoms (Vandecasteele and De Deene 2013c). The cylindrical phantom and calibration phantoms were insulated with water perfused thermal pads (cPad^{TM}, Waegener, Baar, Switzerland) at a fixed temperature. The thermal pads are connected to a temperature controlled water bath filled with GdDTPA doped water solution (T_1 and T_2 lower than 60 ms) to avoid imaging artefacts caused by the convective flow of the water. The temperature in the centre of the cylindrical phantom and in one calibration phantom was monitored with a fibre optic temperature measurement system (Reflex 4, Neoptix, Canada, nominal accuracy = 0.3°C). The phantom was wrapped in the temperature

controlled thermal pads 12 hours prior to scanning to equilibrate the temperature in the large cylindrical phantom and the calibration phantoms. During scanning the same set-up was used to minimise temperature differences between the calibration phantoms and the large cylindrical phantom.

Because the length of the cylindrical phantom is larger than the size of the head coil, an inhomogeneous B_1-field in the region protruding the coil was suspected. To determine the optimal set-up, two MRI measurements were performed. First, the region of dose maximum (approximately 2 cm from the top of the cylindrical phantom) was carefully positioned at the centre of the head coil. In a second measurement, the phantom was positioned so that the middle of the cylindrical phantom (approximately 15 cm from the top of the phantom) coincides with the centre of the coil.

A coronal slice through the centre of the cylindrical phantom was acquired using the following imaging parameters: voxel size $1 \times 1 \times 10$ mm^3, TR = 3 s, number of equidistant echoes = 32, TE = 40 ms - 1280 ms and NEX = 1. R_2 maps were calculated as described elsewhere (De Deene *et al* 1998, Vandecasteele and De Deene 2013a). The dose-R_2 relation was derived from the calibration phantoms and applied to the R_2 maps.

The depth dose distribution was extracted from the coronal measured slice by averaging out over a region of 1 cm perpendicular to the beam direction through the middle of the beam.

2.3. IMRT dose verification

2.3.1. Humanoid head phantom The goal of this experiment is to validate the two radiation dosimetry techniques by comparing their measured dose distributions against TPS calculated dose distributions. Because of the fact that two different dosimeters are used, contained in different radiological materials (borosilicate glass and FEP) with each their optimal dosimetric range, two treatment plans were optimised. For these two treatment plans two CT scans were acquired of the head phantom: one scan with the polymer gel dosimeter in borosilicate glass container and one with the radiochromic gel dosimeter in FAP container.

A realistic IMRT treatment plan for a brain tumour was chosen to test the 3D dosimetry techniques in a clinical setting. For this purpose, a dedicated head phantom was constructed from epoxy resin, thickened by glass microspheres. The shape of the head phantom was based on the Rando-Alderson phantom (Alderson Research Laboratories, Stanford CT) (figure 2). In the centre of the phantom, a hollow cylindrical PVC tube was inserted of inner diameter 10.7 cm and length 45 cm which fits the 3D dosimeter phantoms. The empty space in between the cast of the head phantom and the PVC tube was filled with a 6 % gelatin gel to which 0.5 % (w/w) NaN_3 was added as fungicide.

2.3.2. Computerised tomography Two helical CT scans (Toshiba Aquilion LB) were acquired of the head phantom: once filled with the polymer gel dosimeter and once

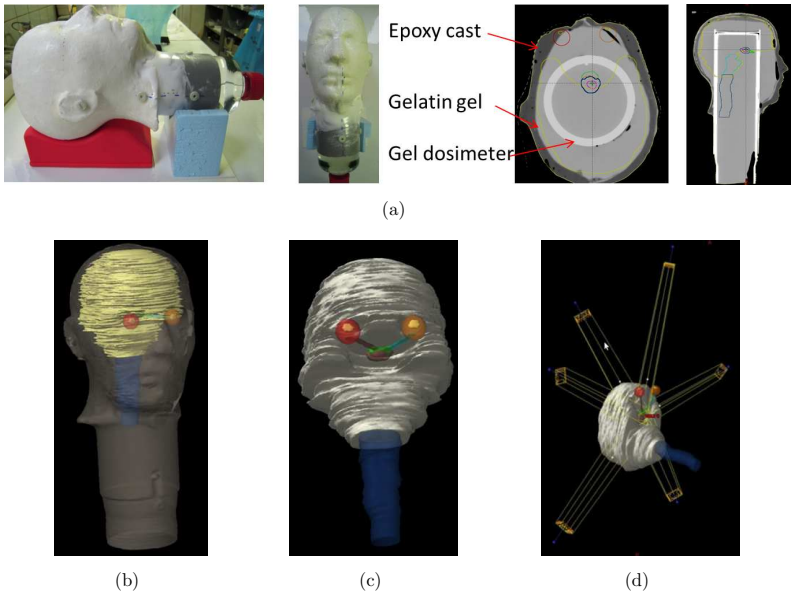

Figure 2. A side and frontal view of the head phantom casted from epoxy resin based on the Rando Alderson head phantom. Also a transverse and coronal CT image is shown displaying the position of the gel dosimeter inside the head phantom. In b, c and d, a print screen from the TPS is shown in which a volume rendering is performed of the PTV and OAR. In (b) the position of some OAR *i.e.* the brain, eyes and optic nerves are displayed relative to the cast of the phantom. In (c) also the CTV (in purple) and the PTV (in brown) are shown relative to the optic chiasm (in green) and the optical nerves. In (d) the orientation of the radiation beams relative to the head phantom is shown.

filled with the radiochromic gel dosimeter. For each CT scan, 450 slices were acquired with following scanning parameters: slice thickness: 1 mm, energy: 135 KVp, exposure: 300 mAs, matrix size (MS): 512 × 512 and field of view (FOV): 262 × 262 mm^2. The head phantom was fixated during the CT scan by a thermoplastic mask and a dedicated head rest to precisely reposition the phantom. Subsequently, the images were sent to the Eclipse treatment planning system (External Beam Planning 8.9.09, Varian Medical systems).

2.3.3. Treatment planning: radiochromic gel dosimetry (plan RGD) In the first treatment plan, the CT dataset of the head phantom with radiochromic gel dosimeter and FEP container was used. The diameter of the FEP container is 1.8 cm smaller than the diameter of the PVC cylinder in which the dosimeter should be positioned

Table 1. Overview of the chosen irradiation parameters for the polymer gel dosimeter (PGD) plan and the radiochromic gel dosimeter (RGD) plan.

Plan		Beam 1	Beam 2	Beam 3	Beam 4	Beam 5	Beam 6
PGD	MU	331	326	335	363	333	328
RGD	MU	721	714	734	792	729	715
	Energy (MV)	6	6	6	6	6	6
	Dose rate (MU/min)	400	400	400	400	400	400
PGD and RGD	Gantry angle (°)	357	72	133	220	288	310
	Collimator angle (°)	30	30	30	30	30	30
	Table angle (°)	0	0	0	0	0	270

during irradiation. To accommodate for this, a stack of polystyrene rings was fabricated which allowed for a perfect positioning of the gel dosimeter in the head phantom. The polystyrene rings are water-equivalent for mega-voltage beams and were custom-made in-house. An IMRT plan for a pituitary adenoma was planned in Eclipse (Varian Medical Systems, USA) in collaboration with the radiation oncologist. The pituitary gland is localised in the sella turcica, at the centre of the skull base. The choice for this particular type of tumour was directed by its central location in a human head which allowed for a practical positioning of a cylindrical cavity, in which a cylindrical dosimeter phantom could be placed. The contours of the clinical target volume (CTV) and organs at risk (OAR) *i.e.* cerebrum, optic chiasm, eye lenses, eyes, optical nerves, spinal cord and brain stem were transposed onto the CT slices on the basis of an anatomical atlas and using the skin as a frame of reference. An isotropic expansion of 0.3 cm of the CTV resulted in the planning target volume (PTV). Because there is some overlap between the optic chiasm and the PTV, a new structure was defined as PTV_optim which comprises the PTV from which the optic chiasm is excluded. The treatment isocentre was chosen in the centre of the PTV_optim.

A sliding window IMRT treatment was optimized for six beam angles of which 5 angles were coplanar. The details are shown in figure 2d and listed in table 1.

A typical pituitary adenoma is irradiated to a dose of 45 Gy in 20 to 25 fraction of about 2 Gy. In this experiment, the range was optimised to the specific dosimeter. A mean dose of 45.0 Gy to the PTV_optim was chosen delivered in two fractions of each 22.5 Gy. During optimisation, upper and lower constraints were given to the OAR and PTV_optim which are listed in table 2.

The dose was calculated by the AAA_8908 algorithm. Each of the six treatment beams delivered 1/6 of the dose to the isocentre. The dose grid resolution was set to $1.0 \times 1.0 \times 1.0$ mm^3.

2.3.4. Treatment planning: polymer gel dosimetry (plan PGD) Following the acquisition of the CT scan of the head phantom and polymer gel dosimeter inside a borosilicate glass container, the images were sent to the planning system. In a first

Table 2. Overview of the constraints imposed on the treatment planning system for optimisation.

Organ	Constraint	Volume of organ	Dose
Brain	upper	0 %	105 %
Eyes (2)	upper	0 %	15 %
Eye lenses (2)	upper	0 %	3 %
Optic chiasm	upper	5 %	100 %
Optic nerves (2)	upper	0 %	90 %
PTV_optim	upper	0 %	105 %
	upper	50 %	100 %
	lower	95 %	96 %
	lower	50 %	100 %

step, the CT dataset of the polymer gel was co-registered with the CT dataset of the radiochromic gel in Eclipse. In a second step, the treatment plan from the PGD plan was copied onto the RGD plan including all structure contours, beam parameters and fluence maps. The mean dose to the PTV_optim was modified as compared to RGD plan to accommodate for the different dosimetric range of the polymer gel dosimeter. A mean dose of approximately 10 Gy to the PTV_optim was chosen as for higher doses the dose response curve starts to saturate and loss of spatial integrity may occur (De Deene 2006a).

2.3.5. Independent validation of the TPS calculated dose maps To validate that the linac delivers what is calculated by the TPS, a reference measurement was performed in the centre of the cylindrical phantom filled with a 6 % gelatin gel using a small volume ionisation chamber (PTW pintpoint 31006). Using a cone beam CT the position of the ion chamber was located and the measured dose could be compared to the calculated dose in the same volume. The ion chamber was positioned in a homogeneous dose region of the PTV_optim structure in the phantom. Additionally, portal dose measurements were performed on all six radiation beams and for both plans to validate the calculated dose distributions using the on board flat panel detector.

2.3.6. Irradiation The irradiation was performed on a Varian Clinac 2300IX. Prior to the treatment delivery, a cone beam CT was acquired to match the phantom position to the treatment planning CT. The phantom with the radiochromic gel dosimeter was irradiated in 2 subsequent fractions resulting in a dose of 45 Gy to the isocentre. The phantom with the polymer gel dosimeter was irradiation to a dose of 10 Gy to the isocentre in one fraction. Next, small calibration vials filled with polymer gel were irradiated to well-defined doses. The calibration phantoms were irradiated in a calibration solid water phantom. The phantom consisted of 10 solid water plates of 14 cm $\times$ 14 cm $\times$ 1 cm in which a cylindrical cut-out allowed for the positioning of calibration phantoms. The dose at each position in the phantom was measured independently with

a pin-point ion chamber measurement. Next the calibration phantom was loaded with calibration vials and irradiated with a 10 × 10 cm^2 6 MV photon beam at a SSD of 90 cm assuring that 1 MU equals 1 cGy at 10 cm depth. In total 17 calibration phantoms were irradiated: 8 calibration phantoms were exposed to a fluence of 925 MU to cover the high radiation dose range and another 9 test tubes were irradiated to 250 MU to cover the lower end radiation dose range.

2.3.7. Radiochromic gel readout The dose distribution in the irradiated radiochromic gel was read out with the Optoscan. A set of 180 projections of 120 mm were acquired with a 2 degree angular increment. 600 spatial increments were acquired per projection yielding a profile resolution of 0.2 mm which is averaged to 1 mm prior to reconstruction. A stack of 30 slices (2 mm slice distance) was acquired. The total scan time amounted to 119 minutes.

The optical density maps were then calibrated to dose maps relative to the isocentre measured dose using the pin-point ion chamber measurement.

2.3.8. Polymer gel readout The irradiated PAGAT gel dosimeter and 14 calibration phantoms were scanned with a 1.5 T clinical MRI scanner (Siemens Magnetom Avanto) using the dedicated temperature stabilisation protocol. The following imaging parameters were used: multiple spin echo sequence with voxel size 1 × 1 × 2 mm^3, TR = 10.000 ms, number of equidistant echoes = 32, TE = 40 ms - 1280 ms, receiver band width = 130 Hz per voxel, 17 concatenations and NEX = 6. R_2 maps were calculated as described elsewhere (Vandecasteele and De Deene 2013a). The dose-R_2 relation was derived from the calibration phantoms and used to calibrate the R_2 maps to dose maps. The temperature was monitored during the first 18 hours of the measurement which took 25 hours in total with optical temperature sensors.

2.3.9. Data processing The measured dose maps were compared with the calculated dose maps in the measured region. Using in-house written Matlab code the MRI measured cylindrical dose distribution extracted from the polymer gel is co-registered onto the planning data based on the outer contour of the cylinder and 1 fiducial marker inside the phantom to eliminate any rotational freedom. The cylindrical dose distribution measured with the Optoscan is also aligned with the planning dose distribution using the outer contours of the phantom and a fiducial marker at the top of the phantom.

To assess the accuracy of the dosimetric technique, absolute dose difference maps were calculated. Using profiles along multiple directions, cranio-caudal, latero-lateral and anterior-posterior, the measured and calculated doses are compared in both low and high dose regions. Also isodose contours of the three orthogonal planes through the isocentre were compared.

To assess the clinical repercussions, 3D gamma maps with 3 % dose difference and 3 mm distance to agreement criteria and 2 % / 2 mm criteria were calculated (Low *et*

al 1998, Low and Dempsey 2003). As already discussed in Vandecasteele and De Deene 2013a, the measurement data was chosen as reference data and the noise-free TPS data was chosen as the evaluated dose distribution. Finally, dose volume histograms (DVH's) are compared in structures that are, entirely, present inside the cylindrical volume: optic chiasm and PTV_optim.

2.4. Spatial integrity of the radiochromic gel dosimeter

Previously, it was reported that the dye molecules in the irradiated radiochromic gel dosimeter diffused at a rate of 2.45×10^{-7} cm^2 s^{-1} (Vandecasteele *et al* 2011). In present study the optical diffusion coefficient was determined again because several observations (data not shown) indicated that the spatial integrity was preserved for several days.

The optical diffusion coefficient was measured by irradiating half of a spectroscopic PMMA cuvette (dimensions $1.0 \times 1.0 \times 4.5$ cm^3) filled with the RGD to a dose of approximately 200 Gy with a 6 MV photon beam. Next, the irradiated spectroscopic sample was positioned in the Optoscan scanner and 988 consecutive profiles of resolution 0.1 mm were acquired along the length of the sample over a period of 16.5 hours. The ambient temperature in the room amounted to 25°C. The diffusion coefficient of the radiochromic gel is derived by fitting the measured optical density profiles to an analytical diffusion function as explained in Vandecasteele *et al* 2011.

The linearity of the dose response of the radiochromic gel was verified by irradiating 5 spectroscopic PMMA cuvettes filled with the radiochromic gel to several well-defined doses between 0 Gy and 50 Gy in a large water container. The samples were read out by an USB 4000 fibre optic spectrometer (Ocean Optics, Dunedin, USA) using an in-house constructed white LED source. The maximum absorption peak (at 633 nm) was used to calculate the optical density difference relative to an unirradiated radiochromic sample. This spectroscopic sample dose response measurement could not be used to calibrate the optical density maps of the volumetric phantom because the dose response between the spectroscopic samples and volumetric phantom (of the same batch of gel) differs over time. This is attributed to a difference in the auto-oxidation rate between spectroscopic samples and the volumetric phantom resulting from their exposure to a different temperature history after fabrication.

Therefore, the dose sensitivity of four batches of radiochromic gel was measured by extracting the dose response information from four different volumetric phantoms exposed to an IMRT treatment (as explained in section 2.3). The dose in the volumetric phantom was independently measured with an ion chamber measurement and correlated to the measured optical density values in the gel in a region of dose maximum and a region of dose minimum. From a linear fit of the optical density values versus the dose response, the dose sensitivity was calculated (Vandecasteele *et al* 2011).

3. Results

3.1. Depth dose measurement

A well defined depth dose distribution (6 MV, 4×4 cm^2 photon beam) was measured with a radiochromic and a polymer gel dosimeter. Both gel measurements are compared against a diamond detector measurement along the central axis of the beam.

3.1.1. Radiochromic gel measurement The radiochromic gel dosimeter (figure 3a) was scanned optically in twenty-four slices, 5 mm apart, using the Optoscan laser scanner.

The measured optical density maps were calibrated to dose maps relative to a diamond detector measured dose value in a reference point at 2.5 cm depth. In figure 3b, six of the twenty-four slices are shown measured 19 minutes after irradiation at various depths. The next day, the same gel was rescanned after being thermally equilibrated to room temperature for 3 hours (in total 21 hours post irradiation). The corresponding dose maps are shown in figure 3c. The central 1×1 cm^2 region of all slices was averaged and compared to a diamond detector measurement as shown in figure 3d. In figure 3e, the dose difference with the diamond detector measurement is calculated relative to the dose maximum of 42.57 Gy.

The mean total noise value of all twenty-four 1×1 cm^2 ROI's amounts to 0.51 Gy (1.2 % of dose maximum) with a mean stochastic noise value of 0.28 Gy and mean structural noise value of 0.41 Gy. Hotspot voxels are observed in the axial images resulting in a dose increase relative to the background value of on average 5 % with a maximum peak value of 8 % dose deviation in 1 voxel. The location of these hotspots does not change between the two measurements as can be seen in figures 3b and 3c at 65 mm depth.

3.1.2. Polymer gel measurement A coronal slice through the middle of the irradiated depth dose distribution in the polymer gel dosimeter (figure 4a) was acquired on a 1.5 T MRI scanner in temperature controlled conditions. The measured R_2 maps were calibrated to dose maps using a set of calibration phantoms irradiated to well defined doses. The dose - R_2 calibration curve is shown in figure 4b and fitted against a mono-exponential function.

The cylindrical gel phantom was scanned in two different set-ups. During the first MRI measurement the cylindrical phantom was positioned with the top of the phantom (the dose maximum region) at the centre of the MRI head coil (figure 4d). During the second measurement, the middle of the phantom (approximately 15 cm from the top of the phantom) was positioned in the centre of the MRI head coil (figure 4e). Depth dose profiles were extracted for both cases from the measured dose maps by averaging a region of 1 cm wide along the depth dose distribution in the centre of the dose map (figure 4c). The calculated percentage dose difference with the diamond detector measured doses relative to the dose maximum is shown in figure 4f.

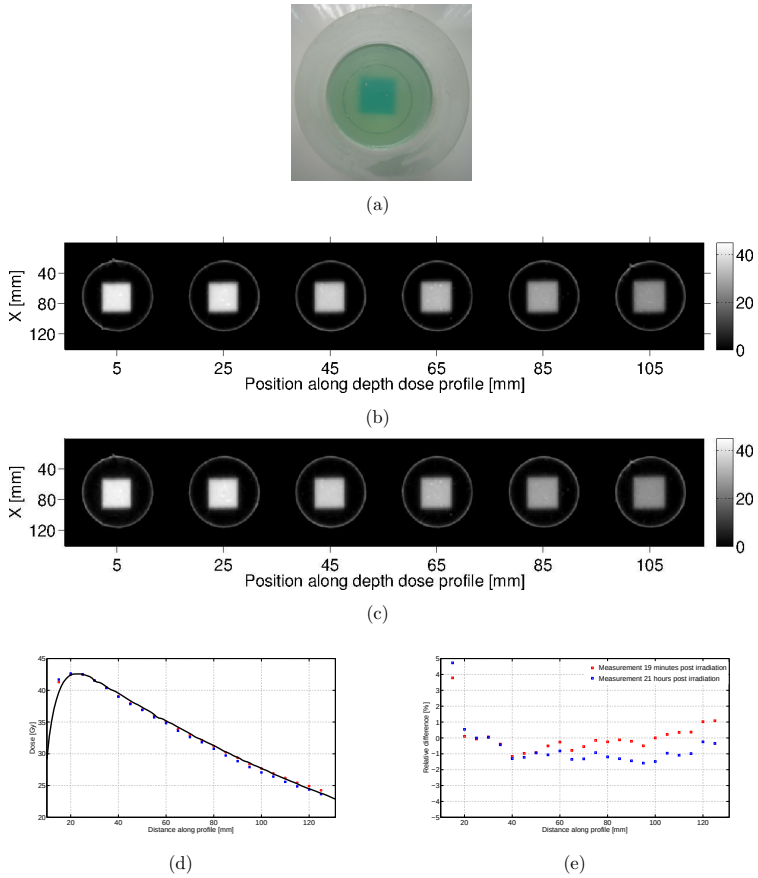

Figure 3. A photograph of the top view of the irradiated radiochromic gel dosimeter is shown in a. In b and c, six of the twenty-four measured dose maps are shown along the depth dose distribution measured 19 minutes and 21 hours post irradiation respectively. The centre 1×1 cm^2 region of each slice was averaged and compared to the diamond detector measured depth dose distribution in d. To assess the dose deviation, a percentage dose difference with the diamond detector measurement is shown relative to the dose maximum of 42.57 Gy.

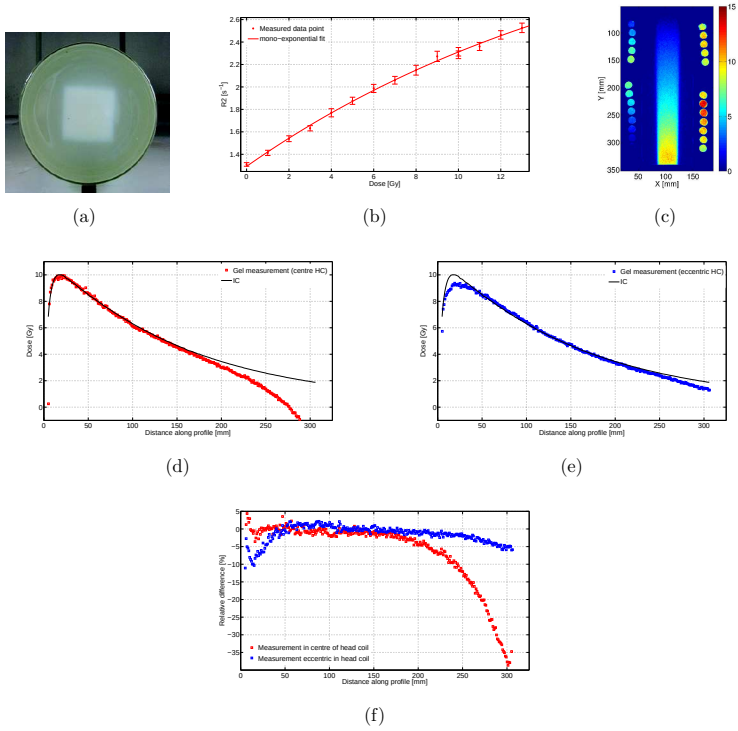

Figure 4. A photograph of the top view of the irradiated polymer gel dosimeter (a) shows the square beam. A dose - R_2 relationship derived from the calibration phantoms and corresponding mono-exponential fit (shown in b) is used to calibrate the MRI measured R_2 maps to dose maps. The resulting dose map of the cylindrical phantom and calibration phantoms is shown in c. Only the calibration phantoms located in the homogeneous region of the MRI coil are used to calculate the dose response curve. A dose profile was extracted from two consecutive MRI measurements of the cylindrical phantom and compared to a diamond detector measurement. During the first MRI measurement the cylindrical phantom was positioned so that the dose maximum was placed in the centre of the MRI head coil (d). During the second measurement, the middle of the phantom was positioned in the centre of the MRI head coil (e). The dose difference with the diamond detector measurement relative to the dose maximum (10 Gy) is shown in f.

3.2. IMRT dose verification

3.2.1. Independent validation of the TPS calculated dose maps Portal dose verification of both clinical treatment plans showed more than 99.4 % of voxels passing the gamma 2 % / 2 mm criteria for all beams of both treatment plans assuring that the planned dose distribution could also be delivered by the linac.

Furthermore, a pin-point ion chamber measurement was performed at the centre of a gelatin gel filled FEP container which was inserted in the head phantom to verify the dose in the centre of the PTV_optim. The position of the ion chamber was verified with a cone beam CT image acquired at the linac. First, the head phantom was irradiated with the RGD plan. The recorded dose amounted to 22.62 Gy which is 0.53 % higher than the planned dose. Next, the same phantom set-up was also irradiated with the PGD plan resulting in a dose of 10.25 Gy which is 1.7 % higher than the planned dose.

3.2.2. Radiochromic gel dosimetry Results of the IMRT treatment verification using a radiochromic gel dosimeter are shown in figure 5. A comparison of the gel measured dose and TPS calculated dose was performed in an axial slice through the isocentre and shown in figure 5a and 5b as an overlay figure on the CT image. A percentage difference map between both is shown in 5c and a gamma (3 % / 3 mm) evaluation map is shown in 5d in which only voxels with a value greater than 1 are displayed.

Visually the TPS calculated (figure 5a) and gel measured dose map (figure 5b) agree well. However, in the radiochromic gel measured dose map artefacts can be seen as local hotspots in the order of 4 to 9 %. This is also clearly visible in the percentage dose map and the gamma map.

A full 3D comparison reveals that the mean 3D dose difference between the planned and measured dose distributions amounts to -0.85 % of the dose at isocentre. The percentage of voxels having an absolute dose deviation of more than 5 % and 6 % amounts to 5.5 % and 3.5 % respectively. About 3.6 % of voxels in the entire volume fail the gamma 3 % / 3 mm while 10.6 % of the voxels fail a gamma criterion of 2 % / 2 mm.

Measured transversal, sagittal and coronal dose maps through the isocentre are shown in figure 5e, 5f and 5g respectively as isodose contours over the color filled contours of the TPS calculated dose maps. Overall, a good agreement between the isodoses is seen. However, dose hotspot are again clearly visibly in the gel measured data.

Profiles through the isocentre slice in an axial plane along the anterior-posterior direction (vertical dashed line in figure 5e, 5h) and a lateral direction (horizontal dashed lines in figure 5e, 5i) are compared. Also a cranio-caudal profile (vertical dashed line in figure 5g) at the centre of the PTV starting from the top of the head is shown in 5j.

3.2.3. Polymer gel dosimetry Results of the IMRT treatment verification using a polymer gel dosimeter are shown in figures 6 and 7. To calibrate the MRI measured

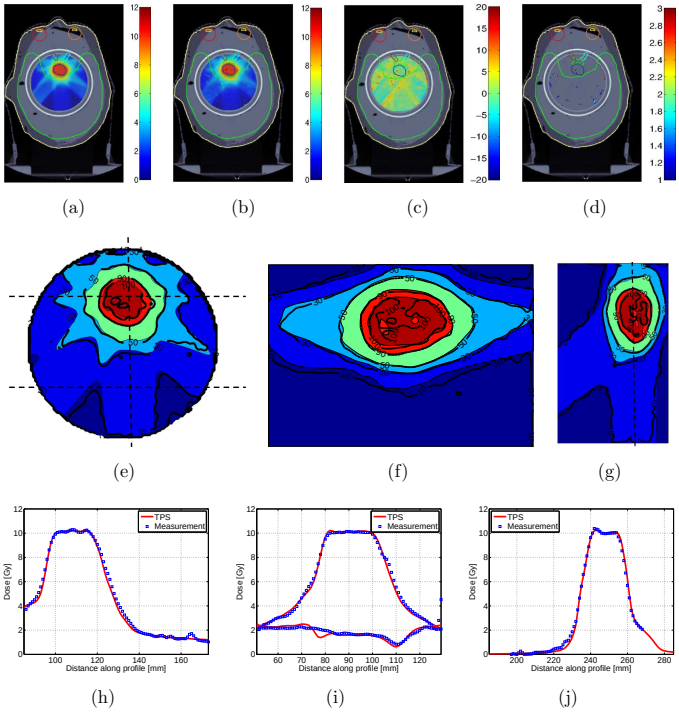

Figure 5. An axial CT image though the isocentre of the head phantom filled with the radiochromic gel dosimeter is shown along with several critical structures and the target. The TPS calculated dose distribution (a) and the gel measured dose distribution (b) are shown as color overlays on the CT images. The color scale is in units of Gy. In (c) a percentage dose difference map and in (d) a 3 % / 3 mm gamma evaluation map are shown. Radiochromic gel measured isodoses (105 %, 100 %, 90 %, 50 %, 30 % and 10 %) overlaid on the treatment planning calculated color filled contours in an axial (e), coronal (f) and sagittal (g) plane through the isocentre. Dose profiles through the isocentre slice of the IMRT irradiation in an axial plane along the anterior-posterior direction (h, vertical dashed line in (e)) and lateral directions (i, horizontal dashed lines in (e)) are displayed. A cranio-caudal dose profile is shown in (j, vertical dashed line in (g)).

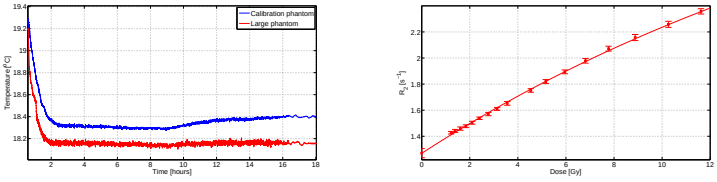

(a) (b)

Figure 6. The temperature history recorded in a calibration phantom and the large cylindrical phantom during the MRI measurement is displayed in a. The dose-R_2 plot extracted from the calibration vials irradiated in the calibration phantom in b. The full line is a mono-exponential fit.

R_2 maps to dose maps, the dose - R_2 relationship was determined by irradiating the calibration vials in a calibration solid water phantom to well defined doses. The calibration phantom is able to generate doses along the entire dynamic range of the dosimeter as shown in figure 6b. The temperature in the cylindrical phantom and one calibration phantom during the first 18 hours of MRI scanning is shown in figure 6a. Two hours after the start of the measurement, the temperature difference stabilises to approximately 0.15 °C. However, 10 hours after the start of the measurement, the temperature difference between calibration phantom and large cylindrical phantom increased to approximately 0.25 °C. A comparison between the gel measured dose and TPS calculated dose in an axial slice through the isocentre is shown in figure 7a and 7b as an overlay figure over the CT image. A percentage difference map between both dose distributions is shown in 7c and a gamma (3 % / 3 mm) evaluation map is shown in 7d in which only voxels with a value greater than 1 are shown.

A high level of visual agreement between the TPS calculated (figure 7a) and gel measured dose map (figure 7b) can be seen. However both the percentage difference map and the gamma evaluation map show a dose over-response at the PTV of approximately 4 %.

A full 3D comparison reveals that the mean 3D dose difference between the planned and measured dose distributions amounts to -0.3 % of the isocentre dose. The amount of voxels with an absolute dose deviation of more than 5 % and 6 % amounts to 2.9 % and 1.7 % respectively. About 1.0 % of the voxels in the entire scanned volume fail the gamma 3 % / 3 mm criterion and 8.4 % of the voxels fail the gamma 2 % / 2 mm criterion.

Measured transversal, sagittal and coronal dose maps through the isocentre are shown in figure 7e, 7f and 7g respectively as isodose contours over the color filled contours of the TPS calculated dose maps. Overall a good agreement between the isodoses is observed.

Profiles through the isocentre slice in an axial plane along the anterior-posterior

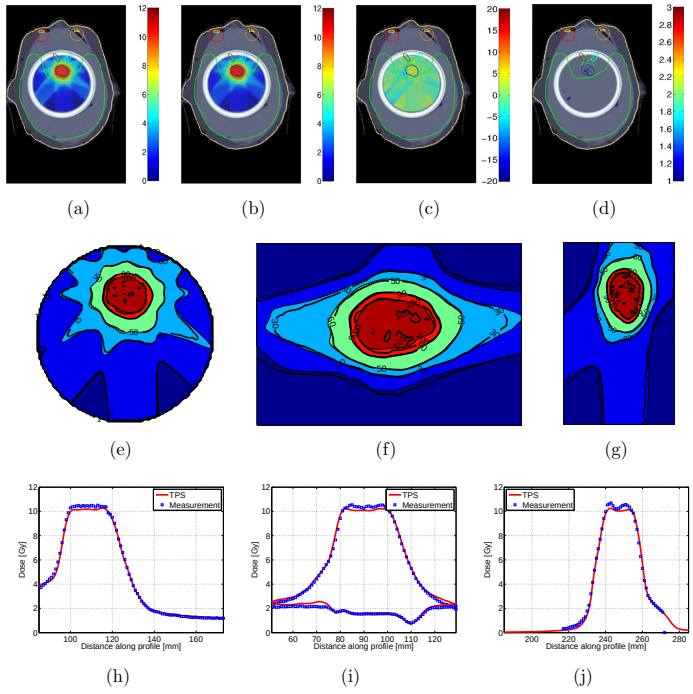

Figure 7. An axial CT image though the isocentre of the head phantom filled with the polymer gel dosimeter is shown along with several critical structures and the target. The TPS calculated dose distribution (a) and the gel measured dose distribution (b) are shown as color overlays on the CT images. The color scale is in units of Gy. In (c) a percentage dose difference map and in (d) a 3 % / 3 mm gamma evaluation map are shown. PAGAT gel measured isodoses (105 %, 100 %, 90 %, 50 %, 30 % and 10 %) overlaid on the treatment planning calculated color filled contours in an axial (e), coronal (f) and sagittal (g) plane through the isocentre. Dose profiles through the isocentre slice of the IMRT irradiation in an axial plane along the anterior-posterior direction (h, see figure 5e for location)) and a lateral directions (i, see figure 5e for location)) are displayed. A cranio-caudal dose profile is shown in (j, see figure 5g for location).

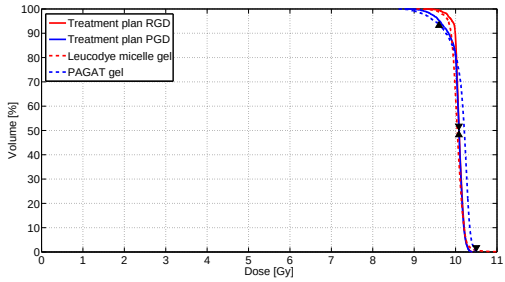

(a)

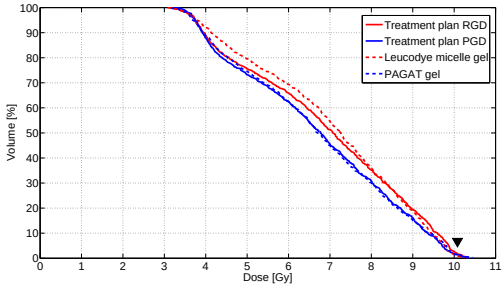

(b)

Figure 8. Dose volume histograms of the PTV_optim (b) and optic chiasm (c) comparing the two plans with the gel measurements. The black triangles indicate the upper constraints (pointing downwards) and lower constraints (pointing upwards) as mentioned in table 2.

direction (vertical orientation in figure 7e, 7h) and a lateral direction (horizontal orientation in figure 7e, 7i) are compared. Also a cranio-caudal profile (vertical orientation in figure 7g) at the centre of the PTV starting from the top of the head is shown in 7j.

3.2.4. IMRT treatment validation Dose volume histograms for the target volume (figure 8a) and one organ at risk (optic chiasm, figure 8b) agree very well with the DVH predicted by the planning system for both dosimetry techniques. All clinical objectives (indicated by black triangles in figure 8a and 8b) were met as measured with radiochromic gel dosimetry. The polymer gel dosimetry experiment shows that the dose in the PTV_optim was exceeded by 4 %.

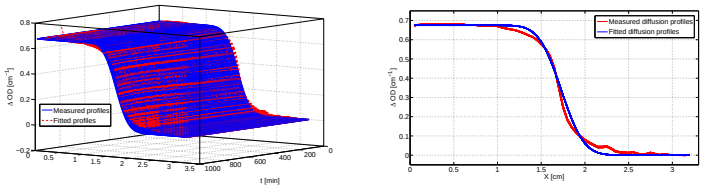

(a) (b)

Figure 9. A 3D plot of the measured diffusion profiles (red) is shown as function of time compared to the calculated profiles (blue) in a. All measured diffusion profiles in a total time span of 16 hours (red) are plotted on top of each other and compared to all fitted diffusion profiles (blue) in b.

3.3. Spatial integrity of radiochromic gel

The spectroscopic sample dose response measurement revealed a linear dose response relationship as was also shown in Jordan and Avaakumov 2009, Vandecasteele *et al* 2011 and Skyt *et al* 2013a. This dose response relationship could not be used to calibrate the volumetric phantom because of a difference in the auto-oxidation rate between the spectroscopic samples and the volumetric phantom. Therefore, the dose sensitivity of four separate measurements of four different batches of gel was extracted from the volumetric phantoms and amounted to $3.19 \pm 0.041 \times 10^{-3}$ cm^{-1} Gy^{-1}. The offset background colouration amounted to $4.31 \pm 0.0087 \times 10^{-2}$ cm^{-1}.

The diffusion coefficient amounted to 4.5×10^{-8} cm^2 s^{-1} (= 0.016 mm^2 h^{-1}). In figure 9a the 3D plot of the measured diffusion profiles is shown as function of time compared to the fitted profiles. To demonstrate the low diffusion coefficient, all diffusion profiles measured in the total time span of 16 hours are plotted on top of each other and compared to the fitted diffusion profiles in figure 9b. Optical density values were corrected for a post irradiation chemical auto-oxidation reaction of 3.83×10^{-5} cm^{-1} h^{-1} (= 0.875 cGy h^{-1}).

4. Discussion

4.1. Depth dose measurement

4.1.1. Radiochromic gel measurement A good dosimetric agreement was found between the radiochromic gel recorded depth dose and the diamond detector recorded depth dose profile with a maximum deviation within ±2 % (omitting the first measurement point). In this first point, a maximum dose deviation of 4.7 % and 3.9 % relative to the dose maximum of 42.57 Gy is observed (15 mm depth) in the first and second measurement respectively (figure 3e). The larger dose deviation in the first point can be attributed to the dose rate dependence as reported in Vandecasteele *et al* 2011, however a slight

energy dependency of the gel can not be entirely excluded.

The deviations in the optically measured dose maps are approximately 2 % of the maximum dose value which predominantly originates from structural dose deviations. This structural noise originates from local dose hotspots of on average 5 % relative to the background value in the axial images. Two hotspots of upto 8 % dose over-response were also recorded. These hotspots are presumed to originate from refractive index variations inside the gel causing a deflection of the laser beam resulting in image artefacts. These refractive index variations probably originate from local variations in gel composition within the gel. During the fabrication of the gel, the negatively charged SDS head groups bind to the positively charged gelatin maze. Trichloroacetic acid causes a drop in the pH of the gel below the isoelectric point of gelatin making it positively charged (Vandecasteele *et al* 2011). Optical swirls or Schlieren can be seen immediately after fabrication when the gel is still in a liquid phase. These Schlieren are no longer visible 2 to 3 hours after fabrication. However it is believed that small refractive index differences may still be present in the gel during optical readout which may be responsible for the dose hotspots. These effects were not reported in Vandecasteele *et al* 2011 and are presumed to be related to the novel fabrication protocol. Further optimisation of the gel fabrication is needed to eliminate these artefacts. This artefact is similar to the Schlieren artefacts reported in Presage dosimeters that are caused by inhomogeneous polymerisation of the polyurethane matrix during fabrication (Doran and Krstajić 2006).

Furthermore, a circular dose deviation of more than 4 % relative to the dose maximum at 5 mm from the edge is visible in the scanned axial slices. This ring artefact is caused by an imperfect match of the refractive index of the gel and the FEP phantom cast. Using an unirradiated pre-scan to correct for this artefact could increase the area in which the dose can be measured. However a sub-millimetre repositioning precision of the phantom in the Optoscan laser scanner is not yet achievable which makes it impossible to perform a correction scan.

When comparing gel measured dose distributions read out 19 minutes after irradiation and gel measured dose distributions read out after storage at 4°C for 19 hours post-irradiation (figure 3b and 3c), the low diffusion coefficient is demonstrated as no loss of spatial integrity can be detected.

4.1.2. Polymer gel measurement It is clear from figure 4d and 4e that the positioning of the phantom in an MRI coil has a significant effect on the dose accuracy. The transmit-receive CP head coil used in this experiment has a finite volume in which the nuclei are excitated with the same flip angle. So by shifting the phantom inside the head coil, a different section of the gel dosimeter was homogeneously exited resulting in a good dosimetric accuracy within ± 4 %. From figure 4d and 4e, it can be seen that this area of uniform excitation is approximately 9 cm at either side from in the centre of the head coil. In this experiment, the head coil was used to increase the signal to noise ratio of the dose maps as compared to the body coil. In De Deene and Vandecasteele (2013) an overview is given of all factors contributing to the overall uncertainty of polymer gel dosimetry.

When dedicated protocols are applied, the random and systematic uncertainties of a polymer gel dosimetry measurement can be reduced to within 5 %.

Additionally, from figure 4c spatial deformations can be observed that can be attributed to gradient non-linearities or B_0 inhomogeneities. In Vandecasteele and De Deene 2013c, a method is suggested to assess and compensate for the influence of B_0 and B_1 non-uniformities.

The temperature stabilisation technique using thermal pads succeeds in minimising temperature drift between calibration phantoms and the volumetric phantom, which is demonstrated by the good dosimetric agreement between the polymer gel recorded and diamond detector recorded depth dose distributions. However, it should be noted that the measurement time of the coronal image acquisition was only 30 minutes.

4.2. IMRT dose verification

4.2.1. Independent validation of the TPS calculated dose maps Both clinical IMRT plans were approved by portal dose verification, assuring that the planned dose distributions could also be delivered by the linac. Additionally, pin-point ion chamber measurements were performed in the centre of the PTV_optim. Good agreement was found for PGD plan and a small over-dosage was recorded for the RGD plan. This dose deviation can be attributed to the use of the FEP phantom instead of glass phantom to position the ion chamber during the dose measurement. The thicker and higher density wall of the glass phantom results in the need for a higher radiation fluence to obtain the same relative dose at the centre of the phantom. Finally, both gel measured dose distributions are compared against the predicted dose distributions calculated for the specific phantom geometry.

4.2.2. Radiochromic gel dosimetry A fair correspondence between the TPS calculated and gel measured dose maps is found. The dose information in a ring of 2 mm from the edge of the radiochromic phantom was omitted from the analysis because of the presence of a circular dose artefact resulting in deviations up to 40 %.

Nonetheless, the results show that 5.5 % of voxels deviate more than 5 % in absolute dose. This is also confirmed by the gamma evaluation (only 89.2 % pass the 2 % / 2 mm criteria) and can be visually inspected in figure 5. The origin of these dose deviations can be attributed to two sources of error. Firstly, the dose in a group of voxels near the edge of the phantom still deviates from the planned dose. As mentioned before in section 4.1.1, this circular dose artefact is caused by a small refractive index matching mismatch.

A second source of dose deviations and the most important one can be found in local hotspots which can be observed in figure 5b. These hotspots exist throughout the dose volume and are caused by small refractive index variation in the gel. They cause significant dose errors up to 10 %. Future research will focus on the fabrication procedure

in order to obtain a more homogeneous gelation of the gel. More research may be needed to study the chemistry of the radiochromic gels and their radio-physical properties. From this and previous studies can be concluded that the fabrication procedure has a large effect on the spatial stability and the dose sensitivity.

As illustrated by three orthogonal planar dose comparisons through the isocentre (figure 5e to 5g) and dose profile comparisons (figure 5h to 5j), the gel measured dose distributions match the TPS predicted dose distributions very well. The TPS predicted and gel measured dose volume histograms for the PTV_optim and optic chiasm also agree very well. The contribution of the dose hotspots can be seen in the tail of the DVH of the PTV_optim in figure 8a indicating that a small volume of the radiochromic gel records a significant over-dosage.

4.2.3. Polymer gel dosimetry The calibration phantoms were irradiated to different well-defined radiation doses using an in-house constructed radiation calibration solid water phantom. Compared to previous calibration protocols in which each individual calibration tube is irradiated perpendicular to the beam's axis at a reference depth in a cubic water phantom, this novel technique is fast and equally reproducible. The dose at each depth in the radiation calibration phantom was measured with an ion chamber prior to usage. The effect of the borosilicate glass wall of each test tube was found to reduce the dose with 1.4 % per millimetre of borosilicate glass material.

A fair agreement was found between the polymer gel measured dose maps and the TPS predicted dose maps. A mean overdose of 4 % at the PTV_optim is reported which is not attributed to an error in the dose delivery. The gamma evaluation also shows 8.4 % of the voxels fail the 2 % / 2 mm criteria predominantly in the PTV_optim region and at the edge of one of the beams (figure 7d). The deviation is attributed to a temperature difference between the calibration phantoms and the large phantom (Vandecasteele and De Deene 2013c). The temperature history during the first 18 hours of the MRI scan suggests a temperature difference of 0.25°C between the calibration phantoms and the large cylindrical phantom. As shown in Vandecasteele and De Deene 2013c this can lead to a dose deviation of approximately 2.25 %. Unfortunately, during the last 8 hours of the experiment no temperature was recorded which could explain larger dose deviations resulting from a higher temperature offset between calibration phantoms and the cylindrical phantom. These results suggest that the technique using thermal pads may not be sufficient to minimise temperature deviation and to keep dose errors below 0.4 Gy. It has been demonstrated that centric k-space MRI signal acquisition would decrease the temperature induced uncertainties provided that the temperature between the calibration phantoms and volumetric phantom is equilibrated at the start of the MRI readout (De Deene and De Wagter, 2001).

4.3. Spatial integrity of radiochromic gel

The dose sensitivity of the radiochromic gel dosimeter amounted to $3.188 \pm 0.041 \times 10^{-3}$ cm^{-1} Gy^{-1} which is 73 % of the dose sensitivity reported in Vandecasteele *et al* 2011. This value is very reproducible shown by the small standard deviation of 1.3 % of the mean value obtained from four measurements. The value of the dose sensitivity and background coloration offset is determined from the volumetric phantoms and not from spectroscopic samples because both values differ due to a difference in auto-oxidation rate. The different auto-oxidation rate is attributed to the fact that the spectroscopic samples and the volumetric phantom do not experience the same temperature history after fabrication. Because a large volume of gel in the volumetric phantom has more thermal inertia than the spectroscopic samples, large temperature differences will occur between the phantom and the spectroscopic samples during cooling of the gel after fabrication (in a refrigerator) and reacclimatising to room temperature before irradiation. These temperature differences will affect the auto-oxidation rate as shown by Vandecasteele *et al* 2011 and Skyt *et al* 2013b.

A high dose delivery is needed because of the low dose sensitivity of the radiochromic gel dosimeter. In the IMRT dose verification experiment, the prescribed dose was set to approximately 45 Gy. This dose assures a high signal-to-noise value in the dose maps. However, it is not typical for radiation therapy dose fractions and makes it hard to record any effects of clinical leaf motion speeds. These high dose requirements could nevertheless be an advantage for stereotactic radiotherapy applications where high single fraction doses are delivered and to verify the overall treatment dose delivery from multiple fractions.

In the present study, the diffusion rate of the radiochromic gel dosimeter measures 5.5 times lower (0.016 mm^2 h^{-1}) than the diffusion coefficient given in a previous study (Vandecasteele *et al* 2011 (0.088 mm^2 h^{-1})) for a gel with similar composition. We attribute this difference to a slight modification in the fabrication protocol . In Vandecasteele *et al* 2011, LMG is dissolved in pure chloroform after which this solution is added to the water - SDS - trichloroacetic acid solution. This fabrication process is very fast as LMG readily dissolves in chloroform. In the present study, LMG is added to a water - SDS - trichloroacetic acid - chloroform solution and stirred for 30 minutes until all dye is dissolved. This fabrication protocol results in a significant reduction in background colour which results in a higher signal to noise ratio as the dynamic range of the gel dosimeter is higher. It is hypothesized that the exposure of LMG to pure chloroform induces chemical changes which affect the diffusion characteristics of the dye molecule. Further research is needed to understand the real mechanism.

The reduced diffusion coefficient of the radiochromic dosimeter enables readout up to 10 hours post-irradiation with sub-millimetre root-mean-square displacement of the dye in the dosimeter and thus without any significant perturbation of the dose distributions. In the present study, the maximum time needed to acquire a full 3D dose matrix amounted to 2.5 hours. In this timespan a root mean square displacement of

only 0.49 mm is predicted.

5. Conclusions

Two full 3D gel dosimeters were assessed for the dose verification of a clinical IMRT treatment. A PAGAT polymer gel dosimeter with MRI readout was compared against a leucodye micelle radiochromic gel dosimeter with optical readout using an in-house developed optical laser CT scanner.

Both gel dosimeters measured a 6 MV photon beam depth dose profile within 4 % accuracy compared to a diamond detector measurement. Ultimately, the two dosimeters were evaluated for a clinical IMRT treatment of a brain tumour. The gel measured dose distributions were compared against treatment planning system (TPS) dose distributions.

The radiochromic gel dosimeter fabricated in this study is a radiation detector with a high spatial stability. In the 3D measured volume of the radiochromic gel, two dose deviations could still be identified. Firstly, the dose in a group of voxels near the edge of the phantom deviated from the planned dose. Secondly, localised dose hotspots in the order of 8 % to 10 % are observed related to chemical inhomogeneities. These dose uncertainties limit the clinical acceptance of this dosimetry technique. Based on the promising results of the micelle gel dosimeter prototype, further chemical optimisation is subject of future work.

Current polymer gel dosimeters are capable of measuring the absolute dose within 5 % accuracy of the whole 3D volume. A temperature stabilisation technique succeeds in increasing the accuracy during short measurements, however to keep the temperature stable during long measurement times in both calibration phantoms and the volumetric phantom is more challenging. Centric k-space MRI signal acquisition can decrease the temperature induced uncertainties provided that the temperature between the calibration phantoms and volumetric phantom is equilibrated at the start of the MRI readout. The polymer gel measurement was also shown to be sensitive to B_0 and B_1 field inhomogeneities. However an accurate 3D dose measurement is possible using a dedicated imaging protocol.

Using both a radiochromic gel dosimeter and a polymer gel dosimeter, we have demonstrated that advanced 3D dosimetry is at the verge of being clinical acceptable in terms of accuracy and time-management. The radiochromic gel dosimetry technique provides many of desired features such as: low cost, easy to fabricate, low diffusion, low toxicity and fast readout. Once the dose hotspot artefacts are eliminated, a larger dissemination of this kind of dosimeters is foreseen.

Still an important role for polymer gel dosimeters is expected in the future of advanced 3D dosimetry. However, the necessity to use temperature stabilisation and other artefact compensation techniques, make it a less user-friendly dosimeter for routine clinical applications. Nevertheless, polymer gel dosimeters have the unique feature of being able to measure absolute radiation doses in anthropomorphically shaped

phantoms. Also, their application in a low density lung dosimetry makes them very valuable (De Deene *et al* 2006b). With the development of MRI - linacs, this type of dosimeter has a unique role to play.

Acknowledgments

This research is supported by the Institute for the Promotion of Innovation though Science and Technology in Flanders (IWT -Vlaanderen). The authors would like to thank Tom Boterberg, Tom Vercauteren, Geert Pittomvils and Leen Paelinck for their valuable help with the treatment planning and Bart Truyens for constructing dedicated equipment that was indispensable in the experimental set-up.

References

Baldock C, De Deene Y, Doran S, Ibbott G, Jirasek A, Lepage M, McAuley K B, Oldham M and Schreiner L J 2010 Polymer gel dosimetry *Phys. Med. Biol.* **55** R1–63

De Deene Y and De Wagter C 2001 Artifacts in multi-echo T2 imaging for high-precision gel dosimetry: III. Effects of temperature drift during scanning *Phys. Med. Biol.* **46** 2697–711

De Deene Y, De Wagter C, Van Duyse B, Derycke S, Mersseman B, De Gersem W, Voet T, Achten E and De Neve W 2000 Validation of MR-based Polymer Gel Dosimetry as a Pre-clinical 3D Verification Tool in Conformal Radiotherapy: Comparison with Film Dosimetry and Computer Planning *Magn. Res. Med.* **43** 116–25

De Deene Y, Pittomvils G and Visalatchi S 2007 The influence of cooling rate on the accuracy of normoxic polymer gel dosimeters *Phys. Med. Biol.* **52** 2719–28

De Deene Y and Vandecasteele J 2013 On the reliability of 3D gel dosimetry *J Phys: Conf Ser* **444** 012015

De Deene Y, Van de Walle R, De Wagter C and Achten E 1998 Mathematical analysis and experimental investigation of noise in quantitative magnetic resonance imaging applied in polymer gel dosimetry *Signal Process.* **70** 85–101

De Deene Y, Vergote K, Claeys C and De Wagter 2006a The fundamental radiation properties of normoxic polymer gel dosimeters: a comparison between a methacrylic acid based gel and acrylamide based gels *Phys. Med. Biol.* **51** 653–73

De Deene Y, Vergote K, Claeys C and De Wagter C 2006b Three dimensional radiation dosimetry in lung-equivalent regions by use of a radiation sensitive gel foam: proof of principle *Med. Phys.* **33** 2586–97

Doran S and Krstajić N 2006 The history and principles of optical computed tomography for scanning 3-D radiation dosimeters *J. Phys.: Conf. Ser.* **56** 45–57

Jordan K and Avaakumov N 2009 Radiochromic leuco dye micelle hydrogels: I. Initial investigation *Phys. Med. Biol.* **54** 6773–89

Low D A and Dempsey J F 2003 Evaluation of the gamma dose distribution comparison method *Med. Phys.* **30** 2455-64

Low D A, Harms W B, Mutic S and Purdy J A 1998 A technique for the quantitative evaluation of dose distributions *Med. Phys.* **25** 656-61

Skyt P S, Wahlstedt I, Yates E S, Muren L P, Petersen J B B and Balling P 2013a Exploring the dose response of radiochromic dosimeters *J. Phys.: Conf. Ser.* **444** 012036

Skyt P S, Kinnari T S, Wahlstedt I, Yates E S, Muren L P, Petersen J B B and Balling P 2013b Diffusion properties of a radiochromic hydrogel dosimeter *J. Phys.: Conf. Ser.* **444** 012038

Vandecasteele J, Ghysel S, Baete S H and De Deene Y 2011 Radio-physical properties of micelle leucodye 3D integrating gel dosimeters *Phys. Med. Biol.* **56** 627–51

Vandecasteele J and De Deene Y 2009 Optimization of a fast optical CT scanner for nPAG gel dosimetry *J. Phys.: Conf. Ser.* **164** 012024

Vandecasteele and De Deene 2013a On the accuracy and precision of 3D polymer gel dosimeters: I. Reproducibility study *Phys. Med. Biol.* **58** 19–42

Vandecasteele and De Deene 2013b On the accuracy and precision of 3D polymer gel dosimeters: II. Physico-chemical effects *Phys. Med. Biol.* **58** 43–61

Vandecasteele and De Deene 2013c On the accuracy and precision of 3D polymer gel dosimeters: III. MRI-related error sources *Phys. Med. Biol.* **58** 63–85

7 Discussion

Radiotherapy aims to achieve maximum cure rate by delivering a lethal dose of radiation to a target volume while minimising the radiation exposure to the surrounding healthy tissues and thus avoiding toxicity. To accomplish this, radiotherapy involves a complex multidisciplinary treatment chain consisting of image acquisition, treatment planning and treatment delivery over the course of several weeks. The accuracy and the precision of the dose delivery achievable over the course of several weeks within one patient and over the course of years between multiple patients is critical to maintain a high percentage of cure rates among the patient population. Dedicated dosimetry is therefore essential in achieving the highest possible dosimetric and geometric accuracy. Uncertainties that accumulate during the consecutive treatment steps may result in a significant effect on the clinical outcome. With the recent developments of dynamic treatment modalities that deliver the radiation dose to the patient by multiple beams that vary in time, the dosimetric needs have changed. Besides the need for a dosimetric verification in three dimensions, an integration of the total delivered dose is essential in assessing the clinical relevance of any accumulated uncertainties affecting the dose distribution. In summary, an ideal 3D dosimeter should exhibit the following characteristics in terms of its functionality in radiotherapy dosimetry:

- Dose integration
- with a high resolution in three dimensions

- humanoid shaped
- meeting desired Resolution-Time-Accuracy-Precision (RTAP) criteria initially proposed for radiosurgery applications (Oldham *et al* 2001):
  1. spatial resolution of 1 mm^3
  2. readout time within 1 hour
  3. dose accuracy of 3 %
  4. noise value within 1 % (1 SD).

This list of functional characteristics are guidelines for the research community. Besides these desired characteristics in terms of functionality, several other more important dosimetric characteristics need to be fulfilled:

- Sensitive to radiation doses used in radiotherapy
- Spatially stable recording of the radiation doses which remain unaffected over significant amounts of time
- Tissue equivalent for all radiation energies that occur in radiotherapy (also for lower energy scattered photons)
- Independent of dose rate variation inevitably occurring in radiotherapy dose depositions.
- Independent of radiation energy spectrum.
- Independent of physical parameters during irradiation such as temperature and pressure
- Pose relative little risk to human health when using the dosimeter

Gel dosimetry has the capability of addressing many of these wanted features as the gels are inherently 3D integrating dosimeters. In this dissertation, we demonstrated and compared the use of two types of gel dosimeters: a polymer gel dosimeter which is read out with MRI and a radiochromic gel dosimeter which is read out with an optical scanner. Each of these gel dosimetry techniques is accompanied with its own strengths and weaknesses. In the next section, the proper use of each of the systems will be discussed taking into account both the needs from a clinical and radiotherapy physics perspective. This dissertation hereby aims at giving a scientific sound estimation of the contribution of different sources of uncertainty in gel dosimetry. As discussed in the introduction, uncertainties are divided into two categories based on their method of evaluation: type A and type B. As all effects discussed here are type A, we will apply a distinction based on

uncertainties originating from random effects and uncertainties originating from systematic effects (table 7.1).

In the next chapters, a summary of all uncertainties originating from physico-chemical, irradiation and readout related effects are discussed for the radiochromic gel system as well as the polymer gel system. Finally, this dissertation aims at giving a standard operating procedure for performing 3D dosimetry using either polymer or radiochromic dosimeters. A thorough knowledge of when and how 3D dosimetry must be put into practice and what results can be expected from a typical 3D gel dosimetry measurement, will facilitate the use of gel dosimetry in a broader community.

7.1 Polymer gel dosimetry

As demonstrated in the introduction (section 1.6) a typical gel dosimetry experiment involves several stages: (1) Gel fabrication, (2) Treatment Planning, (3) Irradiation, (4) Scanning and (5) Post-processing. During each of these stages both random and systematic effects will influence the overall dosimetric and geometric uncertainty of the dose registration. The work presented in papers I to III, demonstrates that the contribution of uncertainties can be reduced to a clinically acceptable level of accuracy by standardising the protocol of a gel dosimetry verification. As there is no "gold standard" for 3D dosimetry, a strong focus was placed on the characterisation of the polymer gel dosimeter as a reference against which all newer 3D dosimetry systems such as radiochromic gel dosimeters and optical readout techniques could be validated. We will first discuss the random uncertainties affecting a 3D dose verification.

7.1.1 Random uncertainty

As can be seen in table 7.1, random uncertainties manifest themselves in all typical stages of gel dosimetry. During the gel fabrication, small variations in concentration of used chemicals and temperature variations during fabrication determine the overall dosimetric precision by influencing the dose response of the gel dosimeter. During irradiation, variations in dose delivery (dose rate, leave propagation, gantry angles,...), phantom (and calibration phantom) positioning, temperature and radiochemical noise will influence the overall geometric and dosimetric precision. During the readout of the gel dosimeter, inherent thermal detector noise induces variations in the measured dose related value (R_2 for polymer gel dosimeters).

	Uncertainties from random effects		Uncertainties from systematic effects	
	Geometric	Dosimetric	Geometric	Dosimetric
Chemical		• Chemical concentrations • Temperature	• Shrinking	• Calibration • Chemical stability • Spatial integrity • Impurities
Radiation	• Phantom positioning • Temperature	• Delivered dose • Temperature • Calibration phantom positioning • Radiochemical noise	• Phantom positioning	• Calibration phantom positioning • Dose rate dependence • Energy dependence • Temperature dependence • Tissue equivalence • Phantom container
Scanning	• Resolution	• Thermal detector noise • Impurities • Dose calibration	• Imaging artefacts	• Voxel shape • Imaging artefacts • Temperature

Table 7.1: *Overview of the uncertainties inherent in gel dosimetry. The uncertainties are divided based on originating from systematic effects and uncertainties originating from random effects. Both random and systematic effects can induce geometric and dosimetric uncertainties originating from the chemical principle of the gel, during the irradiation and during the scanning of the gel.*

By choosing optimised operating procedures and protocols, some of the dosimetric and geometric random uncertainties can be minimised. For example, by fabricating a large batch of gel which is only in the end stage of fabrication divided into a volumetric phantom part and calibrations phantom part, differences in uncertainties in fabrications parameters such as temperature and concentration will be eliminated assuring an optimal calibration. Furthermore, before and during irradiation, the phantom and calibration phantoms should be stored together so that a similar temperature history is experienced. Uncertainties in phantom and calibration phantom positioning can be minimised by using dedicated fixation tools from which the positioning precision can be optimised. It is believed that chemical uncertainties and uncertainties during irradiation can be assumed to be less than 1 % if optimal protocols are applied.

However, scanning of the gel phantoms will have a more profound effect on the random uncertainty of the acquired dose measurement due to inherent thermal detector noise in MRI. These readout uncertainties can be optimised by the choice of scanning protocol (when, how long, where and how phantoms are positioned in the MRI scanner) and the imaging sequence and post processing techniques applied. For example, the use of a small amount of calibration phantoms scanned separately from the volumetric phantom with a suboptimal imaging sequence and post processing technique will result in large uncertainties. As shown by De Deene *et al* 1998a and De Deene and Baldock 2002, images acquired using a multiple spin-echo imaging sequence with an optimised number of echoes processed using a chi-square based minimisation to calculate the R_2 values will greatly reduce the noise.

To assess the influence of random uncertainties in gel dosimetry, the concept of the intrinsic dosimetric precision was proposed, which compares the relative dose resolution $D^p_{\Delta\%}$ (introduced by Baldock *et al* 2001b) independent of spatial resolution (ΔV) and acquisition time ($\sqrt{t_{meas}}$) (equation 7.1, De Deene 2009).

$$IP_D = \left(D^p_{\Delta\%}\Delta V\sqrt{t_{meas}}\right)^{-1} \tag{7.1}$$

The relative dose resolution is defined as the minimal separation at which two doses can be distinguished with a given level of confidence (usually p = 95 %, 2 SD) and is an intrinsic lower limit indication of the random uncertainty of the measured dose relative to an applied dose range (equation 7.2).

$$D^{95\%}_{\Delta\%} = 2.77 \cdot \frac{\sigma_D}{D_{max} - D_{min}} = 2.77 \cdot \frac{\sigma_{R2}}{R_{2,max} - R_{2,min}} \tag{7.2}$$

In the reproducibility study explained in paper I the relative dose resolution (p = 95 %) was calculated and typically (depending on the chosen chemical composition and fabrication protocol) amounts to approximately 3 %. The intrinsic dosimetric precision in this example amounts to 0.26 mm^{-3} $s^{-1/2}$ with a measurement time of 13 m 36 s and a resolution of 5 mm^3. It should be noted that this represents the intrinsic lower limit of the random uncertainty because random variations in the chemical composition, irradiation procedure and calibration have not been included.

7.1.2 Systematic uncertainty

In this dissertation, mainly systematic effects that affect the geometric and dosimetric uncertainty were investigated. In a reproducibility study presented in paper I, an intra-batch experiment (8 separate dosimetry experiments using 1 batch of gel) and an inter-batch (8 separate dosimetry experiments using 8 different batches) were performed using an optimised protocol for fabrication, irradiation and scanning. These experiments revealed a poor dosimetric accuracy resulting in mean dose discrepancies between gel and ion chamber measurements up to 13.7 %. This low accuracy was attributed to a systematic deviation related to the calibration. In the past, several authors also found discrepancies related to the calibration protocol (Low *et al* 1999, Cosgrove *et al* 2000, Cardenas *et al* 2002, Watanabe *et al* 2005, Crescenti *et al* 2007). These discrepancies were attributed to volumetric effects (MacDougall *et al* 2008, Dumas *et al* 2006, Xu *et al* 2010, De Deene *et al* 2002a, Vergote *et al* 2004), cooling history (De Deene *et al* 2007), temperature during irradiation (Salomons *et al* 2002, Sedaghat *et al* 2010, Sedaghat *et al* 2011b), oxygen contamination effects (Hepworth *et al* 1999, Sedaghat *et al* 2011a) and imaging artifacts (De Deene *et al* 2000a, 2000b, De Deene and De Wagter 2001). Despite the fact that all these effects were already taken into account when the reproducibility study was designed, the study still showed large discrepancies.

Several calibration methods have been proposed in the literature. The most frequently used method is based on a dose-R_2 curve obtained from a series of calibration phantoms irradiated to various doses (Baldock *et al* 1998a, 1999, De Deene *et al* 2000c, McJury *et al* 1999) or by use of a single calibration phantom with a well-defined dose distribution (Maryanski *et al* 1994, 1996, Oldham *et al* 1998a, 1998b, Olding *et al* 2011). A Monte Carlo study showed that the most accurate calibration method used test tube calibration phantoms perpendicular to the beam's axis (Taylor *et al* 2007). This technique was therefore also applied in the reproducibility study. Nevertheless, the use of this "optimised" protocol did not result in the anticipated accuracy.

To elucidate the origins of this systematic uncertainty, several experiments were set-up to investigate physico-chemical (paper II) and MRI related (paper III) effects that may attribute to the systematic uncertainty in polymer gel dosimetry.

7.1.2.1 Physico-chemical effects attributing to systematic uncertainty

In table 7.2 an overview of known effects that influence the systematic uncertainty originating from physico-chemical origins are listed. Many physico-chemical aspects have already been extensively investigated by several authors. In paper II some of these effects were reinvestigated (the effect of the temperature history (before, during and after irradiation)) while some new hypotheses were added (oxygen exposure (after irradiation) and a recipient wall effect). From table 7.2, it is obvious that the contribution of systematic uncertainties originating from physico-chemical effects is limited within 2 % when the appropriate protocols are followed. These protocols involve cooling down the phantom and calibration vials in a controlled fashion after fabrication to limit spatial variations of the dose sensitivity within a gel dosimeter. Also the use of appropriate phantom container materials which limit oxygen diffusion into the gel before irradiation is crucial. Another important step is to scan both the calibration vials and the phantom simultaneously at least 12 hours after irradiation to allow the polymerisation reaction to finish (stabilise) and to limit any temporal differences in post irradiation polymerisation. Furthermore, it is important to avoid large temperature fluctuations during irradiation and limit the maximum dose delivered to the phantom to avoid loss of spatial dose integrity. It should be stressed that this list of uncertainties only applies to PAGAT polymer gel dosimeters. For example, the temperature sensitivity during irradiation and dose rate dependency are much larger for metacrylic acid based dosimeters which will strongly affect the uncertainty (De Deene *et al* 2006a).

7.1.2.2 MRI effects attributing to systematic uncertainty

Several MRI scanning related factors can add to systematic uncertainties. These factors are summarised in table 7.3 and sorted on the basis of their effect (*i.e.* whether they result in dosimetric or geometric uncertainties). In paper III, the effects of B_0-field and B_1-field non-uniformity, dielectric effects (losses and standing waves) and temperature inhomogeneity during scanning were quantified. The values listed, serve as a general example and depend on the type of scanner, magnetic field strength, shape of the phantom and coils used.

Physico-chemical mechanism	**Magnitude**	**Estimated Δ (%)**	Reference
Temperature differences during storage			II, a
• *refrigerator*	15°C (5h)	5%	
• controlled environment	4°C (5h)	**1%**	
Temperature differences during irradiation	3°C	**1%**	II, b
Temporal instability:			I
• *Sequential scan*	5 h	2.5%	
• Simultaneous scan	1 h	**1%**	
Spatial dose integrity			c
• Maximum dose < 15 Gy	-	< **1%**	
• *Maximum dose > 15 Gy*	-	≥ 5%	
Dose rate dependence	-	< **1%**	b
Oxygen infiltration			II
• *PMMA*	-	≥10%	
• Barex^{TM} or glass	-	< **1%**	
Recipient wall effect	-	< **1%**	II
Polymerisation induced shrinkage	-	< **1%**	-

Table 7.2: *Overview of estimated systematic uncertainties (Δ) in MRI polymer gel dosimetry originating from physico-chemical mechanisms. In bold are the lower limit uncertainty values associated with applying an optimised protocol. The physico-chemical mechanisms indicated in italic represent bad practice. References to papers included in this dissertation are indicated in Roman numerals. Additional references are: (a) De Deene et al 2007, (b) De Deene et al 2006a, (c) Vergote et al 2004b.*

B_0-field inhomogeneities up to 5 ppm can result in dose deviations up to 4 % and pixel shifts in the order of 2.5 pixels (1.5 T) to 5 pixels (3 T). By increasing the receiver band width (rBW) these pixel shifts can be significantly reduced at the cost of a reduction of signal to noise or total measuring time. Careful phantom construction to minimise sharp boundaries between the phantom and air will avoid susceptibility artefacts. Because humanoid shaped phantoms are one of the big advantages of polymer gel dosimetry, compensation of these artefacts cannot always be accomplished. However, by placing the whole phantom in a water container these artefacts can be easily minimised.

Uncertainties originating from B_1-field inhomogeneities are governed by the dielectric properties of the gel dosimeter and the coil geometry. The effect of coil geometry manifests itself predominately in large phantoms and can result in uncertainties as large as 25 %. Compensation strategies can be applied, reducing the uncertainties to within 3 %. This effect emphasises the importance of using volume coils dedicated to the shape and size of the gel dosimeter. At higher field strengths ($\geq$ 3 T) the dielectric properties of the gel can result in standing waves and losses. This can lead to large uncertainties that are phantom specific. Doping the gel with NaCl can reduce these uncertainties, however the influence of NaCl on the radiophysical properties of PAGAT polymer gel dosimeters needs to be fully assessed. For methacrylic acid based gel dosimeters, Hayashia *et al* 2012 reported that inorganic salt acts as an accelerator for radiation-induced free-radical polymerisation. Finally, these uncertainties originating from B_0-field and B_1-field non-uniformities can be easily quantified and compensated by scanning a non-irradiated gel phantom.

Ultimately, temperature variations over time and local temperature inhomogeneities in a volume of gel during scanning were found to severely compromise the accuracy of gel dosimetry and pose the most significant systematic uncertainty in polymer gel dosimeters. When calibration vials are at a different temperature than the phantom or when the spatial temperature distribution varies within the phantom, a significant systematic dose uncertainty will be introduced. In paper III it is shown that a temperature difference of 1°C results in an uncertainty of 8 % at a dose of 10 Gy in a PAGAT gel of 6 % total monomer concentration (3 % acrylamide and 3 % bis). By applying active temperature stabilisation strategies and centric k-space ordering, these uncertainties can be reduced to within 3 %. As shown in paper V, a temperature stabilisation technique using thermal pads succeeds in reducing the dosimetric uncertainties during short measurements. However, it is more challenging to keep the temperature stable during long measurements in both calibration vials and volumetric phan-

MRI mechanism	**Magnitude**	**Estimated Δ (%)**	Reference
	Geometric uncertainties		
B_0 - field inhomogeneities			III
• Spherical volume of 40 cm	ΔB_0 = 0.5 ppm	**0.25 pixel**	
• Spherical volume of 50 cm	ΔB_0 = 2 ppm	**1 pixel**	
Gradient non-linearity	< 1 %	< **1 pixel**	-
Eddy currents	-	1.5 pixel	a
Magnetic susceptibility differences	ΔB_0 = 5 ppm		III
• *Without correction*		2.5 to 5 pixels	
• Applying corrections		**1.25 to 2.5 pixels**	
Chemical shifts	-	-	-
	Dosimetric uncertainties		
Eddy currents			a
• *Without EC compensation*	1 ppm	8 %	
• Applying EC compensation	-	**1 %**	
B_0-field inhomogeneities	-		III
• Spherical volume of 40 cm	ΔB_0 = 0.5 ppm	<1 %	
• Spherical volume of 50 cm	ΔB_0 = 2 ppm	<1 %	
Magnetic susceptibility differences	ΔB_0 = 5 ppm		III
• *Without compensation*		4 %	
• With compensation		< **1 %**	
B_1-field inhomogeneities	ΔB_1 = 10 %	1.5 %	III, b
	ΔB_1 = *20 %*	5 %	
	ΔB_1 = *30 %*	8 %	
	ΔB_1 = *40 %*	13 %	
	ΔB_1 = *50 %*	20 %	
	With compensation	< **3 %**	
Standing Waves and losses	≥ 3 T	50 %	III
	With compensation	< **3 %**	
Slice profile imperfections	-	-	-
Temperature fluctuations			III
• *without temperature control*	1°C	8 % to 15 %	
• Active temperature control	0.3°C	< **3 %**	
Temperature drift			c
• *Linear k-space ordering*	1°C	8 % to 15 %	
• Centric k-space ordering	1°C	< **1 %**	
Molecular self diffusion	-	-	-

Table 7.3: *Overview of estimated systematic uncertainties (Δ) in MRI polymer gel dosimetry originating from scanning related mechanisms. In bold are the lower limit uncertainty values associated with applying an optimised protocol. The MRI mechanisms indicated in italic represent bad practice. References to papers included in this dissertation are indicated in Roman numerals. Additional references are: (a) De Deene et al 2000a, (b) De Deene et al 2000b, (c) De Deene and De Wagter 2001.*

tom. In paper I is shown that scanning a phantom and calibration phantoms in a closed cylindrical water recipient perfused with a GdDTPA-doped water solution connected to a temperature controller, absolute 3D radiation dosimetry by use of external calibration phantoms is possible with a dose uncertainty within 2.58 % when active temperature stabilisation to within 0.2°C is performed. This temperature stabilisation protocol is, however, not 'user-friendly' and alternative solutions need to be investigated in the future.

The combined scanner related sources of uncertainties can be reduced to within 4 % by applying a proper scanning set-up and using temperature stabilisation complemented with B_0- and B_1-field compensation methods.

7.1.3 Overall uncertainty of polymer gel dosimetry

Polymer gel dosimeters are dosimetric integrating dosimeters that can be shaped in any body part and can be read out using MRI with a high resolution in all three-dimensions. When all rules of good practice are implemented during a polymer gel dosimetry experiment, the combined uncertainty of random (3 %) and systematic effects (4 %) is limited to approximately 5 % (see also De Deene and Vandecasteele 2013a). They are suited to be used in the typical radiotherapy dose ranges, remain stable over significant amounts of time, are tissue equivalent, independent of dose rate, energy spectrum and other physical properties during irradiation. This set of characteristics makes the PAGAT polymer gel dosimeter an excellent candidate for clinical dose verifications. To achieve this degree of certainty however, the user has to invest a lot of time in optimising fabrication, irradiation and scanning protocols. Nonetheless, the dosimetric data resulting from such an experiment is unobtainable with any other dosimetry technique.

7.2 Radiochromic gel dosimetry

The widespread use of polymer gel dosimeters is impeded because of three main factors: the need for expert knowledge how to work with highly toxic chemicals in a laboratory setting in dosimeters that are extremely sensitive to oxygen contamination (1), the need for access to MRI scanners (2) and expert knowledge to dedicated imaging sequences (3). The first issue has already been largely improved since the introduction of normoxic gel dosimeters which avoids the need for expensive specialised laboratory equipment to limit oxygen contamination. However the use of less toxic monomers is still a matter of ongoing research. The limited access to MRI scanners and even more importantly, a limited expertise on quantitative image sequences

with adequate artefact compensation protocols have resulted in reluctance to implement a gel dosimetry program in routine QA. To get around this issue, the research toward more accessible readout techniques such as optical transmission tomography scanners was promoted. To fully grasp the possibility of optical scanners, the development of dedicated (gel) dosimeters soon followed. In paper IV, an optimised radiochromic micelle gel dosimeter was proposed as a modification of a micelle gel dosimeter investigated by Jordan and Avaakumov 2011. This radiochromic gel dosimeter was reviewed in terms of dose sensitivity, dose rate dependence, energy dependence, temperature dependence (during irradiation and readout), tissue equivalence and diffusion properties. In paper V, the radiochromic gel dosimeter was benchmarked using a clinical IMRT dose verification measurement. To assess the performance of radiochromic gel dosimetry, all known random and systematic effects affecting the overall uncertainty are summarised.

7.2.1 Random uncertainty

The random uncertainty is mainly caused by noise during the scanning of the gel dosimeter while random effects originating from fabrication and irradiation can be mostly neglected (the same arguments apply here as those for the polymer gel dosimeters). It should be noted that during fabrication of the radiochromic gel, random variations in the refractive index of the gel can result in *Schlieren* artefacts as discussed in paper V. The exact origin of these artefacts are a matter of speculation and we choose to discuss these artefacts as factors affecting the systematic uncertainty although they have a random component.

Unlike thermal detector noise in MRI, the detector noise in optical CT is less of a limiting factor because a high number of photons can be used to improve the signal to noise without severe implications to scan time. In optical CT, the noise is predominantly caused by imperfections of the surfaces and media through which the light propagates before being measured by the detector. These surfaces can become scratched or dusty and dust particles floating in the air and refractive index matching solution also contribute to the noise value.

To asses the random uncertainties in optical CT, the relative dose resolution (p = 95 %) of the radiochromic gel dosimeter used in our studies (paper V) was calculated (equation 7.3).

$$D_{\Delta\%}^{95\%} = 2.77 \cdot \frac{\sigma_D}{D_{max} - D_{min}} = 2.77 \cdot \frac{\sigma_{OD}}{OD_{max} - OD_{min}} \tag{7.3}$$

The relative dose resolution amounts to approximately 3 %. The intrinsic dosimetric precision (equation 7.1) therefore amounts to 1.55 mm^{-3} $\text{s}^{-1/2}$

with a measurement time of 4 minutes and a resolution of 1.3 mm^3.

7.2.2 Systematic uncertainty

7.2.2.1 Physico-chemical effects attributing to systematic uncertainty

The influence of radio-physical effects on the accuracy of dose verification were investigated in paper IV and paper V. An overview of all known physico-chemical effects influencing the systematic uncertainty are listed in table 7.4. These listed values represent uncertainties associated with a typical radiochromic gel dosimetry experiment and may vary depending on the size and composition of the gel dosimeter phantom. In this example, a typical cylindrical phantom of 10 cm diameter filled with a leucodye micelle gel are used.

The most important physico-chemical effects to impact the uncertainty of radiochromic gel dosimetry are the presence of trapped air bubbles in the gel during fabrication resulting in dose deviations up to 20 % and more. This can be easily avoided by careful pouring the gel in the containers. Optical swirls or *Schlieren* resulting from refractive index variation in the gel cause a deflection of the laser beam during readout and were detected in paper V. These *Schlieren* artefacts are responsible for uncertainties of approximately 10 % and are attributed to the fabrication procedure. Further research will have to focus on the fabrication procedure and chemical composition in order to eliminate these unwanted artefacts. Auto-oxidation and diffusion can result in temporal and spatial uncertainties, respectively. Compensation strategies are easily implemented by reducing the total scan time to limit the diffusion of the reporter molecules or correcting for the auto-oxidation by post-processing. The reported values for the diffusion coefficient of the radiochromic gel dosimeter are not in agreement which warrant further experiments (Vandecasteele et al 2011, Skyt et al 2013, Vandecasteele and De Deene 2013d). Because the auto-oxidation is temperature dependent, it is advised to maintain a stable temperature history during scanning to simplify correction. Additionally, the response of the radiochromic gel is temperature dependent during readout (section 7.2.2.2), which provides another argument in favour of (passive) temperature stabilisation strategies. Temperature during scanning was also found to be an important parameter in experiments performed by Olding and Schreiner (2011) in which they use Fricke Xylenol Orange Gelatin gels and the commercial Vista cone-beam optical CT scanner (approximately 2.5 % attenuation increase per degree Celsius). In this particular situation an active temperature stabilisation was required within $\pm$ 0.1°C at the point of scanning.

Physico-chemical mechanism	**Magnitude**	**Estimated Δ (%)**	Reference
Temperature differences during irradiation	1°C	**2 %**	IV
Temporal instability (auto oxidation):			V
• *Without correction*	2 h	3.5 %	
• With correction	2 h	**< 1 %**	
Spatial integrity			IV, V
• Scan time ≤ 10 h	-	**< 1 mm**	
• *Scan time ≥ 10 h*	-	> 1 mm	
Dose rate dependence	Depth dose measurement	5 %	IV
	Clinical dose verification	**3 %**	
Optical impurities			IV, V
• *Air bubbles*	-	> 20 %	
• *"Schlieren"*	-	10 %	

Table 7.4: *Overview of estimated systematic uncertainties (Δ) in optical CT radiochromic gel dosimetry originating from physico-chemical mechanisms. In bold are the lower limit uncertainty values associated with applying an optimised protocol. The physico-chemical mechanisms indicated in italic represent bad practice. References to papers included in this dissertation are indicated in Roman numerals.*

During irradiation, variations in temperature should be minimised because a temperature difference of 1°C will result in a dose response difference of approximately 2 % as shown by paper IV.

A significant dose rate dependence of the radiochromic gel is observed in paper IV and is in accordance with other findings (Skyt *et al* 2013a). The quantitative effect of this on clinical dose verifications is not straightforward to assess, however in paper IV it is shown that for a depth dose measurement of a photon beam, dose deviations of approximately 5 % can be expected at a depth of 30 cm. The penumbra regions in dose distributions will be also influenced by a dose rate dependency and dosimetry measurements should always be carefully interpreted. In typical clinical dose distributions each dose point is built up from the contribution of multiple dose rates which will reduce the uncertainty. On the basis of the results found in paper V, we estimate a value of approximately 3 %, but this should be experimentally validated in future experiments.

From table 7.4 it is obvious that the contribution of systematic uncertainties originating from physico-chemical effects can amount to approximately 10 % mainly due to a possibility of *Schlieren* artefacts in the gel. Without *Schlieren* artefacts, the physico-chemical uncertainties would be reduced to within 4 %.

7.2.2.2 Optical scanning effects attributing to systematic uncertainty

The optical scanning of radiochromic gel dosimeters introduces systematic uncertainties in the recorded dose maps. These may result from machine related and phantom (or object) related effects. The systematic uncertainties originating from scanning related effects are summarised in table 7.5. These listed values are associated with a typical radiochromic gel dosimetry experiment and may vary depending on the optical scanner configuration. In table 7.5, the typical configuration of the in-house built Optoscan optical laser CT scanner are considered.

Machine related effects originate from imperfections in the scanning device such as temporal laser intensity variations, multiple reflections and refractions between the scanner building materials, refractive index solution mismatches and phantom positioning.

Laser intensity variations can be easily corrected for by performing a differential measurement of the blank laser intensity. Depending on the frequency of the laser output variations, corrections can also be applied on the actual dataset of the irradiated phantom by post processing.

Multiple reflections and refractions of the laser beam can result in orientation dependent signal variations in the transmission profiles. Reducing

the number of reflecting surfaces in an optical scanning apparatus will diminish these unwanted reflections. In the Optoscan, the laser beam is aimed at a coated lens configuration in an off-centre plane to further reduce any reflections between the two lenses. The number of perpendicular surfaces the laser beam passes through before hitting the detector has also been reduced as compared to an older version of the Optoscan to reduce multiple reflections of the laser beam (Vandecasteele and De Deene 2009a). Radiochromic gel dosimeters have been investigated as an alternative for polymer gels for optical readout because polymer gel systems suffer from refractive index changes as function of dose resulting in refraction artefacts. No quantitative measurement on reflections and refractions can be given but an indication of the reduced uncertainty can be found when the results reported in Vandecasteele and De Deene 2009b are compared with results in paper V.

By devoting enough time to optimise the composition of the refractive index matching solution (solution of propylene glycol in water), any refractive index mismatch can be minimised. These mismatches result in a signal loss at the edges of the phantom presenting itself as a circular artefact. Moreover, these edge artefacts can be significantly reduced by the acquisition of a correction scan of the same phantom prior to irradiation. This requires the ability to position the phantom highly reproducible (sub-millimetre) but has the additional benefit of removing any background absorption, directional variations in light source intensity, spatial variations in detector sensitivity and phantom imperfections. Any irreproducibility in positioning however, will cause severe artefacts. Presently such positioning protocols have not yet been implemented in the Optoscan and are of future interest.

Object related effects originate from the dosimeter itself and manifest themselves as temperature drift of the gel phantom, imperfections in the phantom container and calibration induced faults.

Temperature drift during scanning has a small influence on the dosimetric uncertainty of approximately 1 % for a temperature difference of 1°C. Temperature variations have a more significant effect on the auto-oxidation rate of the gel after irradiation as mentioned in section 7.2.2.1.

Gel dosimeters require containers for mechanical rigidity and to avoid contact of the gel with the refractive index solution in the optical scanner. Different materials can be used such as borosilicate glass, PMMA, Barex and Fluorinated-ethylene-Propylene (FEP, teflon) containers. The refractive index of the teflon (FEP) containers resembles the refractive index of the gel more closely which minimises the edge artefacts. Careful manipulations and maintenance of the container help to minimise imperfections such as scratches and will further limit uncertainties.

Optical CT mechanism	**Magnitude**	**Estimated Δ (%)**	Reference
Recipient wall effect			V
• Refractive index of container	*Glass (RI = 1.51),* *PMMA (RI = 1.49),* *Barex (RI = 1.50), ...*	Between 1 % and 20 % (depending on thickness)	
	FEP Teflon (RI = 1.34)	**< 1%**	
• Scratches			V, a
◦ *Without compensation*		> 5 %	
◦ With compensation		**< 1 %**	
Refractive index solution mismatch			V
• *Without compensation*		> 5 % and > 1 mm	
• With compensation		**< 1 % and < 1 mm**	
Laser output variations			a
• *Without compensation*		up to 10 %	
• With compensation		**< 1 %**	
Reflections and refractions			-
• *Without compensation*		between 1 and 10 %	
• With compensation		**< 1 %**	
Temperature fluctuations during scanning	5 °C	**< 1 %**	IV
Reproducibility of phantom positioning	> *sub millimetre* < sub millimetre	between 1 % and 20 % **< 1 %**	-
Calibration			V
• *Using small cuvettes*	-	5 % - 10 %	
• Using volumetric phantom	-	**< 1 %**	

Table 7.5: *Overview of estimated systematic uncertainties (Δ) in radiochromic gel dosimetry originating from scanning related mechanisms. In bold are the lower limit uncertainty values associated with applying an optimised protocol. The Optical CT mechanisms indicated in italic represent bad practice. References to papers included in this dissertation are indicated in Roman numerals. Additional references are: (a) Vandecasteele and De Deene 2009a, (b) Vandecasteele and De Deene 2009b.*

A well-established calibration technique should be applied to convert optical density maps to dose maps to eliminate any systematic uncertainties. The use of small spectroscopic samples usually fails because of the large volume difference between these calibration samples and the large volumetric phantom. This results in a different temperature history of the calibration samples and the volumetric phantoms, affecting the auto-oxidation rate and pre-irradiation background coloration of the gel samples. Best results are obtained by inserting a well-characterised dosimeter (such as an ionisation chamber) in a similar gel phantom and measuring the dose in one or several points from the same irradiation procedure as delivered on the actual radiochromic gel phantom. The measured dose points can then be correlated to the measured optical density value from which a linear dose response function is extracted to calibrate the optical density maps to dose maps. This method was applied in paper V.

A total systematic uncertainty from scanning related effects should be within 2 %. However in Paper V the overall systematic uncertainty was limited to approximately 5 % due to refractive index mismatches and a less than sub-millimetre accuracy in phantom positioning making a correction scan impossible.

7.2.3 Overall uncertainty of radiochromic gel dosimetry

Radiochromic gel dosimeters are dosimetric integrating dosimeters which can be read out using optical readout techniques with a high resolution in all three-dimensions. When all rules of good practice are implemented during a radiochromic gel dosimetry experiment, the combined uncertainty of random and systematic effects amounts to approximately 11 %. The radio-physical uncertainties of *Schlieren* artefacts and dose rate dependency combined with the scanning related uncertainties from a refractive index solution mismatch and phantom positioning irreproducibility are the main sources of overall uncertainty. Paper IV showed that the dose rate dependence has a potential for improvement and further research should focus on trying to eliminate the dose rate dependence through extensive chemical analysis and optimisation of the formulation. The same applies to *Schlieren* artefacts which need to be eliminated by optimising the fabrication protocol. Further adaptation of the Optoscan scanner needs to incorporate a highly reproducible technique in positioning the phantom so correction scans will allow to significantly reduce the scanning related uncertainties down to 2 %. When suggested adaptations are incorporated, radiochromic gel dosimetry is expected to reach a comparable level of uncertainty as polymer gel

dosimeter with the advantage of the ease of fabrication of the gel, low cost and quick readout possibilities, insensitivity to oxygen and a linear dose response to large radiation doses.

7.3 Comparison of polymer gel dosimetry and radiochromic gel dosimetry

Polymer gel dosimeters and radiochromic gel dosimeters both possess several of the desired characteristics of an ideal 3D dosimeter: they both are integrating radiation dosimeters with a high resolution in three dimensions suitable for use in radiotherapy dose verifications. They are both tissue equivalent for most radiation energies that occur in radiotherapy and independent of the radiation energy spectrum of clinical high energetic photon beams. Both dosimetry techniques are somewhat insensitive to radiation doses frequently used in radiotherapy on a daily basis. Polymer gel dosimeters require a target dose of approximately 10 Gy, while radiochromic gel dosimeters require a target dose of approximately 45 Gy to provide excellent dose resolution. However, the use of such high doses is clearly not typical for radiotherapy treatment doses given in one fraction (on average 2 Gy) and important effects of *e.g.* clinical leaf motion speeds are not recorded when the entire dose on the dosimeter is delivered. These high dose requirements could nevertheless be an advantage for stereotactic radiotherapy applications where high single fraction doses are delivered. Finally, it can be argued that gel dosimetry has the purpose to verify the overall treatment dose delivery from multiple fractions and thus using a polymer gel dosimeter or radiochromic gel dosimeter allows for the verification of the sum of multiple fractions.

Each gel dosimeter has furthermore its own advantages and disadvantages.

Polymer gel dosimeters can be humanoid shaped allowing to record the entire dose distribution including low doses close to the surface. This can be of great clinical importance to quantify the amount of low radiation doses given over large volumes of healthy tissue. Care should be taken when acquiring dose information from entrance or exit doses located very close to the edge of the phantom because of susceptibility artefact during scanning and potential oxygen contamination. Polymer gel dosimeters remain relative stable for prolonged amounts of time although an increase in the background R_2 value is expected due to changes in the mesh formed by gelatin. A strict minimum time span of 12 hours between irradiation and scanning should allow the polymerisation reaction to stabilise. Polymer gel dosimeters are independent of dose rates typically encountered in

radiotherapy treatments and independent of most physical parameters during irradiation such as pressure and temperature. Polymer gel dosimeters are usually read out using MRI, however optical read out has also been investigated. Artefacts correlated with refractive index changes as function of dose are reported and can increase the uncertainties of optical readout. Also laser scanning systems are preferred because light scattering by the formed polymers in the gel creates stray light which is not easily eliminated in pixelated optical scanners.

Radiochromic gel dosimeters are limited to a cylindrical or spherical shape because of refractive effects on the container of the dosimeter. Potentially, post processing can eliminate some of these artefacts (Rankine and Oldham *et al* 2013) which could expand the dosimeters to more humanoid shapes, however more research is needed to evaluate the accuracy of these techniques. A cylindrical phantom limits the volume in which radiation doses can be measured and renders dose measurements in low-dose areas located relatively far from the target site impossible. These low dose areas can be of great significance from a radio-biological point-of-view. Measuring surface doses close to the phantom edge can be difficult because of potential refractive index mismatches. A correction scan could allow for accurate measurements, however a dedicated procedure for reproducible repositioning of the phantom is essential (Oldham *et al* 2006, Sakhalkar *et al* 2009). The time span during which radiochromic gel dosimeters are stable is limited due to an auto-oxidation reaction and diffusion of dye molecules and therefore, they should be imaged as soon as possible after the irradiation. An advantage of radiochromic gel dosimeters however is the fact that they can be imaged almost immediately after irradiation, reducing the total time needed to perform a 3D dosimetry measurement. Radiochromic gel dosimeters are shown to be dose rate dependent and this will affect the lower limit uncertainty which can be achieved with this type of dosimeter. Further simulations and experiments should be performed to quantify the effect of the dose rate dependency for clinical dose verifications. The radiochromic gel is furthermore found to be sensitive to temperature variations during irradiation (and readout) which requires temperature stabilisation measures.

The intrinsic dosimetric precision of polymer gel dosimetry was found to be 6 times lower than the dosimetric precision of radiochromic gel dosimetry mainly because of the fact that optical CT is able to scan much faster and with a higher resolution than MRI resulting in an equivalent dosimetric resolution. In terms of systematic uncertainties, polymer gel dosimetry can be confidently performed measuring dose values within 5 % uncertainty. Radiochromic gel dosimetry suffers from some systematic uncertainties related to the fabrication (*Schlieren* artefacts) and scanning (refractive index

mismatching and irreproducible positioning) limiting the overall accuracy.

7.4 Future perspectives

The dose distribution in modern radiotherapy treatments is designed to be highly conformed to a target. Additionally, inside the high dose region, dose heterogeneities are included to target these zones in the tumour which are suspected to have the highest malignancy based on functional imaging. These innovations can increase the possibility of (partially) missing the target and therefore the focus of dosimetry needs to be shifted to verifying a whole 3D dose distribution. These 3D dosimeters can detect differences between planned and delivered dose distributions and will facilitate the implementation of a new and more complex methods of dose delivery.

In the specific case of rotational techniques such as tomotherapy and IMAT, the doses are delivered dynamically during which multiple beam defining parameters such as the dose rate, radiation fluence and shape of the beam and beam angle vary continuously. Both polymer gel dosimeters as well as radiochromic gel dosimeters integrate the dose from one or multiple treatment fractions which allows for the investigation of patient set-up.

Adaptive radiotherapy where treatment planning is optimised on a daily or weekly basis based on anatomical or functional images is on the verge of clinical application. 3D dosimeters such as polymer gels and radiochromic gels will prove to be of great importance to simulate the effect of dose accumulation in deforming anatomy and to validate software algorithms that calculated the dose-warping in a patient. Gel dosimeters are easily deformed and their gelatine concentration can be optimised for the mechanical properties that are needed. A thorough evaluation of the radio-physical properties is needed to guaranty the accuracy and precision of the gel dosimeters with altered gelatin concentration.

Patient set-up and tumour and organ motion studies especially in rotational and dynamic techniques will further benefit from 3D dose measurements to validate robust treatment planning algorithms and tumour tracking efficacy.

At some stage these advanced treatment techniques will find implementation in peripheral radiotherapy centres where an overall QA system is needed to safeguard the whole treatment chain including 3D imaging of the patient, transfer of scans to the treatment planning computer, treatment planning, positioning the patient, transfer of treatment protocol to the treatment machine and treatment delivery. In these centres, the choice between polymer gels or radiochromic gels will facilitate the application of 3D gel dosimetry to extensively validate new treatment options. Centres can

choose between dose assessment in a time-consuming protocol, offering dose information in a large humanoid shaped volume or a fast dose verification in a small cylindrical phantom.

Small field dosimetry is challenging for many radiation detectors because of their finite size resulting in partial volume averaging effects and charged particle disequilibrium. Gel dosimeters could play an important role in acquiring small field output factors during commissioning of a treatment planning system because they are tissue equivalent dosimeters and integrate both the phantom and detector material resulting in a dosimeter that avoids perturbation of the radiation beam. For this purpose, gel dosimeters will need to be highly accurate and dedicated protocols should be developed. Some initial results for radiochromic gel dosimeters are looking promising as shown by Babic *et al* 2009a.

In particle therapy applications such as proton therapy and carbon ion therapy, 3D dose measurements could significantly improve the knowledge of the dose deposition in and around the Bragg peak in clinical situations. However, both the radiochromic gel dosimeter as the polymer gel dosimeter show a dependence on the linear energy transfer (LET) (Zhao *et al* 2012, Heufelder *et al* 2003, Gustavsson *et al* 2004) limiting their use in these rapidly evolving treatment delivery areas. Future optimisation of the chemical composition of the gel dosimeters may result in LET independent formulations allowing quantitative 3D dosimetry of particle therapy.

Gel dosimetry could furthermore allow for measuring radiation dose deposition in lower density materials using radiation sensitive foams and thus mimicking the dose deposition in the lungs. Several proofs of concept have already been proposed in the literature (De Deene *et al* 2006b and De Deene and Vandecasteele 2013b).

Alternative polymer gel dosimeter compositions should be further investigated to minimise the chemical toxicity and temperature dependence during scanning. However we are confident that gel dosimetry has reached a clinical acceptable level of uncertainties provided that appropriate measures and a strict gel dosimetry protocol is followed. Radiochromic gel dosimeters allow for a compact and cheap alternative albeit with the compromise of a limitation in geometrical shape and reduced measuring volume. Further optimisation is required to reduce the dose rate dependency and *Schlieren* artefacts.

When a similar clinical acceptable level of uncertainty is reached, both gel dosimeters can furthermore support multi-centre clinical trials on the implementation and benchmarking of new advanced radiotherapy treatment techniques and can play a vital role in developing and implementing nationwide credentialing and audit programmes.

8 Conclusion

Radiotherapy has evolved from using a limited amount of geometrically quite simple beams to a highly sophisticated treatment modality which uses modulation of the number of fields, the angle from which they incident on the patient and the fluence of radiation within each field. Real-time imaging during treatment and functional and anatomical information enable further minimisation of uncertainties in the dose delivery. To assure that the correct radiation dose distribution is delivered to the patient, hence patient-safety, comprehensive quality assurance techniques need to be applied on a regular basis. An important tool for the end-to-end verifications of radiotherapy treatment dose delivery is 3D gel dosimetry which has several advantages compared to other dosimetry techniques. Gel dosimetry allows for the quantitative visualisation of the radiation dose distribution in all points of three-dimensional space in a phantom of humanoid shape. As part of this research, two gel dosimetry techniques were investigated.

The polymer gel dosimeter consists of vinyl monomers and an antioxidant which are dissolved in a gelatin matrix. Upon irradiation, polymer structures are formed due to a radiation induced polymerisation reaction. The created polymer molecules are immobilised by the gelatin matrix. The spatial distribution of these polymers can be imaged using MRI. In previous studies, this dosimeter was shown to have superior radio-physical properties for radiotherapy dosimetry. However the normoxic polymer gel dosimeter had a low accuracy and precision which resulted in only a few clinics worldwide able to incorporate it in their QA programs. The first objective of

this work was to validate the dosimetric accuracy and precision of normoxic polymer gel dosimeters with MRI readout assuring that a "gold standard" 3D dosimeter is available against which all alternative 3D dosimetry systems could be benchmarked. By performing a reproducibility study, a poor dosimetric accuracy was found which was attributed to the calibration using small calibration vials. In a concurrent study, an analysis of the chemical and radio-physical characteristics of the gel was performed to quantify the influence of the temperature history (pre-, during and post-irradiation), oxygen exposure (post-irradiation) and recipient wall effects. It was shown that these effects had only a minor influence on the overall uncertainty of the gel dosimeter. In a third study, several MRI related sources of uncertainties were quantified: B_0-field and B_1-field non-uniformities, dielectric effects (losses and standing waves) and temperature drifts during scanning. This study demonstrated that temperature stabilisation techniques are vital in performing accurate dose measurements. When strict experimental procedures are followed, as described in this dissertation, the overall uncertainty is limited to approximately 5 %.

In the radiochromic gel dosimeter, micelles are used to homogeneously dissolve a leucodye in a gelatine matrix. The leucodye is oxidised to its chromatic form upon irradiation and can be imaged with optical transmission measurements using an in-house built optical laser CT scanner. To quantify random and systematic uncertainties associated with radiochromic gel dosimetry, a study was performed to investigate the radio-physical characteristics of the gel. In this study, the gel was shown to be dose rate dependent, ultimately limiting the minimal dosimetric uncertainty. However, we found that there is room for improvement of the dose rate dependency. Further research into the chemistry of radiochromic gels is needed to minimise the dose rate dependency through extensive chemical analysis and optimisation of the formulation. Furthermore, uncertainties related to temperature variations (during irradiation and scanning), spatial instability and atomic composition were quantified. The radiochromic gel which is read out using the optical laser CT scanner was benchmarked against the polymer gel which is read out using an MRI-scanner for a clinical IMRT dose verification of a brain tumour. This study revealed that the radiochromic gel suffered from radio-physical uncertainties originating from Schlieren artefacts combined with scanning related uncertainties from a refractive index solution mismatch and phantom positioning irreproducibility. Schlieren artefacts need to be eliminated by optimising the fabrication protocol and further adaptation of the optical laser CT scanner needs to incorporate a highly reproducible technique in positioning the phantom.

The results from this dissertation provide a recipe to measure radio-

therapy delivered dose distributions with an integrated 3D dosimeter with reduced uncertainties within clinical acceptable levels. Polymer gel dosimeters are dose-integrating dosimeters that can be humanoid shaped and can be read out using MRI with a high resolution in all three-dimensions allowing to record the entire dose distribution including low doses close to the surface (skin). They are suitable in typical radiotherapy dose ranges, remain stable over significant amounts of time, are tissue equivalent, independent of dose rate, energy spectrum and other physical properties during irradiation. This set of characteristics makes the PAGAT polymer gel dosimeter an ideal candidate for clinical dose verifications. To achieve this degree of certainty however, the user has to invest a lot of time in optimising fabrication, irradiation and scanning protocols. Radiochromic gel dosimeters need to be further optimised in terms of chemical composition and fabrication procedure. It is expected that these dosimeters can reach a comparable level of uncertainty as polymer gel dosimeters, with the expectation of reduced cost, easier fabrication, fast readout and linear dose response over a large dynamic range.

Bibliography

Abramson F P and Firestone R F 1966 Combined effects of dose rate and temperature in the radiolysis of liquid chloroform. Application of homogeneous kinetics to the radiolytic system *J Phys Chem* **70** 3596–605

Adamovics J, Guo P, Burgess D, Manzoor A and Oldham M 2006 PRESAGE - Development and optimization studies of a 3D radiochromic plastic dosimeter ? Part 2 *J Phys: Conf Ser* **56** 176–8

Adamovics J and Maryanski M J 2003 New 3D radiochromic solid polymer dosimeter from leuco dyes and a transparent polymeric matrix *Med Phys* **30** 1349

Adamovics J and Maryanski M J 2006 Characterisation of Presage: a new 3D radiochromic solid polymer dosemeter for ionizing radiation *Radiat Prot Dosim* **120** 107–12

Alexander P, Charlesby A and Ross M 1954 The degradation of solid polymethylmethacrylate by ionizing radiations *Proc R Soc A* **223** 392

Amin M N, Horsfield M A, Bonnett D E, Dunn M J, Poulton M and Harding P F 2003 A comparison of polyacrylamide gels and radiochromic film for source measurements in intravascular brachytherapy *Br J Radiol* **76** 824–31

Appleby A 1987 Imaging of spatial radiation dose distribution in agarose gels using magnetic resonance *Med Phys* **14** 382–4

Appleby A and Leghrouz A 1991 Imaging of radiation dose by visible color development in ferrous agarose xylenol orange gels *Med Phys* **18** 309–12

Armstrong W A 1958 Radiation chemistry of solutions I. Use of leuco trialrylmethane compounds for chemical dosimetry *Radiat Res* **8** 375–87

Ash D and Bates T 1994 Report on the clinical effects of inadvertent radiation underdosage in 1045 patients *J Clin Oncol* **6** 214–25

Audet C, Hilts M, Jirasek A and Duzenli C 2002 CT gel dosimetry technique: comparison of a planned and measured 3D stereotactic dose volume *J Appl Clin Med Phys* **3** 110–8

Babic S, Battista J and Jordan K 2009 Radiochromic leuco dye micelle hydrogels: II. Low diffusion rate leuco crystal violet gel *Phys Med Biol* **54** 6791–808

Babic S, McNiven A, Battista J and Jordan K 2009 Three-dimensional dosimetry of small megavoltage radiation fields using radiochromic gels and optical CT scanning *Phys Med Biol.* **54** 2463–81

Baker C R, Quine T E, Brunt J N and Kacperek A 2009 Monte Carlo simulation and polymer gel dosimetry of 60 MeV clinical proton beams for the treatment of ocular tumours *Appl Radiat Isot* **67** 402–5

Baldock C 2006 Historical overview of the development of gel dosimetry *J Phys: Conf Ser* **56** 14–22

Baldock C, Burford R P, Billingham N, Wagner G S, Patval S, Badawi R D and Keevil S F 1998a Experimental procedure for the manufacture and calibration of polyacrylamide gel (PAG) for magnetic resonance imaging (MRI) radiation dosimetry *Phys Med Biol* **43** 695–702

Baldock C, De Deene Y, Doran S, Ibbot G, Jirasek A, Lepage M, McAuley K B, Oldham M and Schreiner L J 2010 Polymer gel dosimetry *Phys Med Biol* **55** R1–R63

Baldock C, Harris P J, Piercy A R and Healy B 2001a Experimental determination of the diffusion coefficient in two-dimensions in ferrous sulphate gels using the finite element method *Australas Phys Eng Sci Med* **24** 19–30

Baldock C, Lepage M, Bäck S Å J, Murry PJ, Jayasekera P M, Porter D and Kron T 2001b Dose resolution in radiotherapy polymer gel dosimetry: effect of echo spacing in MRI pulse sequence *Phys Med Biol* **46** 449–60

Baldock C, Murry P and Kron T 1999 Uncertainty analysis in polymer gel dosimetry *Phys Med Biol* **44** N243–6

Baldock C, Rintoul L, Keevil S F, Pope J M and George G A 1998b Fourier transform Raman spectroscopy of polyacrylamide gel (PAGs) for radiation dosimetry *Phys Med Biol* **43** 3617–27

Baras P, Seimenis I, Sandilos P, Vlahos L, Bieganski T, Georgiou E, Pantelis E, Papagiannis P and Sakelliou L 2005 An evaluation of the TSE MR sequence for time efficient data acquisition in polymer gel dosimetry of applications involving high doses and steep dose gradients. *Med Phys* **32** 3339–45

Basran P S and Woo M K 2008 An analysis of tolerance levels in IMRT quality assurance procedures *Med Phys* **35** 2300–7

Baxter J N and Johnston F J 1968 Gamma radiolysis studies of the chloroacetic acids *Radiat. Res.* **33** 331–24

Bayreder C, Georg D, Moser E and Berg A 2006 Basic investigations on the performance of a normoxic polymer gel with tetrakis-hydroxymethyl-phosphonium chloride as an oxygen scavenger: reproducibility, accuracy, stability and dose rate dependence *Med Phys* **33** 2506–18

Bero M A, Gilboy W B, Glover P M and El-masri H M 2000 Tissue-equivalent gel for non-invasive spatial radiation dose measurements *Nucl Instrum Method B* **166** 820–5

Bissonnette J P, Moseley D J and Jaffray D A 2008 A quality assurance program for image quality of cone-beam CT guidance in radiation therapy *Med Phys* **35** 1807–15

Björeland A, Lindvall P, Karlsson A, Gustavsson H, Bäck S Å J, Karlsson M and Bergenheim T A 2008 Liquid ionization chamber calibrated gel dosimetry in conformal stereotactic radiotherapy of brain lesions *Acta Oncol* **47** 1099–109

Bloembergen N, Purcell E M and Pound V 1948 Relaxation effects in nuclear magnetic resonance absorption *Phys Rev* **73** 679–712

Both S, Alecu I M, Stan A R, Alecu M, Ciura A, Hansen J M 2007 A study to establish reasonable action limits for patient-specific quality assurance in intensity-modulated radiation therapy *J Appl Clin Med Phys* **8** 1–8

Boni A L 1961 A polyacrylamide gamma dosimeter *Radiat Res* **14** 374–80

Bortfeld T, Schmidt-Ullrich R, De Neve W, and Wazer D E 2005 Image-guided IMRT *Springer* 1st edition

Boudou C, Troprs I, Rousseau J, Lamalle L, Adam JF, Estve F and Elleaume H 2007 Polymer gel dosimetry for synchrotron stereotactic

radiotherapy and iodine dose-enhancement measurements. *Phys Med Biol* **52** 4881–92

Brahme A 1988 Accuracy requirements and quality assurance of external beam therapy with photons and electrons *Acta Oncologica, (Suppl. 1)*

Broggi S, Cattaneo G M, Molinelli S, Maggiulli E, Del Vecchio A, Longobardi B 2008 Results of a two-year quality control program for a helical tomotherapy unit *Radiother Oncol* **86** 231–41

Bujold A, Craig T, Jaffray D and Dawson LA 2012 Image-guided radiotherapy: has it influenced patient outcomes? *Semin Radiat Oncol* **22** 50-61

Campbell W G, Rudko D A, Braam N A, Wells D M and Jirasek A 2013 A prototype fan-beam optical CT scanner for 3D dosimetry *Med Phys* **40** 061712

Cardenas R L, Cheng K H, Verhey L J, Xia P, Davis L and Cannon B 2002 A self consistent normalized calibration protocol for three dimensional magnetic resonance gel dosimetry *Magn Reson Imaging* **20** 667–79

Ceberg S, Gagne I, Gustafsson H, Scherman J B, Korreman S S, Kristoffersen F K, Hilts M and Bäck S Å J 2010 RapidArc treatment verification in 3D using polymer gel dosimetry and Monte Carlo simulation *Phys Med Biol* **55** 4885–98

Ceberg S, Karlsson A, Gustavsson H, Wittgren L and Bäck S Å J 2008 Verification of dynamic radiotherapy: the potential for 3D dosimetry under respiratory-like motion using polymer gel *Phys Med Biol* **53** N387–N396

Chan MF, Fung AY, Hu YC, Chui CS, Amols H, Zaider M and Abramson D 2001 The measurement of three dimensional dose distribution of a ruthenium-106 ophthalmological applicator using magnetic resonance imaging of BANG polymer gels. *J Appl Clin Med Phys* **2** 85–9

Cheng H W, Ho C J, Lee C C, Tu S J, Shih B Y and Chao T C 2011 Development of a novel optical CT employing a laser to create a collimated line-source with a flat-top intensity distribution *Radiat Meas* **46** 1932–5

Chu K C, Jordan K J, Battista J, Van Dyk J and Rutt B K 2000 Polyvinyl alcohol-Fricke hydrogel and cryogel: two new gel dosimetry systems for low Fe^{3+} diffusion *Phys Med Biol* **45** 955–69

Conklin J, Deshpande R, Battista J and Jordan K 2006 Fast laser optical CT scanner with rotating mirror and Fresnel lenses *J Phys: Conf Ser* **56** 211–3

Cosgrove V P, Murphy P S, McJury M, Adams E J, Warrington A P, Leach M O and Webb S 2000 The reproducibility of polyacrylamide gel dosimetry applied to stereotactic conformal radiotherapy *Phys Med Biol* **45** 1195–210

Crescenti R A, Scheib S G, Schneider U and Gianolini S 2007b Introducing gel dosimetry in a clinical environment: customization of polymer gel composition and magnetic resonance imaging parameters used for 3D dose verifications in radiosurgery and intensity modulated radiotherapy *Med Phys* **34** 1286–97

Day M J and Stein G 1950 Chemical effects of ionizing radiation in some gels *Nature* **166** 146–7

De Deene Y 2009 Review of quantitative MRI principles for gel dosimetry *J Phys: Conf Ser* **164** 012033

De Deene Y and Baldock C 2002 Optimization of multiple spin-echo sequences for 3D polymer gel dosimetry *Phys Med Biol* **47** 3117–41

De Deene Y and De Wagter C 2001 Artifacts in multi-echo T2 imaging for high-precision gel dosimetry: III. Effects of temperature drift during scanning *Phys Med Biol* **46** 2697–711

De Deene Y, De Wagter C and De Neve W 2000b Artifacts in multi-echo T2 imaging for high-precision gel dosimetry: II. Analysis of B1 field inhomogeneity *Phys Med Biol* **45** 1825–39

De Deene Y, De Wagter C, De Neve W and Achten E 2000a Artifacts in multi-echo T2 imaging for high-precision gel dosimetry: I. Analysis and compensation of eddy currents *Phys Med Biol* **45** 1807–23

De Deene Y, De Wagter C, Van Duyse B, Derycke S, De Neve W and Achten E 1998b Three-dimensional dosimetry using polymer gel and magnetic resonance imaging applied to the verification of conformal radiation therapy in head-and-neck cancer *Radiother Oncol* **48** 283–91

De Deene Y, De Wagter C, Van Duyse B, Derycke S, Mersseman B, De Gersem W, Voet T, Achten E and De Neve W 2000c Validation of MR-based polymer gel dosimetry as a preclinical three-dimensional verification tool in conformal radiotherapy *Magn Reson Med* **43** 116–25

De Deene Y, Hanselaer P, De Wagter C, Achten E and De Neve W 2000d An investigation of the chemical stability of a monomer/polymer gel dosimeter *Phys Med Biol* **45** 859–78

De Deene Y, Hurley C, Venning A, Vergote K, Mather M, Healy B and Baldock C 2002b A basic study of some normoxic polymer gel dosimeters *Phys Med Biol* **47** 3441–63

De Deene Y, Pittomvils G and Visalatchi S 2007 The influence of cooling rate on the accuracy of normoxic polymer gel dosimeters *Phys Med Biol* **52** 2719–28

De Deene Y, Reynaert N and De Wagter C 2001 On the accuracy of monomer/polymer gel dosimetry in the proximity of a high-dose-rate 192 Ir source *Phys Med Biol* **46** 2801–25

De Deene Y, Van de Walle R, De Wagter C and Achten E 1998a Mathematical analysis and experimental investigation of noise in quantitative magnetic resonance imaging applied in polymer gel dosimetry *Signal Process.* **70** 85–101

De Deene Y and Vandecasteele J 2013a On the reliability of 3D gel dosimetry *J Phys: Conf Ser* (in press)

De Deene Y and Vandecasteele J 2013b Low-density polymer gel dosimeters for 3D radiation dosimetry in the thoracic region : A preliminary study *J Phys: Conf Ser* (in press)

De Deene Y, Venning A, Hurley C, Healy B J and Baldock C 2002a Dose-response stability and integrity of the dose distribution of various polymer gel dosimeters *Phys Med Biol* **47** 2459–70

De Deene Y, Vergote K, Claeys C and De Wagter C 2006a The fundamental radiation properties of normoxic polymer gel dosimeters: a comparison between a methacrylic acid based gel and acrylamide based gels *Phys Med Biol* **51** 653–73

De Deene Y, Vergote K, Claeys C and De Wagter C 2006b Three dimensional radiation dosimetry in lung-equivalent regions by use of a radiation sensitive gel foam: proof of principle *Med Phys* **33** 2586–97

Deman P, Vautrin M, Stupar V, Barbier E L, Elleaume H, Esteve F and Adam J F 2011 Monochromatic minibeam radiotherapy: theoretical and experimental dosimetry for preclinical treatment plans *Phys Med Biol* **56** 4465–80

De Wagter C 2004 The ideal dosimeter for intensity modulated radiation therapy (IMRT): what is required? *J Phys: Conf Ser* **3** 4–8

Doran S J 2009 The history and principles of optical computed tomography for scanning 3D radiation dosimeters: 2008 update *J Phys: Conf Ser* **164** 012020

Doran S J, Koerkamp K K, Bero M A, Jenneson P, Morton E J and Gilboy W B 2001 A CCD-based optical-CT scanner for high-resolution 3D-imaging of radiation dose distributions: equipment specifications, optical simulations and preliminary results *Phys Med Biol* **46** 3191–213

Doran S J and Krstajic N 2006 The history and principles of optical computed tomography for scanning 3-D radiation dosimeters *J Phys: Conf Ser* **56** 45–57

Dumas E M, Leclerc G and Lepage M 2006 Effect of container size on the accuracy of polymer gel dosimetry *J Phys: Conf Ser* **56** 239–41

Duthoy W, De Gersem W, Vergote K, Boterberg T, Derie C, Smeets P, De Wagter C and De Neve W 2004 Clinical implementation of intensity-modulated arc therapy (IMAT) for rectal cancer *Int J Radiat Oncol Biol Phys* **60** 794–806

Duthoy W, De Gersem W, Vergote K, Coghe M, Boterberg T, De Deene Y, De Wagter C, Van Belle S and De Neve W 2003 Whole abdominopelvic radiotherapy (WAPRT) using intensity-modulated arc therapy (IMAT): first clinical experience *Int J Radiat Oncol Biol Phys* **57** 1019–32

Dutreix A 1984 When and how can we improve precision in radiotherapy? *Radiother Oncol* **2** 275–292

Ertl A, Berg A, Zehetmayer M and Frigo P 2000 High-resolution dose profile studies based on MR imaging with polymer BANG gels in stereotactic radiation techniques *Magn Reson Imaging* **18** 343–9

Farajollahi A R, Bonnett D E, Ratcliffe A J, Aukett R J and Mills J A, 1999 An investigation into the use of polymer gel dosimetry in low dose rate brachytherapy *Br J Radiol* **72** 1085–92

Farajollahi A R, Bonnett D E, Tattam D and Green S 2000 The potential use of polymer gel dosimetry in boron neutron capture therapy *Phys Med Biol* **45** N9–14

Fearon T, Criss V R and Luban N L 2005 Blood irradiator dosimetry with BANG polymer gels *Transfusion* **45** 1658–62

Fong P M, Keil D C, Does M D and Gore J C 2001 Polymer gels for magnetic resonance imaging of radiation dose distributions at normal room atmosphere *Phys Med Biol* **46** 3105–13

Fragoso M, Love P A, Verhaegen F, Nalder C, Bidmead A M, Leach M and Webb S 2004 The dose distribution of low dose rate Cs-137 in intracavitary brachytherapy: comparison of Monte Carlo simulation, treatment planning calculation and polymer gel measurement *Phys Med Biol* **49** 5459–74

Fricke H and Morse S 1927 The chemical action of Roentgen rays on dilute ferrous sulphate solutions as a measure of radiation dose *Am J Roentgenol Radium Ther Nucl Med* **18** 430–2

Fruhner H and Kretzschmar G 1989 Effect of pH on the binding of alkyl sulphates to gelatin *Colloid Polym Sci* **267** 839–43

Giacomo P 1981 Recommendations of Working group on the statement of uncertainties INC-1 (1980) *Metrologica* **17** 73–74

Gifford K A, Horton J L Jr, Jackson E F, Steger T R 3rd, Heard M P, Mourtada F, Lawyer A A and Ibbott G S 2005 Comparison of Monte Carlo calculations around a Fletcher Suit Delclos ovoid with radiochromic film and normoxic polymer gel dosimetry *Med Phys* **32** 2288–94

Gopishankar N, Watanabe Y, Subbiah V 2011 MRI-based polymer gel dosimetry for validating plans with multiple matrices in Gamma Knife stereotactic radiosurgery *J Appl Clin Med Phys* **12** 3333

Gore J C, Kang Y S and Schulz R J 1984 Measurement of radiation dose distributions by nuclear magnetic resonance (NMR) imaging *Phys Med Biol* **29** 1189–97

Gore J C, Ranade M, Maryanski M J and Schulz R J 1996 Radiation dose distributions in three dimensions from tomographic optical density scanning of polymer gels: I. Development of an optical scanner *Phys Med Biol* **41** 2695–704

Goyal P S and Aswal V K 2001 Micellar structure and inter-micelle interactions in micellar solutions: results of small angle neutron scattering studies *Curr Sci* **80** 972–9

Grebe G, Pfaender M, Roll M and Luedemann L 2001 Dynamic arc radiosurgery and radiotherapy: commissioning and verification of dose distributions *Int J Radiat Oncol Biol Phys* **49** 1451–60

Gupta B and Gomathy K 1974 Consistency of ferrous sulphate-benzoic acid-xylenol orange dosimeter *Int J Appl Radiat Isot* **25** 509–13

Gupta B, Kini U, Bhat R, and Madhvanath U 1982 Use of the FBX dosemeter for the calibration of cobalt-60 and high energy teletherapy machines *Phys Med Biol* **27** 235–45

Gupta B and Narayan G 1985 G(Fe^{3+}) values in the FBX dosimeter *Phys Med Biol* **30** 337–40

Gustavsson H, Bäck S ÅJ, Medin J, Grusell E and Olsson L E 2004 Linear energy transfer dependence of a normoxic polymer gel dosimeter investigated using proton beam absorbed dose measurements *Phys Med Biol* **49** 3847–55

Gustavsson H, Karlsson A, Bäck S ÅJ, Olsson L E, Haraldsson P, Engstrum P and Nystrum H 2003 MAGIC-type polymer gel for three-dimensional dosimetry: intensity-modulated radiation therapy verification *Med Phys* **30** 1264–71

Hafeli U O, Roberts W K, Meier D S, Ciezki J P, Pauer G J, Lee E J and Weinhous M S 2000 Dosimetry of a W-188/Re-188 beta line source for endovascular brachytherapy *Med Phys* **27** 668–75

Haldar J, Aswal V K, Goyal P S and Bhattacharya S 2001 Molecular Modulation of Surfactant Aggregation in Water: Effect of the Incorporation of Multiple Headgroups on Micellar Properties *Angew Chem Int Ed Engl* **40** 1228–32

Hanks GE, Kerring DF, Kramer S Patterns of Care Study Newsletter, Carcinoma of the Cervix 1990-1991; Vol 1 Philadelphia, USA: American College of Radiology

Hartmann 2009 Radiotherapy and Brachytherapy - NATO Science for Peace and Security Series B: Physics and Biophysics pp.11–27

Hayashia S, Fujiwarab F, Usuia S and Tominagaa T 2012 Effect of inorganic salt on the dose sensitivity of polymer gel dosimeter *Rad Phys Chem* **81** 884-8

Hepworth S J, Leach M O and Doran S J 1999 Dynamics of polymerization in polyacrylamide gel (PAG) dosimeters: (II) modeling oxygen diffusion *Phys Med Biol* **44** 1875–84

Heufelder J, Stiefel S, Pfaender M, L demann L, Grebe G and Heese J 2003 Use of BANG polymer gel for dose measurements in a 68 MeV proton beam *Med Phys* **30** 1235–40

Hiraoka T, Fukuda N, Hoshino K 1992 Development of a gel phantom for dose distributions by MR imager *Nippon Acta Radiologica* **52** 1039–41

Hoecker F E and Watkins I W 1958 Radiation polymerization dosimetry *Int J Appl Radiat Isot* **3** 31–5

Howell R M, Smith I P and Jarrio C S 2008 Establishing action levels for EPID-based QA for IMRT *J Appl Clin Med Phys* **9** 2721

Hurley C, McLucas C, Pedrazzini G and Baldock C 2006 High-resolution gel dosimetry of a HDR brachytherapy source using normoxic polymer gel dosimeters: preliminary study *Nucl Instrum Methods Phys Res A* **565** 801–11

Ibbott GS 2010 QA in Radiation Therapy: The RPC Perspective *J Phys: Conf Ser* **250** 012001

Ibbott G S, Maryanski M J, Eastman P, Holcomb S D, Zhang Y, Avison R G, Sanders M and Gore J C 1997 Three-dimensional visualization and measurement of conformal dose distributions using magnetic resonance imaging of BANG polymer gel dosimeters *Int J Radiat Oncol Biol Phys* **38** 1097–103

International Commission on Radiation Units and Measurements (ICRU) 1976 Determination of Absorbed Dose in a Patient Irradiated by Beams of X or Gamma Rays in Radiotherapy Procedures. ICRU Report 24. Bethesda, MD: ICRU, 1976.

Isbakan F, Ulgen Y, Bilge H, Ozen Z, Agus O and Buyuksarac B 2007 Gamma Knife 3-D dose distribution near the area of tissue inhomogeneities by normoxic gel dosimetry *Med Phys* **34** 1623–30

Islam K T S, Dempsey J F, Ranade M, Maryanski M J and Low D A 2003 Initial evaluation of commercial optical-CT-based 3D gel dosimeter *Med Phys* **30** 2159–68

JGCM 2008 Evaluation of measurement data - guide to the expression of uncertainty in measurement available at www.bipm.org

Jin H, Palta J, Suh T S and Kim S 2008 A generalized a priori dose uncertainty model of IMRT delivery *Med Phys* **35** 982–96

Jirasek A, Carrick J and Hilts M 2012 An x-ray CT polymer gel dosimetry prototype: I. Remnant artefact removal *Phys Med Biol* **57** 3137–55

Jirasek A I, Duzenli C, Audet C and Eldridge J 2001 Characterization of monomer/crosslinker consumption and polymer formation observed in FT-Raman spectra of irradiated polyacrylamide gels *Phys Med Biol* **46** 151–65

Jirasek A, Rudko D, Wells D 2009 A prototype fan-beam optical CT scanner for polymer gel dosimetry *J Phys: Conf Ser* **164** 012025

Johnston H, Hilts M, Carrick J and Jirasek A 2012 An x-ray CT polymer gel dosimetry prototype: II. Gel characterization and clinical application *Phys Med Biol* **57** 3155–71

Jordan K and Avvakumov N 2009 Radiochromic leuco dye micelle hydrogels: I. Initial investigation *Phys Med Biol* **54** 6773–89

Karaiskos P, Petrokokkinos L, Tatsis E, Angelopoulos A, Baras P, Kozicki M, Papagiannis P, Rosiak JM, Sakelliou L, Sandilos P and Vlachos L 2005 Dose verification of single shot gamma knife applications using VIPAR polymer gel and MRI *Phys Med Biol* **50** 1235–50

Karlsson A, Gustavsson H, Mansson S, McAuley K B and Bäck S A J 2007 Dose integration characteristics in a normoxic polymer gel dosimetry investigated using sequential beam irradiation *Phys Med Biol* **52** 4697–706

Kennan R P, Maryanski M J, Zhong J and Gore J C 1992 Hydrodynamic effects and cross relaxation in cross linked polymer gels *Proc Int Soc for Magnetic Resonance in Medicine* (New York)

Khan F M 1993 The physics of radiation therapy *Lippincott Williams & Wilkins*, 2^{nd} edition

Kipouros P, Papagiannis P, Sakelliou L, Karaiskos P, Sandilos P, Baras P, Seimenis I, Kozicki M, Anagnostopoulos G and Baras D 2003 3D dose verification in Ir-192 HDR prostate monotherapy using polymer gels and MRI *Med Phys* **30** 2031–9

Korreman S S 2012 Motion in radiotherapy: photon therapy *Phys Med Biol* **57** R161–91

Krstajic N and Doran S 2006 Focusing optics of a parallel beam CCD optical tomography apparatus for 3D radiation gel dosimetry *Phys Med Biol* **51** 2055–75

Krstajic N and Doran S 2007 Fast laser scanning optical-CT apparatus for 3D radiation dosimetry *Phys Med Biol* **52** N257–63

Leer JW 1998 Practical guidelines for the implementation of a quality system in radiotherapy. ESTRO Physics for Clinical Radiotherapy Booklet No. 4. Brussels, Belgium: European Society for Therapeutic Radiology and Oncology (ESTRO)

Lepage M, Whittaker A K, Rintoul L, Bäck S A and Baldock C 2001 The relationship between radiation-induced chemical processes and transverse relaxation times in polymer gel dosimeters *Phys Med Biol* **46** 1061–74

Levitt S H, Purdy J A, Perez C A and Vijayakumar S 2006 Technical basis of radiation therapy Practical clinical applications *Springer*, 4th revised edition

Lin M H, Huang T C, Kao M J, Wu J, Chen C L, Wu T H 2009 Three-dimensional dosimetry in brachytherapy: A MAGAT study *Appl Radiat Isot* **67** 1432–7

Lopatiuk-Tirpak O, Langen K M, Meeks S L, Kupelian P A, Zeidan O A and Maryanski M J 2008 Performance evaluation of an improved optical computed tomography polymer gel dosimeter system for 3D dose verification of static and dynamic phantom deliveries *Med Phys* **35** 3447–59

Love P A, Evans P M, Leach M O and Webb S 2003 Polymer gel measurement of dose homogeneity in the breast: comparing MLC intensity modulation with standard wedged delivery *Phys Med Biol* **48** 1065–74

Low D A, Dempsey J F, Venkatesan R, Mutic S, Markman J, Haacke E M and Purdy J A 1999 Evaluation of polymer gels and MRI as a 3-D dosimeter for intensity-modulated radiation therapy *Med Phys* **26** 1542–51

Low D A, Moran J M, Dempsey J F, Dong L and Oldham M 2011 Dosimetry tools and techniques for IMRT *Med Phys* **38** 1313–38

MacDougall N D, Miquel M E and Keevil S F 2008 Effects of phantom volume and shape on the accuracy of MRI BANG gel dosimetry using BANG3 *Br J Radiol* **81** 46–50

Marks L B, Light K L, Hubbs J L, Georgas D L, Jones E L, Wright M C 2007 The impact of advanced technologies on treatment deviations in radiation treatment delivery *Int J Radiat Oncol Biol Phys* **69** 1579–86

Maryanski M J, Gore J C and Schulz R J 1992 3-D radiation dosimetry by MRI: solvent proton relaxation enhancement by radiation-controlled polymerisation and cross-linking in gels *Proc Int Soc for Magnetic Resonance in Medicine* (New York)

Maryanski M J, Schulz R J, Ibbott G S, Gatenby J C, Xie J, Horton D and Gore J C 1994 Magnetic resonance imaging of radiation dose distributions using a polymer-gel dosimeter *Phys Med Biol* **39** 1437–55

Maryanski M J, Zastavker Y Z and Gore J C 1996 Radiation dose distributions in three dimensions from tomographic optical density scanning of polymer gels: II. Optical properties of the BANG polymer gel *Phys Med Biol* **41** 2705–17

Mather M L and Baldock C 2003 Ultrasound tomography imaging of radiation dose distributions in polymer gel dosimeters: preliminary study *Med Phys* **30** 2140–8

Mayer R R, Ma F, Chen Y, Miller R I, Belard A, McDonough J, O'Connell JJ 2012 Enhanced dosimetry procedures and assessment for EBT2 radiochromic film *Med Phys* **39** 2147–55

McCullough and Holmes 1985 Acceptance testing of computerized radiation therapy treatment planning systems: Direct utilization of CT scan data *Med Phys* **12** 237–42

McJury M, Tapper P D, Cosgrove V P, Murphy P S, Griffin S, Leach M O, Webb S and Oldham M 1999 Experimental 3D dosimetry around a high-dose-rate clinical ^{192}Ir source using a polyacrylamide gel (PAG) dosimeter *Phys Med Biol* **44** 2431–44

Micke A, Lewis D F and Yu X 2011 Multichannel film dosimetry with nonuniformity correction *Med Phys* **38** 2523–34

Mijnheer B J 2007 Techniek in de radiotherapie, Hoofdstuk 12: Kwaliteitscontrole van radiotherapieapparatuur *Elsevier gezondheidszorg* 2^e druk, 1^e oplage, pp. 507–546

Mijnheer BJ, Battermann JJ, Wambersie A. 1987 What degree of accuracy is required and can be achieved in photon and neutron therapy? *Radiotherapy and Oncology* **8** 237–52.

Moutsatsos A, Petrokokkinos L, Karaiskos P, Papagiannis P, Georgiou E, Dardoufas K, Sandilos P, Torrens M, Pantelis E, Kantemiris I, Sakelliou L and Seimenis I 2009 Gamma knife output factor measurements using VIP polymer gel dosimetry. *Med Phys* **36** 4277–87

Morrison R 1975 The results of treatment of cancer of the bladder: a clinical contribution to radiobiology *Clin Radiol* **26** 67–75

Munro A J 2007 Hidden danger, obvious opportunity: error and risk in the management of cancer *Brit J Radiol* **80** 955–66

Novotny J Jr, Dvorak P, Spevacek V, Tintera J, Novotny J, Cechak T and Liscak R 2002 Quality control of the stereotactic radiosurgery procedure with the polymer-gel dosimetry *Radiother Oncol* **63** 223–30

Oldham M, McJury M, Baustert I B, Webb S and Leach M O 1998a Improving calibration accuracy in gel dosimetry *Phys Med Biol* **43** 2709–20

Oldham M 2006 3D dosimetry by optical-CT scanning *J Phys: Conf Ser* **56** 58–71

Oldham M, Baustert I, Lord C, Smith T A D, McJury M, Warrington A P, Leach M O and Webb S 1998b An investigation into the dosimetry of a nine-field tomotherapy irradiation using BANG-gel dosimetry *Phys Med Biol* **43** 1113–32

Oldham M, Siewerdsen J H, Shetty A and Jaffray D A 2001 High resolution gel-dosimetry by optical-CT and MR scanning *Med Phys* **28** 1436–45

Olding T and Schreiner L J 2011 Cone-beam optical computed tomography for gel dosimetry II: imaging protocols *Phys Med Biol* **56** 1256–79

Olsson L E, Fransson A, Ericsson A and Mattsson S 1990 MR imaging of absorbed dose distributions for radiotherapy using ferrous sulphate gels *Phys Med Biol* **35** 1623–31

Olsson L E, Westrin B A, Fransson A and Nordell B 1992 Diffusion of ferric ions in agarose dosimeter gels *Phys Med Biol* **37** 2243–52

Ottolenghi M and Stein G 1961 The radiation chemistry of chloroform *Radiat Res* **14** 281–90

Pantelis E, Antypas C, Petrokokkinos L, Karaiskos P, Papagiannis P, Kozicki M, Georgiou E, Sakelliou L and Seimenis I 2008 Dosimetric characterization of CyberKnife radiosurgical photon beams using polymer gels *Med Phys* **35** 2312–20

Papadakis A E, Maris T G, Zacharakis G, Papoutsaki V, Varveris C, Ripoll J and Damilakis J 2011 Technical Note: A fast laser-based optical-CT scanner for three-dimensional radiation dosimetry *Med Phys* **38** 830–5

Papagiannis P, Karaiskos P, Kozicki M, Rosiak J M, Sakelliou L, Sandilos P, Seimenis I and Torrens M 2005 Three-dimensional dose verification of the clinical application of gamma knife stereotactic radiosurgery using polymer gel and MRI *Phys Med Biol* **50** 1979–90

Papagiannis P, Pantelis E, Georgiou E, Karaiskos P, Angelopoulos A, Sakelliou L, Stiliaris S, Baltas D, Seimenis I 2006 Polymer gel dosimetry for the TG-43 dosimetric characterization of a new ^{125}I interstitial brachytherapy seed *Phys Med Biol* **51** 2101–11

Papagiannis P, Pappas E, Kipouros P, Angelopoulos A, Sakelliou L, Baras P, Karaiskos P, Seimenis I, Sandilos P and Baltas D 2001 Dosimetry close to an ^{192}Ir HDR source using N-vinylpyrrolidone based polymer gels and magnetic resonance imaging *Med Phys* **28** 1416–26

Pappas E, Seimenis I, Angelopoulos A, Georgolopoulou P, Kamariotaki Paparigopoulou M, Maris T, Sakelliou L, Sandilos P and Vlachos L 2001 Narrow stereotactic beam profile measurements using N-vinylpyrrolidone based polymer gels and magnetic resonance imaging *Phys Med Biol* **46** 783–97

Pappas E, Maris TG, Zacharopoulou F, Papadakis A, Manolopoulos S, Green S and Wojnecki C 2008 Small SRS photon field profile dosimetry performed using a PinPoint air ion chamber, a diamond detector, a novel silicon-diode array (DOSI), and polymer gel dosimetry. Analysis and intercomparison *Med Phys* **35** 4640–8

Perez CA, Stanley K, Rubin P, Kramer S, Brady L, Perez-Tamayo R, Brown GS, Concannon J, Rotman M and Seydel HG 1980 A prospective randomized study of various irradiation doses and fractionation

schedules in the treatment of inoperable Non-Oat cell carcinoma of the lung. *Cancer* **45** 2744–2753

Petrokokkinos L, Zourari K, Pantelis E, Moutsatsos A, Karaiskos P, Sakelliou L, Seimenis I, Georgiou E and Papagiannis P 2011 Dosimetric accuracy of a deterministic radiation transport based ^{192}Ir brachytherapy treatment planning system. Part II: Monte Carlo and experimental verification of a multiple source dwell position plan employing a shielded applicator *Med Phys* **38** 1981–92

Pourfallah T A, Allahverdi M, Alam N R, Ay M R, Zahmatkesh M H and Ibbott G S 2008 Performance evaluation of MRI-based PAGAT polymer gel dosimeter in an inhomogeneous phantom using EGSnrc code on a Co-60 machine *Appl Radiat Isot* **67** 186–91

Pourfallah T A, Allahverdi M, Alam N R, Ay M R, Zahmatkesh M H 2009 Differential dose volume histograms of Gamma knife in the presence of inhomogeneities using MRI-polymer gel dosimetry and MC simulation *Med Phys* **36** 3002–12

Ramm D, Rutten T P, Shepherd J, Bezak E 2012 Optical CT scanner for in-air readout of gels for external radiation beam 3D dosimetry *Phys Med Biol* **57** 3853–68

Rankine L and Oldham M 2013 On the feasibility of optical-CT imaging in media of different refractive index. *Med Phys* **40** 051701.

Rezansoff B J, McCallum K J and Woods R J 1970 Radiolysis of aqueous chloroform solutions *Can J Chem* **48** 271–6

Sakhalkar H, Adamovics J, Ibbott G and Oldham M 2009 A comprehensive evaluation of the PRESAGE/optical-CT 3D dosimetry system *Med Phys* **36** 71–82

Sakhalkar H S and Oldham M 2008 Fast, high-resolution 3D dosimetry utilizing a novel optical-CT scanner incorporating tertiary telecentric collimation *Med Phys* **35** 101–11

Salomons G J, Park Y S, McAuley K B and Schreiner L J 2002 Temperature increases associated with polymerization of irradiated PAG dosimeters *Phys Med Biol* **47** 1435–48

Sandilos P, Angelopoulos A, Baras P, Dardoufas K, Karaiskos P, Kipouros P, Kozicki M, Rosiak JM, Sakelliou L, Seimenis I and Vlahos L 2004 Dose verification in clinical IMRT prostate incidents *Int J Rad Oncol Biol Phys* **59** 1540–7

Sandilos P, Baras P, Georgiou E, Dardoufas K, Karaiskos P, Papagiannis P, Paschalis T, Tatsis E, Torrens M and Vlahos L 2006a Fast, three-dimensional, MR imaging for polymer gel dosimetric applications involving high-dose and steep dose gradients *Nucl Instrum Methods Phys Res A* **569** 572–6

Sandilos P, Tatsis E, Vlachos L, Karaiskos P, Georgiou E, Kipouros P, Torrens M and Angelopoulos A 2006b Mechanical and dose delivery accuracy evaluation in radiosurgery using polymer gels *J Appl Clin Med Phys* **7** 13–21

Scheib S G and Gianolini S 2002 Three-dimensional dose verification using BANG gel: a clinical example *J Neurosurg* **97** 582–7

Schreiner L J 2006 Dosimetry in modern radiation therapy: limitations and needs *J Phys: Conf Ser* **56** 1–13

Schreiner L J 2011 On the quality assurance and verification of modern radiation therapy treatment *J Med Phys* **36** 189-91

Sedaghat M, Bujold R and Lepage M 2010 Effect of the exothermal polymerization reaction on polymer gel dosimetric measurements *J Phys: Conf Ser* **250** 012018

Sedaghat M, Bujold R and Lepage M 2011a Severe dose inaccuracies caused by an oxygen-antioxidant imbalance in normoxic polymer gel dosimeters *Phys Med Biol* **56** 601–25

Sedaghat M, Bujold R and Lepage M 2011b Investigating potential physicochemical errors in polymer gel dosimeters *Phys Med Biol* **56** 6083–107

Shafiq J, Barton M, Noble D, Lemer C and Donaldson L J 2009 An international review of patient safety measures in radiotherapy practice *Radiother Oncol* **92** 15–21

Shukovsky LT 1970 Dose, time, volume relationships in squamous cell carcinoma of the supraglottic larynx *Am J Roentgenol* **108** 27–29

Skyt P S, Balling P, Petersen J B, Yates E S and Muren L P 2011 Temperature dependence of the dose response for a solid state radiochromic dosimeter during irradiation and storage *Med Phys* **38** 2806

Skyt P S, Kinnari T S, Wahlstedt I, Yates E S, Muren L P, Petersen J B B and Balling P 2013b Diffusion properties of a radiochromic hydrogel dosimeter *J Phys: Conf Ser* **444** 012038

Skyt P S, Wahlstedt I, Muren L P, Petersen J B, Balling P 2012 Temperature and temporal dependence of the optical response for a radiochromic dosimeter *Med Phys* **39** 7232–6

Skyt P S, Wahlstedt I, Yates E S, Muren L P, Petersen J B B and Balling P 2013a Exploring the dose response of radiochromic dosimeters *J Phys: Conf Ser* **444** 012036

Steward R D and Li A X 2007 BGRT: Biologically guided radiation therapy - The future is fast approaching *Med Phys* **34** 3739–51

Tarte B and van Doorn T 1993 Optical scanning of ferrous sulphate gels for radiotherapy treatment dosimetry *Proc. ACPSEM/BECON* 93

Taylor M L, Franich R D, Johnston P N, Millar R M, Trapp J V 2007 Systematic variations in polymer gel dosimeter calibration due to container influence and deviations from water equivalence *Phys Med Biol* **52** 3991–4005

Thomas A, Newton J, Adamovics J and Oldham M 2011b Commissioning and benchmarking a 3D dosimetry system for clinical use *Med Phys* **38** 4846–57.

Thomas A, Newton J and Oldham M 2011a A method to correct for stray light in telecentric optical-CT imaging of radiochromic dosimeters *Phys Med Biol* **56** 4433–51

Trapp J V, Kairn T, Crowe S and Fielding A 2009 Internal calibration of gel dosimeters: A feasibility study *J Phys: Conf Ser* **164** 012014

Tremblay N M, Hubert-Tremblay V, Bujold R, Beddar A S, Beaulieu L and Lepage M 2011 Accurate calibration of a polymer gel dosimeter with a plastic scintillation detector. *Med Phys* **38** 2754–61

Uusi-Simola J, Heikkinen S, Kotiluoto P, Sern T, Seppl T, Auterinen I, Savolainen S 2007 MAGIC polymer gel for dosimetric verification in boron neutron capture therapy *J Appl Clin Med Phys* **8** 114–23

Vandecasteele J and De Deene Y 2009a Optimization of a fast optical CT scanner for nPAG gel dosimetry *J Phys: Conf Ser* **164** 012024

Vandecasteele J and De Deene Y 2009b Preliminary evaluation of optical CT scanning versus MRI for nPAG gel dosimetry: the Ghent experience *J Phys: Conf Ser* **164** 012034

Vandecasteele J, Ghysel S, Baete S H and De Deene Y 2011 Radiophysical properties of micelle leucodye 3D integrating gel dosimeters *Phys Med Biol* **56** 627–51

Vandecasteele J and De Deene Y 2013a On the accuracy and precision of 3D polymer gel dosimeters: I. Reproducibility study *Phys Med Biol* **58** 19–42

Vandecasteele J and De Deene Y 2013b On the accuracy and precision of 3D polymer gel dosimeters: II. Physico-chemical effects *Phys Med Biol* **58** 43–61

Vandecasteele J and De Deene Y 2013c On the accuracy and precision of 3D polymer gel dosimeters: III. MRI-related error sources *Phys Med Biol* **58** 63–85

Vandecasteele J and De Deene Y 2013d Evaluation of radiochromic gel dosimetry and polymer gel dosimetry in a clinical dose verification *Phys Med Biol* **58** 6241–62

Van Doorn T, Bhat M, Rutten T P, Tran T and Costanzo A 2005 A fast, high spatial resolution optical tomographic scanner for measurement of absorption in gel dosimetry *Australas Phys Eng Sci Med* **28** 76–85

Vergote K, De Deene Y, Claus F, De Gersem W, Van Duyse B, Paelinck L, Achten E, De Neve W and De Wagter C 2003 Application of monomer/polymer gel dosimetry to study the effects of tissue inhomogeneities on intensity-modulated radiation therapy (IMRT) dose distributions *Radiother Oncol* **67** 119–28

Vergote K, De Deene Y, Duthoy W, De Gersem W, De Neve W and Achten E 2004a Validation and application of polymer gel dosimetry for the dose verification of an intensity-modulated arc therapy (IMAT) treatment *Phys Med Biol* **49** 287–305

Vergote K, De Deene Y, Vanden Bussche E and De Wagter C 2004b On the relation between the spatial dose integrity and the temporal instability of polymer gel dosimeters *Phys Med Biol* **49** 4507–22

Watanabe Y, Akimitsu T, Hirokawa Y, Mooij R B and Perera G M 2005 Evaluation of dose delivery accuracy of Gamma Knife by polymer gel dosimetry *J Appl Clin Med Phys* **6** 133–42

Watanabe Y, Gopishankar N, 2010 Three-dimensional dosimetry of TomoTherapy by MRI-based polymer gel technique *J Appl Clin Med Phys* **12** 3273

Wolodzko J G, Marsden C and Appleby A 1999 CCD imaging for optical tomography of gel radiation dosimeters *Med Phys* **26** 2508–13

World Health Organization (WHO) 1988 Quality Assurance in Radiotherapy. Geneva: WHO

World Health Organization (WHO) 2008 Radiotherapy Risk Profile - Technical Manual Geneva: WHO

Wustneck R, Wetzel R, Buder E and Hermel H 1988 The modification of the triple helical structure of gelatin in aqueous solution I. The influence of anionic surfactants, pH-value, and temperature *Colloid Polym Sci* **266** 1061–7

Wuu C-S, Schiff P, Maryanski M J, Liu T, Borzillary S and Weinberger J 2003 Dosimetry study of Re-188 liquid balloon for intravascular brachytherapy using polymer gel dosimeters and laser-beam optical-CT scanner *Med Phys* **30** 132–7

Xu Y and Wuu C-S 2004 Performance of a commercial optical-CT scanner and polymer gel dosimeters for 3D dose verification *Med Phys* **31** 3024–33

Xu Y, Wuu C S and Maryanski M J 2010 Sensitivity calibration procedures in optical-CT scanning of BANG 3 polymer gel dosimeters *Med Phys* **37** 861–8

Yan D, Vicini F, Wong J and Martinez A. 1997 Adaptive radiation therapy *Phys Med Biol* **42** 123-32

Yeo U J, Taylor M L, Supple J R , Smith R L, Dunn L, Kron T and Franich R D 2012 Is it sensible to deform dose? 3D experimental validation of dose-warping *Med Phys* **39** 5065

Zeidan O A, Sriprisan S I, Lopatiuk-Tirpak O, Kupelian P A, Meeks S L, Hsi W C, Li Z, Palta J R, Maryanski M J 2010 Dosimetric evaluation of a novel polymer gel dosimeter for proton therapy *Med Phys* **37** 2145–52

Zhao L, Newton J, Oldham M, Das IJ, Cheng CW, Adamovics J. 2012 Feasibility of using PRESAGE for relative 3D dosimetry of small proton fields. *Phys Med Biol* **57** N431–43

Zimmerman J R and Brittin W E 1957 Nuclear magnetic resonance studies in multiple phase systems: lifetime of a water molecule in an adsorbing phase on silica gel *J Phys Chem* **61** 1328

Publications in international journals

1. Steven Baete, **Jan Vandecasteele**, Luc Colman, Wilfried De Neve and Yves De Deene 2010 An oxygen-consuming phantom simulating perfused tissue to explore oxygen dynamics and F-19 MRI oximetry *Magnetic Resonance in Physics and Medicine* **23** 217-26

2. Steven Baete, **Jan Vandecasteele** and Yves De Deene 2011 19F MRI oximetry: simulation of perfluorocarbon distribution impact *Physics in Medicine and Biology* **56** 2535-57

3. **Jan Vandecasteele**, Sara Ghysel, Steven Baete and Yves De Deene 2011 Radio-physical properties of micelle leucodye 3D integrating gel dosimeters *Physics in Medicine and Biology* **56** 627-51

4. **Jan Vandecasteele** and Yves De Deene 2013 On the validity of 3D polymer gel dosimetry, I: reproducibility study *Physics in Medicine and Biology* **58** 19-42

5. **Jan Vandecasteele** and Yves De Deene 2013 On the validity of 3D polymer gel dosimetry, II: physico-chemical effects *Physics in Medicine and Biology* **58** 43-61

6. **Jan Vandecasteele** and Yves De Deene 2013 On the validity of 3D polymer gel dosimetry, III: MRI-related error sources *Physics in Medicine and Biology* **58** 63-85

7. **Jan Vandecasteele** and Yves De Deene Evaluation of radiochromic gel dosimetry and polymer gel dosimetry in a clinical dose verification *Physics in Medicine and Biology* **58** 6241-6262

Publications in international conferences

1. **Jan Vandecasteele** and Yves De Deene 2009 Optimization of a fast optical CT scanner for nPAG gel dosimetry *Journal of Physics: Conference Series* **164** 012024

2. Giuliana Russo, **Jan Vandecasteele**, Tom Vercauteren, Salvatore De Pasquale and Yves De Deene (2009) Reproducibility study of normoxic polyacrylamide gel (nPAG) dosimeters *Journal of Physics: Conference Series* **164** 012010

3. **Jan Vandecasteele** and Yves De Deene 2009 Comparison of optical CT imaging versus NMR imaging for nPAG gel dosimetry *IFMBE Proceedings* **22** 936-9

4. **Jan Vandecasteele** and Yves De Deene 2009 Preliminary evaluation of optical CT scanning versus MRI for nPAG gel dosimetry: the Ghent experience *Journal of Physics: Conference Series* **164** 012034

5. **Jan Vandecasteele**, Sara Ghysel and Yves De Deene 2010 Dose rate dependency of micelle leucodye 3D gel dosimeters *Journal of Physics: Conference Series* **250** 012009

6. **Jan Vandecasteele** and Yves De Deene 2013 Polymer gel dosimetry of an electron beam in the presence of a magnetic field *Journal of Physics: Conference Series* **444** 012104

7. **Jan Vandecasteele** and Yves De Deene 2013 Optical laser scanning of a leucodye micelle gel: preliminary results of a 3D dose verification of an IMRT treatment for a brain tumor *Journal of Physics: Conference Series* **444** 012053

8. Yves De Deene, **Jan Vandecasteele** and Tom Vercauteren 2013 Low-density polymer gel dosimeters for 3D radiation dosimetry in the thoracic region : A preliminary study *Journal of Physics: Conference Series* **444** 012026

9. Yves De Deene and **Jan Vandecasteele** 2013 On the reliability of 3D gel dosimetry *Journal of Physics: Conference Series* **444** 012015

Publications in national conferences

1. Charlotte Bauwens, Yves De Deene, **Jan Vandecasteele** and Steven Baete 2010 Development of a three-dimensional optical sensitive radiation dosimeter for high-precision radiation therapy *Annual symposium of the Belgian Hospital Physicists Association, 25th, Abstracts* 14

2. **Jan Vandecasteele**, Frederic Duprez and Yves De Deene 2010 Pitfalls for 3D dosimetry for the verification of an IMRT treatment *Annual symposium of the Belgian Hospital Physicists Association, 25th, Abstracts* 37

3. **Jan Vandecasteele** and Yves De Deene 2012 Overall accuracy and precision of MRI polymer gel dosimetry: investigation of physicochemical and MRI error sources *Annual symposium of the Belgian Hospital Physicists Association, 27th, Abstracts* 58

4. **Jan Vandecasteele** and Yves De Deene 2013 3D dose verification of an IMRT treatment for a brain tumor: Optical laser scanning of a leucodye gel versus MRI scanning of a polymer gel *Annual symposium of the Belgian Hospital Physicists Association, 28th, Abstracts* 124